GSI

FAIR

ECRIS 24

26th International Workshop on Electron Cyclotron Resonance Ion Sources

15.-19. September 2024

Welcome Hotel City Center
Darmstadt
GERMANY

PROCEEDINGS

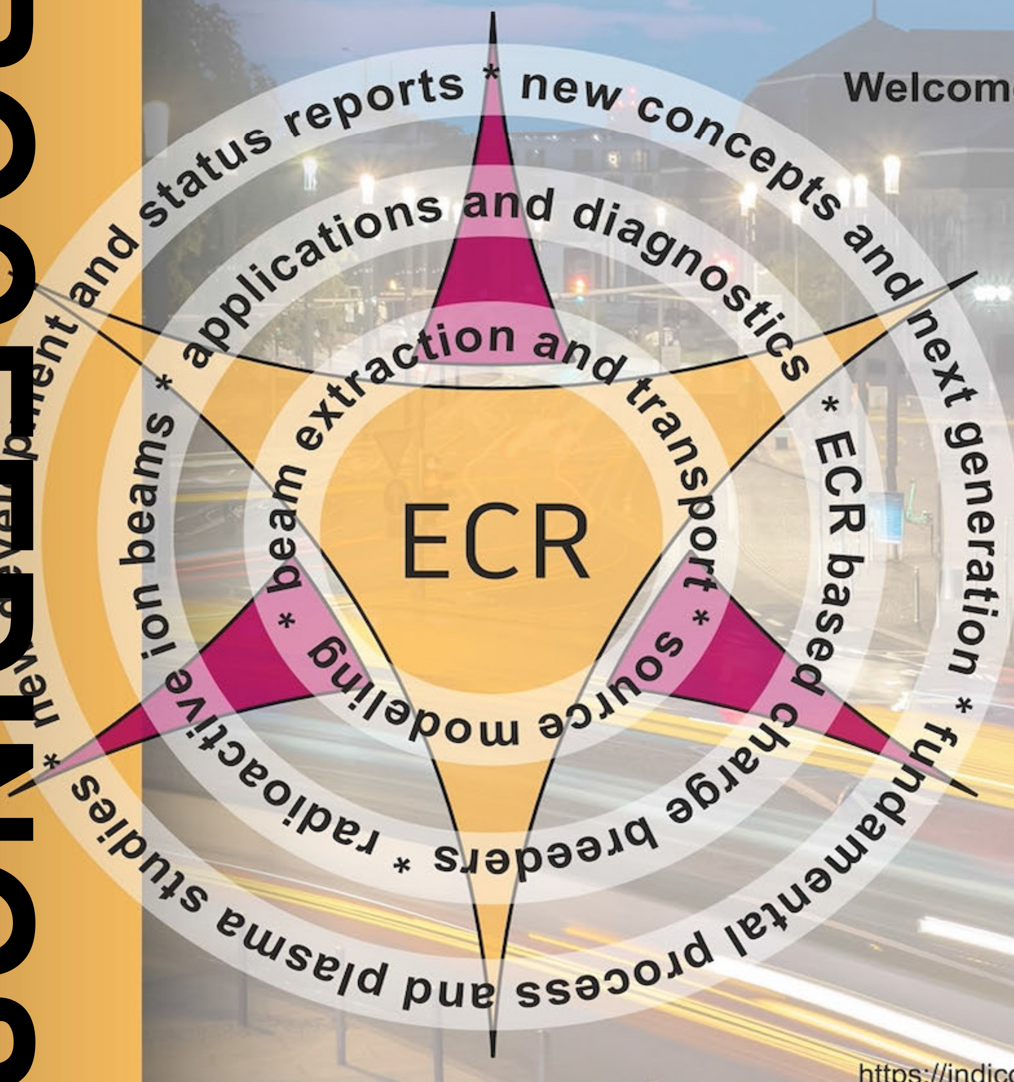

ScanMe

Picture: © J.Mäder

https://indico.gsi.de/event/17948/overview

Dear colleagues and participants of ECRIS2024,

GSI/FAIR was honored to host the 26th International Workshop on ECR Ion Sources (ECRIS2024), which took place from Sunday, September 15 to Thursday, September 19 2024 at the Welcome Hotel in the city center of Darmstadt, Germany.

ECRIS2024 was the 26th event in a long-standing series that began in Karlsruhe, Germany, in 1978. More recent editions were held in Busan, Korea (2016), Catania, Italy (2018), East Lansing, USA (2020), and Gandhinagar, India (2022).

The ECRIS Workshop focused on the design, construction, development, and operation of ECR ion sources and their components. It emphasized operational experience with existing facilities, advances in the physics and technology of plasmas and ion sources, progress in new projects and infrastructure modernization, as well as trends in the proposal, design, and application of ion sources for ion beam production and their associated systems.

The scientific program covered a wide range of topics related to ECR ion sources and associated research:

o New development and status reports
o New concepts and next generation
o Fundamental process and plasma studies
o ECR-based charge breeders
o Radioactive ion beams
o Applications and diagnostics
o Beam extraction and transport
o Source modelling

A total of 61 contributions were submitted: 31 oral presentations and 30 posters. Eleven oral presentations were held from Monday, September 16 to Wednesday, September 18 in the main conference hall of the conference Hotel. Two poster sessions were held on Monday, September 16 and Tuesday, September 17 afternoons in a dedicated conference area at the conference Hotel.

The final session, including the closing remarks, took place on Thursday, September 19 at the main lecture hall of GSI in Darmstadt.

Social activities included an excursion to the city of Frankfurt am Main, featuring a river cruise on the Main and a social dinner in the heart of the city. In addition, participants were offered a guided tour of the GSI accelerator complex and the FAIR construction site.

In recognition of outstanding contributions to the field of ECR ion sources and to encourage promising young researchers, Pantechnik—the world leader in commercial ECR ion sources—awarded the 7th *Richard Geller Prize* during the workshop. Dr. Junwei Guo, from FRIB at Michigan State University (East Lansing, USA), was selected by the award committee as the recipient of the prize *"for his extensive contribution to the development and operations of high-frequency superconducting ECR ion sources."*

The event was financially supported by seven sponsors. Their generous contributions are gratefully acknowledged, as they were primarily used to reduce the conference fee for students, thereby fostering early-career engagement within the community and strengthening collaboration with industrial partners.

On behalf of the local organizing committee, it was my great pleasure and honor to welcome and meet the 89 participants of ECRIS2024.

Sincerely,

Fabio Maimone
Chairman of ECRIS2024

International Advisory Committee (IAC)

Fabio Maimone	Chair	GSI	Germany
Sandor Biri		ATOMKI	Hungary
Luigi Celona		INFN-LNS	Italy
Atsushi Kitagawa		NIRS	Japan
Hannu Koivisto		JYFL	Finland
Guillaume Machicoane		FRIB-MSU	USA
Laurent Maunoury		Normandy Hadrontherapy	France
Takahide Nakagawa		RIKEN	Japan
Liangting Sun		IMP	China
Thomas Thuillier		LPSC	France
Sudhirsinh Vala		IPR	India
Richard C. Vondrasek		ANL	USA
Mi-Sook Won		KBSI	South Korea
Daniel Xie		Lawrence Berkeley Lab	USA

Local Organizing Committee (LOC)

Fabio Maimone	Chair	GSI	Germany
Frank Herfurth		GSI	Germany
Wolfgang Geithner		GSI	Germany
Ralph Hollinger		GSI	Germany
Aleksey Adonin		GSI	Germany
Rustam Berezov		GSI	Germany
Ralf Lang		GSI	Germany
Jan Mäder		GSI	Germany
Aleksandr Andreev		GSI	Germany
Michael Galonska		GSI	Germany

ECRIS Workshop Secretariat (EWS)

Paola Lindenberg	GSI	Germany
Lea Wunderlich	GSI	Germany

JACoW Editorial Team (JET)

Raphael Müller	GSI	Germany
Volker RW Schaa	GSI	Germany

Contents

ISBN: 978-3-95450-257-8 ISSN: 2222-5692 doi:10.18429/JACoW-ECRIS2024-MOA3

DEVELOPMENT TOWARDS INTENSE URANIUM ION BEAM PRODUCTION OF THE RIKEN 28 GHz SC-ECRIS

G. Q. Saquilayan†, Y. Higurashi, T. Nagatomo, J. Ohnishi, O. Kamigaito
RIKEN Nishina Center for Accelerator Based Science, Wako, Japan

Abstract

With the ongoing beam development for high intensity uranium beam production, we report the status and progress of the RIKEN 28-GHz Superconducting Electron Cyclotron Resonance Ion Source. The achieved beam currents for the uranium U^{35+} beam has reached up to 250 eμA as a result of optimizing the material consumption rates for high intensity beam production. The target beam intensity for U^{35+} is expected to yield 10 mA of extraction current and the analysis of beam emittance is estimated to be in the range of 0.25 π mm mrad. Furthermore, a semi-empirical method was used to examine a so-called initial emittance value and growth that correspond to space charge effects. Experiments to further investigate the initial beam emittance and the influence of space charge effects are still ongoing.

INTRODUCTION

High intensity Uranium U^{35+} ion beams are produced in the 28 GHz superconducting electron cyclotron resonance ion source (SC-ECRIS) and accelerated to high energies in the Radioactive Isotope Beam Factory (RIBF) at RIKEN [1]. With the increased demand for even higher intensity uranium beams for various nuclear physics research in RIBF, efforts have been made towards improving the performance of the SC-ECRIS. Currently, beam intensities for U^{35+} has reached up to 250 eμA beam current. This was possible through development techniques in optimizing the material consumption rates aimed at high intensity beam production [2]. Investigating the beam quality through beam emittance is the next step to confirm unforeseen issues of beam loss and aberrations along beamline components which is detrimental to the accelerator.

There have been many experimental and numerical studies on the beam emittance growth of the extracted beam from the ECRIS [3-5]. The analysis of beam emittances is complex since the ion source operational parameters, space charge effects and beamline components can easily affect the beam during transport.

The beam emittance from the ECRIS has been known to be mainly influenced by the ion temperature and the axial magnetic field at the extraction region [6]. In the case of highly charged ion production, electrons have much higher temperatures than ions and it has been a reasonable assumption that the dominant contributing factor to beam emittance is the magnetic field effect. Space charge effects on produced ion beams in the ECRIS have also been widely studied since this defocusing of the beam leads to growth in the emittance size and is found to be proportional to the beam intensity. In addition, interaction with downstream components along the beamline must also contribute to an emittance growth. In this paper, beam emittance measurement and analysis of the uranium U^{35+} beam is presented. A systematic study of different operational ECRIS parameters and its effect on the beam emittance size is examined.

URANIUM BEAM PRODUCTION

The RIKEN 28-GHz superconducting ECR ion source (SC-ECRIS) has been developed for providing high intensity heavy ion beams for the RI beam factory. Details regarding the design of the ion source has been previously reported [7]. Superconducting coil assembly with six solenoid coils and one hexapole coil allows the adjustment of the magnetic field at the B minimum to have control on the magnetic field gradient. This means it can produce a mirror magnetic field distribution from the so-called “classical B_{min}” to “Flat B_{min}” [8]. Basic specifications for the RIKEN 28-GHz ECRIS are listed in table 1.

Table 1: Specifications for the R28-GHz SC-ECRIS

Operational Frequency	28 GHz, 18GHz
Max. RF Power	10kW
Max. Magnetic Field	3.8 T
Max. Extraction	22 kV
Chamber Dimensions	Ø150 mm L525 mm
Extraction Aperture Radius	5 mm

With plans to improve the accelerator in the RIBF for studies on nuclear physics now requires output beam intensities of U^{35+} at 300 eμA from the ECRIS. Improvements on the design and performance of the high temperature oven was a crucial factor in increasing the achievable uranium beam intensities. Optimization of the material consumption rates which aimed at high intensity beam production has then allowed the beam current to reach 250 eμA.

With accumulated data sets for U^{35+} beam production, the beam intensity with respect to microwave power is shown in Fig. 1a. Assuming a linear relation between the two parameters, beam currents of 300 eμA will need ~4kW of microwave power and the corresponding extraction currents will be in the range of 10 mA as shown in Fig. 1b. From these expected beam conditions, ion source parameters should be checked thoroughly since high power operation may have some unforeseen issues in the ion source.

† glynnismae.saquilayan@riken.jp

ISBN: 978-3-95450-257-8 ISSN: 2222-5692 doi:10.18429/JACoW-ECRIS2024-MOA3

It is also important that before continuing towards operating at higher range of beam intensities, the beam quality should also be checked and confirm good beam optics to avoid any damages to the accelerator.

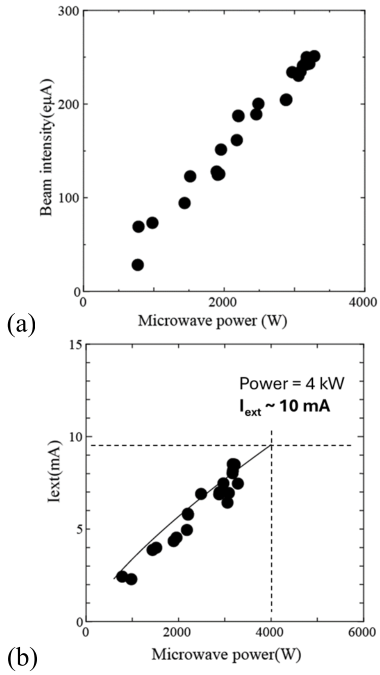

Figure 1: Measurements of uranium U^{35+} beam parameters with respect to microwave power: (a) beam intensity and (b) extraction current.

Measurement of Beam Emittance

The highly charged ions generated in the SC-ECRIS are extracted and then separated using a dipole analyzing magnet. Beam emittances are measured in the diagnostics chamber after mass separation. In the diagnostics chamber, a movable slit is used to scan across the beam and the emittance signals are measured from wire scanners. Other diagnostic tools such as a Faraday cup and profile monitors were used to confirm the beam parameters. The normalized root mean square emittances ε_{nrms} were calculated from the experimental measurements. In previous studies on the U^{35+} extracted beam from the SC-ECRIS, the beam focusing solenoid lens showed separate effects on the horizontal and vertical beam emittances [9]. For low solenoid coil current operation, the focusing effect is weaker and the horizontal x component was found to be around 0.1 π mm mrad larger than the vertical y component. This suggested possible beam aberration may occur along the beamline, as it passes through the dipole analyzing magnet down to the diagnostics chamber. Reduction of the beam size was possible with stronger focusing of the solenoid lens. However, strong focusing may result in a difference in the beam edge focusing angle and these uncertainties should be carefully considered in the analysis of beam emittances.

DISCUSSION

The measured beam emittance of uranium beams was analyzed with different beam conditions. One of the parameters that was observed to greatly influence the measured emittances is the extraction current. Over a range of generated beam intensities, the normalized rms y-emittance at a fixed extraction current of 5.5 mA showed small variations as shown in Fig. 2. For a 50 eμA difference in beam intensities, the obtained beam emittances did not greatly change and was constant around 0.15 π mm mrad.

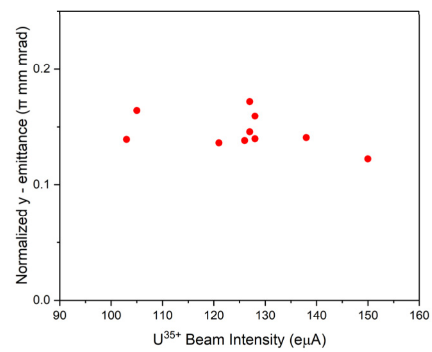

Figure 2: Normalized rms y-emittance measurements over the range of produced beam intensities for uranium U^{35+} having a fixed extraction current of 5.5 mA.

The extraction current represents the sum of all ion species present in the extracted beam. Because of this proportionality, the extraction current was used as a good indicator for estimating the total beam current of the ECRIS.

Examining the effect of the extraction ion current, the x and y normalized rms beam emittances for uranium of 35+ ion charge state with the operational microwave frequency of 28 and 18 GHz is shown in Fig. 3. As previously discussed, the x-component of the beam emittance measurement shows higher emittance values due to possible beam aberration on beamline components. From here on, we will examine only the y-component of beam emittance to avoid any uncertainties in the analysis. With the minimal influence on the beamline components, we can assume that the measured normalized beam emittance can be described by a simple equation,

$$\varepsilon = \sqrt{\varepsilon_0^2 + K(I_{ext})^2} \quad [\pi \text{ mm mrad}] \qquad (1)$$

where ε is the normalized rms beam emittance, ε_0 is an initial beam emittance in π mm mrad, K is a constant describing the beam distribution and I_{ext} is the extraction current in mA [10-11]. The term KI_{ext}^2 is assumed to be related to the effect of space charge where I_{ext} is used to indicate the total beam current. Using Eq. (1), the ε_0 can be determined with the assumption that I_{ext} approaches zero and reveals the initial value to be 0.067 π mm mrad. As shown in Fig. 4, the data measurements and calculated values for ε_0 and ε beam emittances are plotted against the extraction current.

To reach the target beam requirement for U^{35+}, it will be necessary to operate the SC-ECRIS with microwave power at ~4 kW and is expected to generate extraction currents in the range of 10 mA. Using the calculated ε, the normalized

ISBN: 978-3-95450-257-8 ISSN: 2222-5692 doi:10.18429/JACoW-ECRIS2024-MOA3

beam emittance at extraction current of 10 mA is estimated to reach 0.25 π mm mrad. These are the predicted beam conditions for high intensity beam operation of uranium U^{35+} at 300 eμA beam current.

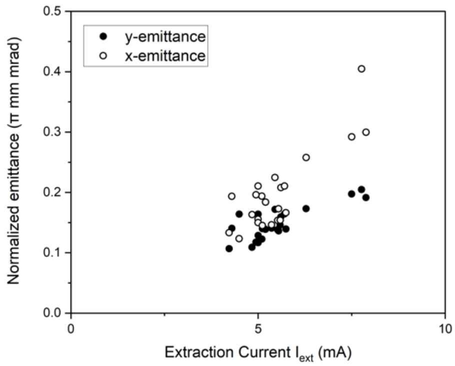

Figure 3: Normalized rms emittance measurements for uranium U^{35+} at different extraction currents.

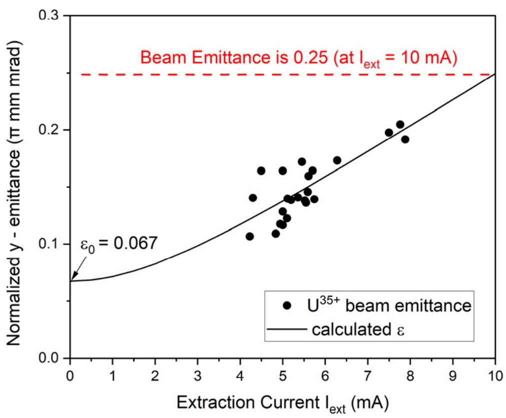

Figure 4: Normalized rms y-emittance measurements for uranium U^{35+} at different extraction currents with the calculated initial beam emittance ε_0 and emittance growth ε.

Based on the measurements, beam conditions with low total current can lead to smaller beam emittance sizes. However, achieving this condition will be challenging while having the objective of producing high beam intensities. As a next step, the optimum ECR parameters to produce high intensity beams will be investigated. A systematic study of the variable ECR parameters such as the microwave power, material consumption rates, and magnetic field strength distribution, will be performed to determine an optimization map and identify the suitable parameters for high intensity beam operation of U^{35+}.

In addition, other steps being considered are space charge compensation techniques to further lower the emittance sizes when necessary. Fundamental studies to understand the beam dynamics in the extraction region are essential and this will be used to properly formulate strategies for space charge beam compensation.

The calculated values for ε_0 represents an initial beam emittance when $I_{ext} = 0$. This may correspond to an emittance influenced by the ion source conditions. As shown in Fig. 5, the graph shows both values for ε_0 and the calculated curves for the magnetic field emittances given by the axial magnetic field strength at the extraction region. The normalized magnetic field emittance is described by the equation [12],

$$\varepsilon_{mag} = 0.032 r^2 B_0 \frac{1}{M/Q} \quad [\pi \text{ mm mrad}] \qquad (2)$$

where r is the radius of the extraction aperture in mm, B_0 is the magnetic field strength in Tesla at the extraction region, and M/Q is the dimensionless mass-charge ratio. Comparing the obtained values of ε_0 to the ε_{mag}, it is found that the experimental measurements have lower emittance sizes. One explanation may be due to the assumptions made for the ε_{mag} having a uniform distribution of the beam size which is often estimated through the diameter of the extraction electrode aperture. From the beam generation in the ECRIS, multiple ion species are co-extracted simultaneously in the extraction region which can affect the effective beam size of a single ion species examined in the beam emittance measurements. Experiments will continue to further investigate the possible beam dynamics that occur during beam extraction.

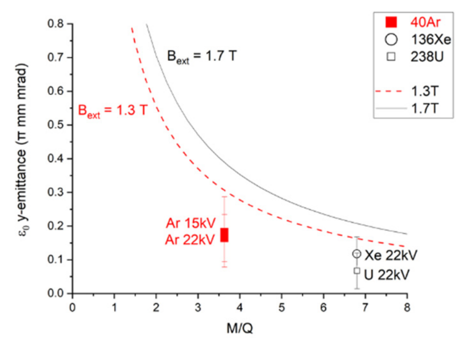

Figure 5: Calculated values for the initial beam emittance ε_0 over the range of mass-charge M/Q values.

Table 2: Parameters for the Different Ion Beams

Ion	V_{ext} (kV)	M/Q	ε_0	K
Ar^{11+}	15	3.6	0.18	3.4E-3
Ar^{11+}	22	3.6	0.16	5.1E-4
Xe^{20+}	22	6.8	0.13	6.7E-4
U^{35+}	22	6.8	0.06	5.7E-4

The calculated values for the different beam conditions are compared in Table 2. For the case of Ar^{11+} ions, experiments with different extraction voltages indicate a difference in their particle velocities. This difference is reflected on the values for the parameter K which is related to space-charge like effects, where the emittance growth is steeper for lower particle velocities. In the case for ions with the same M/Q such as Xe^{20+} and U^{35+} ions, the two beam conditions have the same extraction voltages such that the observed space-charge like effects are both similar. As I_{ext} approaches zero, the initial emittance ε_0 values which may be

ISBN: 978-3-95450-257-8 ISSN: 2222-5692 doi:10.18429/JACoW-ECRIS2024-MOA3

related to the ion source parameters showed a difference in the calculated values. This difference is thought to be influenced by the spatial distribution relating to the angular momentum of the ions caused by the axial magnetic fields during beam extraction. Further investigation is necessary to confirm these effects.

SUMMARY

Development of the RIKEN 28-GHz SC-ECRIS is moving towards intense uranium ion beam production aiming for the beam requirement of ~300 eμA for U^{35+}. Uranium beams up to 250 eμA has been achieved through the development of the high temperature oven to yield optimized material consumption rates for high intensity beam production. As progress moves towards more intense beams, the beam emittance growth was investigated from the experimental measurements. A semi-empirical method was tested and the using the conditions for the target beam requirement, the beam emittance at 10 mA extraction current was estimated to reach 0.25 π mm mrad. Emittance values that correspond to an initial beam emittance and emittance growth relating to space charge effects are being investigated.

REFERENCES

[1] Y. Yano, "The RIKEN RI beam factory project: A status report", *Nucl. Instrum. Methods B*. vol. 261 p.1009, 2007. doi:10.1016/j.nimb.2007.04.174

[2] Y. Higurashi, *et. al*., "Producing intense uranium ion beam for RIKEN RI beam factory*", J. Phys.: Conf. Ser*., Vol. 2743, p.012051, 2024. doi:10.1088/1742-6596/2743/1/012051

[3] D. Leitner, *et. al.*, "Ion beam properties for ECR ion source injector systems", *JINST* Vol. 6, p.P07010, 2011. doi:10.1088/1748-0221/6/07/P07010

[4] V. Mironov, *et. al.*, "Numerical model of electron cyclotron resonance", *Phys. Rev. ST Accel. Beams* Vol. 18, p.123401, 2015. doi:10.1103/PhysRevSTAB.18.123401

[5] D. Winklehner, *et. al.*, "Comparison of extraction and beam transport simulations with emittance measurements from the ECR ion source venus", *JINST* Vol. 5, p.P12001, 2010. doi:10.1088/1748-0221/5/12/P12001

[6] R. Geller, *Electron Cyclotron Resonance Ion Source and ECR Plasmas*. London, UK. Institute of Physics Publishing, 1996.

[7] T. Nakagawa, *et. al.*, "First results from the new RIKEN superconducting electron cyclotron resonance ion source", *Rev. Sci. Instrum.,* Vol. 81, p.02A320, 2010. doi:10.1063/1.3259232

[8] G. D. Alton and D. N. Smithe, "Design studies for an ECR ion source", *Rev. Sci. Instrum.,* Vol. 65, pp775-787, 1994. doi:10.1063/1.1144954

[9] Y. Higurashi, *et. al.*, "Recent developments of RIKEN 28-GHz SC-ECRIS", in *Proc. of 22nd Int. Workshop on ECR ion sources*, Busan, South Korea, Aug – Sept 2016, pp.10-13. doi:10.18429/JACoW-ECRIS2016-WEBO01

[10] G. Q. Saquilayan, *et. al*., "Beam Emittance Growth of Highly Charged Ion Beams from the RIKEN 28-GHz SC-ECRIS*", J. Phys.: Conf. Ser*., Vol. 2743, p.012081, 2024. doi: 10.1088/1742-6596/2743/1/012081

[11] Y. Batygin, "Dynamics of intense particle beam in axial-symmetric magnetic field" *Nucl. Instrum. Methods A*, Vol. 772, pp.93-102, 2015. doi:10.1016/j.nima.2014.10.034

[12] W. Krauss-Vogt, *et. al.*, "Emittance and matching of ECR sources", *Nucl. Instrum. Methods A*, Vol. 268, p.5, 1988. doi:10.1016/0168-9002(88)90586-4

ISBN: 978-3-95450-257-8 ISSN: 2222-5692 doi:10.18429/JACoW-ECRIS2024-MOB1

GANIL ION SOURCES: OPTIMISATION FOR OPERATION

M. Dubois, F. Lemagnen, L. Gouleuf, V. Metayer, B. Osmond
GANIL, Grand Accélérateur National d'Ions Lourds, CEA-DSM/CNRS-IN2P3, Caen, France

Abstract

The GANIL (Grand Accélérateur National d'Ions Lourds) in Caen has been producing and accelerating stable and radioactive ion beams for nuclear physics, atomic physics, radiobiology and materials irradiation since 1982.

Long-term stability of the beam, which is a key parameter for accelerator operation and success of physics experiments is targeted. At the same time, improving stability will also reduce the need of on-call work for ion source experts.

Recently, studies and tests have been carried out to increase the intensity and/or stability of the metal ion beams by modifying the injection of the ion source on ECR4/4M. Depending on the configuration, the gain on intensity shall be up to a factor of 2 on the charge state required for acceleration, and stability has also been improved compared to previous one.

INTRODUCTION

GANIL laboratory is initially based on Cyclotron accelerators able to produce Carbone to Uranium ion beam with a maximum energy of 95MeV/u. To provide ion beams, two 14 GHz ECR4/4M ion sources [1, 2] are installed into the machine injectors. They provide around 4000 hours of total beam per year, of several type of ions (Fig. 1).

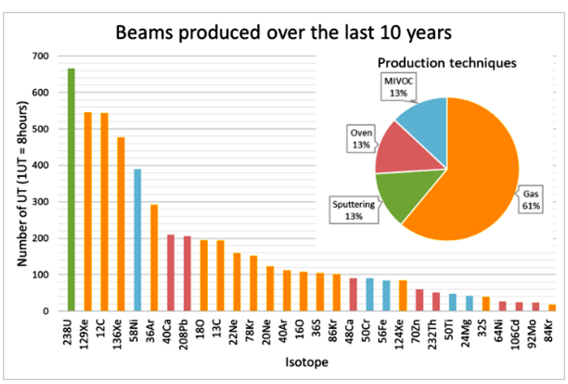

Figure 1: Beams produced by ECR4/4M over the last 10 years.

On the new SPIRAL2 accelerator (based superconducting LINAC), two injectors are installed: One dedicated to light element (2.45 GHz – H^+/D^+), and one dedicated to heavy ions (18 GHz – A/Q<3 - Phoenix V3). Main beams produced are currently proton and deuteron beams for Neutron for Science experimental hall, until the S^3 facility starts its experimental programme in 2026.

New experimental facilities will be set up in the coming years to offer more scientific possibilities for physicists. At the same time, new projects are being under construction or studied to deliver new attractive ion beams (Fig. 2).

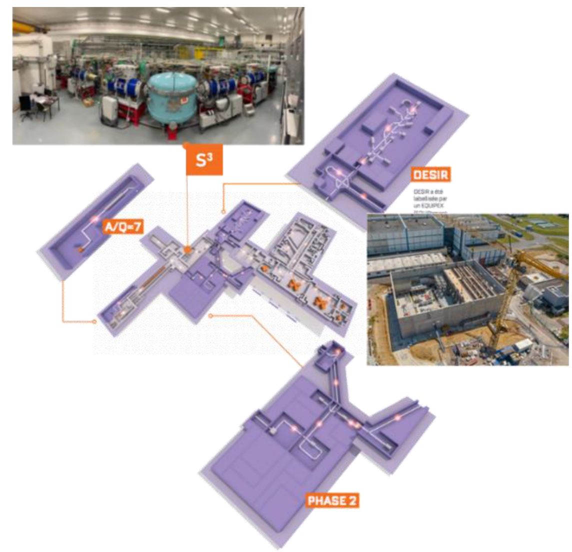

Figure 2: Layout of actual and future building at GANIL.

S^3

The Super Separator Spectrometer (S^3) [3] set up will start running in 2026 for the production and studies of super heavy elements. To create them, a high intense heavy ion beams (Q/A=1/3 => $^{14}Ca^{14+}$, $^{48}Ca^{16+}$, $^{58}Ni^{19+}$, 2 pμA) have to be provide by the heavy ion source injector on SPIRAL2 over a long period (3 weeks–1.5 month).

DESIR

DESIR [4] experimental hall, currently under construction, will use radioactive ion beams produced by S^3 and SPIRAL1 facility at 2027 horizon for experiments with low energy beams.

NEWGAIN (A/Q<7)

The NEWGAIN project [5] aims to install a new injector (Ion source + RFQ) for the SPIRAL2 accelerator with the goal of accelerating a beam characterized by A/Q<7.

A new 28 GHz superconducting ions source ASTERICS [6] is being studied to provide a 10 pμA of metallic beams up to ^{238}U. The new low-energy beamline and a RFQ are currently under construction and will start operating by 2028. The ion source will be assembled and commissioned at LPSC, Grenoble and hence moved to GANIL by 2030.

Future Upgrade for GANIL-SPIRAL2

Beyond 2030, future upgrade applied to GANIL-SPIRAL2 [7] is under evaluation: the design of a new radioactive ion beam (RIB) production facility that will be able to provide RIBs to DESIR for low-energy experiments or to adapt the beam to accelerate it to a range of 50–70 MeV/u before sending it to GANIL's existing experimental areas.

ISBN: 978-3-95450-257-8 ISSN: 2222-5692 doi:10.18429/JACoW-ECRIS2024-MOB1

CHALLENGES FOR FUTURE OPERATION AT GANIL-SPIRAL2

By 2030, GANIL aims to increase the beam time available on both machine, to over seven months per year. This represents a significant challenge, as it requires the simultaneous operation of multiple ion sources, each optimized for specific operations.

By 2026, S^3 will requiring new metallic ion beams optimised to deliver an intensity up to 2 pμA, initially with the A/Q<3 SPIRAL2 injector, and up to 10 pμA with the new Asterics 28 GHz SC ion source injector (A/Q<7).

Combined with these objectives, the aim of the cyclotron facility is to ensure that the facility can meet the demands of the nuclear physics community for the next 20 years. This requires continuous improvement in term of stability, intensity, and operational reliability. To achieve this objective, a project is underway to increase the reliability of the cyclotron accelerator complex, by changing or refurbishing the old power supplies, RF cavities, cooling system, etc.

CYCLOTRON ION SOURCES OPTIMISATION

Requirements for performances of ion sources on cyclotron accelerators are to provide beams with medium charge states of beam from Carbon to Uranium, with an intensity in the range of 1 μAe to a maximum of 50 μAe (maximum intensity usable by cyclotron). ECR4/4M ion sources are able to produce beams from gaseous and metallic elements by using several technique, like sputtering rod, oven and MIVOC. For the next 20 years, some studies are underway to evaluate the possibility to change ion sources to increase intensities available for physicist, especially for beams between Nickel to Uranium where ECR4/4M ion sources have some intensities limitation.

In the meantime, some studies was carried out on current ions sources to optimise the stability and improve intensities.

Stability

Cyclotron ion sources are located in the main cyclotrons building, where temperature variations of up to 10 °C can be observed depending on external conditions, leading to fluctuations in several parameters (extraction pressure, drain current, beam intensity). As a result, operators must regulary adjust parameters to stabilize the beam intensity. For example, in 2022 with $^{48}Ca^{10+}$ beam, 15 adjustments were necessary over two days to limit the intensity variation around 40 %. The initial source settings gradually degrade, which requiring sometimes a complete tuning by an expert. Analysis revealed that the UDV valves were the most sensitive to external conditions. To fix this, a temperature regulation at 40 °C was installed around the valves, immediately stabilizing the injected flux. Improvement was observed with a $^{129}Xe^{23+}$ beam, showing around 5 % stability over four days without adjustments. This was also noted with metallic beams with $^{238}U^{31+}$ beam. Online adjustments were reduced during 15 days operation: 45 in 2023 compare to 5 in 2024.

Diagnostic

On-line non interceptive diagnostic is one of the main requirement for monitoring ion sources, particularly when beam is delivered as part of physics experiments. Optical Emission Spectroscopy (OES) is a technique already used in other laboratories [8]. In our case, an optical fibre was installed directly behind a glass window in line with the injection source. This location allows us to be close to the plasma and effectively detect the photons emitted by plasma. Connected to the optical fibre, a visible light spectrometer (model FLAME from OceanOptics) measure intensities emitted on a range of wavelengths between 350 nm and 1000 nm.

To evaluate this technique for on-line diagnostic, a plasma of Argon + Helium was produced, with an intensity of 80 μAe of $^{40}Ar^{9+}$ measured on Faraday cup after the mass separator. A measurement of light emitted by the plasma was carried out and analysed to get an initial situation of the plasma parameters (Fig. 3).

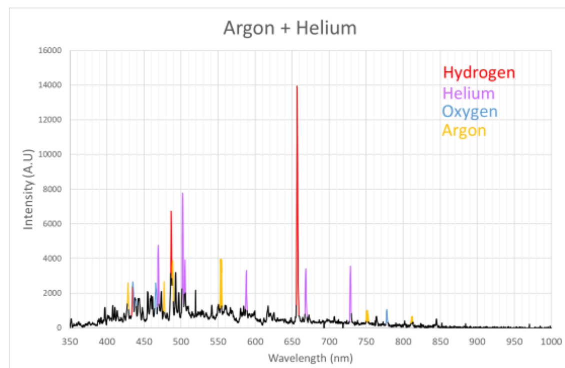

Figure 3: Measurement of light emitted by Argon + Helium plasma on ECR4M. Identification of wavelength: Hydrogen (H I= 656 nm), $^{40}Ar^{9+}$ (Ar X = 553 nm) and Helium (He I = 668 nm). *Data from the NIST website database.*

Ion source parameters was monitored along 2 days without any tuning modifications: intensity on FC, drain current, extraction pressure, building temperature (Fig. 4) and intensities of the three wavelength selected (Fig. 5).

Conclusions of these measurements are:

- Outgassing from the vacuum chamber due to rising building temperatures leads to hydrogen pollution in the plasma. This uncontrolled hydrogen altering the initial tuning and affecting the source delivered intensities. To improve beam stability, controlling this pollution is necessary.
- The OES used as diagnostic is able to give information about the quantity of elements present into the plasma. That mean it's possible to have an idea of intensities extracted by the source without interceptive measurements as show with Ar^{9+} in Fig. 5. This technique have to be used for metallic ion beam to estimate atom flux deliver by the oven along the time.

These measurement shown that it could be interesting to develop a specific diagnostic to help operators during experiments.

ISBN: 978-3-95450-257-8 ISSN: 2222-5692 doi:10.18429/JACoW-ECRIS2024-MOB1

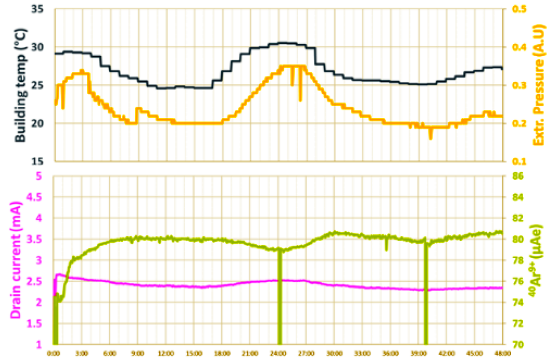

Figure 4: Evolution of ion source parameters and building temperature.

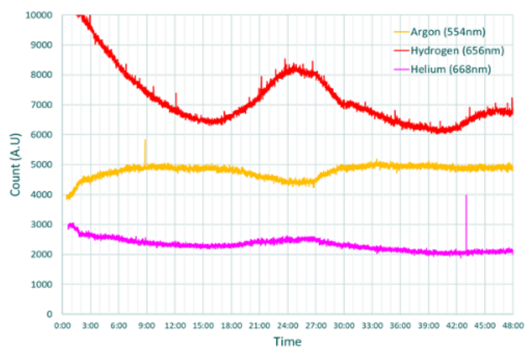

Figure 5: Evolution of light intensities of selected wavelengths.

Improvements of Metallic Ion Beams

Up to 2021, the standard ECR4/4M ion source configuration was used, especially at the injection side where oven, sputtering rods and MIVOC technic was designed to be inserted into the coaxial RF tube transition. This situation involve some limitations, especially considering the diameter of device have to be insert close to plasma chamber. Moreover, electrical configuration of the high voltage platform/cabinet did not allow to bias the oven.

Since 2021, tests have been carried out to adapt the source injection to better optimised devices. For example, we observed limitations when using the MIVOC technique concerning the amount of vapour that could be injected into the plasma chamber due to the low conductance between the sample and the plasma chamber. In 2022, the original coaxial tube was removed and replaced by a wider tube between the sample and the plasma chamber. The results show that we were able to increase the intensity of the $^{58}Ni^{11+}$, with better stability for more than 2 weeks without any technical problems.

Uranium Beam and High Temperature Oven The uranium beam has been the most used beam at GANIL over the last 10 years. Up until now, the sputtering method was used to produce this beam. Following the development of the resistive high-temperature oven [9] at GANIL, a test of uranium production from a UO_2 compound was carried out on the ECR4M source. The source injection was modified to accommodate this new oven, which has an external diameter of 20 mm. In this configuration, the oven acts as a coaxial tube for RF injection.

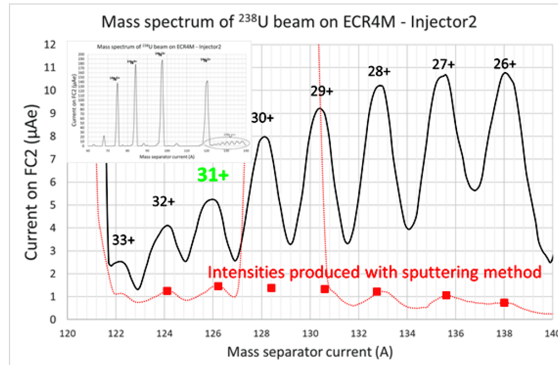

Figure 6: Charge state distribution of Uranium beam produce with HT Oven. Conditions: Oven 107 A (>1900 °C), N_2 support gas, HV: 20.6 kV, RF power: 400 W, no bias.

Results of this test shown:

- The resistive HT Oven is able to evaporate UO_2 into an high magnetic field configuration.
- Performances with oven are better than sputtering method (× 3.3 on 31^+, × 5 on 28^+), see Fig. 6.
- RF transmission is not affected by the size of oven.

The beam was tested for 3 days with an intensity of 3 µAe of $^{238}U^{31+}$.

Bias Oven Applied for Metallic Ion Beam Production Bias disc effect is a technique used to improve the extraction of beam, especially for high charge state beam [10]. To evaluate the potential improvement for metallic ion beams at GANIL, a test was carried out with Lead beam on injector 2-ECR4M. First of all, a standard configuration was used, without bias oven or coaxial tube. After optimisation to maximize 28^+ charge state, performances were similar to reference [11]. Secondly, the electrical configuration was changed to be able to bias the oven. An optimisation was done on 28^+ charge state. The results meet with conclusions of bias disc effect: The beam transport up to the first faraday cup increase by a factor 2 (average on all charge state), and the intensities extracted from the ion source increased for high charge states (Fig. 7).

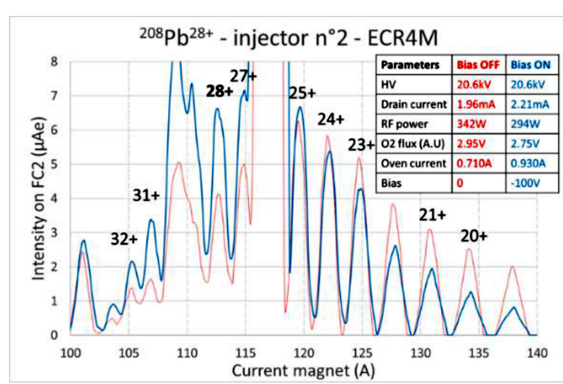

Figure 7: Charge states distribution comparison between bias oven and no bias oven.

ISBN: 978-3-95450-257-8 ISSN: 2222-5692 doi:10.18429/JACoW-ECRIS2024-MOB1

Another tests was performed with O, Ar, Xe gas and results are similar. Conclusion is that the used of bias oven can improve all metallic ion beam produce by oven technique by a factor of 2. In consequence, electrical configuration is under modification on both cyclotron injectors to get the possibility of biasing oven for the future beams.

SPIRAL2 HEAVY ION SOURCE

The A/Q<3 injector will be used to provide high intensity, high charge state metallic and gaseous beams to LINAC for long term operation (3 weeks to 1.5 month depending the physics experiments). To meet the requirement, a 18 GHz room temperature ion source was designed, and commissioning at LPSC up to 2019, called Phoenix V3. Intensities produced by the ion source are close to required intensities (i.e >10 pµAe for light gaseous beam (O, Ne, Ar) and between 1 and 2 pµAe for metallic one (Ca, Ni).

Reliability

After one year of operation and commissioning at GANIL (40 kV and 60 kV operation), technical problems have been identified to meet with long-term 60 kV operation. Investigations and modifications have been done between 2022 and 2023 to improve reliability of the injector:

- The injection plug was adapted to protect the bias discs insulators to reduce metallisation. At the same time, the hole for oven port has been increase to 25 mm.
- The extraction electrodes have been modified, in length and shape to protect insulator to metallisation.
- The coils located in iron yoke has been protected from internal insulator by stainless steel liner and a Kapton layer because of electric impact was observed.

Metallic Beams Optimisation

The ^{48}Ca beam is a beam requested for the S^3 scientific programme. Because of the rarity of this isotope, an effort must be made to maximise the efficiency of the ion source in order to reduce isotope consumption. One way to reduce this consumption is to use a hot liner installed in the plasma chamber, the aim of which is to re-evaporate the calcium atoms that have not interacted with the plasma.

This technique was tested with the Phoenix V3 ion source and a 0.1 mm Tantalum liner was inserted into the plasma chamber. After a period of outgassing, Tantalum pollution was observed on the mass spectra, and the experiment was then interrupted. Finally, a hole appeared in the liner, revealing a degradation of the radial magnetic field. Magnetic field measurements confirmed this degradation (Fig. 8).

The hexapole was dismantled from the ion source and investigations were carried out. Finally, a magnet was found broken (30° S near the main pole magnet).

All these modification were effective by spring 2024. Last results for He^{2+} an $^{40}Ar^{14+}$ indicated an improvement on beam intensities around 20 % ($^{40}Ar^{14+}$: 130 => 156 µAe; $^{4}He^{2+}$: 4.3 => 5 mA).

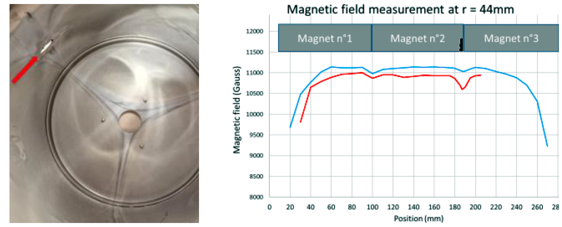

Figure 8: Hole on Tantalum liner (left), radial magnetic field measurement before (red) and after (bleu) repair.

CONCLUSION AND PERSPECTIVES

GANIL got ambitious objectives about technical development to increase beam time with new setup for physics experiments. On cyclotron, some ways are existing to improve the beam quality coming from ECR4/4M ion source meanwhile a potential new ion sources installation. These improvements have now to be used on-line after an electrical adaptation on HV platform.

On SPIRAL2, heavy ion source is now reliable and available to progress on beams development. A program is identified to reach 2 pµA for species like ^{48}Ca, ^{50}Cr, ^{50}Ti, by using new inductive/resistive high temperature oven, recycling technique, double frequency, OES.

REFERENCES

[1] P. Sortais *et al.*, “Ecris development at GANIL”, *Rev. Sci. Instrum.*, vol. 61, pp. 288–290, 1990. doi:10.1063/1.1141324

[2] R. Leroy *et al.*, “ECRIS optimisation for on line production”, in *Proc. 12th ECRIS Workshop*, Wako, Japan, 25-27 Apr 1995, Japan, vol. INS-J-182, p. 57. https://inis.iaea.org/collection/NCLCollectionStore/_Public/28/037/28037314.pdf

[3] A. Douart *et al.*, “The Super Separator Spectrometer (S^3) for the SPIRAL2 facility”, *J. Phys.: Conf. Ser.*, vol. 1643, p. 012032, 2020. doi:10.1088/1742-6596/1643/1/012032

[4] B. Blank, “The DESIR facility at SPIRAL2”, *Pramana-J. Phys.*, vol. 75, pp. 343-353, 2010. doi:10.1007/s12043-010-0121-9

[5] M. H. Moscatello *et al.*, “NEWGAIN project at GANIL-SPIRAL2: design of the new heavy ion injector for the superconducting linac”, in *Proc. IPAC’23*, Venice, Italy, May 2023, pp. 1765-1767. doi:10.18429/JACoW-IPAC2023-TUPA193

[6] T. Thuillier *et al.*, “ASTERICS, a new 28 GHz electron cyclotron resonance ion source for the SPIRAL2 accelerator”, *J. Phys.: Conf. Ser.*, vol. 2743, p. 012059, 2024. doi:10.1088/1742-6596/2743/1/012059

[7] H. Franberg Delahaye *et al.*, “Future upgrades for GANIL”, in *Proc. IPAC’24*, Nashville, TN, May 2024, pp. 1199-1201. doi:10.18429/JACoW-IPAC2024-TUPC79

[8] F. Maimone *et al.*, “Stable and intense Ca ion beam production with a microwave shielded oven and an optical spectrometer as diagnostic tool”, in *Proc. ECRIS’20*, East Lansing, MI, USA, Sep. 2020, pp. 50–53. doi:10.18429/JACoW-ECRIS2020-MOZZO03

ISBN: 978-3-95450-257-8 ISSN: 2222-5692 doi:10.18429/JACoW-ECRIS2024-MOB1

[9] O. Bajeat *et al.*, "Metal evaporation study using the GANIL high temperature oven for intense metal ion beams production", *J. Phys.: Conf. Ser.*, vol. 2244, p. 012017, 2022. doi:10.1088/1742-6596/2244/1/012017

[10] L. Kenéz *et al.*, "Study of the biased-disc effect using Langmuir-probes inserted in the hot region of the electron cyclotron resonance ion source (ECRIS) plasma", *Phys. Lett. A*, vol. 372, no. 16, pp. 2887-2892, 2008. doi:10.1016/j.physleta.2007.12.037

[11] C. Barue *et al.* "Status Report on Metallic Beam Production at GANIL/SPIRAL 2", in *Proc. ECRIS2016*, Busan, Korea, Aug.-Sep. 2016, pp. 92–97. doi:10.18429/JACoW-ECRIS2016-WEPP05

ISBN: 978-3-95450-257-8 ISSN: 2222-5692 doi:10.18429/JACoW-ECRIS2024-MOB2

ECRIS OPERATION AND DEVELOPMENTS AT TRIUMF

F. Ames*, J. Adegun, C.R.J. Charles, K. Jayamanna, O. Kester, B. Schultz
TRIUMF, Wesbrook Mall Vancouver BC, Canada

Abstract

Rare isotope beams are used at the ISAC facility at TRIUMF for studies mainly in nuclear and astrophysics and applications ranging from material science to medicine. The isotopes are produced via the ISOL technique and ionized via a set of different ion sources depending on the application. In cases where highly charged ions are needed charge state breeding is done with a 14.5 GHz PHOENIX ECR ion source from PANTECHNIK. The source has been operational for over a decade, providing a wide range of ions from Na to U at A/Q < 7 for post-acceleration. A second ECR ion source, a SUPERNANOGAN, also from PANTECHNIK, is used to provide highly charged ions from stable isotopes either for set-up and calibration for the rare isotope beams or for nuclear reaction studies with stable ions. A summary of the results and the challenges and improvements to the original sources are presented. For the charge state breeding, this mainly optimizes the efficiency and purity of the delivered beams. In the case of the SUPERNANOGAN, special emphasis is put on operational aspects to cover a wide range of elements and ensure easy switchover. The latest in this series of improvements is the implementation of two-frequency plasma heating in both ion sources.

INTRODUCTION

At most rare isotope beams facilities, highly charged ions are not produced directly after the production target, but singly or low charged ions are injected into an ion source for charge state breeding like ECR ion sources or Electron Beam Ion Sources (EBIS) [1]. This allows the decoupling of the isotope production process in a highly radioactive environment and the production of the highly charged ions in a more accessible and controllable area. At TRIUMF, rare isotopes are produced by impinging up to 100 μA of 480 MeV protons on one of two solid targets. The targets are kept at high temperatures to allow the products to diffuse into an ion source for singly charged ions. Extracted ions are accelerated to up to 60 keV, mass separated and guided either directly to experiments or into a post accelerator, which consists of an RFQ, a room temperature drift tube linac (DTL) and a superconducting accelerator [2]. In the case of masses A > 30, higher charge states are needed for the post-acceleration, which is achieved by injecting the ions into the charge state breeder source and selecting the desired charge state with a Nier-type spectrometer before sending them to the accelerator [3]. The intensity of the rare isotopes can vary from up to several nA for isotopes close to stability to only a few per second for the most exotic ones. That means high efficiency for the charge state breeding is needed. In most cases the intensity of ions from the support gas of the ECRIS but also from residual gas and impurities of the source materials exceeds the intensity of the desired ions by many orders of magnitude. It is imperative to minimize the amount of residual gas and other impurities as much as possible by using high-purity gases and materials close to the ECR plasma and selecting a charge state of the radioactive ions with minimum overlap. Even with this, further purification by stripping at higher energy may be needed. Tools have been developed to guide this purification process and to choose the most optimal conditions for the experiments. Additionally, a SUPERNANOGAN ECR ion source from PANTECHNIK, part of the TRIUMF Off-line Ion Sources (OLIS) terminal, provides pilot beams for setting up the accelerators and stable ion beams for the experiments.

CHARGE STATE BREEDING

Several changes to the original design of the source have been implemented. Already shortly after taking it into operation in 2005 at a test set-up, it became clear that both the injection and extraction optics were not ideal for the requirement to operate at different voltages to match the energy acceptance of the RFQ (2.04 keV*A/Q). A two-step deceleration and acceleration scheme has been implemented on both sides, which gives the flexibility to operate at a source voltage between 10 and 15 kV. The next big change was the exchange of the stainless steel plasma chamber for aluminum and the application of an additional coating of pure aluminum to it in 2012. This reduced the background of ions from the stainless-steel components and slightly increased the efficiency. In 2014, the original Klystron RF amplifier was replaced by a TWT, which allowed some small-range frequency tuning. Most recently, two, two-frequency plasma heating has been implemented. It uses one waveguide to transport microwave power at two frequencies between 13 and 14.5 GHz into the source at up to 200 W each. Besides increasing the global charge breeding efficiency, it also shifts the charge state distribution to higher charges. More details and results are described in [4].

Charge State Distributions and Efficiencies

Figure 1 shows the charge state Q with the maximum intensity, or the one used for the experiment as a function of the atomic number Z, for all stable or radioactive isotopes used so far. The solid line indicates the minimum charge state, which is needed to satisfy the acceptance of the accelerator chain of A/Q < 7. It shows that up to about Z = 65, the charge state with the highest efficiency for the charge state breeding can be chosen. For neutron deficient isotopes the required charge state is lower, whereas for neutron rich isotopes a higher charge state is needed. For higher atomic

* ames@triumf.ca

ISBN: 978-3-95450-257-8 ISSN: 2222-5692 doi:10.18429/JACoW-ECRIS2024-MOB2

numbers, a higher charge state may be used with some losses. The different values for the same atomic number reflect the need for different charge states for different numbers of neutrons or for improvements over the years of operation. The heaviest radioactive isotope delivered to an experiment so far is the neutron-deficient isotope $^{158}_{68}$Er with a charge state of 23+. Figure 2 shows the efficiency of the charge state

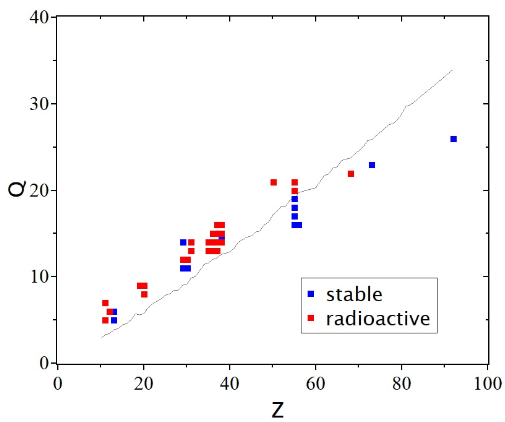

Figure 1: Charge state with the maximum intensity as a function of the atomic number Z red radioactive (see text for details).

breeding to the charge state of radioactive ions used for the experiment again as a function of the mass. It can be up to about 7 % for ideal cases, but in general it is around 3 %. The efficiency for radioactive ions, as used by the experiment in many cases, is slightly lower than for stable ions. Using the two-frequency plasma heating up to 9 % have been achieved for $^{133}Cs^{26+}$ [4]. The most abundant charge state cannot be used in many cases due to the background at this A/Q value. Additionally, losses due to the decay reduce the efficiency of short-lived isotopes. Again, different values for the same mass reflect changes over time.

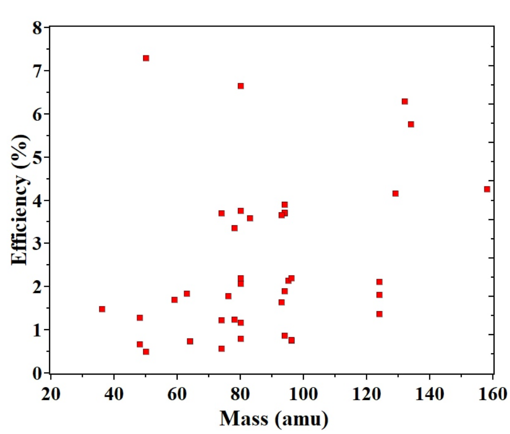

Figure 2: Efficiency for the charge breeding of radioactive ions as a function of mass as used for experiments.

Purification

Figure 3 shows a typical ion current as a function of A/Q in the interesting region between 5 and 7 from the charge breeder source. Although the source was operated with pure He gas, charge states of isotopes of C, O, N, and Ar can be clearly identified, besides some other less abundant elements. Some of the peaks can go up to the μA level. The figure shows the change in the spectrum after exchanging the stainless steel plasma chamber for aluminum. Ion intensities from Fe, Ni, Mo, and other common components of steel are significantly reduced or missing. Even with this, the background intensity at an A/Q value can be orders of magnitude higher than that of the desired radioactive isotope. A

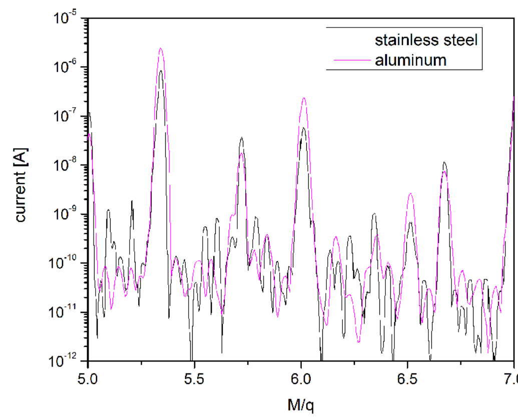

Figure 3: Ion current as a function of mass to charge ratio from the charge state breeder [3].

possible solution to this would be operating at an ultra-high vacuum. The TRIUMF source operates in the mid 10^{-8} Torr range. That means even an improvement of 2 or 3 orders of magnitude, which might be possible, will not completely solve this problem. Another option is an increase in mass resolving power for selecting the desired A/Q value. With a 4 rms emittance of about 20 μA from the source, this would be very costly if no major beam losses can be accepted. TRIUMF has chosen a more pragmatic way of dealing with this problem [5]. First, a software tool has been developed which lets the operator select the charge state, which is still close to the maximum in the charge state distribution but with a minimum in the background. It identifies possible background ions from stable elements within an A/Q window of 1/200, the resolving power of the charge state selector. The total intensity is based on previous measurements and identifications of the components. After this, the mass dependencies of the linear accelerator components, like the RF phases, are used to add further resolving power. Finally, if more background reduction is needed, a stripper foil can be introduced after the DTL at an energy of 1.5 MeV/u. Although the stripping will introduce some losses, it will eliminate nearly all ions with a different mass, as they will end up in different A/Q values. Only direct isobars can remain, but

ISBN: 978-3-95450-257-8 ISSN: 2222-5692 doi:10.18429/JACoW-ECRIS2024-MOB2

depending on the Z dependence of the stripping efficiency, they can be reduced as well.

OFF-LINE ION SOURCE

The TRIUMF off-line ion source (OLIS) provides beams of stable isotopes as pilot beams for beamline and accelerator setup and for experiments with accelerated stable beams. For setup and tuning, currents around 1 nA are usually sufficient. Intensities for accelerated stable isotopes for experiments may be up to the space charge limit of the accelerator around a few μA. Three ion sources are available to cover the entire mass range. A surface source is mainly used for alkali elements. A 2.45 GHz microwave-driven plasma ion source can deliver singly to low-charge ions. This source is operated mainly with gaseous elements, but it can also deliver other elements evaporated from an oven or from sputter samples. The third one is an ECR ion source (a 14.5 GHz SUPERNANOGAN from PANTECHNIK) for highly charged ions. Similar to the plasma ion source, it can deliver beams of gaseous elements and of condensable elements from ovens or via sputtering [6, 7].

Recent Results

The OLIS ECR ion source has been equipped with two-frequency heating. A TWT RF amplifier operating between 12.75 GHz and 14.5 GHz with an output power of up to 200 W and a solid-state amplifier with the same frequency range and maximum power of 50 W. Contrary to the charge breeder source, the two different RF frequencies can be coupled via two waveguides. Most recent results have been published in [8]. In most cases, a total power below 100 W is sufficient to deliver the desired intensities and charge states. For optimization, the frequencies and power can be scanned independently by observing the output current at the desired A/Q value to find the best conditions. Typically, the difference is around 0.8 GHz. As an example, 12.98 GHz and 13.78 GHz in the case of Kr ions. With dual-frequency heating, the current has increased by a factor of 2 compared to single-frequency heating at the same total power. As this source is very efficient compared to the microwave plasma source, it can also be used to deliver low-charged ions. This is important in cases where expensive materials are used or yields from evaporation or sputtering are low. An example of this is Cerium. It was used for an experiment to produce CeF molecules by sending a beam of Ce^{+} or Ce^{2+} through a gas reaction cell. Ce was produced by sputtering, and the support gas pressure in the ECR ion source was adjusted so that highly charged ions were suppressed, and only the low charges remained [9].

FUTURE DEVELOPMENTS

Charge State Breeder Improvements

Although the efficiency of the charge state breeding has improved over the past years, it is still lower than reported in other places [1]. Detailed ion optical simulations have shown that the reason for this is mainly the ion injection into the source. The present design uses an opening in the iron joke for the solenoid field, which has an asymmetric cutout. This is used for connecting the waveguide for the RF and the gas inlet. It introduces steering to the injected beam, which is difficult to compensate, and ions can be lost. A new design has been developed which uses a cylindrical symmetric yoke. It will also require some changes to the plasma chamber, which then allows the connection of two waveguides. Details of the new design are presented in [10].

Off-line Ion Source

Constant developments are underway to improve reliability and stability and meet the experimenters' requests for specific beams from the off-line ECR ion source. This mainly involves changes to the gas inlet system to optimize for specific gas compositions and testing and optimizing materials to be used in the oven or as sputtering targets. With its present configuration, the ion source is not optimized for the operation at a wide range of ion energies as required for the experiments. This causes beam losses in the transport, especially in the section close to the source. Although this is usually not a big problem for stable ions, it can cause instabilities in the beam. Beam losses that cause sputtering and material deposition make frequent cleaning and maintenance of this beamline section necessary. Therefore, a two-step acceleration at the extraction is being developed in a manner similar to that of the charge breeder source. It will be accompanied by changes in the ion optical components directly after the extraction to match the new design to the beam transport.

REFERENCES

[1] L. Maunoury, N. Bidault, J. Angot, A. Galata, R. Vondrasek, and F. Wenander, "Charge breeders: Development of diagnostic tools to probe the underlying physics", *Review of Scientific Instruments*, vol. 93, no. 2, p. 021 101, 2022. doi:10.1063/5.0076254

[2] P. G. Bricault, F. Ames, M. Dombsky, P. Kunz, and J. Lassen, "Rare isotope beams at ISAC—target & ion source systems", *Hyperfine Interactions*, vol. 225, no. 1-3, pp. 25–49, 2014. doi:10.1007/s10751-013-0880-z

[3] F. Ames, R. Baartman, P. Bricault, and K. Jayamanna, "Charge state breeding of radioactive isotopes for ISAC", *Hyperfine Interactions*, vol. 225, no. 1-3, pp. 63–67, 2014. doi:10.1007/s10751-013-0882-x

[4] J. Adegun, F. Ames, and O. Kester, "Upgrade and Improvement of the TRIUMF ECRIS Charge State Booster", in *Journal of Physics: Conference Series*, p. 012 064, 2024. doi:10.1088/1742-6596/2743/1/012064

[5] M. Marchetto, F. Ames, B. Davids, R. E. Laxdal, and A. C. Morton, "In flight ion separation using a Linac chain", in *Proc. LINAC'12*, Tel Aviv, Israel, Sep. 2012, pp. 1059–1063.

[6] K. Jayamanna *et al.*, "Off-line ion source terminal for ISAC at TRIUMF", *Review of Scientific Instruments*, vol. 79, no. 2, p. 02C711, 2008. doi:10.1063/1.2816928

ISBN: 978-3-95450-257-8 ISSN: 2222-5692 doi:10.18429/JACoW-ECRIS2024-MOB2

[7] K. Jayamanna *et al.*, "A multicharge ion source (Supernanogan) for the OLIS facility at ISAC/TRIUMF", *Review of Scientific Instruments*, vol. 81, no. 2, p. 02A331, 2010. doi:10.1063/1.3303819

[8] K. Jayamanna *et al.*, "Dual Frequency Enhancement of the Supernanogan Multi-Charged Ion Source at TRIUMF ISAC Facility", in *Journal of Physics: Conference Series*, p. 012 053, 2024. doi:10.1088/1742-6596/2743/1/012053

[9] P. Justus, C. R. J. Charles, F. Ames, K. Jayamanna, and S. Malbrunot-Ettenauer, "Creation and characterisation of multi-charged cerium beams at TRIUMF's OLIS", in *Journal of Physics: Conference Series*, p. 012 055, 2024. doi:10.1088/1742-6596/2743/1/012055

[10] J. Adegun, "Design of a new iron plug for the TRIUMF ECRIS charge state booster", in *26th International Workshop on Electron Cyclotron Resonance Ion Sources*, p. MOAB01, 2024, this conference.

ISBN: 978-3-95450-257-8 ISSN: 2222-5692 doi:10.18429/JACoW-ECRIS2024-MOC1

RECENT ACHIEVEMENTS IN THE PRODUCTION OF METALLIC ION BEAMS WITH THE CAPRICE ECRIS AT GSI

A. Andreev*, M. Galonska, R. Hollinger, R. Lang, J. Mäder, F. Maimone
GSI Helmholtzzentrum für Schwerionenforschung, Darmstadt, Germany

Abstract

The GSI CAPRICE Electron Cyclotron Resonance Ion Source (ECRIS) provides highly-charged ion beams for various experiments at GSI, enabling the delivery of continuous wave (CW) metallic ion beams with low material consumption, which is crucial for producing high charge state ion beams from rare or extremely rare isotopes such as ^{48}Ca. These metallic beams are produced utilizing the thermal evaporation technique by resistively heated ovens. Due to the research groups' demand for higher beam intensities and the introduction of new ion species, the CAPRICE ECRIS is now required to deliver increased ion currents of higher charge states, as well as to establish the production of the new beams.

INTRODUCTION

The CAPRICE Electron Cyclotron Resonance Ion Source (ECRIS) at the High Charge State Injector (HLI) of GSI is routinely used for the production of highly charged ion beams from both gaseous and metallic elements. The latter are produced utilizing the thermal evaporation technique by resistively heated ovens. This technique has been continuously optimized over the years to ensure high beam intensity and stable long-term operation. To ensure stable and reliable metal ion beam production, the ovens undergo a carefully controlled preparation process using a specialized oven preparation stand. Over the past years, significant developments have been made to optimize the production of metallic ion beams with CAPRICE ECRIS at GSI, improving both beam intensity and stability. A key focus has been on addressing the challenges associated with the long-term operation of the ECRIS due to material buildup within the plasma chamber, particularly during ^{48}Ca ion beam operation [1].

A diagnostic tool based on an optical emission spectrometer (OES) installed at the ECRIS at the HLI allows to monitor plasma condition in real time. The diagnostic capabilities of optical emission spectroscopy have been successfully utilized to detect plasma instabilities and to adjust ECRIS parameters accordingly, allowing for improved beam stability and performance. It has been demonstrated that the OES can be used to detect parasitic microwave heating of the oven and identify long-term instabilities during gaseous and metal ion beam operation [1, 2].

Metal ion beams are often requested for various research activities, including those conducted by the Super Heavy Element (SHE) groups. To meet their demand, a test campaign was conducted to establish and improve the production of high charge states of enriched ^{54}Cr and ^{55}Mn ion beams. During the tests, plasma and oven images were captured using a CCD camera to support the operation and enable real-time monitoring of the material consumption. Additionally, the use of a hot screen was investigated to protect the ceramic insulators in the extraction system from metal deposition, thereby improving the operational stability of the ECRIS. This paper describes the operational experience, the intensities and stability achieved for the aforementioned elements.

EXPERIMENTAL SETUP

Oven Preparation Stand

To produce metal ion beams, the CAPRICE ECRIS at GSI utilizes resistively heated ovens [3]. This method allows to produce metal ion beam with low material consumption and precise control over the evaporation rate, contributing to the stability and reproducibility of the beam. Before beam operation, the ovens are conditioned in a dedicated oven preparation stand, which allows to perform a controlled heating of the ovens in a vacuum environment. This conditioning process allows to remove residual gases and contaminants from the ovens, ensuring optimal conditions for material evaporation. It allows to improve the stability of the ion beam and extends the operational lifetime of the ovens and minimize downtime during the accelerator operation.

The oven preparation stand has recently undergone a redesign to further improve its functionality and efficiency. Figure 1 shows a photograph of the redesigned stand. It is

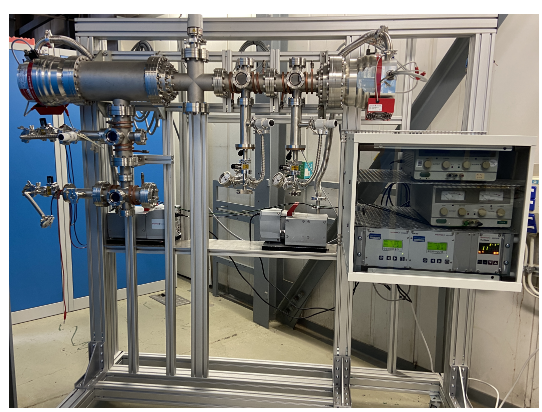

Figure 1: Photograph of the oven preparation stand.

equipped with airlocks that enable conditioning of several ovens simultaneously, increasing the operational efficiency. To further improve control over the oven preparation process, it is planned to equip the stand with a camera monitoring

* a.andreev@gsi.de

ISBN: 978-3-95450-257-8 ISSN: 2222-5692 doi:10.18429/JACoW-ECRIS2024-MOC1

system, which will provide a real-time visual feedback during conditioning. Additionally, a residual gas analyzer will be integrated for precise analysis and control of the gas and vapor composition.

Optical Emission Spectroscopy

To monitor the plasma condition in real time, the OES is used in conjunction with the plasma and oven images provided by a CCD camera [4]. Using the NIST database [5] the emission lines corresponding to the element of interest can be identified. Observing time variations of their intensity provides information about the internal plasma condition during the ECRIS operation and allows for real-time adjustments to the ECRIS operating parameters, ensuring high-intensity and stable beam production. The use of this diagnostic setup was investigated during the tests with ^{54}Cr and ^{55}Mn, aiming to support the ECRIS operation.

Due to the relatively high vapor pressure of Cr, the operational temperatures of the oven were required to be around 1500 degrees Celsius, utilizing more than 40 W of heating power. Within this temperature range, the emission spectrum in the visible wavelength domain is mainly characterized by thermal radiation from the oven. As a result, it was not possible to clearly identify individual emission lines of Cr in the measured wavelength range.

During ^{55}Mn beam operation, the emission line at 810 nm was monitored to estimate the amount of material present in the plasma. Additionally, the infrared part of the spectrum, specifically around 827 nm, was tracked to estimate the relative oven temperature (see Fig. 2). This allows to detect parasitic heating of the oven caused by coupled microwaves, which can affect the material production rate and degrade the ion beam stability. Combined with the oven conditioning process, this approach, as previously reported for ^{48}Ca ion beam operation [1], has proven effective for optimizing ECRIS performance and ensuring long-term operational stability.

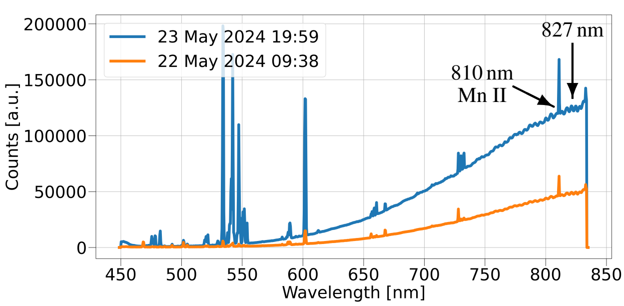

Figure 2: Example for OES measurements during ^{55}Mn ion beam operation.

EXPERIMENTAL RESULTS

Chromium Ion Beam

The recent measurement campaign focused on establishing and improving the production of high charge states of enriched ^{54}Cr ion beam. While the CAPRICE ECRIS at GSI has been successfully used to produce ^{54}Cr ion beams at lower charge states, such as ^{54}Cr^{7+} and ^{54}Cr^{8+} [3], this campaign aimed to meet the demand for higher charge states.

Based on prior short-term tests and previous Cr beam times, the desired target intensity 50 µA of ^{54}Cr^{10+} was set. Figure 3 shows the intensity of ^{54}Cr^{10+} measured during three days of the ECRIS operation with helium as a support gas. The desired target intensity was reached at the beginning

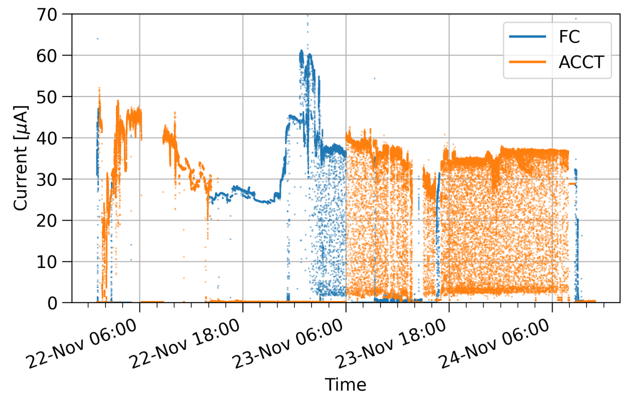

Figure 3: ^{54}Cr^{10+} intensity measured during 3 days of the ECRIS operation. FC denotes measurements taken with a Faraday cup during accelerator maintenance, while ACCT represents measurements from an AC current transformer.

of the ECRIS operation, however the ECRIS performance was impacted by discharges in the extraction system, which appeared on the second day of the ECRIS operation. As their frequency increased over time, the beam stability significantly degraded and the target intensity could not be maintained. A subsequent inspection of the extraction system revealed metal traces deposited on the ceramic insulators in the extraction column (see Fig. 4). An electron microscope

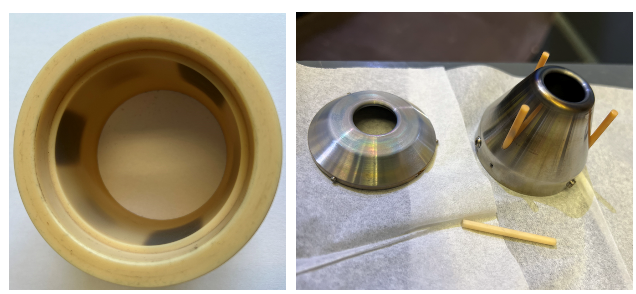

Figure 4: Photographs of ceramic isolators in the extraction column after the ^{54}Cr operation.

investigation confirmed the presence of chromium, but could not verify if it was the only component. To address this issue and mitigate the metallic buildup on the ceramic surfaces, a series of tests with a hot screen is planned. Similar tests conducted during ^{55}Mn operation have already demonstrated the effectiveness of the hot screen in improving operational stability, as discussed later in this paper. Figure 5 shows a typical mass-to-charge spectrum of the extracted ion beam. The overall consumption of ^{54}Cr material was 8 mg/h on average (without material recycling).

ISBN: 978-3-95450-257-8 ISSN: 2222-5692 doi:10.18429/JACoW-ECRIS2024-MOC1

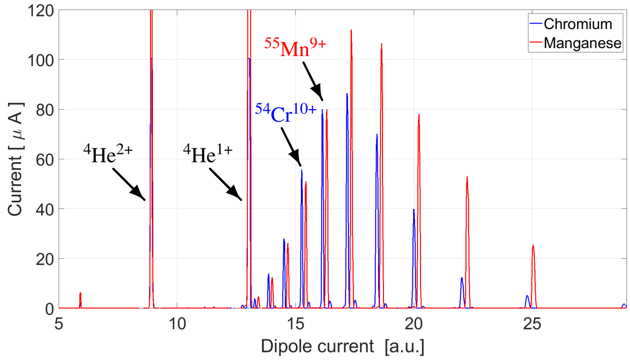

Figure 5: Mass-to-charge spectra of ^{54}Cr (blue) and ^{55}Mn (red), optimized for ^{54}Cr^{10+} and ^{55}Mn^{9+}, respectively.

The possibility of using a tungsten mesh to prevent parasitic microwave heating of the oven, a technique that was previously successful for ^{48}Ca operation [4], was tested. Although the ECRIS operation was more stable with the mesh installed, the build-up of condensed material on the mesh led to reduced ^{54}Cr^{10+} intensity indicating that this approach may not be optimal for long-term Cr operation. Figure 6a shows a photograph of the tungsten mesh after ^{54}Cr beam operation.

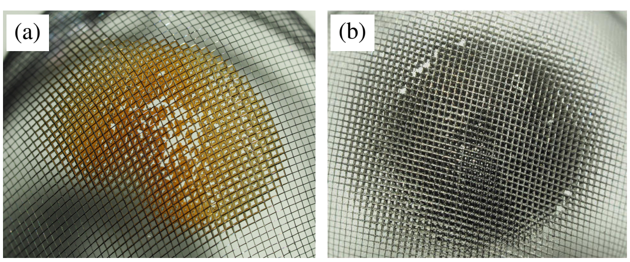

Figure 6: Photographs of the tungsten meshes after ^{54}Cr (a) and ^{55}Mn (b) operation.

Manganese Ion Beam

The beam establishment tests were conducted at the EIS test bench to produce the ^{55}Mn ion beam for the first time using the CAPRICE ECRIS at GSI. The aim of this test campaign was to determine the achievable beam intensity of higher charge states for ^{55}Mn, with a focus on ^{55}Mn^{9+} production.

The intensity of ^{55}Mn^{9+} beam measured during the three day beam establishment test with the hot screen installed and helium as a support gas is shown in Fig. 7. An average intensity of 80 µA was achieved for ^{55}Mn^{9+}. Similar to the ^{54}Cr beam tests, discharges appeared in the extraction system on the second day of ECRIS operation. However, their frequency was low enough to maintain stable operation and production of ^{55}Mn^{9+} beam. The use of the hot screen improved beam stability and delayed the onset of discharges, enabling stable operation at high intensities with minimal disruptions. A typical mass-to-charge spectrum for ^{55}Mn obtained during the tests is shown in Fig. 5. The overall average consumption of ^{55}Mn material was 8.1 mg/h (without material recycling).

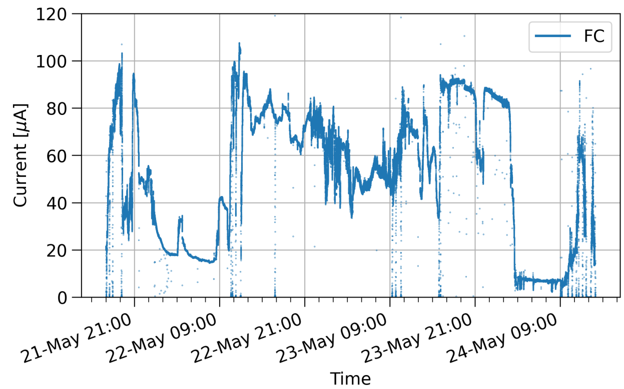

Figure 7: ^{55}Mn^{9+} intensity measured during 3 days of the ECRIS operation.

In addition to the hot screen tests, experiments with a tungsten mesh were also carried out. During ^{55}Mn operation the mesh was completely clogged with a condensed material after one day of the ECRIS operation, preventing further ^{55}Mn evaporation and beam production (see Fig. 6b).

OES Results with Manganese Ion Beam

During the ^{55}Mn^{9+} ion beam establishment tests, the OES was employed to monitor plasma condition and detect parasitic heating effects of the oven. The time variations of two specific emission lines were monitored: the Mn II emission line at 810 nm and an emission line at 827 nm, closer to the infrared part of the optical spectrum, which was selected to estimate the relative oven temperature (see Fig. 2).

Figure 8 presents the time variations of key ECRIS parameters and normalized emission line intensities. Both figures, show the ^{55}Mn^{9+} ion beam current, along with oven current and reflected microwave power in Fig. 8a, and ion source pressure and drain current of the extraction power supply in Fig. 8b.

In both cases, the OES data reveal a strong correlation between the intensity of the Mn II emission line and the ^{55}Mn^{9+} beam current. The emission line at 827 nm shows clear variations in response to changes in the oven temperature, indicating parasitic heating of the oven due to coupled microwave power. As the reflected power decreases (see Fig. 8a), the oven temperature increases, leading to a higher production rate of ^{55}Mn, as reflected by the rising intensity of the Mn II emission line and a corresponding increase in the ^{55}Mn^{9+} ion beam current. These changes in reflected power also correlate with periodic minima and maxima in the oven current. A decrease in reflected power indicates a stronger microwave coupling, with a portion of the microwave power heating the oven. As the oven temperature rises, its resistance increases, leading to a reduction in the current flowing through the oven. When reflected power increases again, the oven cools down, resulting in a decrease in both the Mn II emission line intensity and the ion beam current.

In Fig. 8b, a similar relationship between the ^{55}Mn^{9+} beam current and the emission line intensities can be observed,

ISBN: 978-3-95450-257-8 ISSN: 2222-5692 doi:10.18429/JACoW-ECRIS2024-MOC1

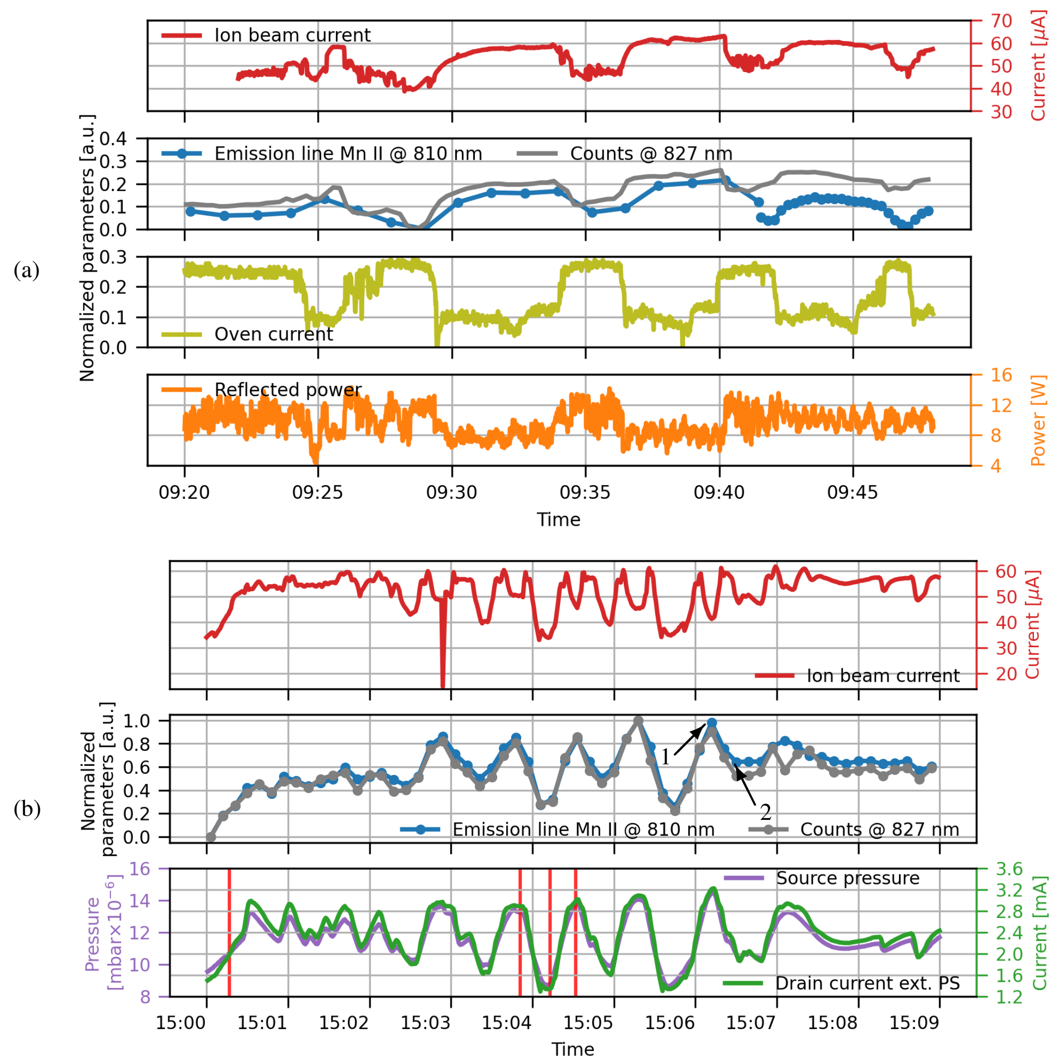

Figure 8: Time variations of selected emission lines and ECRIS parameters illustrating (a) the effect of parasitic heating of the oven by coupled microwaves, (b) ion source pressure variations. The red vertical lines mark the time when the gas valve settings were changed. The time instants marked as (1) and (2) correspond to the CCD images shown in Fig. 9.

together with the influence of the source pressure. The beam current shows a local minimum at the maxima of the Mn II emission line, which can be explained by a shift of the plasma's charge state distribution towards lower charge states. The red vertical lines in the figure indicate the moments when the gas valve settings were manually adjusted, leading to corresponding changes in the source pressure.

Additionally, plasma images taken at the local maxima and minima of the emission lines visually confirm the beam intensity variations (see Fig. 9). The brighter plasma image corresponds to a higher total extracted ion beam current, while the darker image indicates reduced beam intensity.

These results highlight the role of OES and CCD plasma and oven imaging as a real-time diagnostic tools for monitoring plasma conditions and detecting parasitic oven heating effects. They provide a feedback on plasma condition enabling better control of the ECRIS operating parameters and allowing to improve the beam intensity and stability.

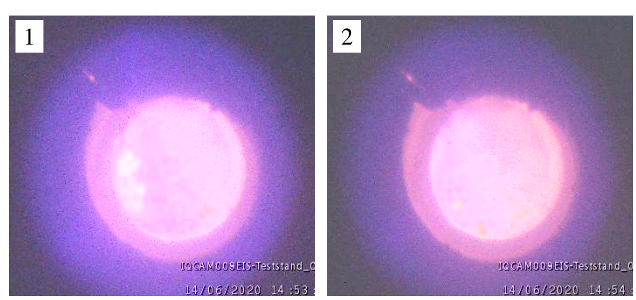

Figure 9: CCD images of the plasma during ^{55}Mn ion beam operation. Annotations (1) and (2) correspond to the time instants marked in Fig. 8b.

ACKNOWLEDGEMENTS

The authors would like to thank Michael Wagner from the GSI Materials Research Department for his support in performing the SEM EDX investigation.

ISBN: 978-3-95450-257-8 ISSN: 2222-5692 doi:10.18429/JACoW-ECRIS2024-MOC1

REFERENCES

[1] F. Maimone *et al.*, "Stable and intense ^{48}Ca ion beam production with a microwave shielded oven and an optical spectrometer as diagnostic tool", in *Proc. ECRIS'20*, East Lansing, MI, USA, Sep. 2020, pp. 50-53. doi:10.18429/JACoW-ECRIS2020-MOZZO03

[2] F. Maimone *et al.*, "Research and development activities to increase the performance of the CAPRICE ECRIS at GSI", *J. Phys.: Conf. Ser.*, vol. 2743, p. 012048, 2024. doi:10.1088/1742-6596/2743/1/012048

[3] K. Tinschert, R. Lang, J. Mäder, F. Maimone, and J. Roßbach, "Metal ion beam production with improved evaporation ovens", in *Proc. ECRIS'12*, Sydney, Australia, Sep. 2012, pp. 140-142.

[4] F. Maimone *et al.*, "Optical spectroscopy as a diagnostic tool for metal ion beam production with an ECRIS", *Rev. Sci. Instrum*, vol. 90, no. 12, p. 123108, Dec. 2019. doi:10.1063/1.5127571

[5] NIST Atomic Spectra Database Lines Form, https://physics.nist.gov/PhysRefData/ASD/lines_form.html

ISBN: 978-3-95450-257-8 ISSN: 2222-5692 doi:10.18429/JACoW-ECRIS2024-MOC2

A NOVEL INDUCTIVE OVEN DESIGN FOR THE PRODUCTION OF HIGH CURRENT, METAL ION BEAMS*

D. S. Todd†, J. Y. Benitez, LBNL, Berkeley, CA, USA

Abstract

Essential to the proposed search for element 120 at LBNL's 88-Inch Cyclotron is the continual delivery of over a particle microamp of ^{50}Ti for weeks-long campaigns spanning many months. The fully-superconducting ECR ion source VENUS will be the injector source for these runs, and we have developed a new inductive oven design that can survive VENUS' high magnetic fields while injecting metallic gas into the plasma with high efficiency. The new oven employs a vertical susceptor to permit use with metals that melt before outgassing sufficiently, while also allowing a rotation of the oven's material exit toward the plasma center for better conversion efficiency to the produced beam. The performance of VENUS with this oven has been outstanding. As reported here, ^{50}Ti^{12+} beams with stable currents between 1.0 and 1.5 pμA from this oven were used to produce two element 116 particles: the first time titanium beams have been used to have been used to create superheavy elements.

INTRODUCTION

Superheavy elements beyond copernicium (element 112) have been discovered by bombarding transuranic targets with high-current ^{48}Ca beams. For element 113, a plutonium target was used, and the target atomic number was increased for each successive element discovery. The short half-lives of target material with atomic number greater than californium (element 98, used to discover element 118) mean that there isn't enough material, nor would it last long enough, to serve as targets for the months-long experiments necessary for superheavy element production. A potential way to move forward is to use as projectile beams elements with higher atomic numbers for these searches .

Earlier this year (2024), researchers at LBNL announced they were able to use ^{50}Ti beams from the 88 Inch Cyclotron incident upon a plutonium target to produce two atoms of element 116 [1]. This was the first time that a titanium beam was used to produce superheavy elements, and this result opens the door to extending the periodic table by using ^{50}Ti beams on californium targets in the search for element 120.

The production and delivery of more than 1 pμA ^{50}Ti beams from the 88-Inch Cyclotron was no small feat: not because the cyclotron couldn't produce this high of currents (it has delivered over 2 pμA ^{48}Ca beams previously [2]), but because titanium beams are notoriously difficult to produce from an ion source. Titanium is highly reactive with other atoms, therefore any deposited on the walls of a plasma source producing these beams will affect plasma stability by pumping background gas in an unpredictable manner. Additionally, for sources relying on outgassing from pure titanium, sufficient partial pressures typically require heating the titanium to over 1600 °C.

Using a novel inductive oven within LBNL's superconducting electron cyclotron resonance (ECR) ion source VENUS, we were able to deliver 80–120 μA ^{50}Ti^{12+}; beams to the cyclotron with excellent stability and a relatively low material consumption rate. The inductive oven used for this work is described as are some of the difficulties overcome en route to its successful deployment.

ION SOURCE AND OVENS

Electron cyclotron resonance (ECR) ion sources produce ion beams from a magnetically confined plasma. This confinement is typically in the form of solenoids for axial confinement and a multipole (typically sextupole) for radial confinement. The superposition of these fields produces a net magnetic field magnitude whose minimum is at the source center and which grows in all directions about this center. Closed surfaces of constant magnetic field surround the source center, and by injecting microwaves with frequency that matches the electron cyclotron frequency on one or more of these surfaces, electron energies can be raised to the point that they can ionize atoms and confined ions. The ion beam species produced are determined by the material injected into the plasma, and these sources have the distinct advantage that beams can be formed from any material introduced to the plasma without destroying it. The easiest means of beam production is the injection of gas into the plasma, and a common means of producing beams from metals is to raise the temperature of the metals to the point its vapor pressure emits sufficient material quantity into the plasma.

Raising the temperature of metals is often performed through the use of ovens. The general oven has some sort of a crucible whose temperature is raised to outgassing temperatures for the material it holds, and often some sort of outlet directs that vaporized material toward the plasma. The low-temperature oven used at LBNL is an example of this, where a heater cartridge conductively heats a crucible containing the material of interest [3]. A series of channels then directs the evaporate toward the plasma. This oven has been extremely successful at efficiently delivering ^{48}Ca to the plasma, primarily as a result of the aiming channels. Consumption rates of this expensive material are typically 0.5 mg/hr. This oven is limited to low temperatures, however, reaching a practical maximum of approximately 700 °C.

Higher temperatures have been reached at LBNL and at other laboratories using resistive ovens [4,5]. Here, a high

* This work was supported by the U.S. Department of Energy, Office of Science, Office of Nuclear Physics under contract number DE-AC02-05CH11231 (LBNL).
† dstodd@lbl.gov

ISBN: 978-3-95450-257-8 ISSN: 2222-5692 doi:10.18429/JACoW-ECRIS2024-MOC2

current is run along the length of a thin walled, typically cylindrical, crucible and ohmic heating is used to reach the desired temperature. These ovens are typically operated vertically so that material may be easily contained, and this orientation allows the use of materials that melt before reaching temperatures providing sufficient partial pressures. These ovens have two real shortcomings: the vertically-run currents are nearly perpendicular to the magnetic fields at the injection end of the source where they are typically installed. For advanced superconducting sources, these fields reach 3–4 Tesla and can produce strong forces perpendicular to the axis of the oven. These forces can be particularly damaging for high temperature ovens as the chemistry that takes place between the crucible and desired material at high temperature can be corrosive and affect the oven's structural integrity. It should be noted that there have been successes with high-temperature resistive ovens in high-field sources, such as with RIKEN's production of high-current vanadium beams in their 28 GHz ECR ion source, but this required research to find an insulator to separate the hot vanadium from their resistive oven to prevent the oven damaging hot chemistry between the vandadium and the oven [6].

As titanium is particularly corrosive and resistive ovens used with it in VENUS were frequently destroyed, we opted to use inductive technology for the oven that would provide high-current ^{50}Ti beams for superheavy element research. Inductive ovens have been successfully used at China's Institute of Modern Physics in and the Facility for Rare Ion Beams in Michigan [7, 8], primarily for the production of high-current uranium beams which require bringing the uranium to temperatures exceeding 2000 °C. These ovens utilize cylindrical coils whose axes are parallel to and offset ~4 cm from the central extraction axis of the source. The susceptor holding the material of interest is coaxial with the coil and nested within an insulator that isolates the susceptor from the coil both thermally and electrically. The susceptor has a hole in the end closest to the source plasma, and it is through this that material escapes in gas form and feeds the plasma. The offset and alignment of this oven mean its output is usually not directed toward the plasma center, so it is expected that a substantial fraction of the ejected material is not ionized by the plasma and deposited on the chamber walls.

As ^{50}Ti, unlike the uranium used at the labs mentioned above, is a low-abundance, expensive isotope, efficient transfer from oven to plasma to beam is a necessity, and titanium's high reactivity means deposited material on the plasma chamber walls typically leads to source instability. For this reason we strove to produce an inductive oven whose output could be aimed at the plasma center to enhance the probability of ionization. To do so, we designed an inductive oven that uses a vertically-aligned coil. Again, the susceptor and surrounding insulator are nested within the coil, but the exit aperture in the susceptor is located in the side of the cylinder rather than the end as is the case with an horizontal oven. The hole in the susceptor is aligned with a larger hole in the surrounding insulator, and these align with a gap between two turns of the inductive coil. The direction of the hole is rotated about the vertical axis so that the output material is directed toward the center of the plasma.

To reach near VENUS' confined plasma, the oven is attached to the end of a 1.1-meter-long shaft. So that the oven may be changed or refilled rapidly, this shaft and the oven at its end must pass through a 38.1-mm- diameter port.

OVEN DESIGN

The goal of the project was to produce an oven capable of delivering >100 µA $^{50}Ti^{12+}$ continually for at least ten days straight at a time while keeping material consumption rates below 5 mg/hour as this low-abundance isotope is expensive. The scale of the inductive oven was set primarily by the fact that it had to pass through the 38.1-mm-diameter port and the idea that the typical oven has a susceptor nested within an insulator nested within the inductive coil.

The coil tubing is 3.97-mm-outer-diameter copper tubing with 0.36-mm-wall-thickness. It is wound on a 3D printed winding fixture so as to produce five full turns with minimum spacing between turns of 1 mm and a tube center radius of 12.5 mm. As shown in Fig. 1, there are two larger gaps at the front side of the oven. The upper gap allows for material to exit the oven while the lower gap serves as a support location for an insulating post that prevents the insulator and susceptor from falling through the coil. This support post is the weak point of the design as if the post breaks the hot oven would fall onto and possibly damage the plasma chamber. For this reason, an aluminum mesh structure was added that surrounds the oven to act as a catch should the insulator fail, though it has yet to do so. This cage and the oven within are outside the plasma.

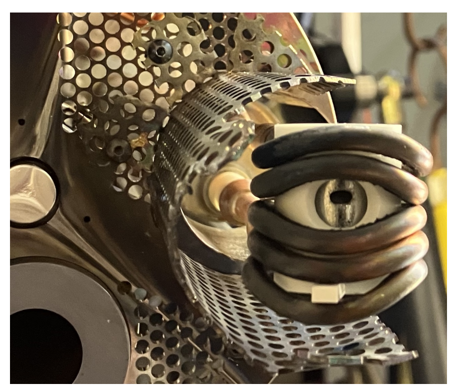

Figure 1: End-on view of the inductive oven when installed in VENUS. The perforated aluminum sheet that acts as a preventative catch should the ceramic support rod (bottom) fail surrounds the oven.

The coil is brazed onto an RF vacuum feedthrough that is welded to the 1.4-m-long shaft used to position the oven an axial distance of approximately 22 cm away from the plasma center. As the feedthroughs are at the plasma end of the shaft, the inside of the shaft is maintained at atmospheric pressure. Hollow, copper tubes run the RF and provide water

ISBN: 978-3-95450-257-8 ISSN: 2222-5692 doi:10.18429/JACoW-ECRIS2024-MOC2

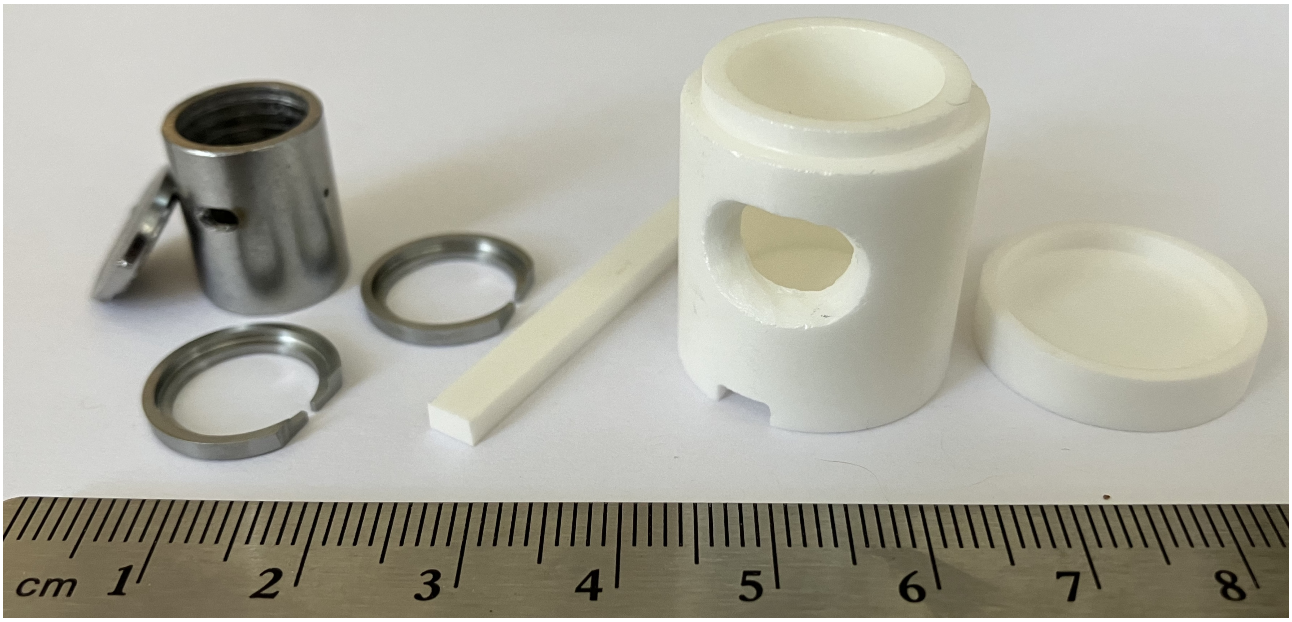

Figure 2: From left to right, the molybdenum susceptor and lid, molybdenum slotted susceptor support rings, yttriated zirconia support rod, slotted cylindrical insulator, and insulating lid.

cooling to the coil. The coil is driven by a commercially-available, 2.4 kW inductive power supply that operates in the 150-400 kHz range. The power supply is maintained at high voltage within the source cage.

The insulating post and the insulator body/lid combination are made from yttria-stabilized zirconia. The insulator thickness is 3 mm with an outer diameter of 21.8 mm. A relatively large hole is placed in one side of the insulator to allow the exit of material from the susceptor housed within it, as shown in Fig. 2. As discussed below, in the final version of the insulator a slot was added to the bottom of the insulator body in which the support post nested which ensured alignment of the insulator was maintained relative to the coil opening, as shown in Fig. 3.

The final susceptor design was a 12.7-mm-diameter, molybdenum cylinder with 1.1-mm-wall-thickness. At 200 kHz operation, this is equivalent to approximately four skin depths so that nearly all flux passing axially through the center is countered by eddy currents in the susceptor body. The susceptor height is 16.5 mm and provides a total capacity of approximately 0.75 cm^3. More typically the susceptor is filled to below the 2.0-mm-tall, 3.8-mm-wide material exit opening in the side, located 9.4 mm from the bottom of the cylinder. This leaves a fill volume of approximately 0.44 cm^3, equivalent to about 2 grams of titanium: enough for ~16 days operation at 5 mg/hour consumption.

The susceptor is thermally isolated from the insulator by molybdenum stand-off rings, shown in the exploded view of Fig. 4. The rings have been machined with angles that keep point-like contact with both the susceptor and the insulator to prevent heat transfer between the two, and the rings maintain a 1-mm-gap between the susceptor and the insulator.

Figure 3: Inductive oven viewed from below. The support post rests on the bottom turn of the coil and a slot in the insulator prevents rotation of the insulator relative to the coils.

RESULTS

The inductive oven has been found to stably produce $^{50}Ti^{12+}$ beams of ~90–120 µA for multiple days without intervention, and did so for the 22 days of running with the cyclotron that led to the production of two elements of 116. During these runs the beam current extracted from the cyclotron was between 1-1.5 pµA, and titanium consumption rates were typically in the range of 2.5–4.5 mg/hr. More

ISBN: 978-3-95450-257-8 ISSN: 2222-5692 doi:10.18429/JACoW-ECRIS2024-MOC2

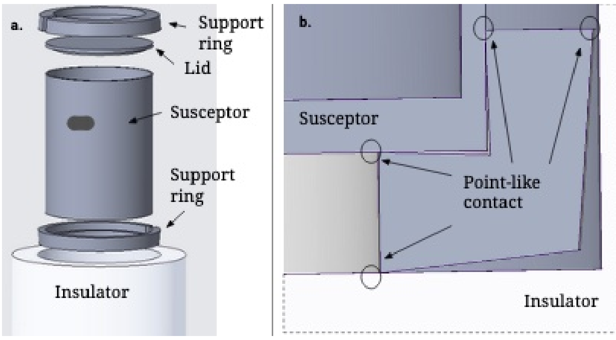

Figure 4: An exploded view of the oven assembly, left, and detail showing the point-like contact the ring makes with both the susceptor and the insulator.

recent runs have consistently been in the low end of this range.

For every run, the insulators become gray and develop cracks, but they hold their shape until the end of the run and haven't caused problems. The body and lid insulators can only be used for one run while the support posts can typically be used multiple times. We have only used one susceptor/lid combination for all of our ^{50}Ti runs to date, and these show no signs of damage.

The coils do collect titanium near the material exit opening. It is not a significant amount and this can be chipped away easily. It should be noted, however, that for one run where the titanium-coated coil had been exposed to atmosphere for three months before its next use, there was significant outgassing inside the source when the coil was energized to a low level. This caused a few hour delay on start up, and could likely be avoided by protecting the coil between runs.

PROBLEMS AND OTHER DEVELOPMENT NOTES

The susceptor itself has clogged twice, and both times were due to suddenly turning the coil power supply off when at high temperature. The reason for this is believed to be the fact that the insulator provides a good thermal barrier from the cool outside world except at the exit aperture, therefore this location would be expected to cool fastest when the power is suddenly turned off. It has been found that as long as the oven is ramped down in a steady manner (as high as 10s of W per minute), no clogging has occurred.

Early iterations of the oven allowed the insulator to rotate relative to the coil and the susceptor relative to the insulator. Both of these caused reduced beam production and usually led to clogging. The addition of a slit to the insulator body, mentioned above, that eliminated the ability of the insulator to rotate stopped rotation clogs. Wedging thin (0.02-mm-thick) strips of molybdenum between the susceptor and the insulate prevented rotations of the susceptor.

An early iteration of the oven used a thin-walled 0.5-mm-thick) tantalum susceptor. At 200 kHz inductive heating, this represented less than one skin depth. As a result, the eddy currents formed in the susceptor were not enough to counter the magnetic flux and eddy currents were formed in the titanium inside the oven. The titanium was heated more quickly than the susceptor, and though we surpassed the desired partial pressure temperature and melted the titanium, the susceptor walls remained colder than the titanium and the titanium condensed and solidified there. Additionally, there was evidence of chemical reactions taking place between the titanium and tungsten. The change to the thicker-walled molybdenum susceptor mentioned above has prevented these problems. An advantage inductive ovens with thick-walled susceptors have over resistive ovens is that nearly all of the inductive power goes into the susceptor. Unlike the resistive oven whose resistance can change as material shifts within the oven itself, the inductive oven temperature is very stable as all the heat goes into the susceptor regardless of the quantity of material inside it.

ACKNOWLEDGEMENTS

The authors would like to acknowledge the efforts of Brian Bell in winding the inductive oven coils and other machining efforts on this project.

REFERENCES

[1] J.M. Gates *et al.*, "Toward the discovery of new elements: Production of livermorium (Z=116) with ^{50}Ti", *Phys. Rev. Lett.*, accepted for publication, 2024.

[2] D.S. Todd *et al.*, "High current beam extraction from the 88-Inch Cyclotron at LBNL", in *Proc. Cyclotrons'13*, Vancouver, Canada, 2013, paper MO2PB02. `https://jacow.org/CYCLOTRONS2013/papers/MO2PB02.pdf`

[3] D.J. Clark and C.M. Lyneis, "The production of beams from solid materials at the LBL ECR source", *J. Phys. Colloques*, vol. 50, no. C1, pp. 759–766, 1989. `doi:10.1051/jphyscol:1989180`

[4] D. Leitner *et al.*, "High intensity production of high and medium charge state uranium and other heavy ion beams with VENUS", *Rev. Sci. Instrum.*, vol. 79, p. 02C710, 2008. `doi:10.1063/1.2816790`

[5] J. Ohnishi *et al.*, "Development of a high-temperature oven for the 28 GHz electron cyclotron resonance ion source", *Rev. Sci. Instrum.*, vol. 85, p. 02A941, 2014. `doi:10.1063/1.4849655`

[6] Y. Higurashi *et al.*, "Intense vanadium ion beam production for superheavy element research experiments", *J. Phys.: Conf. Ser.*, vol. 2743, p. 012052, 2024. `doi:10.1088/1742-6596/2743/1/012052`

[7] W. Lu *et al.*, "Production of metallic ion beams by electron cyclotron resonance ion sources equipped with inductive heating ovens at the Institute of Modern Physics", *Rev. Sci. Instrum.*, vol. 92, p. 033302, 2021. `doi:10.1063/5.0041671`

[8] H. Ren *et al.*, "Development and status of the FRIB 28 GHz SC ECRIS" *J. Phys.: Conf. Ser.*, vol. 2244, p. 012008, 2022. `doi:10.1088/1742-6596/2244/1/012008`

26th Int. Workshop Electron Cyclotron Resonance Ion Sources ECRIS2024, Darmstadt, Germany JACoW Publishing
ISBN: 978-3-95450-257-8 ISSN: 2222-5692 doi:10.18429/JACoW-ECRIS2024-MOD1

DEVELOPMENT OF DEUTERIUM-DEUTERIUM COMPACT NEUTRON SOURCE

A. Pérez*,[1],V. Etxebarria[1], I. Arredondo[1], J. Portilla[1], Javier Praena[2], A. Roldán[3], J.Feuchtwanger[1]
[1]Department of Electricity and Electronics, University of the Basque Country, Leioa, Spain
[2]Department of Atomic, Molecular and Nuclear Physics, University of Granada, Granada, Spain
[3]Department of Electronics and Computer Technology, University of Granada, Granada, Spain

Abstract

In the present work, we will present the status of the deuterium-deuterium (D-D) neutron source that is being developed in collaboration between the University of Granada and the University of the Basque Country. Our neutron source consists of an Electron Cyclotron Resonance (ECR) ion source which accelerates a deuteron beam towards a deuterated target. The ionization to achieve the deuterium plasma is achieved by radiating the cylindrical ERC plasma chamber with a magnetron 2.45 GHz signal and an 875 G magnetic field generated by 6 NdFeB magnets located around the plasma chamber. Moreover, a cylindrical alumina Radio Frequency (RF) window is used to keep the vacuum status from the ambient pressure condition inside the WR340 and helping the plasma to ignite. Once the plasma is generated, the deuterons are extracted from the plasma chamber using a Pierce electrode geometry and three other electrostatic lenses, fixed to different negative potentials. The beam is accelerated towards the copper target disk with a deuterated titanium mesh fixed to –100 kV which generates the desired neutron radiation. There are several applications of D-D neutron sources across scientific and industrial domains. In case of the University of Granada and its deep relation with the IFMIF-DONES neutron source, it is worth to mention that we plan to carry out experiments for determining the cross-sections of relevant isotopes in the studies of IFMIF-DONES for a better simulation of the behaviour of such material under high neutron flux irradiation.

INTRODUCTION

A deuterium-deuterium (D-D) compact neutron source is being developed in collaboration of the University of the Basque Country and the University of Granada. The main goal of this project is to gain scientific and engineering know-how on this type of source. The source will be based on the D-D fusion reaction described as $^2H(d,n)^3He$ [1-2]]. By colliding with deuterium positive ions, known as deuterons, a 3.27 MeV reaction is generated, where 2.45 MeV corresponds to a neutron and the other 0.82 MeV corresponds to a nucleus of ^{3}He. The full 3D design of the neutron source can be seen in Figure 1. First, the radio frequency (RF) subsystem where a high-power RF signal is generated and transmitted toward the plasma chamber. This Rf signal combined to a proper magnetic field generates an electron cyclotron resonance (ECR) deuterium plasma formed of deuterons. As these deuterons have a positive charge, fixing the target to a negative potential will extract them from the plasma chamber and accelerate them towards it. The target is deuterated, so as the ion beam impacts the target the D-D reaction is going to be produced and 10^7 neutron flux will be generated [3-4].

This paper is organized in the following way. Each section will describe a different subsystem of the D-D source. Moreover, the actual state of the project will be described with the conclusions. Finally, the future works are given.

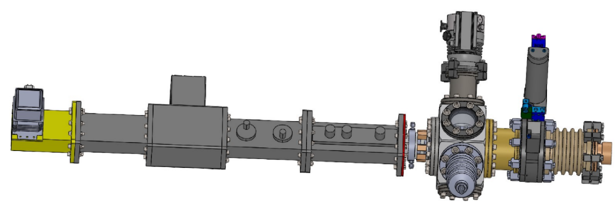

Figure 1: D-D source full 3D model design.

RF DESIGN

As stated in the previous section, an RF signal is needed to ionize the deuterium inside the plasma chamber. This RF signal is generated using a high-power magnetron able to achieve 1.3 kW of power with a frequency of 2.45 GHz. Once the RF wave is generated it needs to be transmitted towards the plasma chamber. A rectangular waveguide chain has been designed for this purpose, using the WR340 standard, which has an operating bandwidth from 2.2 GHz to 3.3 GHz. Following the magnetron an adaptor from magnetron to WR340 is used to optimize the power coupling from the RF source to the rest of the system. Then, a 3 kW water-cooled isolator has been implemented to avoid damaging the magnetron with the reflected power coming from the plasma chamber. Moreover, a directional coupler has been added to the design to monitor both forward and reflected power to the plasma chamber. Finally, a 3 manual probe tuner is used to modify the impedance of the WR340 system. When plasma is ignited, the impedance seen from the WR340 system towards the plasma chamber changes, and this will lead to worse RF coupling. Varying the position of the manual probes and monitoring the reflected power from the directional coupler, the impedance from the WR340 system can be modified to adapt it to the one in the plasma chamber. By doing so, the RF coupling will improve so with less RF power higher ion fractioned plasmas will be achieved.

* andoni.perezs@ehu.eus

ISBN: 978-3-95450-257-8 ISSN: 2222-5692 doi:10.18429/JACoW-ECRIS2024-MOD1

PLASMA CHAMBER

In the design of our D-D source, is in the plasma chamber where the deuterons are generated. For this purpose, an ECR plasma is ignited from deuterium by ionizing it with a 2.45 GHz RF signal and fixing a magnetic field around the chamber. In order to have an ECR plasma the RF signal's frequency and the magnetic field follow the relationship stated in Eq. (1). Being q the electron charge in C, B the value of the magnetic field in T, and m_e the electron mass in kg.

$$f = \frac{q \cdot B}{2\pi \cdot m_e} (\mathrm{Hz}) \tag{1}$$

Electromagnetic Simulation

As the plasma chamber has a cylindrical shape, with a radius of 20 mm and a length of 50 mm, an iris has been designed to adapt the impedance of the chamber and the one of the previous WR340 RF chain. Moreover, the RF subsystem works at ambient pressure while the plasma chamber needs to be in vacuum conditions. Therefore, a system capable of adapting the impedance and keep the vacuum state inside the chamber is needed. As seen in Figure 2, two 30 mm diameter and 5 mm long iris have been designed which added to the 38 mm diameter and 13 mm long alumina disk in the middle of both iris, and the plasma chamber can adapt the RF signal coming from the magnetron. The RF characterization results for the whole plasma chamber geometry suggest the designed work as expected having $S_{11} = -9.23$ dB at a frequency of 2.446 GHz. Moreover, the results obtained for the S_{11} parameter with the CST software and characterization with a Vector Network Analyzer (VNA) only had a variation of 1 dB in magnitude and 10 MHz in frequency. The vacuum state is conserved by one face of the alumina disk and an O-ring being pushed by it. Furthermore, the alumina is not only used as an RF window to maintain the pressure inside the chamber but also to help the plasma ignition. When an RF signal goes through the alumina disk, excited electrons are pulled out from the ceramic material and contribute to the ionization of the desired gas.

Magnetic Design

On the other hand, a magnetic field needs to be induced inside the plasma chamber for an ECR plasma to ignite. In our case, for a 2.45 GHz signal the magnetic field needed is of 875 G, following Eq. (1). For this purpose, 6 NdFeB magnets with a dimension of 15 x 15 x 24 mm are located around the plasma chamber. These magnets were chosen for their low cost and appropriate properties for the magnetic field values wanted to achieve. Apart from the magnets, three iron disks are needed to support the magnets around the chamber and optimize the magnetic field values which are seen in Figure 3.

HV EXTRACTOR

Once the plasma is ignited the next step is to form the ion beam. For our D-D source, the beam will be formed by

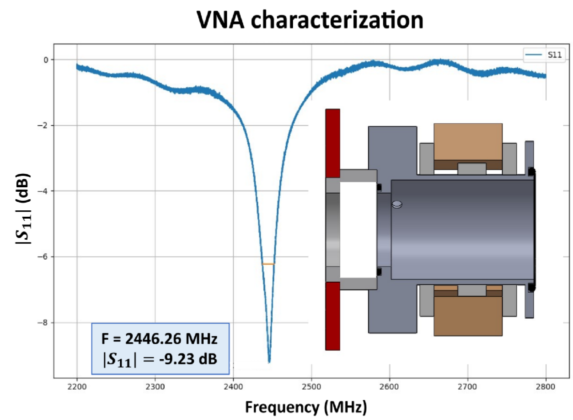

Figure 2: VNA S_{11} measurement and plasma chamber 3D model.

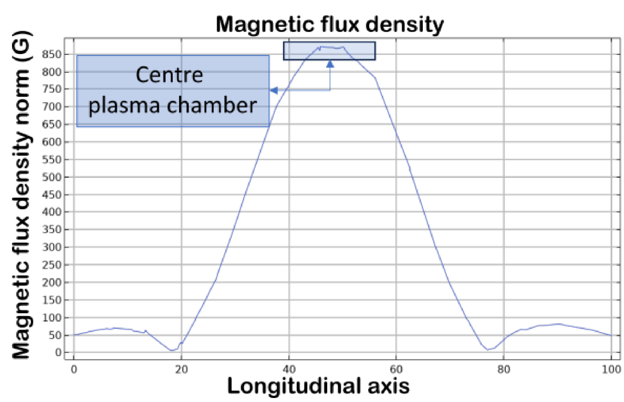

Figure 3: Magnetic field in the plasma chamber longitudinal axis.

deuterons, so it is a positive ion beam and negative potentials need to be fixed in order to accelerate and be able to extract the ions from the plasma.

Electrostatic Simulation

The ion beam extraction and acceleration will be achieved by fixing negative potentials to different electrodes. The number of electrodes, potential, and position are simulated in SIMION. The first electrode is the plasma electrode, which needs to have an angle of 67.5° to the beam axis (22.5° to the perpendicular). The shape of the electric field in the extraction gap will shape the beam as it is extracted so having this angle will produce an extraction field that has a zero transverse value at the edge of the beam, thus not having any focusing effect on the beam. This special shape is called pierce electrode geometry and will be fixed to the same potential as the plasma chamber, 0 V.

If the deuterated target is fixed to a negative potential the ion beam will be accelerated towards the target. Nevertheless, the beam will be highly focused on the center of the target, only using the 0,13 % of the target surface. A low dispersion of the beam around the target could lead to heating problems and waste of the target's deuterium. After the

ISBN: 978-3-95450-257-8 ISSN: 2222-5692 doi:10.18429/JACoW-ECRIS2024-MOD1

first iterations, the addition of an electrostatic lens inside the vacuum chamber has proved to improve the dispersion of the beam towards the target. Having the target to -100 kV and the lens at -60 kV the beam impacts the 14.23 % of the target's surface. In the following iterations, the addition of more lenses will be studied.

Except for the target and the possible electrostatic lenses inside the vacuum chamber, the whole system is fixed to 0 V. To avoid HV discharges a PEEK tube will be used to isolate the high voltage from the target from the rest of the system. PEEK is a common material used for HV isolation for its high dielectric strength of 73 kV/mm.

TARGET

The target the deuteron beam will be accelerated towards consists of a metallic coin that has a titanium mesh with deuterium deposited in one of its faces. In this way, when the ion beam arrives, the deuterons impact the deposited deuterium and produce the $^2H(d,n)^3He$ reaction having the desired 2.45 MeV neutrons. As seen in Figure 4, the target will be mounted in a threaded system so it can be easily changed.

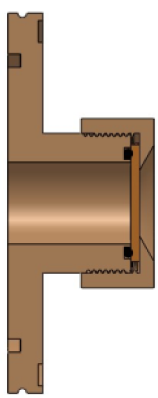

Figure 4: 3D target design.

ACTUAL STATE AND FUTURE WORKS

For the time this contribution is being written the RF system, plasma chamber and vacuum chamber have been implemented in the real-life design, Figure 5. At the moment the first deuterium plasmas are being ignited at low RF power, testing parameters such as the gas flow, temperature of critical components, or the forward and reflected power.

The remaining work can be divided into two groups: testing the already implemented parts and finishing the designing of the HV extractor and target to obtain neutrons. With the onsite parts, several testing will be done as in the RF part to obtain the minimum value of RF input necessary to ignite plasma. Currently, it is 100 W because it is the lowest RF power level the magnetron can provide. Moreover, adapt the impedance of the plasma chamber while plasma is ignited using the tuner so more power is coupled into the plasma chamber. Furthermore, Langmuir probe measurements will be performed to study the behaviour of the

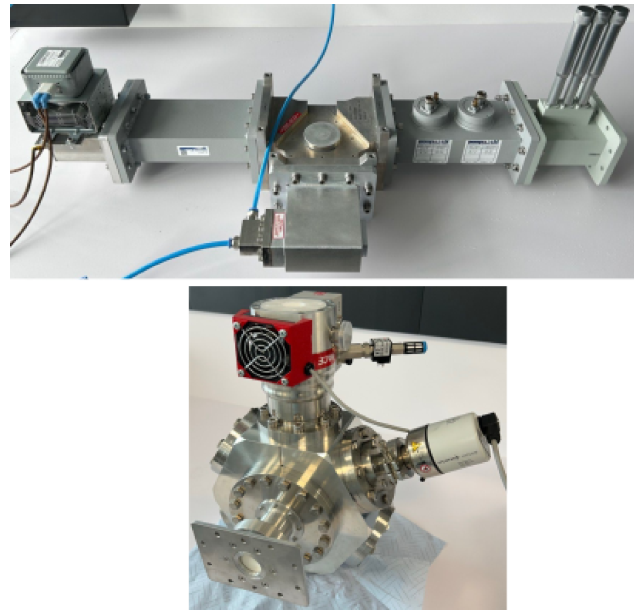

Figure 5: RF subsystem, plasma chamber, and vacuum chamber installed.

plasma that is being generated. On the other hand, the electrostatic simulations for beam extraction and the target for neutron generation will be executed. In order to implement the neutron generation, a radioprotection bunker needs to be build. The design of this bunker is being performed in the simulation software MCNP.

CONCLUSION

The magnetron and the WR340 chain have been fully tested with positive results. As mentioned in previous sections, the adaptation from WR340 to the plasma chamber geometry works as expected in the simulations as the magnets geometry do. The first tests to ignite plasma have started with promising results and the HV design process is coming to an end.

REFERENCES

[1] J. Csikai, Handbook of Fast Neutron Generators, CRC Press, 1987, ISBN: 0-8493-2967-1.

[2] Q. Ji, C.-J. Lin, C. Tindall, M. Garcia-Sciveres, T. Schenkel, and B. A. Ludewigt, "Note: Coincidence measurements of 3He and neutrons from a compact D-D neutron generator", *Rev. Sci. Instrum.*, vol. 88, no. 5, May 2017. doi:10.1063/1.4981896

[3] M. Fuller, M. Piestrup, C. Gary, J. Harris, G. Jones, J. Vainionpaa, D. Williams, J. Cremer, A. Bell, G. McRae, D. Faber, B. Ludewigt, J. Kwan, J. Reijonen, K.-N Leung, "Long-Lifetime High-Yield Neutron Generators using the DD reaction", Max 2009.

[4] Z.-W. Huang, J.-R. Wang, Z. Wei, X.-L. Lu, Z.-W. Ma, J.-L. Ran, Z.-M. Zhang, Z.-E. Yao, Y. Zhang, "Development of a compact D-D neutron generator", *Journal of Instrumentations*, vol. 13, January 2018. doi:10.1088/1748-0221/13/01/P01013

ISBN: 978-3-95450-257-8 ISSN: 2222-5692 doi:10.18429/JACoW-ECRIS2024-MOD2

CHARACTERIZATION OF THE ECR ION SOURCE LEGIS EXTRACTION SYSTEM AND ITS LOW ENERGY BEAM TRANSPORT LINE AT LEGNARO NATIONAL LABORATORIES

G. R. Mascali*,[1], L. Bellan, O. Carletto, M. Comunian,
P. Francescon, A. Galatà, C. S. Gallo, D. Martini
INFN - Laboratori Nazionali di Legnaro, Legnaro (PD), Italy
[1]also at Dip. di Fisica, Sapienza Università di Roma, Roma, Italy

Abstract

At INFN-Legnaro National Laboratories the heavy ions accelerator complex is fed with beams produced by a permanent magnet Electron Cyclotron Resonance ion source called LEGIS (LEGnaro ecrIS). Although suitable intensities and charge states to fulfill the requests of the users are normally guaranteed, the first part of the Low Energy Beam Transport line (LEBT) downstream of the ion source suffers from non-negligible losses and a lack of scalability when switching between ions with different mass-over-charge ratios, thus leading to a machine preparation time longer than would be desirable. These criticalities called for a deep characterization of the beam coming out from the ion source, especially in the case of high charge states heavy ions production, normally showing the lowest intensities. This contribution describes the numerical studies performed on the extraction system of the LEGIS source and its LEBT. The physics case used is a $^{208}Pb^{31+}$ beam produced for a nuclear physics experiment in fall 2022. As will be shown, the results shed light on the reasons for the bad reproducibility and transmission, mostly due to aberrations induced on the extracted beam by the first optical elements.

INTRODUCTION

Electron Cyclotron Resonance Ion Source (ECRIS) [1] extraction systems for highly charged heavy ions beams necessitate of detailed studies, since they have to manage several ion species with different intensities, while ensuring the proper beam quality for the injection in the accelerators. Indeed, the beam quality directly affects the global acceleration line in terms of transmission, while the charge states are important in relation with the final beam energy.

At INFN–Legnaro National Laboratories (LNL) the PIAVE-ALPI [2–4] heavy ions accelerator complex is fed with highly charged heavy ions by a 2nd generation ECRIS called LEGIS (LEGnaro ecrIS) [5]. It is a full permanent magnet source of the Supernanogan type produced by the Pantechnik company [6], with an operating frequency range between 14 and 14.5 GHz. In order to match the optimum $\beta = v/c$ for the injection into PIAVE, LEGIS and the first part of the LEBT are installed on a high voltage platform (maximum voltage 400 kV).

Suitable intensities for the requests coming from the nuclear physics community are normally produced. Despite that, operational experience evidenced a not satisfactory transmission in the LEBT line installed on the platform, as well as a lack of scalability of the values of the steerers mounted in the downstream fixed-β magnetic beam line towards PIAVE.

To shed light on the above-mentioned criticalities, we carried out numerical simulations of beam extraction from LEGIS and its transport in the first part of the LEBT line, taking as case study the production of a lead beam for a nuclear physics experiments performed in fall 2022 at LNL.

This paper describes the results coming out from the simulations, drawing some conclusions on the possible explanations for the criticalities observed and the actions could be undertaken to solve them.

LEGIS AND THE LNL ACCELERATOR COMPLEX

The LEGIS source can produce heavy ions beam currents of the order of μA for the PIAVE-ALPI accelerator complex. Its extraction system consists of four electrodes (see Fig. 1): the plasma electrode, with a 7 mm extraction aperture and a voltage of 24 kV (voltage V_s always fixed), a puller (maximum operational voltage $V_p = -6$ kV), an electrostatic lens named focus (max voltage $V_f = 1$ kV) and a ground electrode. It is directly coupled to the analysis dipole, characterized by a maximum field of 0.5 T, a bending radius of 500 mm, a pole gap of 80 mm and edge angles of 28.3°, both at the entrance and at the exit. A selection slit (10 mm opening usually) and a Faraday cup are mounted more or less at its image point: this first part of the LEBT, installed on the high voltage platform (as shown in Fig. 1), is generally used to characterize the LEGIS' performances and is the part of the line object of the studies presented in this paper.

The line on the platform continues with a double Einzel lens (max operational voltage $V_{ein} = 10$ kV) that focuses the selected beam into the accelerating column, followed by an electrostatic triplet (max voltage $V_{trip} = 4$ kV) outside of the platform. From this point, the line continues with a fixed-β magnetic beam line for the injection in the PIAVE-ALPI accelerator complex.

PIAVE (Positive Ion Accelerator for Very-low Energy) is a positive ions linear accelerator preceded by a three harmonic buncher (40, 80, 160 MHz) and consisting of two 80 MHz superconducting RFQs, with β equal to 0.0089 and 0.0035 at the RFQs entrance and exit, respectively. The RFQs are

* giadarachele.mascali@uniroma1.it, giada.mascali@lnl.infn.it

ISBN: 978-3-95450-257-8 ISSN: 2222-5692 doi:10.18429/JACoW-ECRIS2024-MOD2

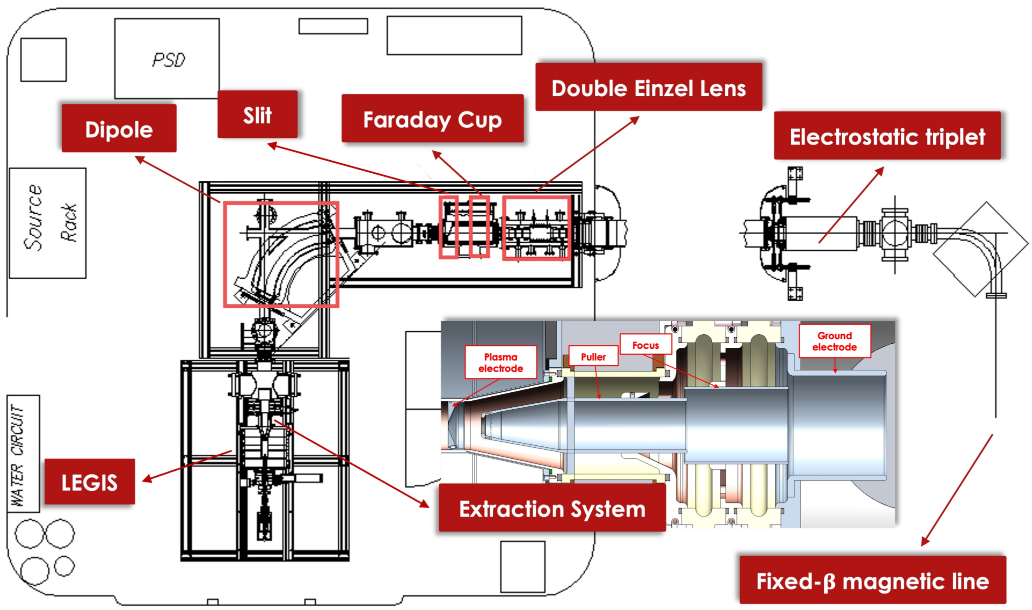

Figure 1: Schematic representation of the LEGIS extraction system and the first part of the downstream LEBT.

characterized by maximum operational accelerating field of 27.10 MV/m and 25.49 MV/m (for $^{238}U^{32+}$).

ALPI (Acceleratore Lineare Per Ioni) is the superconducting booster consisting of 20 cryostats, each containing 4 quarter-wave resonators (QWRs) and operating at 80 MHz (first 6 low-β cryostats) and 160 MHz (the others high-β cryostats), with a maximum accelerating field of 5 MV/m. Beams can reach 10 MeV/A of energy for a mass-over-charge ratio of 7.

SIMULATIONS OF BEAM EXTRACTION AND TRANSPORT

The operational experience with LEGIS revealed some criticalities, in particular: a transmission to the Faraday Cup on the platform not higher than 50 %; the fact that the steerers' values in the fixed-β magnetic line downstream of the LEBT line do not scale following the mass-over-charge ratio as expected. To find possible explanations, we carried out extensive numerical simulations of the beam extracted from LEGIS and its transport through the first part of the LEBT.

The case study considered is a ^{208}Pb beam produced by means of a resistive oven for a nuclear physics experiment scheduled in fall 2022 at INFN-LNL. All the parameters have been optimized to deliver the charge state 31^+ with a suitable intensity: Table 1 shows the main ones relevant for the studies presented in this paper.

The extraction from LEGIS has been simulated for the first time by using the code IBSimu [7], considering a total beam current of 1.9 mA and a space charge compensation at 98 %. The input distribution consisted of ions from Pb^{14+} to Pb^{32+} and from O^{1+} to O^{4+}, resembling the spectrum acquired during the experiment. Figure 2 shows the simulated Pb^{31+} horizontal emittance: it can be seen that the

Table 1: Main Parameters Used for the Production and Transport of the $^{208}Pb^{31+}$ Beam

P [W]	f [GHz]	I_{tot} [μA]	$I_{Pb^{31+}}$ [μA]	V_{plat} [kV]
304	14.328	1900	2.7	224.68

V_s [kV]	V_p [kV]	V_f [kV]	V_{ein} [kV]	V_{trip} [kV]
24	-1	1	6.4, 4	4

beam has a limited divergence and, above all, a normalized rms emittance of 0.039 64 mm·mrad, well within the limit of acceptance expected for PIAVE (0.1 mm·mrad).

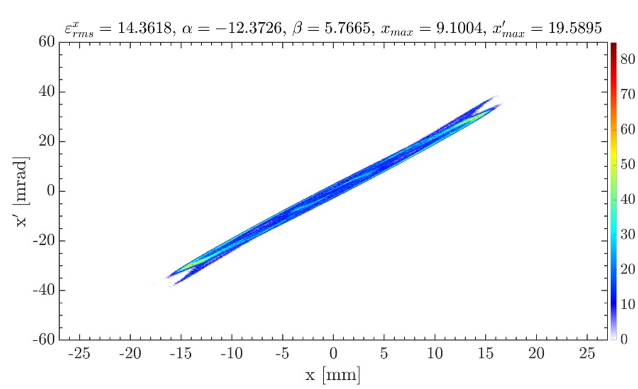

Figure 2: Phase space distribution of the Pb^{31+} numerically obtained by means of the code IBSimu.

The extraction simulation results have been the input to simulate the beam transport through the first part of the LEBT installed on the platform, using the TraceWin software [8]. As a first step, the beamline acceptance was evaluated for each ion considered for the simulations: it has been

ISBN: 978-3-95450-257-8 ISSN: 2222-5692 doi:10.18429/JACoW-ECRIS2024-MOD2

found that it exists a significant mismatch with the beam emittance at the entrance of the line, being more evident for the O^{4+} shown in Fig. 3. As a confirmation of this effect, the calculated transmission of the O^{4+} revealed to be the lowest one (~23 %).

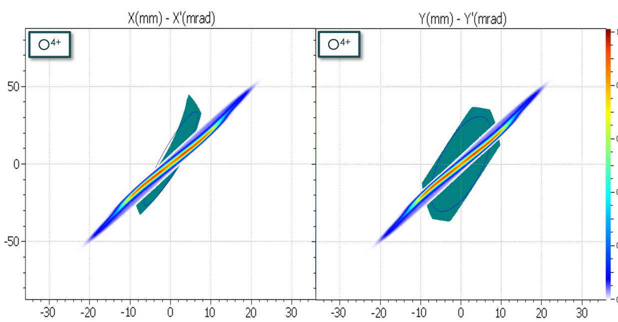

Figure 3: Emittance-acceptance mismatch with the LEBT for the O^{4+}.

This first outcome of the simulations gave us already a possible explanation for the low transmission to the Faraday cup experimentally observed.

The study proceeded by evaluating, for all the ions, the density levels along the LEBT: Figure 4 shows the results in the direction corresponding to the bending plane for the lowest (among all ions) and highest (for lead) mass-over-charge ratio. It is evident that both beams, initially centered (in position and distribution) on the nominal trajectory, emerge off-centered after passing through the dipole, with the focus well preceding or following the slit position.

These aberrations can be explained by the non-linear effects induced by the dipole magnetic field depending on the beams' width with respect to the bending radius in the middle of the analysis dipole. In addition to the beam losses, these lead to the distortion of the distributions.

Indeed, the $^{208}Pb^{31+}$, whose dynamics is closer to the nominal one, suffers from fewer losses since its smaller width and intensity allowed a beam focusing closer to the slit, as shown in Fig. 5, favoring consequently the transmission.

In addition, the evaluation of the transmission along the global line confirmed that the losses are not only due to the cuts at the slit, but are observed all along the beam-line.

The influence of the nonlinear contributions on the beam quality can be verified comparing the beams emittance computed at the entrance and exit of the LEBT. We observed two different trends for lead and oxygen ions: for the former, the emittance increases due to the not suitable optics; for the latter, beam losses are dominant and lead to an overall decrease of the emittance.

More interesting results emerged by comparing the emittances of the transported beams and those computed at the beam line entrance for the same beams' percentage of the transmitted one (Fig. 6). In this case all beams show an emittance deterioration, up to a factor more than 3 for the Pb^{31+}. However, as we can see, that did not prevent the injection in PIAVE, since the emittance values (all <0.08 mm·mrad) are

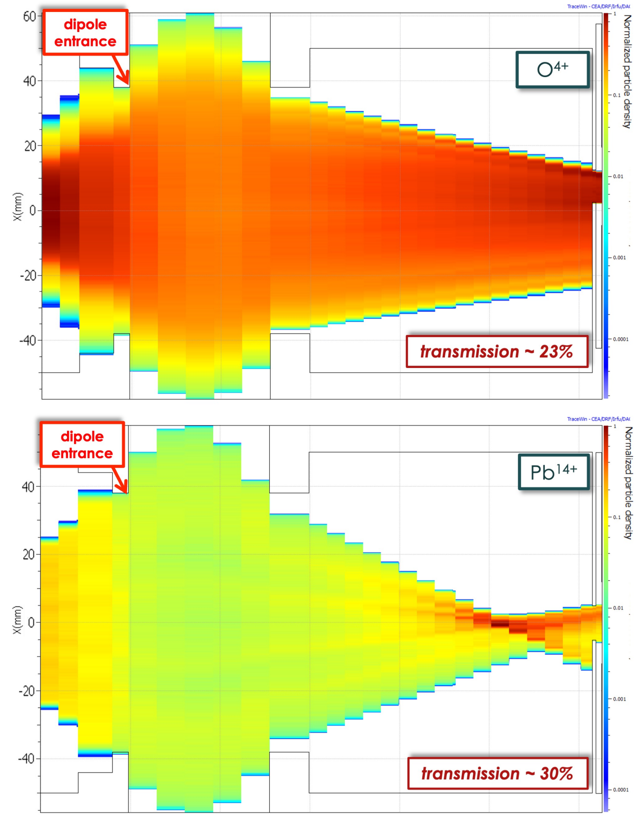

Figure 4: Density levels in the bending plane of the O^{4+} and Pb^{14+} beams.

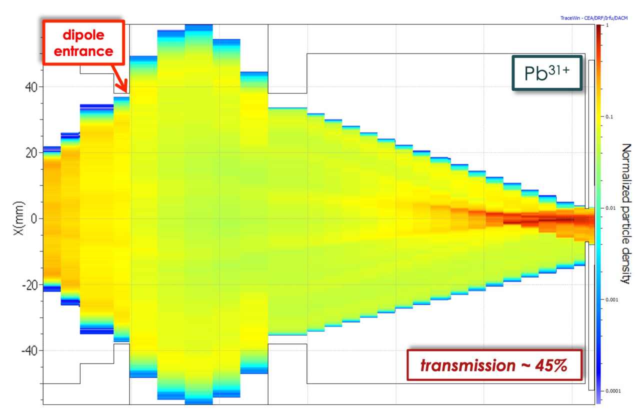

Figure 5: Density levels in the bending plane of the optimized Pb^{31+}.

still within the acceptance limit expected for its RFQs. As a proof, the experimentally measured transmission of $^{208}Pb^{31+}$ through PIAVE turned out to be close to the nominal one.

All these evidences can be also observed in the phase space distributions' deformation at the end of the line with respect to those at the beginning (see Fig. 7), which led to the emittances deterioration and confirmed the presence of non-linear forces in the dipole.

Finally, as shown in Fig. 8, a complete misalignment of the centroid of each beam, with specific values for each ion,

ISBN: 978-3-95450-257-8 ISSN: 2222-5692 doi:10.18429/JACoW-ECRIS2024-MOD2

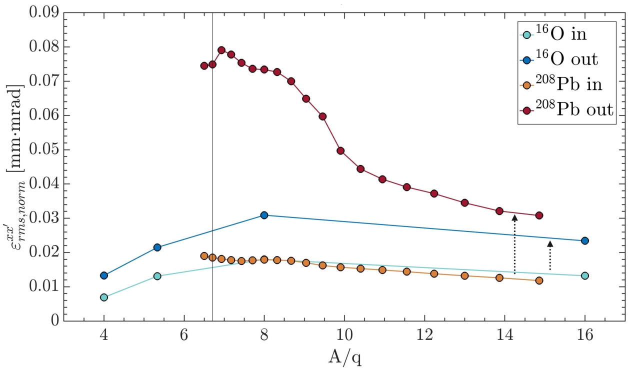

Figure 6: Comparison between input and output emittances of the same beam percentage.

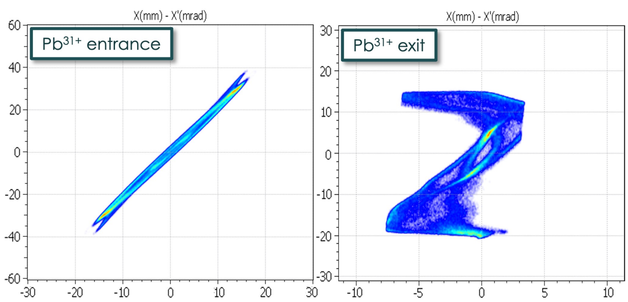

Figure 7: Comparison between the Pb^{31+} emittance distributions in the phase space at the LEBT entrance and exit.

came out from the evaluation of the average position and divergence as a function of the mass-over-charge ratio.

As a consequence, the steerers in the fixed-β magnetic line towards PIAVE have to deal not only with eventual mechanical misalignments (normally fixed), but also with those induced by the transport process. It is an important result that can explain the experimental observation according to which steerers values exhibit deviation of up to 60 % from expectations based on the theoretical scaling with the mass-over-charge ratio.

CONCLUSIONS AND PERSPECTIVES

Beams extracted from LEGIS has been simulated for the first time thanks to IBSimu. These have allowed to carry out many simulations of the beams transport along the LEBT, that shed light on the reasons for the experimentally observed criticalities. In particular, the almost 50 % losses could be traced back to an emittance-acceptance mismatch in the LEBT line. In addition, an optic not suitable for transport through the dipole has been found, that leads to the beam quality deterioration due to non-linear effects. This brought to off-centered average positions and divergences of each beam centroid, with different values for each mass-over-charge ratio, thus explaining the steerers non-scalability in the fixed-β magnetic line towards PIAVE, as experimentally expected.

From these results some possible solutions have been identified. Firstly, the modification of the LEBT line layout by

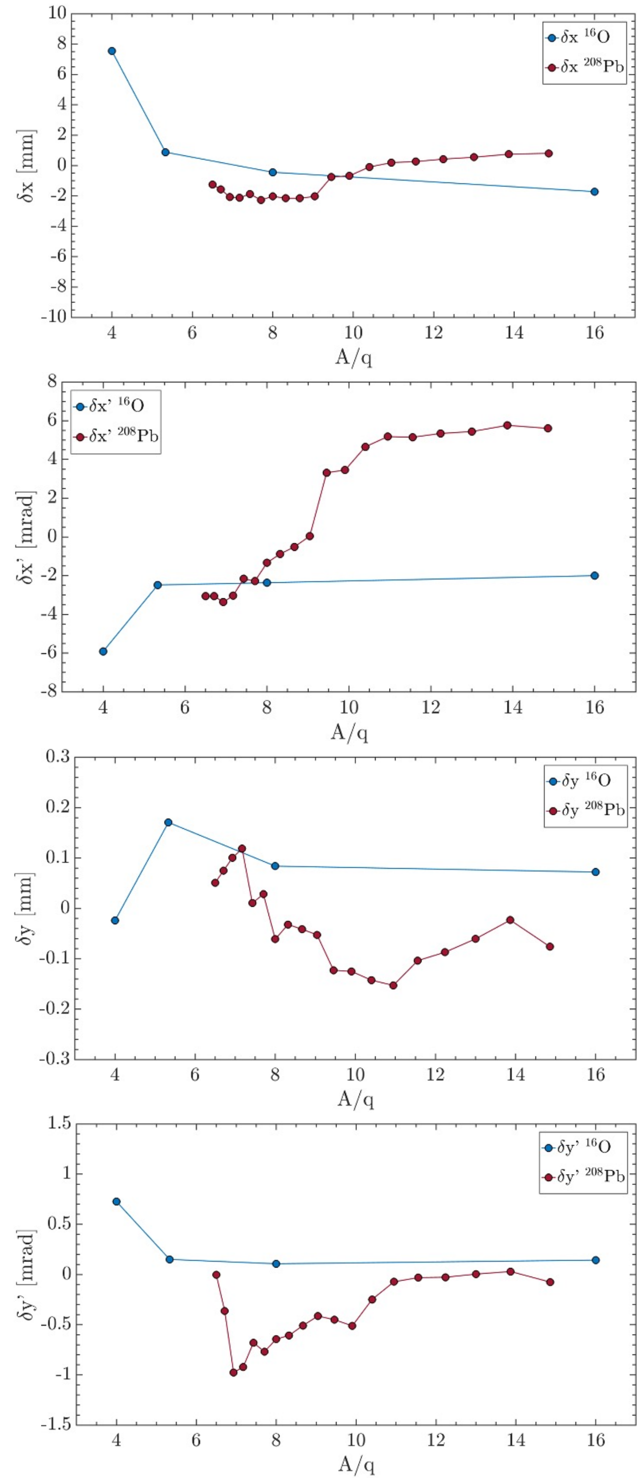

Figure 8: Average position and divergence in the transverse plane of the centroid of each beam as a function of the mass-over-charge ratio.

installing the source closer to the dipole or by interposing a lens between them, in order to improve the matching between the beams' emittance and the acceptance of the LEBT. Secondly, the design of a new extraction system to produce beams with more suitable qualities.

ISBN: 978-3-95450-257-8 ISSN: 2222-5692 doi:10.18429/JACoW-ECRIS2024-MOD2

REFERENCES

[1] R. Geller, *Electron Cyclotron Resonance Ion Sources and ECR Plasmas*, Institute of Physics Publishing: Bristol, UK, 1996.

[2] G. Bisoffi *et al.*, "Completion of the First Superconducting RFQ at INFN-LNL", in *Proc. SRF'99*, Santa Fe, NM, USA, Nov. 1999, paper WEP001, pp. 367–371. https://jacow.org/srf99/papers/WEP001.pdf

[3] A. Lombardi *et al.*, "PIAVE the Legnaro New Positive Ion Injector Based on Superconducting RFQs", in *Proc. LINAC'00*, Monterey, California, USA, paper TU205, pp. 356–360, 2000. https://jacow.org/l00/papers/TU205.pdf

[4] L. Bellan *et al.*, "New techniques method for improving the performance of the ALPI Linac", *J. Instrum.*, vol. 19, p. T03005, 2024. doi:10.1088/1748-0221/19/03/T03005

[5] A. Galatà *et al.*, "First beams from the new electron cyclotron resonance source LEGIS (LEGnaro ecrIS) at INFN-LNL", *Rev. Sci. Instrum.*, vol. 81, p. 02A315, 2010. doi:10.1063/1.3258609

[6] Pantechnik, https://www.pantechnik.com

[7] IBSimu, http://ibsimu.sourceforge.net

[8] TraceWin, https://www.dacm-logiciels.fr

ISBN: 978-3-95450-257-8 ISSN: 2222-5692 doi:10.18429/JACoW-ECRIS2024-MOP01

CHARACTERIZATION OF THE 2.45 GHz DREEBIT ECRIS VIA OPTICAL SPECTROSCOPY

M. Molodtsova*, A. Philipp†, E. Ritter, Dreebit GmbH, Großröhrsdorf, Germany

Abstract

ECR ion sources are widely used at many research institutions to provide ions for various experimental setups. DREEBIT GmbH aims to industrialize this type of ion source technology. Our goal is to build table-top sized ion sources which can easily be handled and integrated into larger machine setups, thereby fulfilling high requirements on beam current, quality, stability and reproducibility in serial production. To achieve this, we had already optimized the microwave injection system and magnetic plasma confinement by introducing a simple method to allow for injection of circularly polarized microwaves and adjusted the magnetic field distribution which led to an 80 GHz increase of proton beam current [1]. In the present work, we show how optical emission spectroscopy was used to gain deeper information about the plasma of this specific type of ion source, independently from its ion extraction system. The plasma characterization includes studies of the electron density and temperature (n_e, T_e) and the density of atomic and molecular hydrogen (n_H, n_{H_2}) showing the performance of the 2.45 GHz DREEBIT ECRIS concerning plasma heating and proton production and indicating how the source performance can be enhanced in further steps.

INTRODUCTION

Electron Cyclotron Resonance Ion Sources (ECRIS) provide low, intermediate and highly charged ions for a broad range of applications, reaching from nuclear [2, 3] over materials [4] to medical physics research. In the future, they can be used in combination with particle accelerators or as part of irradiation facilities, e.g., for industrial semiconductor manufacturing or cancer therapy [5]. The goal of the present work is to characterize the plasma of the table-top sized 2.45 GHz DREEBIT ECRIS run with hydrogen in order to gain better understanding of the possibilities for source improvement. Using optical emission spectroscopy (OES) the intensities of the hydrogen Balmer and Fulcher lines depending on the power of the injected microwave and the phase shift of the two injected microwaves were studied. The electron density n_e, temperature T_e and ratio of atomic to molecular hydrogen n_H/n_{H_2} were deduced from the optical spectra using the Yacora solver [6].

EXPERIMENTAL METHOD

An Ocean Insight Flame UV-VIS Spectrometer was used for the optical spectroscopy setup. The spectrometer is sensitive in the wavelength range from 200 to 850 nm with a resolution of 1.37 nm. To couple the light into the spectrometer a reflective collimator with UV-enhanced aluminum coating with a diameter of $d = 8.5$ mm was employed. An optical cable with a fiber diameter of 200 µm couples the collimator to the spectrometer device. Intensity calibration was conducted on-site by using an Ulbricht sphere. The line of sight where the plasma was characterized is shown in Fig. 1.

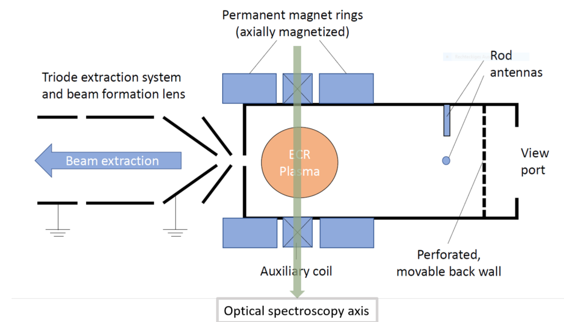

Figure 1: Experimental setup with optical spectroscopy axis marked in green.

The optical light emitted by the atomic and molecular hydrogen ions reveals information about the plasma. The Balmer line ratio H_β/H_γ relates to the electron density, the ratio between the Balmer line H_γ and the integrated Fulcher lines is a measure for the dissociation ratio, as the Fulcher lines are emitted during relaxation of excited vibrational and rotational states of the H_2 molecule [7]. While individual line ratios had been used to identify plasma parameters like the electron density directly in the past, this method was replaced by the Yacora solver, employing a collisional radiative model and identifying the best agreement between simulated and actual line ratios under variation of the desired plasma parameters.

RESULTS

In two separated measurement campaigns a scan of the microwave power and the phase shift of the two injected microwaves were performed. From this data set a range of the plasma parameters electron density n_e, electron temperature T_e and the neutral density ratio n_H/n_{H_2} were determined to characterize the plasma. The findings from the OES measurements are compared to measured spectra of extracted ions.

OES Measurements

Microwave Power Scan at 100° Phase Shift Figure 2 shows the results of the microwave power scan. Here, the intensity ratios of subsequent Balmer lines are shown as black (H_α/H_β), red (H_β/H_γ) and green (H_γ/H_δ) data points. Moreover, the previously discussed ratio of $H_\gamma/H_{\mathrm{Ful}}$

* maria.molodtsova@dreebit.com
† alexandra.philipp@dreebit.com

ISBN: 978-3-95450-257-8 ISSN: 2222-5692 doi:10.18429/JACoW-ECRIS2024-MOP01

is shown in blue. It is visible that all line ratios increase with the microwave power. However, the red data points, which are a measure for the electron density, do not exhibit such a clear trend and the data is difficult to interpret. For this reason, the Yacora results are discussed in the next step.

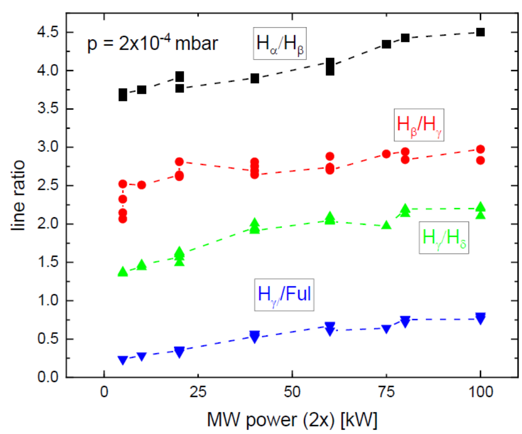

Figure 2: Microwave power scan at 100° phase shift.

Phase Shift Scan at (2x) 75 W Microwave Power Furthermore, the phase shift between the two injected microwaves was investigated by scanning the whole range of phase shifts, while maintaining the microwave power at (2x) 75 W and the pressure at $2 \cdot 10^{-4}$ mbar. Figure 3 shows the results of the phase scan. It is noticeable that there is almost no visible dependence of the line intensity ratios with the phase shift, which indicates that the plasma parameters are constant at the location of the optical spectroscopy axis.

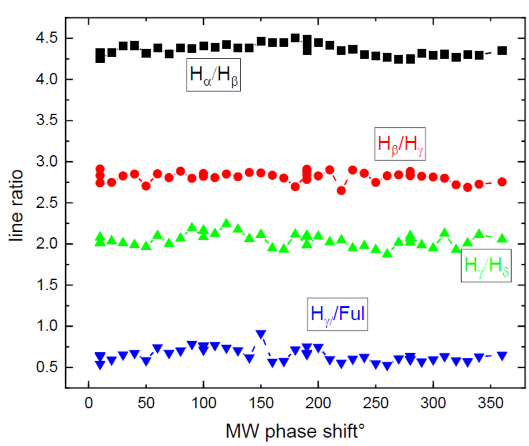

Figure 3: Microwave phase shift scan at (2x) 75 W microwave power and p = $2 \cdot 10^{-4}$ mbar.

Yacora Results

The electron density n_e, temperature T_e and the ratio of n_H/n_{H_2} can be reconstructed using the Yacora solver, which provides a collisional radiative analysis model for OES on hydrogen and helium plasmas. Yacora simulates the hydrogen line ratios under variation of the plasma parameters. By comparing the calculated results to the measured spectra the best match can be identified revealing the actual plasma parameters of interest. Among these parameters, the temperature T_e and the ratio n_H/n_{H_2} can not be reconstructed independently because they are strongly correlated due to their impact on line emission in the present parameter phase space. As a result only ranges of possible solutions can be determined, allowing for a coarse analysis of these parameters.

Figure 4 shows the electron density in dependence on the microwave power for a plasma length of $l_{plasma} = 5$ cm and $l_{plasma} = 10$ cm. The diameter of the plasma chamber is 10 cm, but the magnetic confinement compresses the plasma to a smaller volume, which is not exactly known. Therefore the electron density is specified for an educated guess of both limits of the possible plasma length as the precise length has not yet been determined. The electron density scales linearly with the plasma length and increases with rising microwave power until it reaches a plateau for values which are higher than 40 W. If assuming that the plasma is confined within a region which has half length of the plasma chamber (5 cm), the electron density is $n_e = 7 \cdot 10^{16}\,\mathrm{m^{-3}}$ at the plateau, a value which is close to the calculated critical density of a 2.45 GHz ECR source, resulting in $n_c = 7.45 \cdot 10^{16}\,\mathrm{m^{-3}}$.

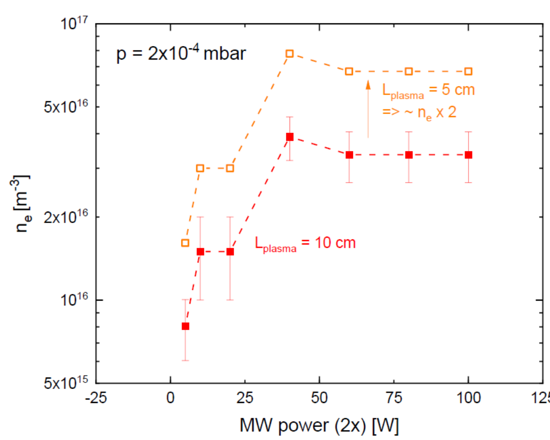

Figure 4: Yacora results for electron density n_e depending on the microwave power, considering 2 different plasma lengths of 5 cm and 10 cm.

Electron densities in other ECR ion sources around the world were found in the same order of magnitude around $10^{17}\,\mathrm{m^{-3}}$ [8–10].

Figures 5 and 6 show the dependence of the electron temperature T_e and the ratio of the atomic and molecular hydrogen density n_H/n_{H_2} on the microwave power. Since both parameters can only be reconstructed in combination, a wide range parameter variation was performed identifying the limits of the parameter space with values for the minima and maxima for T_e as well as n_H/n_{H_2}. Assuming individual values outside of these extrema, Yacora could not find any matching solution for the measured spectra at all, indicating that the actual values for T_e and n_H/n_{H_2} lie within the presented range. It is visible that the region for the electron temperature is quite large for microwave powers above (2x) 40 W. The upper limit is at the maximum of the phase space for the Yacora solver, indicating that an electron ensemble

ISBN: 978-3-95450-257-8 ISSN: 2222-5692 doi:10.18429/JACoW-ECRIS2024-MOP01

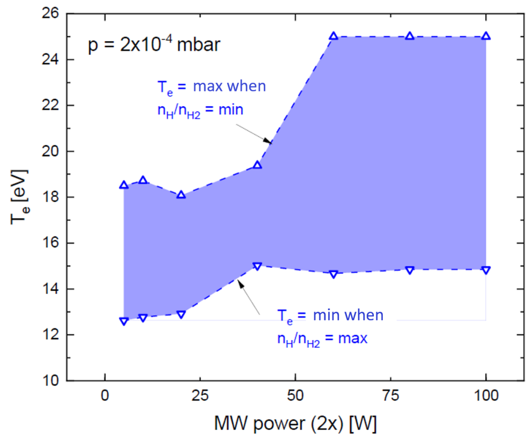

Figure 5: Yacora results for electron temperature T_e in dependence of microwave power.

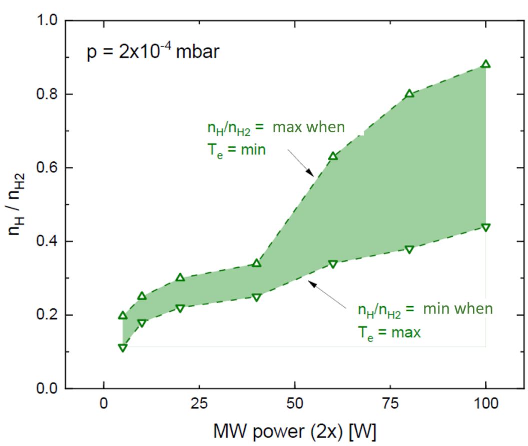

Figure 6: Yacora results for the ratio n_H/n_{H_2} in dependence of microwave power.

with an even higher temperature could lead to the observed line intensities. However, for temperatures higher than 25 eV the Yacora model is no longer accurate enough. The minimum of the temperatures is at 15 eV for a microwave power higher than (2x) 40 W. This lower limit of T_e is comparable with electron temperatures found by other research groups for a 2.45 GHz ECRIS [8, 10].

Extracted Ions

In addition to the analysis of the plasma emission via optical spectroscopy, it is also possible to extract ions from the plasma chamber and evaluate them using a dipole magnet, which separates the ions according to their mass to charge ratio. Extracted ions were measured in dependence on the microwave power and the phase shift of the two injected microwaves.

It was found that the intensity ratio of extracted ions I_H/I_{H_2} strongly depends on the microwave power, as shown in Fig. 7. At low microwave powers the ratio of molecular hydrogen corresponds to $I_H/I_{H_2} = 0.3$. With increasing power the ratio grows and becomes larger than 1 from 60 W on and reaches up to 1.4 for 80 W. A similar behaviour could be observed in the OES measurements, like shown in Fig. 6. Both the

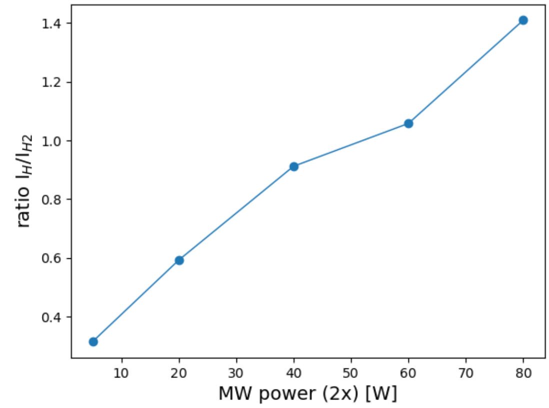

Figure 7: Intensity ratios of extracted atomic to molecular hydrogen I_H/I_{H_2} in dependence on microwave power.

minimum and maximum boundaries of the ratio n_H/n_{H_2} are increasing with the power. The upper limit is more trustworthy, since it is associated with the lower limit of the electron temperature. However, the absolute values of the dissociation ratio derived from the ion extraction measurements are higher than the OES results, even if the minimum electron temperature is assumed. Therefore, it is concluded that the differences in the extracted spectra and OES measurements originate from the different locations of spectroscopy and ion extraction within the plasma.

The OES data suggests that the phase shift has almost no influence on the ratio n_H/n_{H_2}. However, from the extracted spectra a slightly different picture is visible. The ratio is always above 1 for all phase shift angles, but the intensity ratio I_H/I_{H_2} is highest with almost 1.4 for phase shift angles between 10° and 100° and decreases to 1.1 for higher microwave phase shift angles, as shown in Fig. 8. This can also be explained with the fact that the extraction of ions and the optical spectroscopy happen at different locations in the plasma. While the spectrometer is looking through the center of the plasma chamber, the ions are extracted from a limited region behind the plasma aperture.

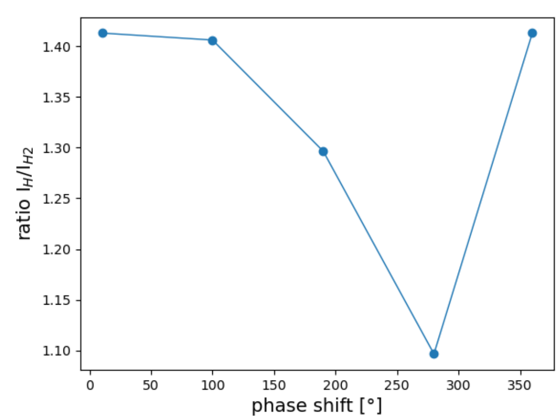

Figure 8: Intensity ratios of extracted atomic to molecular hydrogen I_H/I_{H_2} in dependence on microwave phase shift.

The polarisation of the injected microwave changes while the wave propagates through and interacts with the plasma. It is interesting to notice that while center of the confinement zone accumulating ions from a larger region along the ion source axis is not sensitive to the initial polarisation of the microwave, the region from where the ions are extracted is indeed sensitive to this parameter.

CONCLUSION

The present work focused on characterizing the DREEBIT 2.45 GHz ECRIS concerning the achieved plasma parameters electron density n_e, electron temperature T_e and dissociation ratio $n_\mathrm{H}/n_{\mathrm{H}_2}$. The plasma parameters were studied under variation of the injected microwave power as well as the phase shift, varying the initial polarization of the wave reaching the plasma.

The scan of the microwave power showed an increase in the electron density up to (2x) 40 W above which a plateau is reached with values between 3 and $7 \cdot 10^{16}\,\mathrm{m}^{-3}$. A more accurate value can be given once the effective length of the investigated plasma has been determined which will be done in the future. The results so far are in reasonable agreement compared to values recorded at other 2.45 GHz ECRIS with similar operation parameters.

The electron temperature T_e also rises with increased microwave power until (2x) 40–50 W. Within the range of possible resulting T_e it is most likely that the lower plateau limit of 15 eV reflects the conditions in reality as this corresponds to the maximum dissociation ratio values.

While n_e and T_e rise only up to a microwave power input of around (2x) 40 W, the dissociation ratio keeps rising up to the maximum power of (2x) 100 W given by the microwave generator, reaching $n_\mathrm{H}/n_{\mathrm{H}_2} = 0.9$. The same correlation is shown by ion extraction measurements although the absolute values for the dissociation ratio are even higher in this case, up to $n_\mathrm{H}/n_{\mathrm{H}_2}$ of 1.4. This is the first discrepancy shown between OES and ion extraction measurements. The second one is that while there is hardly any reaction to be observed via OES, the dissociation ratio does depend on the right phase shift between the two injected microwave signals defining the initial polarization of the microwave reaching the plasma. Both discrepancies can be explained by the different positions of OES and the region from where ions are extracted.

We conclude that while the electron heating and proton production have been optimized there is still room for improvement concerning the extraction of ions out of the plasma, the region from where ions are drawn to form the beam appears to be limited and does not reach the center of the plasma confinement where the OES line of sight is situated. In the near future, our R&D will focus on the optimization of the extraction lens system concerning beam current and emittance.

ACKNOWLEDGEMENTS

We wish to acknowledge the research group of Prof. Fantz from the *AG Experimentelle Plasmaphysik (EPP)* at University of Augsburg/IPP Garching, especially S. Briefi and D. Rauner for their help with the experimental campaign and data analysis.

REFERENCES

[1] A. Philipp, M. Molodtsova, and E. Ritter, "Two-rod-antenna microwave injection system for production of circularly polarized microwaves in cylindrical ECRIS cavities", *J. Phys. Conf. Ser.*, vol. 2244, no. 1, p. 012 011, 2022. doi:10.1088/1742-6596/2244/1/012011

[2] R. Pardo, "Review of high intensity ion source development and operation", *Rev. Sci. Instrum.*, vol. 90, no. 12, p. 123 312, 2019. doi:10.1063/1.5128507

[3] M. Kreller *et al.*, "An ECRIS Facility for Investigating Nuclear Reactions in Astrophysical Plasmas", in *Proc. Int. Workshop on ECR Ion Sources (ECRIS'16)*, Busan, Korea, pp. 59–63, 2016. doi:10.18429/JACoW-ECRIS2016-WEBO01

[4] S. Jiang *et al.*, "Reduced spin torque nano-oscillator linewidth using He+ irradiation", *Appl. Phys. Lett.*, vol. 116, no. 7, p. 072 403, 2020. doi:10.1063/1.5137837

[5] A. Degiovanni *et al.*, "Status of the Commissioning of the LIGHT Prototype", in *Proc. 9th Int. Part. Accel. Conf. (IPAC'18)*, Vancouver, BC, Canada, pp. 425–428, 2018. doi:10.18429/JACoW-IPAC2018-MOPML014

[6] D. Wünderlich, M. Giacomin, R. Ritz, and U. Fantz, "Yacora on the Web: Online collisional radiative models for plasmas containing H, H_2 or He", *J. Quant. Spectrosc. Radiat. Transfer*, vol. 240, p. 106 695, 2020. doi:10.1016/j.jqsrt.2019.106695

[7] S. Briefi and U. Fantz, "A revised comprehensive approach for determining the H_2 and D_2 rovibrational population from the Fulcher-α emission in low temperature plasmas", *Plasma Sources Sci. Technol.*, vol. 29, no. 12, p. 125 019, 2020. doi:10.1088/1361-6595/abc085

[8] Y. Xu *et al.*, "Emission spectroscopy diagnostic of plasma inside 2.45 GHz ECR ion source at PKU", in *Proc. ECRIS'14*, paper MOOBMH04, pp. 20–22, 2016. https://jacow.org/ecris2014/papers/moobmh04.pdf

[9] D. Mascali *et al.*, "Electromagnetic diagnostics of ECR-Ion Sources plasmas: optical/X-ray imaging and spectroscopy", *J. Instrum.*, vol. 12, no. 12, p. C12047, 2017. doi:10.1088/1748-0221/12/12/C12047

[10] G. Castro, D. Mascali, M. Mazzaglia, S. Briefi, U. Fantz, and R. Miracoli, "Multidiagnostics investigation of the role of the magnetic field profile in a simple mirror trap", *Phys. Rev. Accel. Beams*, vol. 22, no. 5, p. 053 404, 2019. doi:10.1103/PhysRevAccelBeams.22.053404

ISBN: 978-3-95450-257-8 ISSN: 2222-5692 doi:10.18429/JACoW-ECRIS2024-MOP03

ALISES II SOURCE IS STILL ALIVE AT CEA SACLAY

O. Delferrière[1,*], A. Dubois[1], Y. Gauthier[1], F. Mezei[2], Y. Sauce[1], J. Schwindling[1], O. Tuske[1], D. Uriot[1]

[1] IRFU, CEA, Université Paris-Saclay, F91191 Gif-sur-Yvette France
[2] MIRROTRON, Konkoly-Thege Miklós út 29-33; H-1121 Budapest, Hungary

Abstract

Developments of ECR intense light ion sources is an important research axis of the Laboratory for Accelerator Study and Development at CEA-Saclay. Starting in the 90's from the SILHI proton source for the IPHI accelerator [1], several high intensity proton or deuteron SILHI-type sources were provided to international facilities like IFMIF, FAIR or SPIRAL2. From 2011, CEA started a new R&D program on high intensity ECR compact ion sources with the ALISES source family. The results obtained with the first ALISES source prototype [2,3] gave us the main goals for the design of the ALISES II source that ran several months on 50 kV BETSI [4] test bench and was dismounted at the end of 2016 to upgrade the test bench to 100kV. However, this source was never reinstalled and has been replaced by the ALISES III source [5] that runs on BETSI up to now. Recently, the ALISES II source and its equipment has been reassembled to be restarted on BETSI for beam characterization before sending it to the MIRROTRON company in Hungary as the proton source for a neutron beam facility. This paper describes the setup on BETSI and proton beam characteristics obtained by emittance measurements and spatial species proportion analysis. A Low Energy Beam Transport line is proposed to match the beam to the already constructed RFQ.

INTRODUCTION

ALISE II ion source was the first compact ECR light ion source at Saclay for proton beam extraction. The source installed on the BETSI test bench in February 2015 allowed a first extracted beam current of 35 mA hydrogen ion beam (H^+ and molecular ions) at 42kV, regularly extracted through a 6 mm diameter plasma electrode with a record of extracted intensity of 38.5mA at 42kV. The source operated up to 50 kV in pulsed or continuous mode. Several experiments were carried out with this source on BETSI up to 2016 like irradiation of scintillators for a 4D emittance meter or beam stop finger bombardment (Fig. 1) for S3 separator of SPIRAL2 project in Caen (France).

The beam emittance was measured with the Allison scanner designed and manufactured by IPHC in Strasbourg (France) for the FAIR project in Darmstadt (Germany). ALISES II ion source was then dismounted while upgrading BETSI test bench to 100kV.

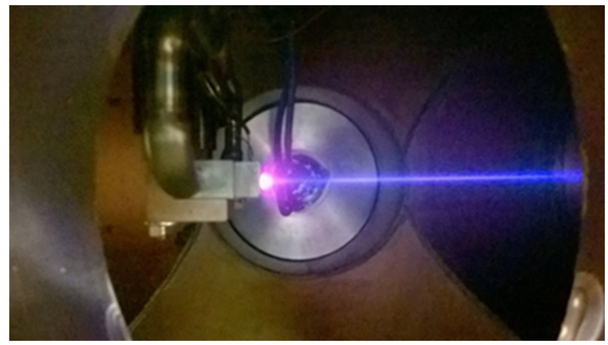

Figure 1: Finger bombardment for S3 separator of SPIRAL2 project.

ORIGINAL SOURCE SETUP AND EVOLUTION

ALISES II Ion source is a compact system originally designed to achieve the same performances as SILHI, around 100 mA of 95keV protons. A three steps ridges transition is implemented to concentrate the 2.45GHz High Frequency (*HF*) microwave onto the 90mm diameter plasma chamber axis. A copper cylinder has been machined to form the plasma chamber and the RF entrance ridged guide in one piece. A smooth ceramic cylinder built in two concentric parts realizes the insulating structure, and is in contact of the copper body. To connect the puller electrode to high voltage, a groove has been machined longitudinally on the external surface of the internal ceramic cylinder, and a hole has been drilled radially on the external ceramic cylinder up to the puller connector. Both the ceramic and the source body are screwed on a copper flange and connected to the RF guide. A tunable magnetic field creates the electron resonance at the cavity's entrance when the magnetic field reaches 87.5mT to give energy to the electrons to ionize the hydrogen gas inside the plasma chamber. To extract the proton beam and also the molecular ion H_2^+ and H_3^+ present in smaller proportion, a five electrodes extraction system is used which comprises the plasma electrode (95kV), the puller electrode (70kV), two ground electrode and the electron repeller (-3kV) placed in between the later. The electron repeller prevents the electrons from the LEBT produced by ionization of the residual gas to go upstream and being accelerated toward the plasma chamber with possible damage of the boron nitride disk at the bottom of the plasma chamber, but also to avoid high power deposition on the 90° RF bend wave-guide. The plasma electrode is fixed on the copper cylinder extremity to close the plasma chamber with an appropriate

ISBN: 978-3-95450-257-8 ISSN: 2222-5692 doi:10.18429/JACoW-ECRIS2024-MOP03

extraction hole. The puller electrode is fixed to the source body by the mean of an intermediate ring shaped ceramic part. Both plasma chamber, ground electrode, RF bent and hollow conductor double pancake coil are cooled. The Fig. 2 shows a cut of the ALISES II source assembly.

In spite ALISES II reach 95KeV without beam extraction, we never obtain stable beam without sparks beyond 75kV. For that reason, next versions of ALISES [6,7] are developed to obtain suitable results at higher energy. One important issue of this source is the HV connection to the puller electrode, very close to the coil witch is at ground. To avoid sparks, 4-electrode extraction system without the puller electrode is used. To optimize the gap distance between plasma electrode and first ground electrode, a specific metallic cylinder is installed between the plasma chamber and the plasma electrode.

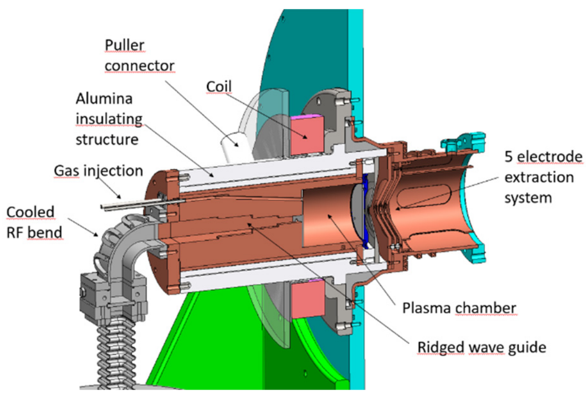

Figure 2: ALISES II source assembly.

MIRROTRON REQUIREMENTS

In the context of compact neutron source, Irfu proposed to MIRROTRON Company to loan ALISES II ion source as injector for a new facility in Hungary to produce neutrons from proton beam impacting high neutron yield target. The beam requirements from MIRROTRON are listed in the Table 1. The Twiss parameters of the RFQ input beam provided by MIRROTRON are as follows, considering 6 times the RMS, assuming waterbag distribution for the LEBT simulations.

Table 1: MIRROTRON Beam Requirements

Energy (keV)	35
Beam current (mA)	30
Duty cycle (Hz)	40
Pulse length (ms)	1.25
Vacuum (mbar) at RFQ input	10^{-6}
RFQ Input Twiss parameter	
α	3.73
β (mm/mrad)	0.34
εs π.mm.mrad (normalized emittance from source)	0.744
εu (π.mm.mrad) (normalized RFQ acceptance	2.108

INSTALLATION ON BETSI

The ion source is connected to the LEBT by the mean of a special frame at ground wich support all the RF chain. Only the back of the source up to the RF window is at high voltage. A simple polyvinyl chloride-Kapton DC-break is used to isolate the magnetron from high voltage. The coil which surround the insulating structure is at ground. The coil can slide along the axis and both longitudinal position and current setting allow optimizing the resonance for beam intensity and stability.

Figure 2: ALISES II on BETSI test bench.

EXPERIMENTAL RESULTS

The 30mA/35keV beam produced in MIRROTRON conditions at 40Hz is very stable. Long runs have been performed such as this of 100 hours recorded and visible on Fig 3. We can observe the 30mA extracted current and high voltage from the power supply and the around 20mA beam current collected at the end of the BETSI 2 solenoids beam line. Producing 1.25ms of proton beam directly from the plasma extraction is not possible due to the time of plasma ignition. Thus, it is necessary to cut in time the beam produced at least with 4ms duration as we can see on Fig 4. This can be done by a chopper or by the RFQ itself with losses on the very first vane part.

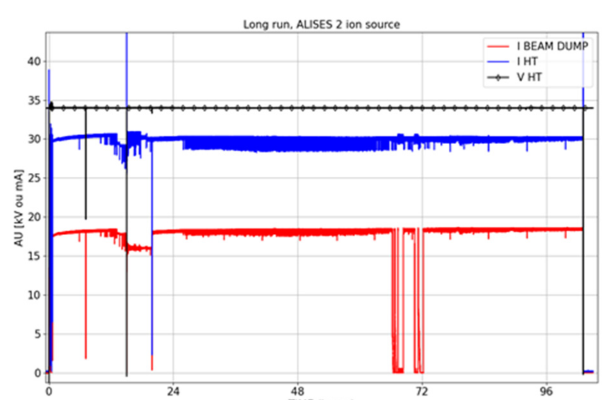

Figure 3: Long run of 100 h.

ISBN: 978-3-95450-257-8 ISSN: 2222-5692 doi:10.18429/JACoW-ECRIS2024-MOP03

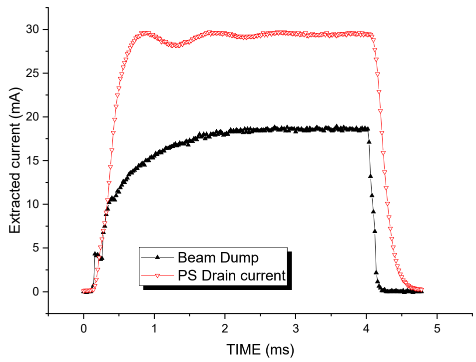

Figure 4: 4ms pulse length on BETSI beam dump.

Emittance measurements are produced with an insertable ESS type Alison scanner [8] positioned between the two solenoids. The measured proton beam rms emittance is of 1.385485 π.mm.mrad.norm. We can observe others species like H_2^+, H_3^+. Heavy elements are present suggesting a not perfect tightness of the source to the vacuum (Fig. 5).

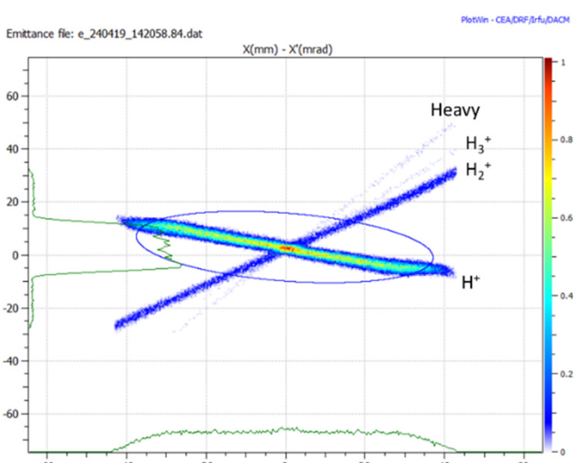

Figure 5: ALISES II emittance measurement.

The beam is also analyzed at the same position with a Wien filter [9] developed at Irfu and with first solenoid off for source characterization. This diagnostic is composed of permanent magnets providing 195 mT fixed magnetic field, and 2 plates biased from 0.V to 4.5 kV. It is motorized and scan the beam radially to determine the species proportion at each radial step from a beamlet defined by a 200µm hole diameter at beam stop diagnostic entrance. On Fig. 6, we can see the results obtained on beam axis. For this analysis, the beam is pulsed at 10Hz with a pulse length of 11ms. The FDW wire signal is sampled on 11ms with sampling frequency at 100kHz, that is to say, the pulse is defined with 110 points. The main species present in the beam are H^+, H_2^+, H_3^+, in proportion of respectively 65%, 17% and 3%. But we can observe first group of N^+, NH^+, O^+, OH^+, H_2O^+, and another one of N_2^+, NO^+, both of 15%.

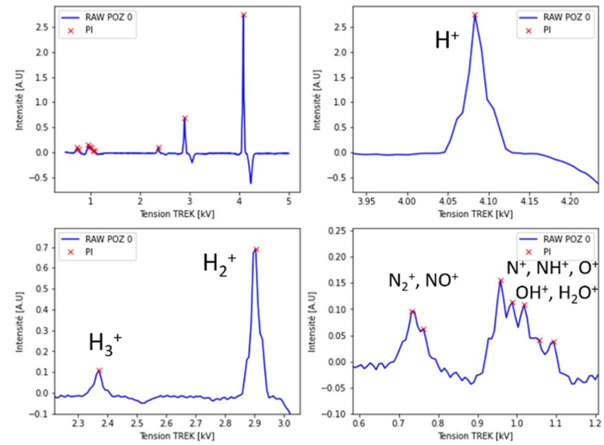

Figure 6: Analysis of ALISES II extracted proton beam.

LEBT PROPOSAL FOR RFQ INJECTION

MIRROTRON Company ask Irfu to propose a Low Energy Beam Transport line to match the ALISES II proton beam with RFQ acceptance. The design consider the first solenoid as closed to the source as possible because of solenoid non-linearity and strong beam divergence. The distance between solenoid is defined by vacuum port size. The space-charge compensation profile along the line is set similar to other lines design at Saclay, like IPHI, IFMIF. The solenoids used are similar to those used for ESS installation. To keep the LEBT as short as possible, horizontal and vertical magnetic dipole correctors are inserted inside each solenoid. The line should be as short as possible to be less than the 3 meters (Fig. 7). The parameters of the line are optimized using Tracewin code [10] with the objective of reaching the adapted Twiss parameters for the injection into the RFQ and keeping the emittance growth as low as possible (Fig. 8).

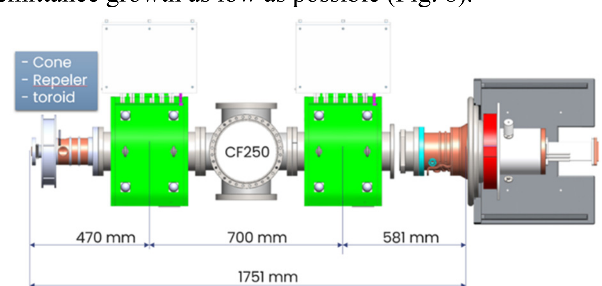

Figure 7: Proposed LEBT for MIRROTRON.

ISBN: 978-3-95450-257-8 ISSN: 2222-5692 doi:10.18429/JACoW-ECRIS2024-MOP03

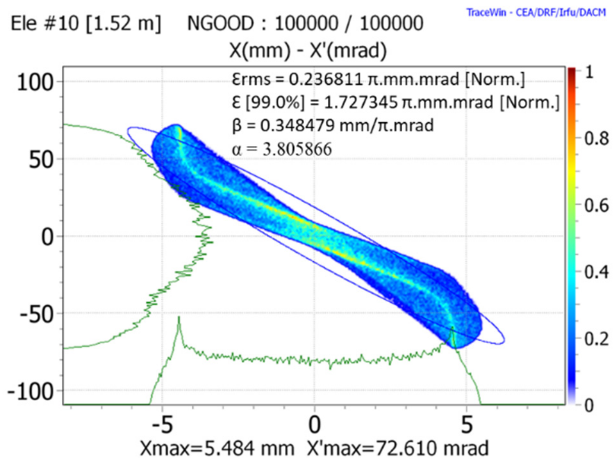

Figure 8: Beam parameters optimized at RFQ entrance.

CONCLUSION

The ALISES II source restarts in stable and reliable conditions for MIRROTRON experiment. The extracted beam purity has been qualified using the Wien filter recently developed at Irfu, allowing radial scanning to determine H^+ proportion evolution from beam center to maximum radius. From emittance measurement, beam simulations have been performed to propose a 2-solenoid LEBT for MIRROTRON installation optimized for RFQ injection. ALISES II source is expected to be delivered at MIRROTRON by the end of 2024.

REFERENCES

[1] J.-M. Lagniel et al., "Status and new developments of the high intensity electron cyclotron resonance source light ion continuous wave, and pulsed mode (invited)," Rev. Sci. Instrum., vol. 71, no. 2, pp. 830–835, Feb. 2000. doi:10.1063/1.1150306

[2] O. Delferriere, Y. Gauthier, R. Gobin, O. Tuske, and F. Harrault, "Development of a Compact High Intensity Ion Source for Light Ions at CEA-Saclay", *in Proc. ECRIS'16*, Busan, Korea, Aug.-Sep. 2016, pp. 73-75. doi:10.18429/JACoW-ECRIS2016-WECO02

[3] O. Tuske et al., "Experimental Studies on the ALISES Ion Source at CEA Saclay", *in Proc. 20th Int. Workshop on ECR Ion Sources (ECRIS'12)*, Sydney, Australia, Sep. 2012, paper WEPP16, pp. 143-145.

[4] O. Tuske et al., "BETSI, a new test bench for ion sources optimization at CEA SACLAY," Rev. Sci. Instrum., vol. 79, no. 02B710, Feb. 2008. doi:10.1063/1.2805625

[5] A. Dubois, O. Delferriere, Y. Gauthier, Y. Sauce, and O. Tuske, "Evolution of ALISES 3 Light Ion Source at CEA Saclay," Journal of Physics: Conference Series, vol. 2743, no. 1, p. 012058, May 2024. doi:10.1088/1742-6596/2743/1/012058

[6] Delferrière, R. Gobin, F. Harrault, S. Nyckees, and O. Tuske, "Improvement of extraction system geometry with suppression of possible Penning discharge ignition," Rev. Sci. Instrum., vol. 85, no. 2, Dec. 2013. doi:10.1063/1.4830361

[7] O. Tuske et al., "For intense proton beam production with compact ion sources: the ALISES ion source family developed at CEA Saclay," Journal of Physics: Conference Series, vol. 2743, no. 1, p. 012057, May 2024. doi:10.1088/1742-6596/2743/1/012057

[8] Tuske et al., "ESS Emittance Measurements at INFN CATANIA", in *Proc. 8th Int. Particle Accelerator Conf. (IPAC'17)*, Copenhagen, Denmark, May 2017, pp. 123-125. doi:10.18429/JACoW-IPAC2017-MOPAB023

[9] A. Dubois et al, Proceeding of ECRIS2024, Darmstadt, Germany

[10] D. Uriot and N. Pichoff, "Status of TraceWin Code", in *Proc. 6th Int. Particle Accelerator Conf. (IPAC'15)*, Richmond, VA, USA, May 2015, pp. 92-94. doi:10.18429/JACoW-IPAC2015-MOPWA008

ISBN: 978-3-95450-257-8 ISSN: 2222-5692 doi:10.18429/JACoW-ECRIS2024-MOP04

ALISES v3 ION SOURCE IN VARIOUS CONFIGURATION ALONG THE YEAR

O. Tuske*, O. Delferriere, A. Dubois, Y. Gauthier, Y. Sauce
Université Paris-Saclay – CEA–Irfu, Gif/Yvette, France

Abstract

ALISES v3 is a very compact light ion source that has been developed at CEA Saclay in 2018. The easy maintenance procedure of this source allowed us to test many different configurations. On the BETSI test bench equipped with a single Alisson Scanner and a pair a solenoid/deviator, we studied the extraction energy influence, we changed the number of electrodes in order to extract different kind of ions other than protons. This paper will describe briefly the ALISES v3 ion source and will present all the results that we gathered in a year with all those modifications

INTRODUCTION

The ALISE v3 ion source, developed at CEA Saclay in 2018, represents a significant advancement in light ion source technology using ECR heating process. It aims to achieve the same performance as the original SILHI source, known for its high intensity proton and deuteron beams, but with a smaller and more user-friendly design. This new iteration incorporates the best aspects of previous ALISE versions, resulting in a more compact and practical configuration. The manufacturing of ALISE v3 coincided with the upgrade of the BETSI (Banc d'Etudes et de Tests des Sources d'Ions) test bench, allowing for thorough testing and analysis of its beam characteristics. This innovative source holds promise for various applications requiring high-intensity light ion beams, offering improved efficiency and ease of maintenance. This article will summarize all the evolution and changes that were made to the original model of the ALISES v3 to increase the availability of the ion source at different energy.

ALISES v3 ION SOURCE ON BETSI TEST BENCH

The BETSI test bench, located at CEA Saclay [1], is a crucial facility dedicated to the optimization and characterization of high-intensity light ion sources. Operational since 2009, it has played a pivotal role in the development and testing of various ion sources, particularly those used in large-scale accelerator projects like Spiral2 and some component of various project (emittance measurement unit and Wien filter). Also this test bench is used for educational purposes with students for Paris-Saclay University. The core of the BETSI test bench is a versatile platform capable of accommodating and testing different ion source types, primarily those based on Electron Cyclotron Resonance (ECR) heating.

* olivier.tuske@cea.fr

The ALISE v3 ion source uses several key technical advantages. Its compact design, with a ceramic diameter of only 150 mm and a length of 300 mm, makes it significantly smaller than traditional high-intensity ion sources. This allows for easier integration into existing accelerator facilities and reduces the overall footprint of the system. Additionally, the simplified structure of the source facilitates maintenance and reduces the risk of operational issues.

A single coil at ground potential provides the magnetic field and is located around the source ceramic. This unique coil was used on both IPHI project (SILHI source [2]) and FAIR project ion source. On this latter project, a single coils was enough to heating up electrons to ignite the plasma source [3].

The gas injection system allow to control the mass flux of the injected gas (hydrogen or helium) that is needed to inject inside the plasma chamber, independently of the temperature in the experimental hall. The PR4000 MKS brand was chosen because of its good behaviour against sparks. The use of metallic capillaries with metallic gasket decrease the possibility of tiny leaks polluting the plasma with air and its components.

The energy id provided by a microwave generator at 2,45 GHz delivered by SAIREM company. Free electrons inside the magnetic field have at a moment the same gyration frequency than the magnetron generator and leads to an efficient energy transfer from the microwaves waves to the kinetic electrons velocity, causing them to get accelerated (heat up) and collide with neutral atoms of the injected gas. These collisions result in the ionization of the atoms of the gas, forming a plasma which contains the desired positive ions, electrons and also some ionized molecules in some cases.

The positive ions are extracted trough the plasma chamber extraction hole, focused and accelerated using a multi-electrode extraction system.

Extraction energy was designed to be 100 kV but unfortunately this value was never reached in normal source operation with the first design of the ceramics. With the second design [4], maximum extraction voltage reach the value of 80 kV but sparks occurs too frequently and did not allow to increase more because the risk of damaging any equipment.

INFLUENCE OF THE COIL POSITION

The single coil of the source can be moved easily. As the position changed, the current value of the Coil Power Supply (C-PS) must also be adjusted in order to keep the resonant zone at the same location to ignite the plasma. As the coil gets further away the RF ridge, the value of the C-PS must

ISBN: 978-3-95450-257-8 ISSN: 2222-5692 doi:10.18429/JACoW-ECRIS2024-MOP04

increase. This has an influence on the magnetic profile in the plasma chamber. In Fig. 1, we show the increased of the extracted proton beam intensity versus the extraction voltage for two positions of the source coil. Electrons seemed to be more efficient for the same RF power to ionized the hydrogen gas and thus produces a higher beam current. From that result, we defined the position of the Coil that delivers the highest extracted intensity.

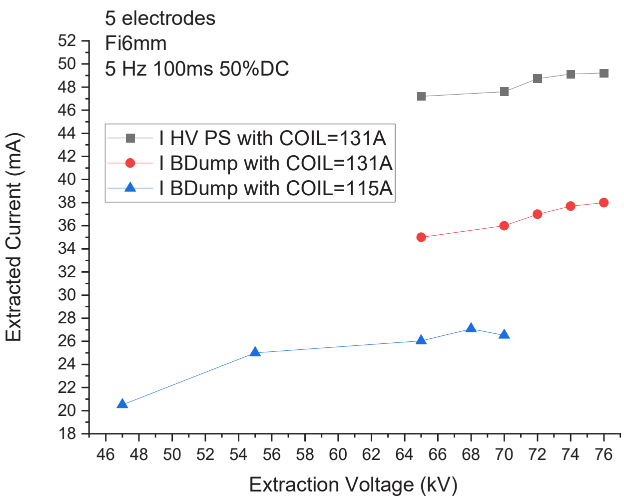

Figure 1: Evolution of Extracted Proton current vs extraction voltage for 2 Source Coil Power Supply (C-PS) value.

Number of Electrodes

On the ALISE v3, the accelerating column can be modified very easily. As the extraction voltage of 100 kV seemed to be impossible to reach even with the second ceramic design, we decide to fix the extraction voltage value around 60 kV and the plasma hole diameter at 6 mm. While the puller electrode was removed, to optimize the beam extraction with 4 electrodes configuration, the extraction gap was reduced by moving the plasma electrode toward the first ground electrode.

On Fig. 2 we can compare the extracted beam (the drain current of the high voltage power supply "I HV PS") with the collected beam intensity at the end of the LEBT (I BDump). With 5 electrodes, I HV PS drain current is higher than with the 4 electrodes configuration. That means that in the first case with a two gaps accelerating system has a better efficiency to pull out particles out of the plasma. But the measured current at the end of the LEBT seemed to higher with the 4 electrodes accelerating configuration, showing that with a single accelerating gap of 12 mm at 60 kV the beam divergence is lower, increasing the transmission of the beam. This behaviour was simulated with IBSIMU code [5] while optimizing the acceleration gap length in order to lower beam divergence.

In order to increase even more the extracted total beam current, the use of a larger diameter plasma electrode aperture hole will be tested soon: from 7 to 9 mm aperture plasma diameter hole.

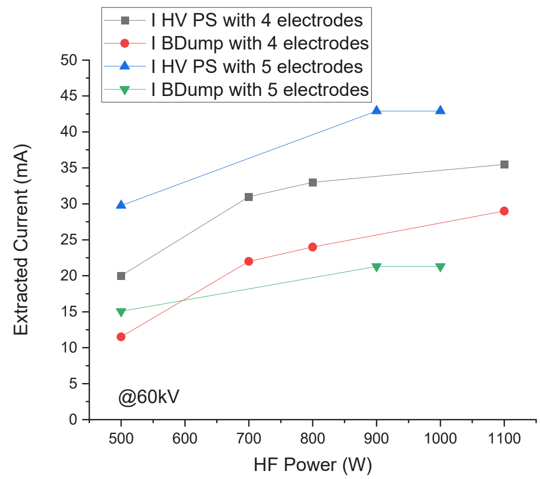

Figure 2: 4 and 5 electrodes configuration, respectively single and double acceleration gap extraction.

Helium Gas in ALISES v3

In order to increase the panel of possibilities of the ALISES v3 ion source, we fed it with helium gas. Helium has a lower ionization level: that means first ionization is possible. Extraction simulations at 60 kV extraction voltage showed that with the same gap length, beam divergence is bit larger because of the space charge effect as Helium atom (He) is four time heavier than hydrogen. Also helium gas is a noble gas: there won't be any "ionized molecules" in the extracted beam and no helium pollution once hydrogen gas will be use again. On Fig. 3 He^+ particle are plotted for various magnetron power. Helium beam is not well transported in BETSI's LEBT, more adapted for hydrogen beam but a constant transmission around 80 % at 60 kV extraction energy for all RF power is observed.

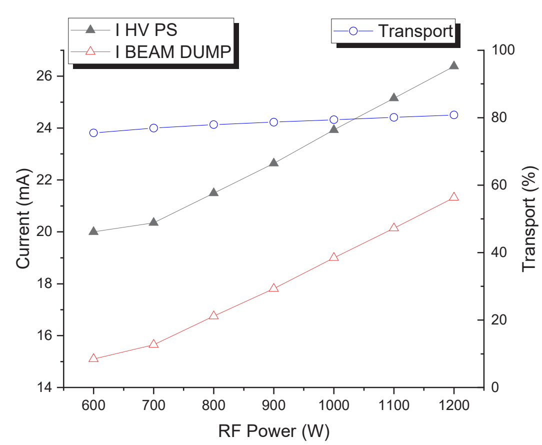

Figure 3: Helium Beam extracted and transported.

Those measurement were done in a single day and we emittance measurement at 900 W after the first solenoid (Fig. 4) were also carried out. The use of TRACEWIN/PLOTWIN code [6] estimates the normalized RMS emittance value around 0.19 $\pi \cdot$ mm $\cdot$ mrad. The beam shape in the phase space is not really what we expected and some simulations are needed to try to reproduce this shape under those conditions.

ISBN: 978-3-95450-257-8 ISSN: 2222-5692 doi:10.18429/JACoW-ECRIS2024-MOP04

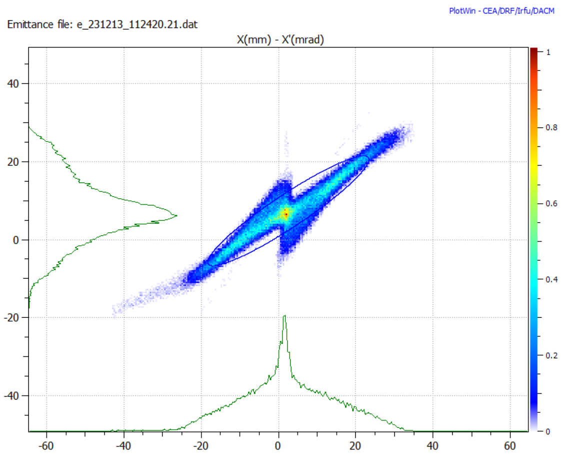

Figure 4: Emittance measurements at 900 W of magnetron power after the 1st solenoid of the LEBT.

CONCLUSION

ALISES v3 is a very compact source, with a easy maintenance procedure. The source can produce routinely up to 50 mA of proton beam, with simple some adaptations. The position if the single source coil has been optimized. The 4 electrodes configuration has demonstrated its versatility up to 60 kV extraction voltage and we continue to reduce beam divergence in order to transport as much particle as possible. Some measurements with helium gas showed interesting results that we will pursued.

REFERENCES

[1] O. Tuske *et al.*, "Experimental Studies on the ALISES Ion Source at CEA Saclay", in *Proc. 20th Int. Workshop on ECR Ion Sources (ECRIS'12)*, Sydney, Australia, Sep. 2012, paper WEPP16, pp. 143-145.

[2] P. Ausset *et al.*, "Status Report on the Saclay High-Intensity Proton Injector Project IPHI", in *Proc. 7th E. Part. Accel. Conf. (EPAC'00)*, Vienna, Austria, Jun. 2000, paper THOAF202, pp. 283-285.

[3] O. Tuske, N. Chauvin, O. Delferriere, J. Fils, and Y. Gauthier, "Commissioning of the ECR ion source of the high intensity proton injector of the Facility for Antiproton and Ion Research (FAIR)", *Rev. Sci. Instrum.*, vol. 89, no. 5, p. 052303, May 2018. doi:10.1063/1.5017783

[4] A. Dubois, O. Delferriere, Y. Gauthier, Y. Sauce, and O. Tuske, "Evolution of ALISES 3 Light Ion Source at CEA Saclay", *J. Phys.: Conf. Ser.*, vol. 2743, no. 1, p. 012058, May 2024. doi:10.1088/1742-6596/2743/1/012058

[5] T. Kalvas, O. Tarvainen, T. Ropponen, O. Steczkiewicz, J. Ärje, and H. Clark, "IBSIMU: A three-dimensional simulation software for charged particle optics", *Rev. Sci. Instrum.*, vol. 81, no. 2, p. 02B703, Feb. 2010. doi:10.1063/1.3258608

[6] D. Uriot and N. Pichoff, "Status of TraceWin Code", in *Proc. 6th Int. Part. Accel. Conf. (IPAC'15)*, Richmond, VA, USA, May 2015, pp. 92-94. doi:10.18429/JACoW-IPAC2015-MOPWA008

ISBN: 978-3-95450-257-8 ISSN: 2222-5692 doi:10.18429/JACoW-ECRIS2024-MOP07

USE OF A 2.45 GHz ECR ION SOURCE FOR THE NEUTRON TARGET DEMONSTRATOR PROJECT*

S. Melanson†, M. Dehnel, A. George, S. Suram, D-Pace Inc., Nelson, BC, Canada

Abstract

D-Pace has licensed a 2.45 GHz ECR ion source from Neutron Therapeutics. The ion source will be used for the Neutron Target Demonstrator project at Los Alamos National Laboratory where 10 mA of singly charged krypton ions at 50 keV are required with a normalized 4-RMS emittance of less than 1 mm·mrad. The goal of the project is to show a reverse kinematics neutron capture reaction with krypton 84 ions. Due to the high radiation environment that the ion source will be subjected to, a solid state microwave power supply will be used instead of the traditional magnetron for the experiment. The main advantage of the solid state power supply is that the output is transmitted by a coax cable instead of a waveguide, so the power supply can be located a long distance away from the ion source without the need for complicated and expensive waveguide. The other advantage of the solid state device is that the frequency can be varied from 2.4 GHz to 2.5 GHz. This gives the operator an extra degree of freedom for tuning. We present how the frequency variation affects the beam parameters.

INTRODUCTION

The Neutron Target Demonstrator (NTD) project at the Los Alamos Neutron Science Center (LANSCE) will be the first demonstration of a reverse kinematics neutron capture reaction [1]. Neutrons will be created by spallation of the 800 MeV proton beam onto a target. A beam of Kr-84 ions will serve as the target ions for the neutron capture reaction $Kr^{84}(n,\gamma)Kr^{85}$. D-Pace is providing LANSCE an ECR ion source system capable of producing mA level beam of Kr-84 at an energy of up to 50 keV. Figure 1 shows a schematic of the NTD as well as a CAD model of the ion source system.

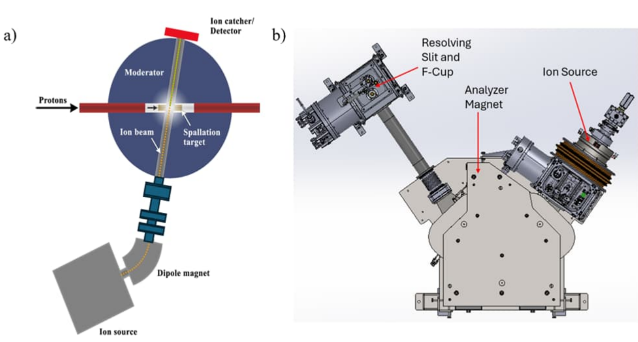

Figure 1:a) Schematic of the NTD project. Figure provided by A. Cooper at LANSCE under LA-UR-24-27491. b) Plan view of the CAD model for the ion source system.

* Work supported by Canada's SR&ED program, MITACS, NRC-IRAP, NSERC, Buckley Systems and BDC
† stephane@d-pace.com

ION SOURCE

D-Pace has licensed a 2.45 GHz ion source from Neutron Therapeutics [2] which is based on the first 2.45 GHz ion source developed by Wills and Taylor [3]. The ion source is commonly used in their boron neutron capture therapy system producing 30 mA DC of protons at an energy of 50 keV.

The microwave injection system consists of a 3-stub tuner, forward and reverse power monitors. A high voltage waveguide break was designed with alternate layers of G10 and aluminium plates to allow for the microwave generator to be grounded while the ion source is at 50 kV. The microwave power is transmitted through an aluminium nitride window to the plasma chamber.

The magnetic field is produced by three solenoids, labelled back, centre and front, where the front solenoid is closest to the extraction and the back solenoid is closest to the microwave injection. The cylindrical plasma chamber is made of aluminium with a diameter of 76 mm and a length of 95 mm. Boron nitride plates are mounted on both the front and the back edges of the plasma chamber.

The extraction system is formed by four molybdenum electrodes. The plasma electrode aperture has a diameter of 6.5 mm. The first ground electrode, the suppression electrode and the second ground electrode apertures have diameters of 9 mm, 11 mm and 11.5 mm respectively. The suppression electrode is commonly biased at -3 kV relative to ground. The ground and suppression electrodes are installed on a moveable trolley allowing for active tuning of the distance between the plasma aperture and the first grounded electrode by 26 mm.

EXTRACTION OF KRYPTON

The test stand used for testing the extraction of Krypton ions for the NTD project is composed of the ion source, an emittance scanner and a Faraday cup. The Allison-type emittance scanner [4] was mounted at $z = 547$ mm where $z = 0$ mm is the ion source's plasma aperture. The emittance scanner can be mounted in both x and y directions. The Faraday cup was located at $z = 714$ mm. A CAD model of the test stand is presented in Fig. 2.

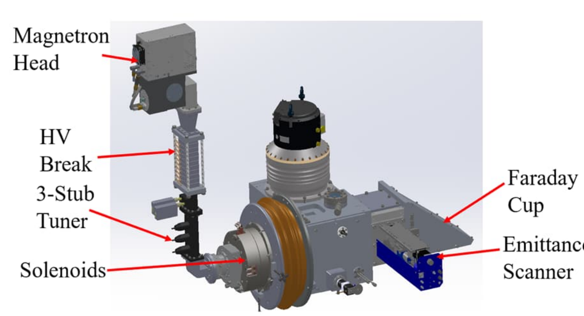

Figure 2: CAD model of the test stand.

ISBN: 978-3-95450-257-8 ISSN: 2222-5692 doi:10.18429/JACoW-ECRIS2024-MOP07

The first tests on the ion source at D-Pace's facility were with hydrogen to confirm the performance of the ion source. The optimum solenoid settings for the extraction of hydrogen beams are presented in Table 1. The optimum gas flow was found to be 1.8-2.2 sccm.

Table 1: Optimum Solenoid Current Range for Hydrogen

Front Solenoid	Center Solenoid	Back Solenoid
50-60 A	5-10 A	75-85 A

The ion source was then optimized for the extraction of krypton. We found that the magnetic field profile needed for krypton was different than hydrogen, with a lower field needed at the extraction. The optimum gas flow is also lower at only 0.1 sccm of Kr gas. A new mass flow controller was ordered to allow for more precise control at the low flows needed. Table 2 presents the optimum solenoid current values for Krypton and Fig. 3 shows the simulated magnetic field on axis for hydrogen and krypton.

Table 2: Optimum Solenoid Current Range for Krypton

Front Solenoid	Center Solenoid	Back Solenoid
0-5 A	50-55 A	75-80 A

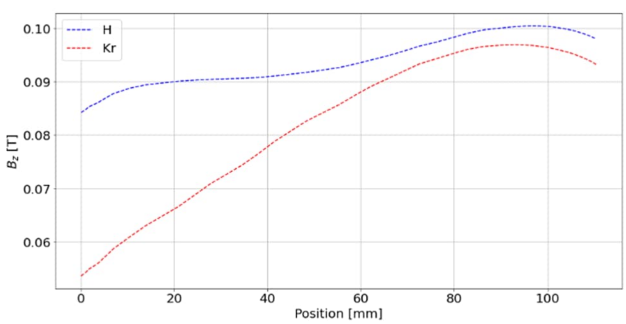

Figure 3: Simulated magnetic field on axis for the extraction of hydrogen and krypton beams. The plasma aperture is located at z=0.

Up to 10 mA of total krypton beam can be extracted out of the ion source at an energy of 50 keV. The charge states have not yet been analysed since the test stand does not yet have a mass spectrometer system installed. Figure 4 plots the beam current as a function of the microwave power and the extraction voltage.

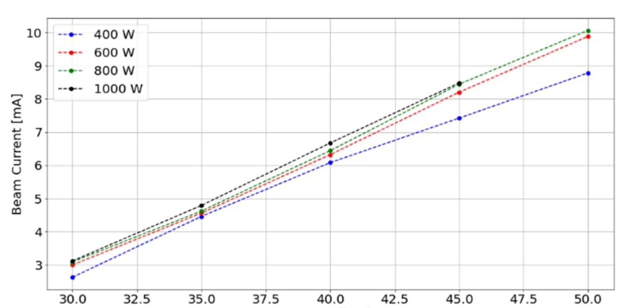

Figure 4: Total extracted krypton beam as a function of the extraction energy for various injected microwave powers.

The beam current is highly dependent on the extraction energy. The extraction gap was actively tuned with every change in energy and microwave power. As expected, the gap increased with the increase in extraction voltage and with the increase in power.

The phase space was analysed in both *x* and *y* planes. The normalized 4-RMS emittance was between 0.04 and 0.05 mm·mrad for the *x* and *y* emittance as can be seen in Fig. 5.

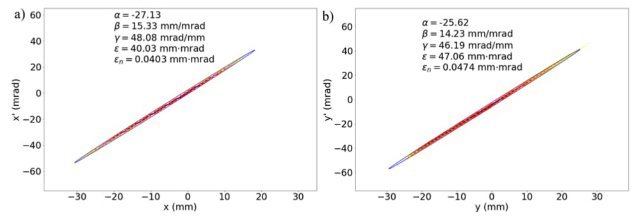

Figure 5: Phase space scans from krypton beams at an extraction energy of 40 keV and a microwave power of 400 W.

SOLID STATE POWER SUPPLY

Due to the high radiation environment of the NTD, there can be no power supplies close to the ion source. This includes the microwave power supply, which will have to be located outside of the bunker, at a minimum of 50 meters away from the ion source. A magnetron could be used, but this would be an expensive and complicated option since a long waveguide would have to be used. Instead, a solid state power supply will be used. A 1.6 kW power supply capable of variable frequency from 2.4 GHz to 2.5 GHz was purchased from RFHIC [5]. The power supply has a coaxial output instead of a waveguide, greatly simplifying the installation of the system for the NTD project. To get the microwave power to the ion source, a 7/16 DIN to WR340 adapter is connected to the ion source's waveguide.

In addition to the coaxial output, another advantage of using solid state power supplies is the ability to vary the microwave frequency. This gives the operator an additional tuning parameter. Figure 6 shows how the krypton beam current varies as a function of the microwave frequency without varying the 3-stub tuners or the magnetic field. From the figure, it is clear that the frequency has a significant influence on the beam current. This is comparable to the influence of the solenoid magnetic field on the beam current for a fixed microwave frequency.

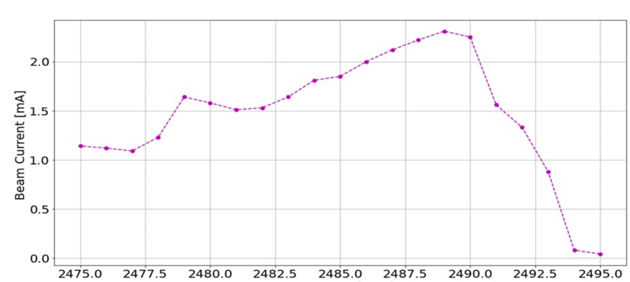

Figure 6: Krypton beam current as a function of the microwave frequency.

ISBN: 978-3-95450-257-8 ISSN: 2222-5692 doi:10.18429/JACoW-ECRIS2024-MOP07

PERMANENT MAGNET SOLENOID

To further simplify the system for the installation in the high radiation environment of the NTD project, D-Pace is investigating the use of permanent magnets to replace the solenoids. This would allow for the operation without any power supplies floating at the ion source voltage, eliminating the need for high voltage and high current cables between the ion source and the power supplies outside of the radiation bunker. A permanent magnet version of the ion source would also reduce the manufacturing and the operating costs as well as simplify the operation of the ion source.

To create the permanent version of the ion source, the solenoid was first simulated using FEMM [6] in a 2D axis-symmetric mode. A good agreement between the simulated model and magnetic field measurements on axis was achieved, confirming the magnetic model. The next step was to create a model with only permanent magnets with the goal of replicating the magnetic field on axis as best as possible. For simplicity of installation, the outer steel shell that houses the solenoid was kept for the permanent magnet version. Standard bar magnets that are available commercially were also used.

The design created uses 2"x1"x1/2" N42 magnets and 1"x1"x1" N52 magnets arranged in a ring configuration. 3D printed plastic parts were manufactured to hold the magnets in place and steel rings were used between the magnet rings to shape the magnetic field as needed. Figure 7 shows the permanent magnet model in FEMM, a CAD model of the assembly and a comparison of the magnetic field on axis between the solenoid and the permanent magnets.

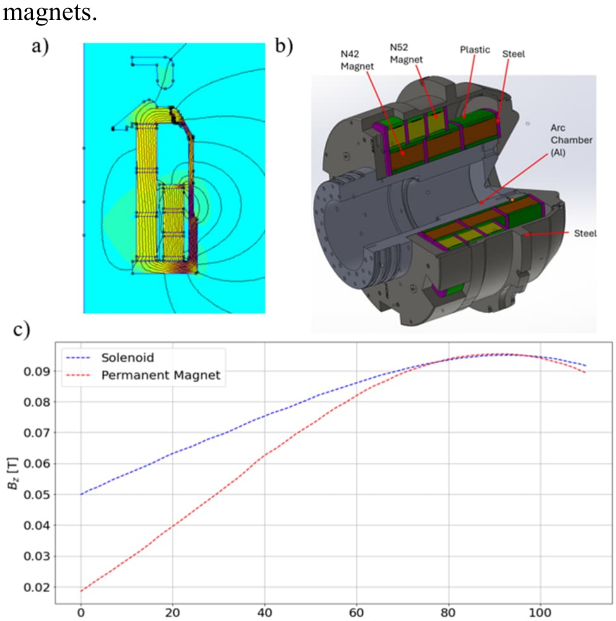

Figure 7: a) FEMM model of permanent magnet solenoid. b) CAD model of the assembly. c) Simulated magnetic field on axis for the solenoid and permanent magnet model.

The permanent magnet assembly was tested on the test stand. A krypton plasma could be ignited in the plasma chamber, however there were frequent high voltage breakdowns when the ion source was set to more than 5 kV. Upon further inspection with a viewing window, a plasma was observed between the ion source and the grounded vacuum box. This plasma discharge is likely caused by the $\vec{E} \times \vec{B}$ trapping of electrons generated in this region. The magnetic field outside the plasma chamber is significantly higher with the permanent magnet than it is for the solenoid, explaining why the discharge is seen only with the permanent magnet version. Figure 8 shows a photograph of the plasma inside the chamber (no voltage applied to the ion source) as well as the discharge seen when a voltage is applied to the ion source.

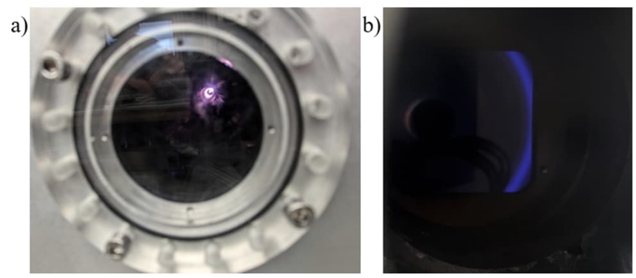

Figure 8: a) Photograph of plasma in the plasma chamber looking through the aperture. b) Glow discharge seen with 5 kV on the ion source.

CONCLUSION AND FUTURE WORK

D-Pace successfully started testing its 2.45 GHz ECR ion source at its facility. This ion source has been shown to extract more than 10 mA of krypton beam and will be used for the Neutron Target Demonstrator project at LANSCE.

A solid state power supply is being used, allowing for variable tuning of the input power frequency.

A permanent magnet version of the ion source is being developed. Initial tests show that a plasma can be generated in the plasma chamber, but frequent breakdowns due to electron trapping in the extraction region prevent the extraction of beam out of the ion source.

The permanent magnet version of the ion source will be redesigned to reduce the magnetic field in the extraction region to prevent the breakdowns seen.

REFERENCES

[1] A. L. Cooper et al., “A high-intensity, low-energy heavy ion source for a neutron target proof-of-principle experiment at LANSCE,” *J. Phys. Conf. Ser.*, vol. 2743, no. 1, p. 012091, May 2024. doi:10.1088/1742-6596/2743/1/012091

[2] Neutron Therapeutics, https://www.neutrontherapeutics.com/

[3] T. Taylor and J. S. C. Wills, “A high-current low-emittance dc ECR proton source,” *Nucl. Instrum. Methods Phys. Res.*, Sect. A, vol. 309, no. 1–2, pp. 37–42, Nov. 1991. doi:10.1016/0168-9002(91)90090-d

[4] P. W. Allison, J. D. Sherman, and D. B. Holtkamp, “An Emittance Scanner for Intense Low-Energy Ion Beams,” *IEEE Trans. Nucl. Sci.*, vol. 30, no. 4, pp. 2204–2206, Aug. 1983. doi:10.1109/tns.1983.4332762

[5] RFHIC, https://www.rfhic.com/

[6] FEMM, https://www.femm.info/

ISBN: 978-3-95450-257-8 ISSN: 2222-5692 doi:10.18429/JACoW-ECRIS2024-MOP08

AUTOMATIC CLASSIFICATION OF PLASMA STATES IN AN ECR-TYPE ION SOURCE*

A. Fernandez†, I. Arredondo, R. Justo, P. Usabiaga, UPV/EHU, Leioa, Spain
J. Feuchtwanger, UPV/EHU and Ikerbasque, Leioa, Spain

Abstract

In this paper we present a methodology to infer the state of the plasma in an ECR source without using any sensor that modifies its behavior. For this purpose, machine learning techniques are explored. In a first stage a characterization experiment is carried out in which the different states of the plasma are detected, using clustering algorithms. Subsequently, a supervised learning paradigm is adopted to train a neural network that is capable of determining the state of the plasma at different working states. The control data: delivered RF power and gas flow, together with the data that can be measured without altering the plasma: incident power, reflected power and plasma luminosity, are provided to the system as an input, in order to achieve the state detection. Moreover, good results can also be achieved without measuring luminosity, which cannot be easily measured when the ECR source is the start of an injector. This methodology has been applied to a low-power ECR source in which low-density hydrogen plasmas are generated at the IZPILab laboratory of the University of the Basque Country.

INTRODUCTION

Electron cyclotron resonance ion sources (ECRIS) are now widely utilized for ion production in both basic research and industrial applications due to their dependability and ability to generate multiply charged ion beams from most stable elements. This widespread adoption is attributed to their consistent performance and versatility across various fields [1].

These sources generate plasma that undergoes state changes over time, necessitating precise measurements to enable effective operation. Furthermore, it is crucial to perform these measurements non-intrusively to avoid interference with the plasma dynamics. This necessity forms the primary motivation for developing the methodology presented in this paper, which aims to infer the state of the plasma in an ECRIS source without employing any sensors that could alter its behavior. This is achieved through the application of advanced Machine Learning (ML) techniques.

Ion Source Operational Details

The source designs and implementations used for the experiments are comprehensively described in Ref. [2]. These designs are tailored for low current industrial and bio-applications, leveraging Electron Cyclotron Resonance (ECR) principles. The main design parameters are summarized in Table 1. Although the table specifically references H_2, the ion source is versatile and can operate with other gases, such as Helium, Nitrogen, or any other elemental gas for ion production.

Table 1: Main Design Parameters of PIT30 Ion Source

ECRIS parameters	
Microwave frequency	3 GHz
Microwave power	<500 W
Gas mass flow	<5 sccm (H_2)
Magnetic field	110 mT
Extraction voltage	≤30 kV
Beam current	<50 µA (H^+)
Beam emittance	<0.2 mm mrad

Figure 1 depicts a CAD-rendered cross-sectional drawing of the proposed plasma chamber, assembled from standard components. This chamber is configured as a circular waveguide, and for the chosen operating frequency, the smallest commercial diameter suitable as a resonant cavity within the CF flange system was DN 63. To produce the required magnetic field within the chamber for electron resonance, permanent magnets were utilized. The magnetic field strength was

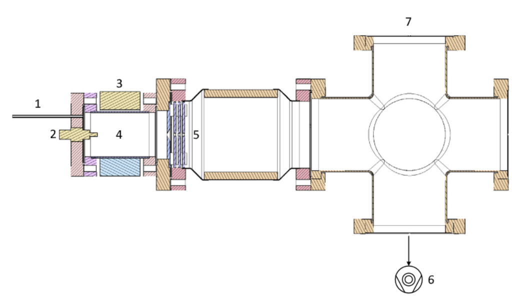

Figure 1: Cross section of a CAD drawing of the proposed plasma chamber made from standard CF components. (1) gas inlet, (2) RF port, (3) magnetic structure, (4) plasma chamber, (5) extraction electrodes, (6) turbo-molecular pump port, (7) pressure sensor, (8) Faraday cup/scintillator screen port. The entire assembly shown is 600 mm long.

determined using the equation for the resonant frequency of a free electron in a magnetic field ($B = 2\pi f \frac{m}{e}$), where B represents the magnetic flux density, f is the frequency of the microwaves, and m and e are the mass and charge of the electron, respectively. For the intended 3 GHz microwaves, this results in an approximate field of 110 mT. To achieve this, a Halbach array consisting of eight permanent magnet bars was designed to create an axial magnetic field aligned with the plasma chamber.

* Work supported by Basque Government Department of Industry grants KK-2024/00065 and KK-2022/00026
† anderrua@gmail.com

ISBN: 978-3-95450-257-8 ISSN: 2222-5692 doi:10.18429/JACoW-ECRIS2024-MOP08

In this source, both the power of the signal transmitted to the chamber (or RF power) and the gas flow can be adjusted. The signal power can be varied using a signal generator capable of producing a variable power signal of up to The hydrogen flow is regulated by a flow controller, allowing independent control of the hydrogen flow up to 5 sccm (standard cubic centimeters per minute under conditions of 273 K temperature and 1.01 bar pressure).

Plasma Chamber Dynamics

The gas transferred to PIT30 is molecular hydrogen (H_2). In the processes that take place in the hydrogen plasma, in addition to protons (H^+), other ionic species such as H_2^+ and H_3^+ are generated. Figure 2 shows the surfaces that define the ionic densities as a function of the two variables (RF power and gas density), and Fig. 3 shows the regimes in which each species is predominant. We consider the plasma has changed its state when the predominant species in the plasma changes.

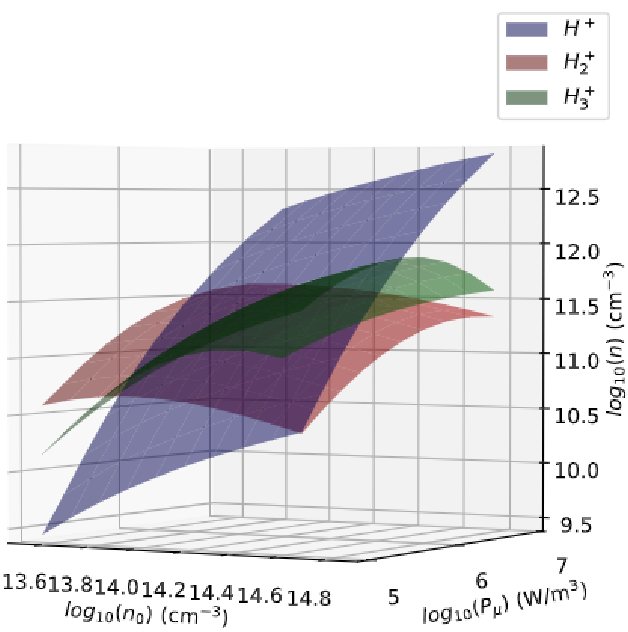

Figure 2: Density of H^+ (blue), H_2^+ (red), and H_3^+ (green) as a function of power density and neutral gas density.

Experimental Data Insights

The dataset used to initially train the algorithms consists of gas and power sweeps in the accelerator source, so that for an introduced power, two gas sweeps were performed, as shown in Fig. 4. Each measurement was always taken in the steady-state regime, thus avoiding introducing noise into the measurements. The following measurements were taken:

Time (s) : Time in seconds, referring to the time interval of each measurement.

Reflected (W) : Reflected power in watts, indicating the amount of power that is not transferred to the plasma and is reflected back to the power source.

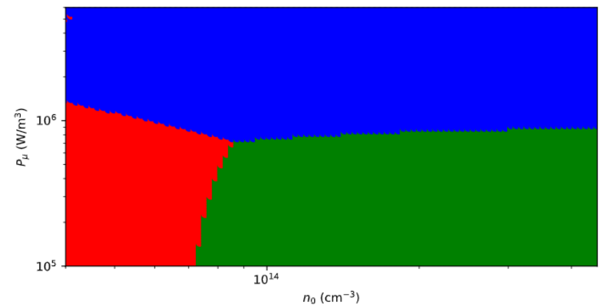

Figure 3: Map of the regions where each species predominates. Blue where protons predominate, red where H_2^+ predominates and green where H_3^+ predominates.

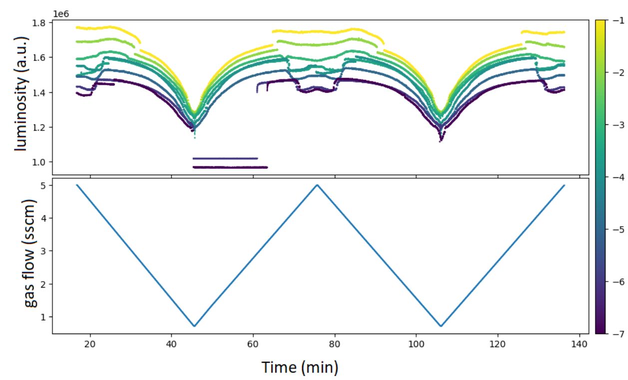

Figure 4: Representation of the acquired data.

Forward (W) Forward power in watts, measuring the amount of power emitted by the power source towards the plasma.

Adaptation (W) Adaptation of the signal injected into the source.

Noise (W) : Noise in watts, quantifying the random perturbation affecting the measurement signals.

Gasflow (sccm) Gas flow in standard cubic centimeter per minute, specifying the volume of gas passing through the system per unit of time.

Rfpower (W) RF power in watts, referring to the radio frequency power used in the source.

Frequency (Hz) Frequency in Hertz, describing the oscillation rate of the injected signal.

Luminosity (u a.) Measured luminosity of the plasma coming from the source, measured in arbitrary units.

If the cross-correlation of these data is studied, it is observed that there is a positive correlation (0.67) between the beam luminosity and the adaptation at the source input. This relationship will be useful later, as it implies that analyzing changes in one of the variables is almost equivalent to analyzing changes in the other, allowing us to eliminate one of the variables without losing significant information. Since luminosity is not always an accessible variable (especially in accelerators where the particle source is already fully integrated), this information suggests that substituting luminosity with adaptation could enable non-intrusive operations in the accelerator.

ISBN: 978-3-95450-257-8 ISSN: 2222-5692 doi:10.18429/JACoW-ECRIS2024-MOP08

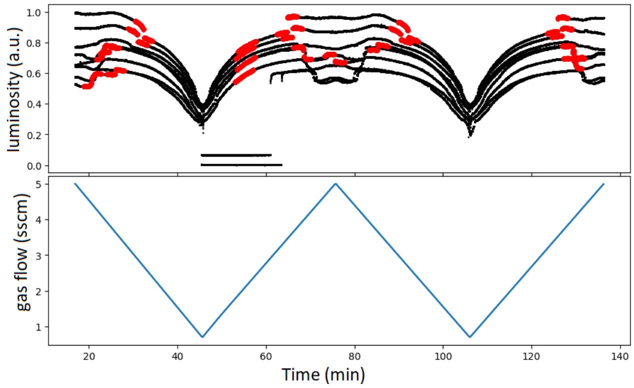

Figure 5: Detected jumps (in red) with configuration 1.

IDENTIFYING PLASMA STATE JUMPS

As previously explained, we designed a method that detects changes in the plasma state of the ion source and classifies them into one of three possible states. Therefore, the main challenge involves two tasks: detecting these changes and classifying them.

The easiest way to find state transitions is to analyze luminosity as a function of time. Whenever the plasma changes state, a sudden change in beam luminosity is observed. Therefore, the analysis of luminosity growth provides the necessary information to locate these transitions.

Firstly, an algorithm is proposed that performs linear regressions for every interval of n points. The slope of this line is proportional to the average growth of luminosity in that interval. Next, the difference in growth between continuous intervals is calculated and compared to the average difference of their neighbors, thereby avoiding issues due to isolated very high or low values. This allows us to identify regions where abrupt changes in growth occur compared to the local growth rate. Finally, the intervals that meet the requirements are selected.

As explained earlier, luminosity and adaptation are correlated variables; therefore, substituting one for the other allows for a similar analysis of plasma behavior. From now on, *configuration 1* will refer to the use of luminosity as the variable, while *configuration 2* will indicate that luminosity has been substituted by the adaptation. In Fig. 5 and Fig. 6, the results of this method in detecting state changes with configuration 1 and configuration 2, respectively are shown.

TECHNIQUES FOR CATEGORIZING PLASMA TRANSITIONS

Once the state changes are detected, we will attempt to classify them into one of three possible states using various algorithms: k-means, Random Forest and neural networks. We will then compare their performance, using the F1-score, to determine the most effective approach.

k-means

Initially, the k-means clustering algorithm is applied [3], utilizing features derived from windows of points around

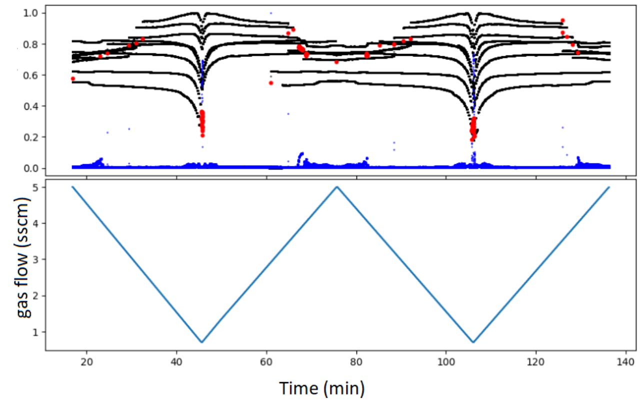

Figure 6: Detected jumps (in red) with configuration 2. The adaptation is shown in black, and the noise in blue.

each identified jump. The variables and parameters used to train the k-means algorithm include: Adaptation, Luminosity, Maximum Luminosity Change, Mean Gas Change, Gas Flow, and RF Power. The optimal number of clusters is four, although initially a classification into three groups was considered. This additional fourth cluster has proven crucial for capturing false positives within the datasets.

The results presented in Fig. 7 effectively illustrate the ability of the k-means algorithm to accurately identify and classify jumps in configuration 1.

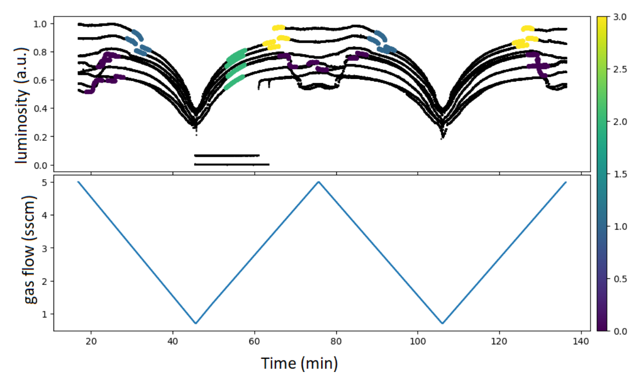

Figure 7: Final result of the k-means algorithm in classifying the detected jumps in configuration 1. False positives are shown in green.

Figure 8 displays the results applied to configuration 2. Although not as precise as when luminosity is included among the variables, due to the correlation between adaptation and luminosity, the algorithm still manages to detect and classify the majority (78.3 %) of the jumps adequately.

Random Forest

After experimenting with the k-means algorithm [4], we opted to try a supervised learning approach using the Random Forest algorithm to classify the data.

To optimize the model's performance, it was configured with the following parameters: number of trees set to 10, maximum depth of the trees set to 5, and the criterion for the quality of the splits set as Gini.

ISBN: 978-3-95450-257-8 ISSN: 2222-5692 doi:10.18429/JACoW-ECRIS2024-MOP08

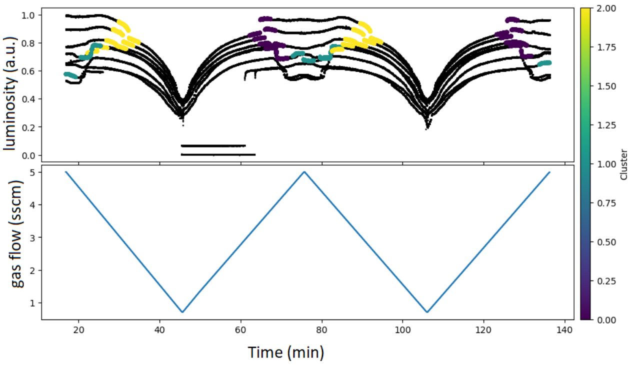

Figure 8: Final result of the k-means algorithm in classifying the detected jumps in configuration 2.

To test de performance a cross-validation was conducted. This process involved dividing the complete dataset into five folds. The model was trained and evaluated five times, each time with a different fold designated as the test set and the remaining as training sets. An F1-score result of 98 % was achieved with configuration 1 and 97 % with configuration 2.

Neural Networks

Finally, the use of neural networks [5] is proposed as a solution to the classification problem. Various types of networks have been explored, with sequential networks and Recurrent neural networks (RNN) proving to be the most effective.

To train the sequential network, the data were split into training and test sets, using 20 % of the data for testing. After experimenting with various configurations, the highest-performing network was set up as follows: a flattening layer, followed by a first dense layer with 512 neurons using the ReLU activation function. The second and third dense layers have 256 and 128 neurons, respectively. The output layer uses the softmax activation function. A F1 Score of 76 % was achieved with configuration 1, and a F1 Score of 64 % with configuration 2.

The RNN model was reconfigured to simplify its structure and adjust its performance. The updated features of the model are as follows: An LSTM layer with 200 hidden units that processes input sequences, where each sequence consists of 1000 time steps, each with 10 features. Additionally, there is a dense output layer with 3 units, utilizing the softmax activation function. A F1 Score of 53.1 % was obtained with luminosity, and an F1 Score of 53.9 % was obtained without luminosity.

Clearly, the sequential network is much more accurate than the RNN. However, we can see that this network achieves very similar results when classifying points with and without luminosity, indicating that with more data, it could be a good solution for performing non-intrusive classification.

Table 2: Comparison of the F1-scores of all Algorithms

	Random Forest	Sequential NN	RNN
Config. 1	98 %	76 %	53 %
Config. 2	97 %	64 %	54 %

CONCLUSION

In this paper, a method has been designed to detect state changes in the plasma of a particle accelerator source. The use of ML has been explored to achieve an automatic identification of the injector's state. Two alternative methods have been developed to detect plasma state transitions, including the possibility of doing so without using luminosity, since obtaining measurements of this variable is very challenging once the accelerator is fully completed. Additionally, it has been verified that the unsupervised learning algorithm k-means is effective in classifying state transitions when luminosity is included, though it is not very accurate when this information is unavailable. Therefore, the use of a Random Forest algorithm has been proposed for these cases. Moreover, neural networks have also been proposed as a solution to the problem and the best architectures have been studied to achieve the most effective classification. Table 2 shows a quick comparison of the F1-scores of all the algorithms.

REFERENCES

[1] R. Geller, *Electron Cyclotron Resonance Ion Sources and ECR Plasmas*, Routledge, New York, 1996. doi:10.1201/9780203758663

[2] J. Feuchtwanger, V. Etxebarria, J. Portilla, J. Jugo, I. Badillo, and I. Arredondo, "New compact ion source design and implementation for low current applications", *Nucl. Instrum. Methods Phys. Res., Sect. A*, vol. 929, pp. 101–106, Jun. 2019. doi:10.1016/j.nima.2019.03.052

[3] H. Steinhaus, "Sur la division des corps matériels en parties", *Bulletin de l'Académie Polonaise des Sciences*, vol. IV, no. C1. III, pp. 801-804, 1956. http://www.laurent-duval.eu/Documents/Steinhaus_H_1956_j-bull-acad-polon-sci_division_cmp-k-means.pdf

[4] T.K. Ho, "Random decision forests", in *Proc. 3rd Int. Conf. Doc. Anal. Recogn.*, vol. 1, pp. 278-282, 1995. doi:10.1109/ICDAR.1995.598994

[5] Y.C. Wu and J.W. Feng, "Development and Application of Artificial Neural Network", *Wireless Pers. Commun.*, vol. 102, pp. 1645-1656, Sep. 2018. doi:10.1007/s11277-017-5224-x

ISBN: 978-3-95450-257-8 ISSN: 2222-5692 doi:10.18429/JACoW-ECRIS2024-MOP09

STATUS REPORT ON 60 GHz ECRIS ACTIVITY

Thomas Andre*, Julien Angot, Maud Baylac, Andrea Cernuschi, Pierre-Olivier Dumont, Etienne Labussière, Myriam Migliore, Christophe Peaucelle, Patrick Sole, Thomas Thuillier, Olivier Zimmerman
Laboratoire de Physique Subatomique et de Cosmologie, Univ. Grenoble Alpes, CNRS, Grenoble INP Institute of Engineering Univ. Grenoble Alpes, LPSC-IN2P3, Grenoble, France
François Debray
Laboratoire National des Champs Magnétiques Intenses, CNRS ALPES, Grenoble, France

Abstract

After a record pulsed ion beam current density measured up to ~1 A cm^{-2} obtained with the 60 GHz SEISM (Sixty gigahErtz Ion Source using Megawatt magnets) ion source in 2014 at LNCMI, the experiment resumed in 2019, following a source repair and a beam line upgrade. New measurements shown a limitation in the beam pulsed current measured at ~0.3 A cm^{-2}. A careful investigation pointed out that the performance reduction is due to the upgrade of the beam line base vacuum from ~10^{-6} mbar to ~10^{-7} mbar. The characteristic time for the ion beam to reach the steady state's space charge compensation is calculated and is found to exceed the 500 µs pulse beam duration in the latter case. This analysis is confirmed using IBSIMU which can reproduce the beam intensities measured in the two pressure configurations, assuming a space charge compensation of 65 % in 2014 and 35 % in 2024. Finally, the development status of the superconducting cusp magnet planned to upgrade the source is presented.

INTRODUCTION

The development of new generation 45 GHz ECR ion sources is ongoing to increase the achievable beam intensities at IMP (Lanzhou, China) [1] and at LBNL (Berkeley, California) [2]. These new developments bring many stimulating technical challenges, among which are the high ion source microwave power and the high intensity ion beam transports. These challenges are being addressed with the LPSC 60 GHz program.

In the 2010s, LPSC developed a 60 GHz ECR ion source named SEISM (Sixty gigahertz Electron cyclotron resonance Ion Source using Megawatt magnets), using a gyrotron delivering high-intensity high-frequency (HF) pulses (up to 1 ms, 300 kW, 2 Hz) [3]. This development was historically intended to be applied to the CERN Beta-Beam factory project, as a radioactive ion source [4]. The source magnetic field is simplified to an axial cusp using a set of un-expensive polyhelix copper coils, resisting to radiations. The SEISM source is installed at the LNCMI high magnetic field facility in Grenoble on a dedicated test bench. The cusp generates a closed ECR magnetic surface at 2.14 T. The source produced its first ion beams in 2014 (extracted from a 1 mm diameter plasma electrode) with a record pulsed current density up to J ≈1 A cm^{-2} [5]. After a long shutdown, the experiment resumed in the allocated room at LNCMI in 2021 and the results obtained so far are presented in this paper.

STATUS OF THE SEISM EXPERIMENT

Experiment Upgrade

After the failure of a set of the ion source copper coils in 2014, new ones were designed and built, using advanced three dimensions printing techniques [6]. Numerical simulations performed with the Tracewin code [7] to reproduce the 2014 results campaign was used to design a new low energy beam line (LEBT), assuming a 80 % ion beam space charge compensation. It is composed of a quadrupole triplet and an available 90° bending magnet (with a 650 mm curvature radius and a 90 mm vertical gap). Figure 1 shows a top view of the experimental beam line. The LEBT is equipped with three faraday cups named: (1) FC-Source, to measure the ion beam intensity 397 mm away from the source extraction, (2) FC-Dipole, located between the quadrupole triplet and the bending magnet and (3) FC-Analysis to measure the beam selected after the dipole. A pepper pot emittancemeter

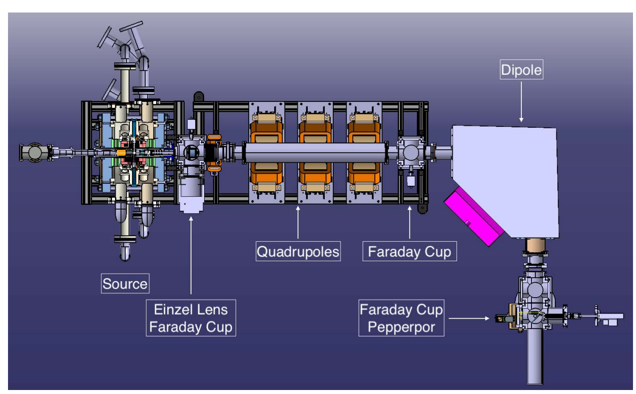

Figure 1: 2D top view of the experimental bench of the SEISM source. From left to right: Source, extraction box (Faraday cup source (FC-source)/Einzel lens), quadrupole triplet, Faraday cup dipole entrance (FC-dipole), dipole, end of line diagnostics (pepperpot/ Faraday cup (FC-analyze)).

is also installed close to FC-Analysis to measure the beam emittance. The IBSIMU simulations indicated a theoretical transmission of 90 % through the LEBT for a 1 mm plasma

* thomas.andre@lpsc.in2p3.fr

ISBN: 978-3-95450-257-8 ISSN: 2222-5692 doi:10.18429/JACoW-ECRIS2024-MOP09

electrode diameter with 1 A cm^{-2} current density [8] . The experimental ion source and the LEBT base vacuum was improved from 10^{-7} mbar to 10^{-6} mbar.

Experimental Results

The primary objectives of the new experimental campaign were to reproduce the former current density results (obtained in 2014) and validate the higher ion beam transport through the new LEBT. In 2022, early beam transport measurement yields appeared below expectation. An Einzel lens was added as close as possible from the ion source extraction, before the quadrupole triplet to enhance the extracted beam focusing. Measurement made in February 2023 with Oxygen support gas at 18 kV source voltage shows a mean extracted current around 1.4 mA in FC-Source, which corresponds to a current density of 180 mA cm^{-2}. Without any focusing, the beam transport in the LEBT is poor, with a transmission about 23 % (ratio of the current measured in FC-dipole and FC-source, see Fig.1). The tuning of the quadrupole triplet and the Einzel lens allowed the transport of 1 mA beam intensity up to FC-Dipole, improving the transmission to 73 % [8].The experiments stopped after the short-circuit of the two injection coils. The experiments resumed in 2024 after the fixing of the damaged coils. The extracted beam current measured with FC-source was studied as a function of the source high voltage. The results are presented on Fig. 2. Figure 2**a** shows the time evolution

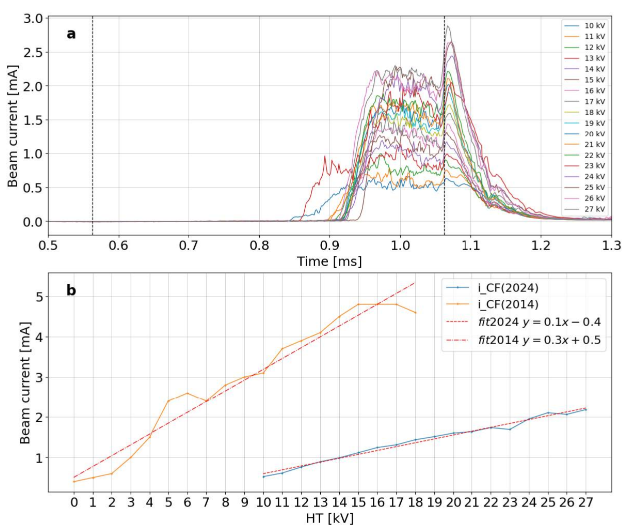

Figure 2: (a) Temporal evolution of the total beam intensity measured in FC-Source for various source high voltage, with a RF power of 80 kW. (b) Evolution of the average ion pulse current as a function of the source high voltage for the 2014 data (orange) and the 2024 data (blue).

of the beam intensity for different extraction voltage. One can see that the ion beam intensity increases with the potential of the source, showing no sign of saturation up to the maximum experimental voltage. The black vertical lines indicate the start and stop time of RF injection in the source. One can also note the presence of an afterglow peak right at the end of the RF pulse. Figure 2**b** shows the mean current intensity (temporal average of the plateau signal) versus the source high voltage for the 2014 (orange curve) and 2024 experiment (blue curve). One can observe that, for both dataset, the current extracted is linearly proportional to the voltage applied. However, the curve slopes and intercepts are different. For 2014 data, the beam intensity increase by ∼300 µA/kV applied whereas, for the data of 2024, the slope is about 100 µA/kV. In short, the current density transported in 2024 is ∼3 times smaller than the one of 2014 (2.2 mA against 7 mA). After carefully checking that the injected RF power in 2024 was equivalent to the 2014's one, the only remaining parameter different from 2014 was LEBT base pressure.

BASE PRESSURE AND SPACE CHARGE COMPENSATION

Having identified the LEBT base pressure level as the possible factor limiting the beam transport, we investigated the characteristic beam space charge compensation time of our experiment, defined as in Ref. [9]:

$$\tau_{\mathrm{SCC}} = \frac{1}{\sigma_i \cdot n_g \cdot v_b} , \tag{1}$$

where σ_i is the ionization cross section of the beam with the residual gas, n_g is the gas density and v_b the velocity of the impinging beam. τ_{SCC} corresponds to the time after which the SCC ratio reached $1/e$ =∼37 %.

The ionization cross-section is estimated with an available experimental measurement done for N$^+$ impact on N_2 [10] at 20 kV, which leads to $\sigma_i \sim 4 \times 10^{-16}$ cm^2. Indeed, the nitrogen mass being close to the nitrogen one, this cross-section is deemed sufficiently close to our experimental configuration to use it as an estimator.

Figure 3 represents the evolution of τ_{SCC} with the LEBT pressure. The green area corresponds to the 2024 operational range while the blue is the 2014's one. The red line represents the 500 µs beam duration. Before the up-

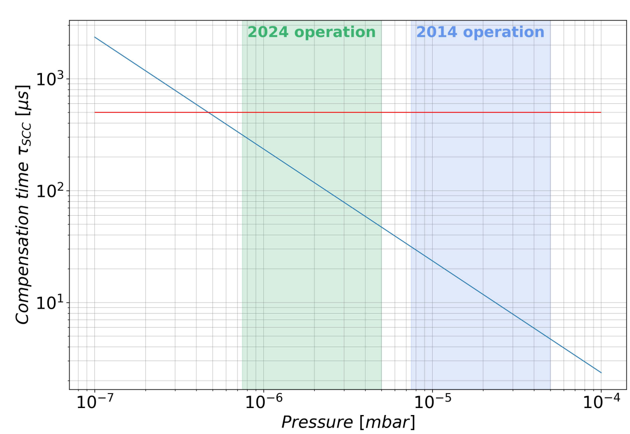

Figure 3: Space Charge compensation time τ_{SCC} as a function of the LEBT pressure. Range of operation of the ion source, blue for 2014, green for 2024.

ISBN: 978-3-95450-257-8 ISSN: 2222-5692 doi:10.18429/JACoW-ECRIS2024-MOP09

grade, due to a rough base vacuum level (7.5×10^{-6} mbar to 5×10^{-5} mbar), τ_{SCC} varies respectively from 31 µs to 5 µs. After the upgrade, the vacuum level span from 7.5×10^{-7} mbar to 5×10^{-6} mbar which gives a τ_{SCC} between respectively 314 µs and 47 µs. One can assume that a SCC steady state is achieved after $T \approx 3 \cdot \tau_{\mathrm{SCC}}$. In 2014, we observed that the worst SCC steady state time is T_{2014} ~90 µs, a value much lower than the beam duration of 500 µs. In comparison, T_{2024} can be three times higher than the beam duration itself, leading to a low SCC and resulting in a low beam transport yield.

The future experimental campaign will investigate the current extracted as a function of the pressure in the beam line injecting heavy noble gas, such as argon or krypton.

PACIFICS PROJECT: FUTURE OF THE 60 GHz PROGRAM

Funding was approved by the French Agence Nationale de la Recherche for the PACIFICS project which will allow pursuing the R&D on the 60 GHz ion source. The project includes the design and procurement of a new superconducting cusp, with a magnetic field intensity on the extraction side adjustable from 2.5 to 3.5 T and the radial component $B_r \leq$ 4 T. Equipped with a 200 mm plasma chamber diameter, the plasma will feature a closed 2.14 T ECR surface inside for all the foreseen magnetic configurations. The superconducting coils have been ordered and are currently under construction. The project also funds the upgrade of the gyrotron high voltage power supply to operate in continuous working (CW) operation to deliver up to 20 kW of 60 GHz RF (see Fig. 4).

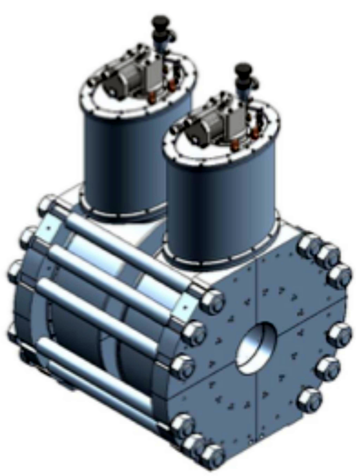

Figure 4: 3D conceptual view of the future superconducting 60 GHz ion source.

One goal of the project is to transform the pulsed current densities measured so far into actual CW high intensity ion beams. Recently, Vybin [11,12] demonstrated the extraction and the transport of ion beams with current density up to 1.15 A cm^{-2} using a point effect extraction system. Such a design will be adapted to the new source to target at least 100 mA beam intensity measured in a faraday cup.

CONCLUSION AND PROSPECTS

The new SEISM LEBT installed since 2019 at LNCMI has demonstrated a significant improvements in the ion beam transmission up to 73%. The reduction of the base pressure in the new LEBT by a decade dramatically increased the time for the pulsed beam to reach a sufficient SCC yield and to be efficiently extracted from the source and transported. This effect resulted in the reduction of the total current extracted from the source with the new LEBT. Such a reduction is well understood by calculating the characteristic time of SCC. The effect is finally reproduced by an (IBSIMU) ion beam simulation with a decrease of the beam SCC from 65% in 2014 down to 35% in 2024. A new system of gas injection will be installed to adjust the LEBT pressure and study the pulsed ion beam current transported as a function fo the pressure and the time. A new budgeted 60 GHz source using superconducting coils, an upgraded CW RF injection and a new extraction system is under design at LPSC. The project's goal is to demonstrate the production of ~100 mA of multi-charged ion beams.

ACKNOWLEDGEMENTS

This work has benefited from state support managed by the National Research Agency under the Future Investment Program with reference ANR-21-ESRE-0049. The authors thanks the European Magnetic Field Laboratory association.

REFERENCES

[1] H. Zhao *et al.*, "Superconducting ECR ion source: From 24-28 GHz SECRAL to 45 GHz fourth generation ECR", *Rev. Sci. Instrum.*, vol. 89, no. 5, p. 052 301, 2018. doi:10.1063/1.5017479

[2] D. Xie *et al.*, "Development status of a next generation ECRIS: MARS-D at LBNL", *Rev. Sci. Instrum.*, vol. 87, no. 2, p. 02A702, 2016. doi:10.1063/1.4931713

[3] L. Latrasse *et al.*, "SEISM: A 60 GHz cusp electron cyclotron resonance ion source", *Rev. Sci. Instrum.*, vol. 81, no. 2, p. 02A324, 2010. doi:10.1063/1.3267297

[4] E. Wildner *et al.*, "Design of a neutrino source based on beta beams", *Phys. Rev. ST Accel. Beams*, vol. 17, no. 7, p. 071 002, 2014. doi:10.1103/PhysRevSTAB.17.071002

[5] T. Lamy *et al.*, "60 GHz ECR Ion Sources", in *Proc. of Heavy Ion Accel. Technol. Conf. (HIAT'15)*, Yokohama, Japan, pp. 277–281, 2015. doi:10.18429/JACoW-HIAT2015-THM2I01

[6] O. Jay, C. Verdy, C. Trophime, Y. Danlos, and F. Debray, "Cold spray manufacturing for structural materials for high field magnet production", in *THERMEC 2018*, pp. 1540–1545, 2019. doi:10.4028/www.scientific.net/MSF.941.1540

[7] D. Uriot and N. Pichoff, *TraceWin*, 2014. https://www.dacm-logiciels.fr/tracewin

[8] T. Andre *et al.*, "SEISM: 60 GHz ECR ion source for future accelerator", in *Proc. 14th Int. Part. Accel. Conf. (IPAC'23)*, Venice, Italy, pp. 2406–2408, 2023. doi:10.18429/JACoW-IPAC2023-TUPM086

ISBN: 978-3-95450-257-8 ISSN: 2222-5692 doi:10.18429/JACoW-ECRIS2024-MOP09

[9] N. Chauvin, *Space-Charge Effect*. 2013, pp. 63–83, contrib. CAS-CERN's Accelerator School: Ion Sources, Senec, Slovakia, 29 May-8 June 2012, edited by R. Bailey. doi:10.5170/CERN-2013-007.63

[10] H. Luna, M. Michael, M. B. Shah, R. E. Johnson, C. J. Latimer, and J. W. McConkey, "Dissociation of N_2 in capture and ionization collisions with fast H^+ and N^+ ions and modeling of positive ion formation in the Titan atmosphere", *J. Geophys. Res.: Planets*, vol. 108, no. E4, 2003. doi:10.1029/2002JE001950

[11] S. Vybin, I. Izotov, and V. Skalyga, "High current ion beam formation with strongly inhomogeneous electrostatic field", *Plasma Sources Sci. Technol.*, vol. 29, no. 11, p. 11LT02, 2020. doi:10.1088/1361-6595/abbf9c

[12] S. Vybin *et al.*, "Experiments on intense ion beam formation with an inhomogeneous electric field", *Plasma Sources Sci. Technol.*, vol. 30, no. 12, p. 125 008, 2021. doi:10.1088/1361-6595/ac38af

ISBN: 978-3-95450-257-8 ISSN: 2222-5692 doi:10.18429/JACoW-ECRIS2024-MOP10

LIGHT IONS FROM THE GTS-LHC ION SOURCE FOR FUTURE PHYSICS AT CERN

Detlef Küchler*, Bichu Bhaskar, Giulia Bellodi, Maciej Slupecki, Richard Scrivens
European Organization for Nuclear Research (CERN), Geneva, Switzerland

Abstract

Starting from 2028, physics programmes using ions at CERN have requested lighter ions than the lead usually produced. The Working Group on Future Ions in the CERN Accelerator Complex has been mandated to assess the feasibility of the production and operation of these new ion species. The ion beam production from two of the chosen elements, krypton and magnesium, was studied in the GTS-LHC ion source, and the preliminary results of beam intensity, stability and emittance will be presented, as well as proposed modifications to improve performance.

INTRODUCTION

The CERN accelerator complex was upgraded in 1994 to deliver heavy lead ions for the ion physics programme of the fixed target experimental area called North Area (NA) of the Superprotonsynchrotron (SPS) and since 2007 for the ion physics programme of the Large Hadron Collider (LHC). Some exceptions to the standard lead operation were indium (2003), oxygen (2005), argon (2015) and xenon (2017).

Recently a working group "Future Ions in the CERN Accelerator Complex" was created to define future ion operation needs based on the requests from the LHC and the fixed target experiments and their implications for the ion injector accelerator complex [1]. The aim is to find synergies between the different experiments to limit the number of different ion species, to study challenges and limitations in the ion accelerator complex and to make proposals to schedule tests of selected ion species.

Presently a limitation for the study of new ion species is the existence of only one ion source in the complex, the GTS-LHC ECR ion source [2], which has to be used for the operation of requested ion beams and the development of new ion beams.

The setup of the ion accelerator chain and the following physics period can be up to 6 months. This means, depending on the physics programme, only two ion species can be operated or studied per year. Only precise long-term schedule allows under this condition to serve all the needs of the ion community.

Due to these long operation periods it requires an excellent long-term stability over weeks or months of the source. This is more demanding than just reaching the target beam intensity, especially for metal ion beams based on oven operation.

For the LHC, the working group studied if by using different ions, the nucleon-nucleon luminosity could be increased. One candidate ion is krypton. With nobel gas ions the source conditioning time is usually shorter, and stable operation is reached within 2 weeks, so a short 3 week test with krypton before the start of the setup of the ion accelerator chain with lead was scheduled in the beginning of 2023.

For the fixed target physics the list of ions to be prepared for the next years could be limited to magnesium and boron. In the beginning of 2024 a 8 weeks test of magnesium was done. Boron has to be tested in one of the following years.

KRYPTON TEST

The aim of this test was to find the settings of the source for a reliable and stable operation, information about the charge state distribution, beam intensity and beam emittance. Due to the short time available the beam could be studied only in the Low Energy Beam Transport (LEBT) and in the following RFQ. The rest of the linear accelerator was not available at that moment. To transport the ion beam through the RFQ the extraction voltage has to be set to a value corresponding to a beam energy of 2.5 keV/u.

The linear accelerator Linac3 injects the ion beam into the Low Energy Ion Ring (LEIR) [3]. Depending on the ion species and the charge state available from the source the beam needs to be stripped at the end of the linear accelerator as only a limited range of charge-over-mass can be injected into LEIR. For the test isotopically pure ^{86}Kr was used (17.3 % abundance in natural krypton). A charge state around Kr^{22+} would have been a good option to avoid stripping.

The source was mechanically already set up for the following lead ion beam commissioning (to minimize the switch-over-time), i.e. the extraction gap was not adjusted for the low extraction voltages needed for the krypton ion beam. Oxygen was used as support gas.

In the first stage of testing a charge distribution peaking at Kr^{19+} could be achieved (see Fig. 1, FC2 is the Faraday cup directly after the separation spectrometer). But this charge state would have been too low for a direct injection into LEIR. After re-adjusting the source parameters a charge state distribution peaking at Kr^{22+} could be achieved (see Fig. 1).

After a couple of days of commissioning we achieved around 120 eμA of Kr^{22+} at an extraction voltage of 9.8 kV out of the source and around 80 eμA out of the RFQ (see Fig. 2). The stability of the ion beam was excellent compared to the standard lead ion beam.

The transverse emittance in front of the RFQ was measured using tomographic reconstruction [4] from beam profile measurements on a profile grid, as a function of current in a upstream quadrupole magnet. The results show that

* email address: detlef.kuchler@cern.ch

ISBN: 978-3-95450-257-8 ISSN: 2222-5692 doi:10.18429/JACoW-ECRIS2024-MOP10

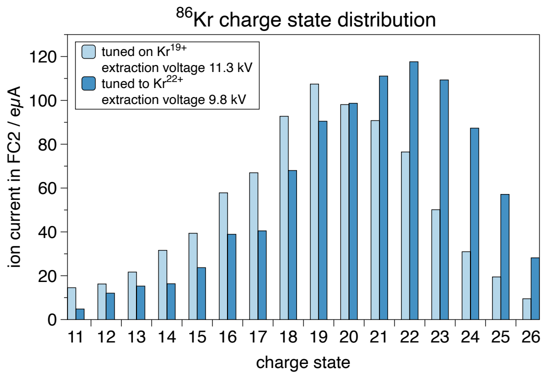

Figure 1: Charge state distributions of the krypton ion beam optimized for two different peak charge states. FC2 is the Faraday cup after the spectrometer.

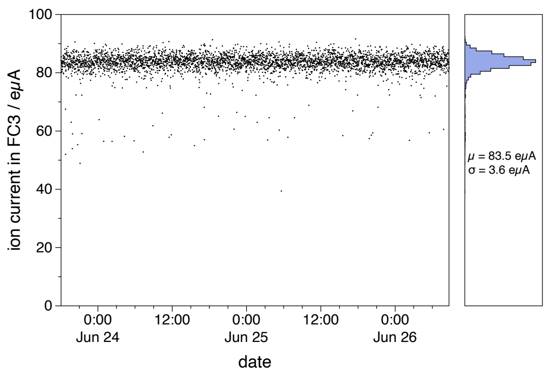

Figure 2: Beam stability of the krypton ion beam out of the RFQ over a period of 48 hours. FC3 is the Faraday cup directly after the RFQ.

the emittance of the krypton ion beam is clearly bigger than the lead ion beam at this location (see Fig. 3). The not well adapted extraction gap may be the reason for this behaviour. Further studies, to better understand this, are needed.

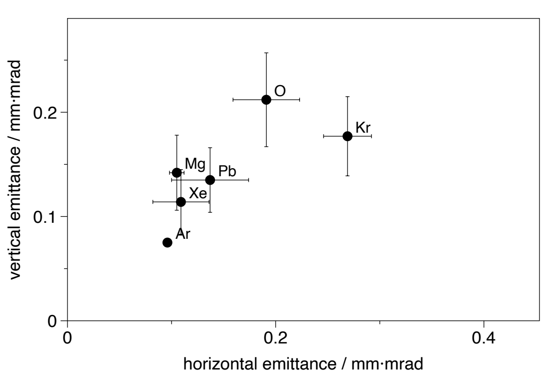

Figure 3: Horizontal and vertical emittances (normalized RMS emittance) of different ion beams in the LEBT. The values are averaged over several measurement campaigns. The error bars represent the rms values. For argon only one measurement was available.

The experiment was very successful. Source and LEBT settings and beam performance values were recorded. No show stoppers could be identified.

MAGNESIUM TEST

The aim of this test was as well as for the krypton test to find the settings of the source for a reliable and stable operation, information about the charge state distribution, beam intensity and beam emittance. Magnesium ions bring the additional challenge of finding suitable parameters for the evaporation and measuring consumption from the micro-oven.

Magnesium consists of three stable isotopes. But as ^{24}Mg has an abundance of 79 % we performed the first test with chemical pure, natural magnesium. The source has two ovens that can be installed in parallel. Each oven could be filled with around 250 mg of magnesium.

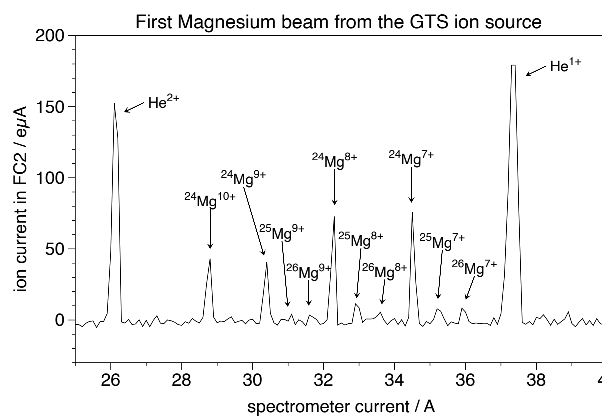

Figure 4: Charge state distribution of the magnesium ion beam. All three magnesium isotopes are visible, the ratio of the intensities roughly correspond to the natural abundance ratios. The peak of He^{1+} is cut due to saturation. FC2 is the Faraday cup after the spectrometer.

Out of the source up to 75 eμA of ^{24}Mg^{7+} (see Fig. 4) could be measured (routinely 30-40 eμA). The charge state 7+ was chosen, as with this charge state no stripping before injection into LEIR is needed. Out of the RFQ the intensity was around 20 eμA and at the end of the linac we measured 10-15 eμA. During the final two days of the test the intensity could be increased to 20 eμA, which would be sufficient for the operation of LEIR. The beam stability over shorter periods was excellent (see Fig. 5). Over periods more than one or two days the stability suffered due to the high material consumption.

As shown in Fig. 3 the emittance for the magnesium ion beam is in the same range as the emittance of the lead ion beam. The transmission through the RFQ was significantly lower than what was observed for other ion species, this is currently not understood (at least not in terms of transverse emittance).

As mentioned earlier 250 mg of material could be installed per oven. Oven operation was limited to 2-5 days with

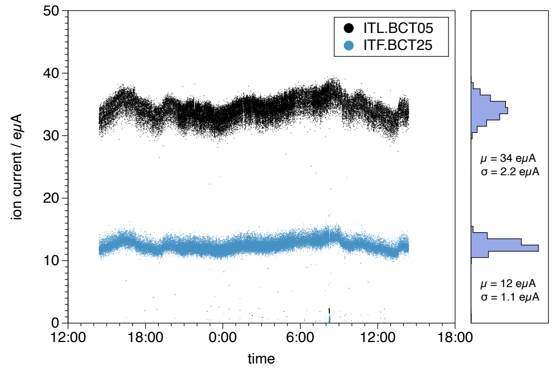

Figure 5: Measurement of the magnesium ion beam stability over a period of 24 h. ITL.BCT05 is the beam transformer in the LEBT in front of the RFQ, ITF.BCT25 is the beam transformer at the end of the linac.

250 mg of Mg installed, which results in an average consumption of 2.7 mg/h over the whole test period. Due to this the ovens had to be regular refilled and there were periods were the source was running with low magnesium input. As a result, the conditioning of the source and the beam stability suffered. The peak performance of the source could only be reached by the end of the test while pushing the oven operation to higher oven power.

For this test source settings and settings for the linear accelerator and beam performance values were recorded. The oven operation was identified as the main performance-limiting factor. No other show stoppers could be found.

CONCLUSIONS AND FUTURE PLANS

Both tests, krypton and magnesium, can be counted as success. Both tests showed that the required charge states and beam intensities can be provided by the source.

During the krypton test the beam could be sent only through a part of the linear accelerator. A follow-up test is needed to send the beam through the whole ion injector chain to study the performance and limitations along the accelerator chain.

For the next test it is also planned to improve the gas injection system to allow the flow rate of the two simultaneously injected gases to be better controlled.

The source extraction gap should be shortened compared to the initial krypton test to see if this lowers the emittance and improves transmission.

The next test with magnesium is scheduled during the Long Shutdown 3 (LS3) period (2026–2028). As the material consumption was the main issue in the present test the installation of a hot screen inside the plasma chamber is foreseen [5]. To achieve similar operation periods per oven as for lead (around 30 days) the magnesium consumption needs to be reduced to values below 0.5 mg/h.

If this test does not show the required results an experiment with magnesocene is foreseen as a fallback solution.

REFERENCES

[1] R. A. Fernandez *et al.*, “Future Ions in the CERN Accelerator Complex WG: Post-LS3 NA61/SHINE light ion beam requirements feasibility study: source operation, radiation protection impact in LINAC 3, LEIR and PS and risk assessment in LEIR”, CERN Document Server, CERN Accelerator Note, to be published.

[2] L. Dumas *et al.*, “Operation of the GTS-LHC Source for the Hadron Injector at CERN”, CERN, Tech. Rep. LHC-PROJECT-Report-985, 2007. `http://cds.cern.ch/record/1019180`

[3] J. Coupard *et al.*, “LHC Injectors Upgrade, Technical Design Report”, CERN, Tech. Rep., 2016. `doi:10.17181/CERN.L6VM.UOMS`

[4] V. Dimov, R. Gaur, J.-B. Lallement, and A. Lombardi, “Emittance reconstruction techniques in presence of space charge applied during the Linac4 beam commissioning”, in *Proc. of ICFA Adv. Beam Dyn. Workshop High-Intensity High-Brightness Hadron Beams (HB’16)*, Malmö, Sweden, pp. 433–438, 2016. `doi:10.18429/JACoW-HB2016-WEPM1Y01`

[5] V. B. Kutner *et al.*, “Production of intense 48Ca ion beam at the U-400 cyclotron”, *Rev. Sci. Instrum.*, vol. 71, no. 2, pp. 860–862, 2000. `doi:10.1063/1.1150313`

ISBN: 978-3-95450-257-8 ISSN: 2222-5692 doi:10.18429/JACoW-ECRIS2024-MOP11

CONTINUOUS DATA-DRIVEN CONTROL OF THE GTS-LHC ION SOURCE AT CERN

V. Kain*, N. Bruchon, D. Küchler, B. Rodriguez Mateos, M. Schenk
CERN, Geneva, Switzerland
S. Hirlander, Paris Lodron University of Salzburg, Salzburg, Austria

Abstract

Recent advances with the CERN infrastructure for machine learning allow to deploy state-of-the-art data-driven control algorithms for stabilising and optimising particle accelerator systems. This contribution summarises the results of the first tests with different algorithms to optimise the intensity out of the CERN LINAC3 source. The task is particularly challenging due to the different latencies for the various control parameters that range from instantaneous to full response after only ~30 minutes. Next steps and vision towards full deployment and autonomous source control will also be discussed.

INTRODUCTION

The GTS-LHC 14.5 GHz Electron Cyclotron Resonance (ECR) ion source [1] at the CERN LINAC3 provides different heavy ion beams for the LHC, as well as the PS and SPS fixed target experiments. In the case of the main species of lead ions, the beams are produced by vaporisation of solid samples that are heated with an oven in the plasma chamber. Tuning the various parameters of the source, such as oven power, to maximise its intensity output as well as ensuring reproducible intensity during the pulse and on a shot-by-shot level is non-trivial and is frequently slow due to conditioning effects. For example, during commissioning or after a stop, the oven's power needs to be slowly ramped up until lead evaporation is initiated. It is then increased over two to four weeks to maintain a sufficiently high evaporation rate until the next oven refill. Figure 1 shows an example of the reconditioning of the source in May 2018 with the discussed slow ramp-up of the oven power and non-linear response of intensity over the course of about 11 h. Various other parameters need to be adjusted as well as part of this process that are not indicated in Fig. 1. All of this is usually done manually.

This paper summarises the first tests of deploying CERN's Generic Optimisation Framework [2] to automatically optimise the intensity out of the LINAC3 source with the final goal of making recovery after oven refills and commissioning more efficient and less dependent on singular experts. Algorithms to stabilise the performance after commissioning were also part of the investigation.

To date, only preliminary tests of various sample-efficient optimisation and stabilisation algorithms could be carried out. However, they were already sufficient to start addressing the challenging aspects of time-varying dynamics and control knobs that act at significantly different time scales. Another test is planned towards the end of the 2024 run where the lessons learned will be incorporated.

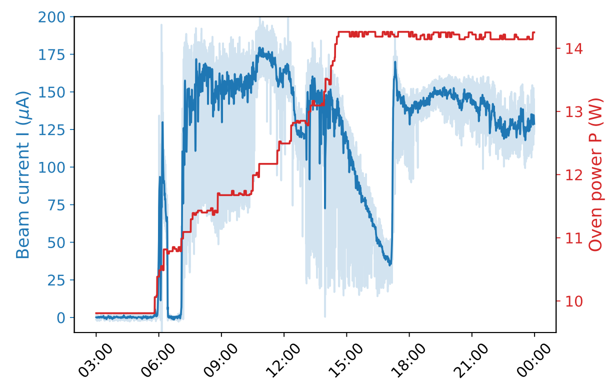

Figure 1: Evolution of the beam current measured by BCT.ITL05 at the end of the Low Energy Beam Transport in blue during lead ion beam setup in May 2018. The oven power (red) needs to be ramped up slowly. In this particular case this phase took roughly 11 h while tuning other parameters in addition.

GENERIC OPTIMISATION FRAMEWORK AND FRONTEND AT CERN

A significant step towards automating parameter optimisation and stabilisation was the implementation of the "Generic Optimisation Framework and Frontend" (GeOFF) in Python at CERN [2]. GeOFF standardises interfaces for optimisation tasks and provides adapters for various third-party packages such as SciPy, Stable Baselines 3, Scikit-Optimize, BoTorch. GeOFF tasks can scale to arbitrary complexity and depend on any Python package; they can use any controls system and even communicate with external simulation tools, as long as they have Python bindings. It comes with a GUI application, readily usable with the CERN control system in the various control rooms. It allows to add custom plotting in addition to a pre-defined set of plots that show the evolution of the objective function and the actors. It also allows to save the optimisation evolution in terms of objective function and actors, which was used to produce the plots in this paper.

* Verena.Kain@cern.ch

ISBN: 978-3-95450-257-8 ISSN: 2222-5692 doi:10.18429/JACoW-ECRIS2024-MOP11

DESCRIPTION OF LINAC3 SOURCE OPTIMISATION PROBLEM AND FIRST TESTS

The tests described in this paper were carried out during a so-called Machine Development (MD) session as part of the LINAC3 lead ion commissioning phase between July 8-10, 2024. The objective was to optimise the intensity out of the source measured by the Beam Current Transformer (BCT) ITL.BCT05 as well as the rms intensity fluctuation σ over the pulse length, i.e. to maximise the intensity and minimise its rms. The objective function y that yielded the best results was

$$y = (-1) \cdot \bar{I} + 2 \cdot \sigma \,, \tag{1}$$

where $\bar{I}$ corresponds to the mean intensity measured at ITL.BCT05 and σ to the standard deviation of the slice of the intensity pulse of interest for injection into the downstream elements followed by the Low Energy Ion Ring (LEIR) [3]. The optimisation task was formulated with up to five degrees of freedom: the currents of the three solenoids that confine the plasma in the plasma chamber, the voltage of the bias disc electrode located at the entrance to the plasma chamber, and finally the oxygen gas injection regulated according to the voltage setting with a feedback controller. The used parameter ranges are summarised in Tab. 1. Whereas the effects of the solenoids and bias disc changes were immediately measurable with the BCT, any changes to the gas injection system would only stabilise after several minutes and a waiting time had to be applied before reading out the BCT. See Fig. 2 for the evolution and the "ringing" of the gas injection measured voltage during one of the optimisation runs. The waiting times when working with the gas injection system were either set to 30 s or 120 s. The plots shown in the following were all from the period with 30 s waiting time. While 30 s might not be long enough for full decay of the "ringing", especially for large settings changes, it was sufficient to allow for convergence for the overall optimisation together with the faster actors. A more detailed study on which waiting time to use will have to be carried out in a future test campaign.

To implement the optimisation task within GeOFF, while respecting the different delays in response for the various control knobs, the problem was split into two optimisation tasks running in parallel and independently with the same objective function. One task would adjust the "fast" degrees of freedom (solenoids and bias disc voltage) and another one would adjust the gas injection and only acquire intensities and rms after 120 s or 30 s, respectively. In a continuous control setup during e.g. gas injection adjustments, the "fast" actors were supposed to catch up with the new conditions of the source and optimise their settings, while the gas reading was stabilising. No other synchronisation between the two optimisation environments was built in during these first tests.

THE ALGORITHMS

In the following, the different algorithms tested during the MD will briefly be introduced. The most relevant results were achieved with Bayesian Optimisation [4] and Adaptive Bayesian Optimisation [5]. Note that the algorithms BOBYQA [6] for optimisation and Extremum Seeking (ES) [7] for stabilisation were also tested briefly – with success however only in the case of BOBYQA. However, we will not discuss BOBYQA and ES results further.

Bayesian Optimisation

Bayesian optimisation (BO) is a powerful black-box optimisation algorithm, which learns a probabilistic model of the objective function with Gaussian processes (GP) [4]. To make use of the model's uncertainty, the so-called *Acquisition Function* is optimised, rather than the mean $\mu(\mathbf{x})$ of the objective function. In our case, we used the *Upper Confidence Bound Acquisition Function* (UCB):

$$a(\mathbf{x}) = \mu(\mathbf{x}) + \sqrt{\beta}\,\sigma(\mathbf{x}) \,, \tag{2}$$

where $\mu(\mathbf{x})$ is the mean of the posterior GP and $\sigma^2(\mathbf{x})$ the variance. β is a hyperparameter that needs to be tuned for the specific application. It defines the balance between exploration and exploitation during the optimisation process. For the LINAC3 source tests, Bayesian Optimisation was implemented with BoTorch in a custom optimiser available in GeOFF only for the LINAC3 optimisation environments. To enforce "smooth" parameter optimisation, *proximal biasing* was applied [8].

Adaptive Bayesian Optimisation

To use Bayesian optimisation as a continuous control algorithm and make the algorithm adapt to changes – hence Adaptive Bayesian Optimisation (ABO), the objective function can be modelled as a function of the control parameters $\mathbf{x}$ and also as a function of time t. The kernel function, or prior covariance, of the GP is chosen such that it can represent the correlations in the data well. Following [5] the kernel that we use in ABO is a composite kernel with a *spectral mixture kernel S* for t and the *Matern kernel M* for $\mathbf{x}$:

$$k([t_1, \mathbf{x_1}], [t_2, \mathbf{x_2}]) = \theta_k \times S(t_1, t_2) \times M(\mathbf{x_1}, \mathbf{x_2}) \,, \tag{3}$$

where θ_k is the output scale.

ABO was implemented with BoTorch [9] and is again only available for the LINAC3 environments in GeOFF. To use ABO for continuous control, the data buffers for conditioning the GP models need to be truncated. These data buffers are also stored for subsequent warm-starts such that random (or any other policy) data collection is not necessary. As for BO, *proximal biasing* was used.

FIRST OBSERVATIONS

Figure 3 shows the evolution of the objective function and the normalised currents of three solenoids during optimisation with BO. *Proximal biasing* ensures that the solenoids

ISBN: 978-3-95450-257-8 ISSN: 2222-5692 doi:10.18429/JACoW-ECRIS2024-MOP11

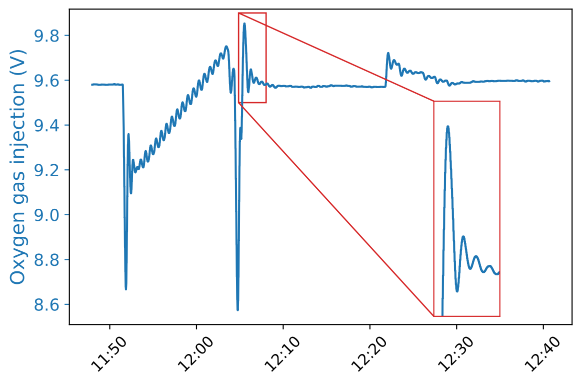

Figure 2: Evolution of the measured gas injection regulation system voltage during one of the tests on 9th of July described below. The larger the step size, the larger the excursions are around the set values. The oscillations settle eventually. See bottom plot of Fig. 5 for the set values during this phase.

smoothly arrive at the optimum settings avoiding big jumps, while the noisy objective function is minimised. The intensity after this optimisation was indeed higher than initially (improvement from 0.45 to 0.5 mA). A similar test with successful convergence was also carried out including the bias disc voltage, indicating that optimisation of the "fast" actors could be relatively easily automated. An important ingredient for good convergence was to not average over several acquisitions and let the GP learn the alleatoric uncertainty.

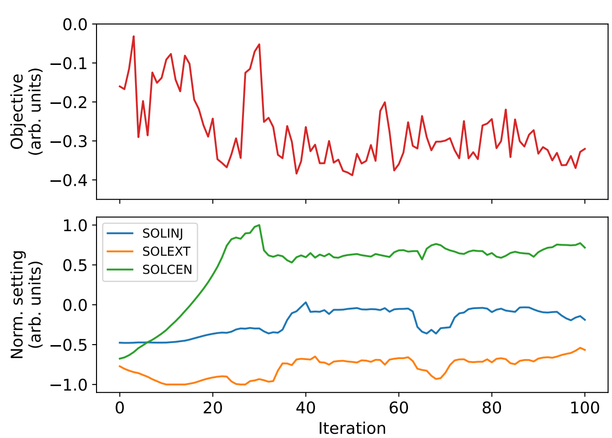

Figure 3: Bayesian Optimisation for the three solenoids around the LINAC3 source plasma chamber using proximal biasing and historical data to condition the GP at the start of the optimisation. The objective function is a combination of mean intensity and rms measured during the slice of interest of the ion pulse, see Eq. (1).

As a next step ABO was tested for the "fast" actors in combination with optimisation of the slow gas injection system. The best configuration was achieved with $\beta = 1.5$ in the UCB acquisition function and $\beta_{prox} = 0.5$ for proximal biasing. Figure 4 shows the evolution of the objective function as well as the three solenoid settings for this case. The GP of the algorithm was conditioned with a previously recorded dataset, thus the solenoids start with good settings and maintain those for the first roughly 115 iterations. The sharp increase of the objective function away from the optimum is caused by the start of the optimisation of the gas injection system, which collected its initial data by a linear ramp of its settings between predefined bounds. See Fig. 2 for the gas injection voltage acquisition and Fig. 5 for the perspective of the controller during the optimisation of this slow actor, respectively. The linear ramp instead of the usual random policy for initial data collection was chosen to minimise the excursions of the gas injection regulation system. The solenoids do not manage to establish the original performance for most of the linear ramp of the gas injection system and stay at the bounds of their allowed ranges (the bounds correspond to $(-1, 1)$ in the plots as GeOFF works with normalised settings). Together the slow and fast tasks converge however eventually to an objective value that is not as good as the initial one, but very close to the optimum obtained during the optimisation phase. Note that the starting gas injection setting and corresponding objective function were not used for building the model, see Fig. 5. This is believed to be the reason for not getting back to the initial optimum. The result is promising and indicates that adequate optimisation of the system gas injection system and solenoids (plus bias disc) is in principle possible with the used techniques. If the optimisation routines were synchronised, where instead of running ABO for the fast actors in the shadow, an optimisation of the fast actors is triggered after each step of the gas injection system, the global optimum should be within reach. This would also allow for easier tuning of the adequate waiting time after changing the settings on the gas injection system.

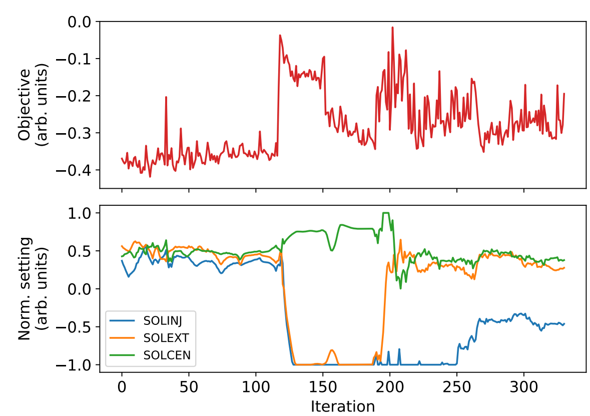

Figure 4: Evolution of objective function (upper plot) and three solenoids (lower plot, normalised settings) during Adaptive Bayesian Optimisation. At iteration ~120, ABO is launched on the gas injection system, see Fig. 5. The three solenoids eventually converge to a new optimum given the changed setting of the gas injection system.

Table 1: Ranges of the Various Parameters used for LINAC3 Source Optimisation

Parameter	Parameter Range	Unit
solenoid inj	[1100, 1265]	A
solenoid cen	[1100, 1140]	A
solenoid ext	[0, 400]	A
bias disc	[0, 500]	V
gas injection	[9, 9.6]	V

NEXT STEPS

Towards the end of the 2024 run another test to control the LINAC3 source is foreseen and the lessons learned so far will be incorporated. Given the results obtained and the experience of the expert, the optimisation task for the next step will be implemented as *one* GeOFF optimisation problem. The different parameters will be optimised/stabilised in a hierarchical and sequential manner: the outer loop will run ABO to optimise the gas injection system; at each iteration of this outer loop, first the solenoids will be optimised with BO (conditioned on previous data) and then the bias disc. The waiting times for the outer loop for the slow gas injection system will be established dynamically based on the acquisition of the gas injection regulation voltage together with the acquisition of the current of the extraction power supply as additional information.

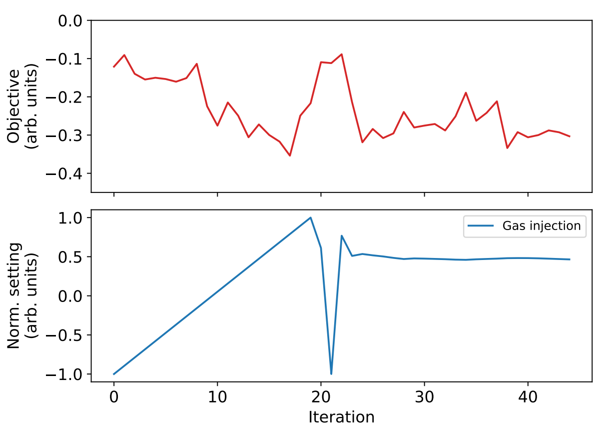

Figure 5: Evolution of objective function (upper plot) and gas injection setting (lower plot, normalised settings) during Adaptive Bayesian Optimisation. The linear ramp is used to avoid large excursions of the gas injection system regulator and "confuse" the "fast" actors that are running ABO in parallel.

SUMMARY

The LINAC3 ECR ion source at CERN provides heavy ion beams for the LHC and the PS and SPS fixed target experiments. Lead ion beams are produced through vaporisation of solid samples in a plasma chamber. Optimising the lead beam intensity out of this source is time consuming, non-trivial and is usually done manually relying on year-long experience of a few experts. This paper summarises the first steps towards automating the source commissioning as well as the performance stabilisation thereafter with algorithms based on Bayesian Optimisation. The CERN Generic Optimisation Framework and Frontend (GeOFF) was used as a platform for implementation and test execution with its ready-made GUI and various features. Particularly challenging for controlling the LINAC3 source are the different latencies in response involved with the various control knobs. This was addressed by running several optimisation/stabilisation tasks in parallel, separating the "slow" and "fast" actors. The first results were promising and showed that Bayesian Optimisation and Adaptive Bayesian Optimisation are sample-efficient enough and can deal well with the noisy environment. For guaranteed convergence it was however proposed for the next test to modify the setup of optimisation tasks and trigger for each iteration of the slow system an optimisation of the fast actors and synchronise the tasks in this manner. Given the results obtained already, this should allow convergence to the global optimum in a robust manner and to track changes adequately.

REFERENCES

[1] C. E. Hill *et al.*, "GTS-LHC: A New Source For The LHC Ion Injector Chain", in *AIP Conference Proceedings*, ECRIS'04, Berkeley, California (USA), March 2005, p. 127–130. doi:10.1063/1.1893381

[2] N. Madysa *et al.*, "Generic Optimisation Framework and Frontend (GeOFF)". doi:10.5281/zenodo.8434512

[3] M. Chanel, "LEIR: the low energy ion ring at CERN,"*Nucl. Instrum. Methods Phys. Res., Sect. A*, vol. 532, no. 1–2, pp. 137–143, Oct. 2004. doi:10.1016/j.nima.2004.06.040

[4] R. Roussel *et al.*, "Bayesian Optimisation Algorithms for accelerator physics", 2023. doi:10.48550/arXiv.2312.05667

[5] A.G. Wilson and R.P. Adams, "Gaussian Process Kernels for Pattern Discovery and Extrapolation", 2013. doi:10.48550/arXiv.1302.4245

[6] M.J.D Powell, "The BOBYQA algorithm for bound constrained optimization without derivatives", DAMTP 2009/NA06, Cambridge, England, 2009. https://ml4physicalsciences.github.io/2021/files/NeurIPS_ML4PS_2021_82.pdf

[7] A. Scheinker *et al.*, "Extremum Seeking Optimal Controls of Unknown Systems", 2018. doi:10.48550/arXiv.1808.05181

[8] R. Roussel *et al.*, "Proximal Biasing for Bayesian Optimization and Characterization of Physical Systems", in *NeurIPS'21*. doi:10.18429/JACoW-ICALEPCS2021-MOPV039

[9] M. Balandat *et al.*, "BoTorch: A Framework for Efficient Monte-Carlo Bayesian Optimization", Advances in Neural Information Processing Systems 33. doi:10.48550/arXiv.1910.06403

26th Int. Workshop Electron Cyclotron Resonance Ion Sources ECRIS2024, Darmstadt, Germany JACoW Publishing
ISBN: 978-3-95450-257-8 ISSN: 2222-5692 doi:10.18429/JACoW-ECRIS2024-MOP13

PRODUCTION OF "COCKTAIL BEAMS" WITH ECR BOOSTER, POST-ACCELERATED FOR INDUSTRIAL APPLICATIONS

R. Frigot, M. Dubois, B. Jacquot, M. Lalande, B. Lucarz, C. Michel, E. Dessay, A. Dubois
GANIL, CEA/CNRS, Caen, France

Abstract

The GANIL (**G**rand **A**ccélérateur **N**ational d'**I**ons **L**ourds) in Caen produces with cyclotrons up to 20 % of the beam times dedicated to industrial applications, such as the irradiation of electronic components. The SAGA project (**S**pace **A**pplication at **G**ANIL **A**ccelerators) aims to increase beam times for these applications in the future in order to meet demand from French and European industries.

INTRODUCTION

In this context, one of the challenges is to be able to switch rapidly from one beam to another in order to optimize the beam time available for irradiation. This project involves technical and organisational developments (on existing GANIL and SPIRAL2 facilities, see Fig. 1) to improve the supply of medium and high energy beams for experimental needs.

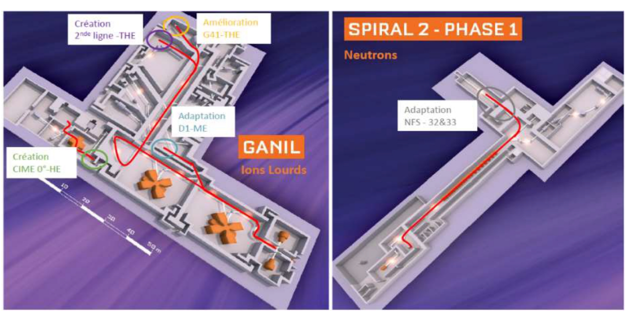

Figure 1: Layout of GANIL/SPIRAL2 accelerators.

The work package *CIME 0°-HE* plans to install a new irradiation station for medium energy beams (up to 20 MeV/u), using the Charge Booster as stable ion source (from SPIRAL1 facility) to provide cocktail beams (Fig. 2).

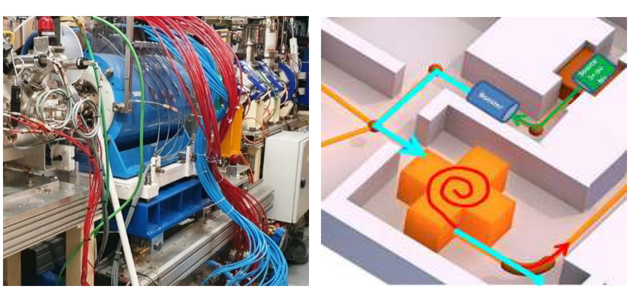

(a) Phoenix Charge Booster (b) ECR SPIRAL1 Facility

Figure 2: Charge breeder (a) and SPIRAL1 layout (b).

To meet the requirements, this ECR Ion Source has to produce several elements, with very close A/Q, which were separated and post-accelerated by CIME cyclotron.

The Phoenix Booster, usually dedicated to increase the charge state of a monocharged radioactive beams produced by target ion source (FEBIAD, surface ionisation ion source), can also produce gaseous stable beams in ECR source mode. However, the needs for industrial application require a cocktail beam including metallic one. That implies few modifications on Booster to be able to provide this cocktail with acceptable intensities.

Finally, the chosen cocktail beam must be optimised to deliver the highest energy reachable with the CIME cyclotron, and to ensure a reasonable switch time between each beam.

EXISTING SPIRAL1 FACILITY

The SPIRAL1 facility at GANIL (Caen, France) is a RIB factory using the ISOL method [1]. It has been providing post-accelerated RIBs to experimental areas since 2001. Over the last decade, SPIRAL1 has been upgraded to provide beams of condensable elements, by coupling one or several types of TISS emitting 1^+ ions [2] to a charge breeder, to boost the charge state of radioactive ions from 1^+ to n^+ for subsequent post-acceleration.

The charge breeder is a PHOENIX type ECR ion source developed at LPSC and tested at ISOLDE, that was then improved before being installed at SPIRAL1 [3, 4].

Standalone, the Booster device can also produce stable beams of gaseous elements.

A post acceleration of these beams, up to 20 MeV/u, is feasible using the CIME cyclotron [5].

SAGA PROJECT – CIME 0°

Irradiation Station Project

The cyclotron extraction line has to be redesigned to accommodate the SAGA's irradiation station (see Fig. 3).

To allow the use of the beam, from 2026 ideally, some arrangements are necessary for tunings and measurements:

- stripper and collimator to vary the flux and/or the energy,
- diagnostics to measure intensities, alignment, shape and homogeneity of the beam,
- wobbler or high gradient quadrupole to adjust irradiation surface.

The chamber, ending the line, would be equipped with a vacuum-atmospheric pressure window to allow irradiation in both modes: in a vacuum or controlled atmosphere. In consequence, a fast protection valve system has to be developed to ensure the protection of devices and cyclotron in the event of a breakage.

ISBN: 978-3-95450-257-8 ISSN: 2222-5692 doi:10.18429/JACoW-ECRIS2024-MOP13

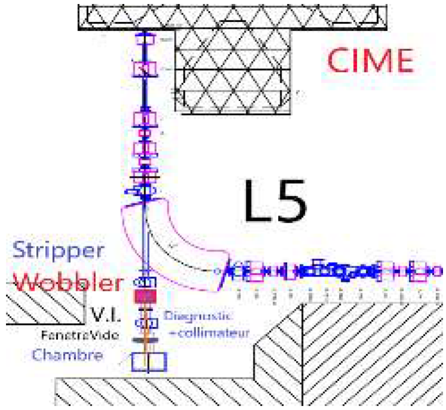

Figure 3: CIME Extraction line and Irradiation station project.

Users Conditions

To meet the requirements for the irradiation of their components, experimenters specified their expectations and the specifications of the beams to be supplied:

- energy beam >12 MeV/u,
- 5 to 10 ions on the largest scale LET,
- intensity >10^4 pps,
- fast beam switch.

LET (Linear Energy Transfer) (Fig. 4) is the amount of energy that an ionizing particle transfers to the material being traversed, per unit of distance. It describes the action of radiation on matter. This parameter depends on the energy beam supplied and the ion chosen.

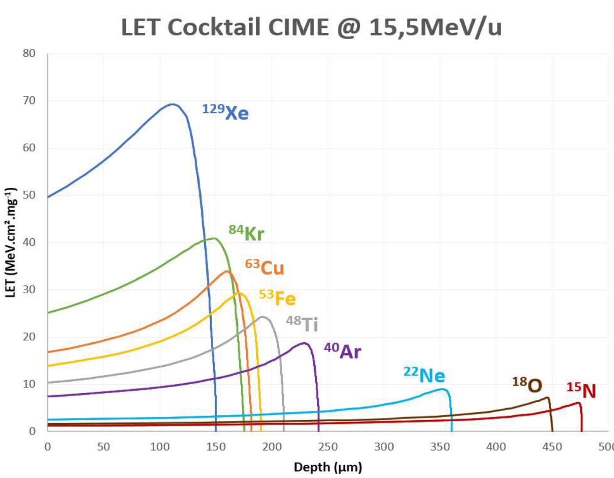

Figure 4: LET for several beams.

Cocktail Beam Proposal

The Accelerators Physic Group and the Target Ion Source Group have jointly established a list of elements that could fulfil the industrials requirements, cyclotron specifications, and Phoenix Booster capacity of production.

This “cocktail beam” combines elements on a large mass scale with a very close A/Q, which avoids repeated adjustments on ion source and extraction line (Figs. 5 and 6). However, the difference of magnetic rigidity between chosen ions is far enough to satisfy the CIME cyclotron resolution.

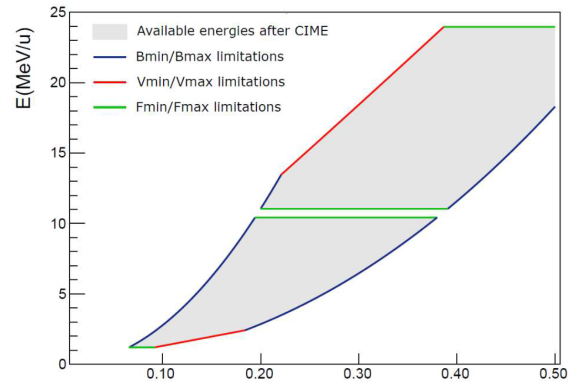

Figure 5: Energies accessible after post-acceleration in CIME as a function of the Q/A ratio. Coloured lines also display the platform limitations in terms of magnetic field, electric field and driving frequency.

	Ions	A/Q	I_{max} Expected (Post-Acceleration)
Energy = 15,5 MeV	$^{15}N^{4+}$	3,750.	10^6pps
	$^{18}O^{5+}$	3,600	>10^8pps
	$^{22}Ne^{6+}$	3,665	10^7pps
	$^{40}Ar^{11+}$	3,632	>10^8pps
	$^{48}Ti^{13+}$	3,682	10^5pps
	$^{56}Fe^{15+}$	3,723	10^6pps
	$^{63}Cu^{17+}$	3,738	10^8pps
	$^{84}Kr^{23+}$	3,643	>> enA
	$^{129}Xe^{35+}$	3,683	10^5pps

Figure 6: Cocktail Beam Proposal for EM 132.

Cyclotron Switch Mode

For the acceleration and extraction of an ion (with q/m ratio), the magnetic field (B) and the HF frequency (F^{RF}) of the cyclotron must be adjusted with great precision, knowing that:

$$q/m = 2\pi[F^{RF}/H]/B^{cyclo}\,, \tag{1}$$

with H as cyclotron harmonics (here $H = 2$ @15.5 MeV/A).

After tuning the ion of reference [q_0/m_0], the switch to an element [q_1/m_1] is therefore obtained by a variation of the RF frequency or of the magnetic field.

The frequency modification requires a scan in position of the HF panels to obtain the resonance. This intervention requires approximately 20-25 minutes and therefore cannot satisfy the switch time requirements.

A variation on cyclotron’s magnetic field (B) below 2 % can be considered without much re-tuning line injection and accelerator. This operation, estimated around 5 minutes, also involves adjusting High-Voltage (V) devices, included Ion Source extraction energy.

Therefore, we obtain:

$$\frac{-(B_1 - B_0)}{B_0} = \frac{Q_1/m_1 - Q_0/m_0)}{Q_0/m_0} = \frac{(V_1 - V_0)}{V_0}\,, \tag{2}$$

$$-\Delta B = \Delta Q/m = \Delta V\,, \tag{3}$$

with ΔB <2 %.

26th Int. Workshop Electron Cyclotron Resonance Ion Sources ECRIS2024, Darmstadt, Germany JACoW Publishing
ISBN: 978-3-95450-257-8 ISSN: 2222-5692 doi:10.18429/JACoW-ECRIS2024-MOP13

COCKTAIL BEAM PRODUCTION

The gaseous elements of the cocktail [Xe, Kr, Ar, Ne, O, N] are produced by injection into the Booster, via the UDV valves and a calibrated leak, or thanks to the residual gases present in the source.

To provide metallic ions, two modifications have been done on the source to allow sputtering method (Fig. 7):

1. The 14 GHz RF Waveguide in Aluminum replaced by a Copper reference. [Cu]
2. A removable rod is install instead of the 8–14 GHz Wave Guide, to fix a sample of the needed metal [Fe, Al, Ag, Ti, ...]

Both elements are insulated and connected to a polarization power supply.

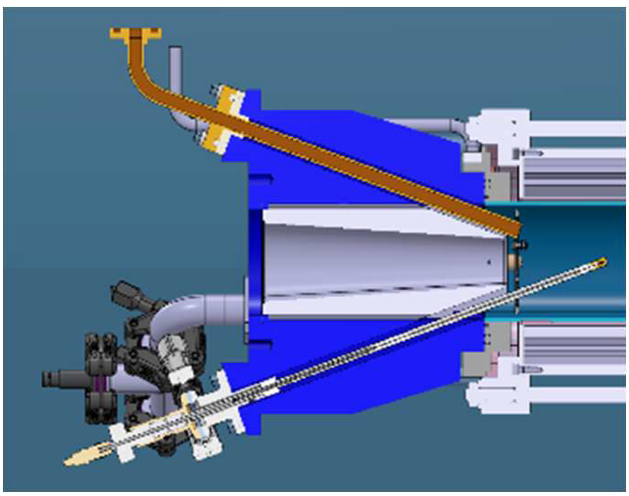

Figure 7: Adaptation of device at injection of charge breeder.

Moreover, some metallic ions are “naturally” produced by sputtering or evaporation of elements located close to the plasma environment (injection nose, plasma electrode, chamber, ...).

Preliminary Tests

Mainly used for charge breeding of 1^+ beams, these preliminary tests consist of checking the functionality of the Booster Phoenix in “ECR Source” mode:

1. after the modifications (waveguide and rod),
2. for the production of cocktail beams (8 to 10 ions) with high extraction voltage (~30 kV),[1]
3. with simultaneous injection of heavy elements [Kr+Xe], to check the respective non-influence on their usual distribution; especially on high charge states.[1]

Concerning point 3, a comparison was carried out between single tuning mode and simultaneous tuning mode.

The respective distributions are shown in Fig. 8 for ^{129}Xe and ^{86}Kr when optimised to a single gas. The results show that the distributions are not significantly affected by the “cocktail” mode (Fig. 9). The maximum charge states for Kr remains around 18^+, while that of Xe is around 26^+.

[1] Conditions required to achieve: post acceleration, energies higher than 12 MeV/A.

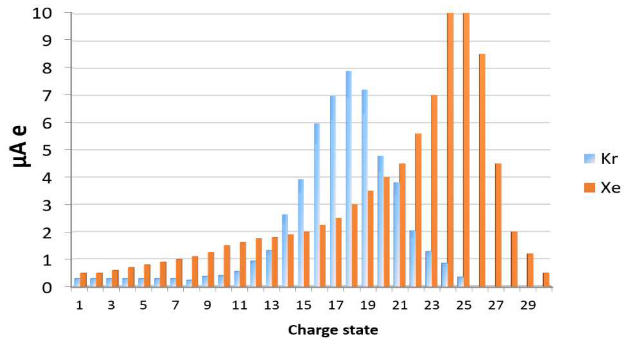

Figure 8: 2018: Booster Phoenix references on ^{129}Xe and ^{86}Kr when it was tuning to optimise single gas.

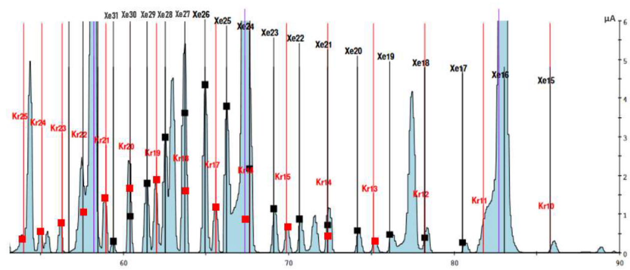

Figure 9: 2024: Distributions of simultaneous ^{129}Xe and ^{86}Kr @31 kV.

The use of the sputtering rod also requires preliminary tests to define the optimal insertion position, relative to the plasma, and the polarization to apply. An incorrect use, which could lead to the contamination of the plasma chamber (deposition on the walls) or even the melting of the sample, would be very critical for the current operation of the Booster with the radioactive beams on SPIRAL1. The 2024 SPIRAL1 planning did not allow to test these points prior to the SAGA experiment. For metallic ions, the strategy is therefore, first, to polarize the waveguide for copper production, and to quantify the rates (post-acceleration) of the elements from the booster parts.

EXPERIMENT RESULTS

Source Settings

Booster parameters for cocktail beam production:

- Gas injection: ^{84}Kr and ^{16}O on UDV valves, ^{129}Xe on calibrated leak,
- High Voltage: 28.37 kV (to reach post-acceleration, a final energy of 15.5 MeV/A),
- RF: 14 GHz (klystron) – power 680 W,
- Magnetic Field (Solenoid coils intensities): Injection 1200 A, Medium 351 A, Extraction 654 A.

The $^{84}Kr^{23+}$, predominant in the cocktail, is used as the reference beam for line transport adjustment and cyclotron tuning (Fig. 10).

From these settings, the theoretical variations are applied to the magnetic field of CIME ($\Delta B*$) and to the high voltages (ΔV), including HV source, to shift on the next element of the cocktail.

ISBN: 978-3-95450-257-8 ISSN: 2222-5692 doi:10.18429/JACoW-ECRIS2024-MOP13

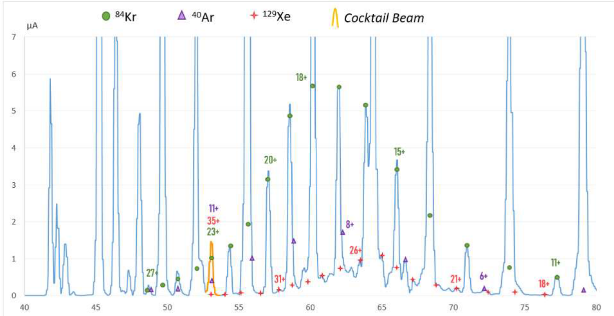

Figure 10: Mass spectra during experiments. In yellow, A/Q used for cocktail beam.

Switch times are recorded and intensities after post-acceleration (Fig. 11) are measured using:

- a faraday cup when I $\geq 10^8$ pps,
- a gas profiler when I $< 10^8$ pps.

	Ions	A/Q	Coeff. for ΔB & ΔV	Switch Time	N_{PPS} (Post-Acceleration)
Energy = 15,5 MeV	$^{84}Kr^{23+}$	*3,643*	*Ref.*		1.10^{10}pps
	$^{40}Ar^{11+}$	3,632	0,997	5 min	2.10^{10}pps
	$^{84}Kr^{23+}$	*3,643*	*Ref.*	5 min	1.10^{10}pps
	$^{22}Ne^{6+}$	1,005	1,005	5 min	2.10^{10}pps
	$^{129}Xe^{35+}$	1,009	1,009	5 min	6.10^{6}pps
	$^{48}Ti^{13+}$	1,011	1,011	5 min	2.10^{5}pps
	$^{63}Cu^{17+}$	1,015	1,015	5 min	2.10^{5}pps
	$^{56}Fe^{15+}$	1,022	1,022	5 min	1.10^{8}pps
	$^{15}N^{4+}$	1,028	1,028	5 min	3.10^{7}pps
	$^{129}Xe^{34+}$	1,039	1,039	10 min	2.10^{6}pps
	$^{27}Al^{7+}$	1,056	1,056	20 min	5.10^{5}pps
	$^{84}Kr^{23+}$	*Ref.*	*Ref.*	25 min	1.10^{6}pps

Figure 11: EM132 SAGA @GANIL – July 2024 : Production rates.

Except for $^{18}O^{5+}$, which is not evaluated regarding its LET proximity with ^{15}N, all elements of the cocktail beam proposal are measured at sufficient rates. Moreover, the switch times between 2 beams, about 5 minutes, are in line with expectations.

Additional test is done to estimate the required delay to switch to an ion whose Q/A implies a greater field variation (Fig. 12). First with $^{129}Xe^{34+}$, needing $\Delta B > 1$ %, intensity is suitable but tuning time doubles. Finally, for $^{27}Al^{7+}$ (metal from the Booster plasma chamber), with $\Delta B \approx 2$ %, the time increases proportionally. These results show that transfer times remain acceptable for industrial applications (~5 min) for magnetic field variations below 1 %.

CONCLUSIONS

GANIL, with its SPIRAL1 facilities (Phoenix Booster + CIME), has the capacity to supply a medium-energy cocktail beam (>12 MeV/A) for industrial applications. The production rates and switching times measured during the EM132 experiment meet initial expectations. The modifications made to the ion source, by replacing the waveguide and installing a sputtering rod, make it possible to produce additional metallic elements.

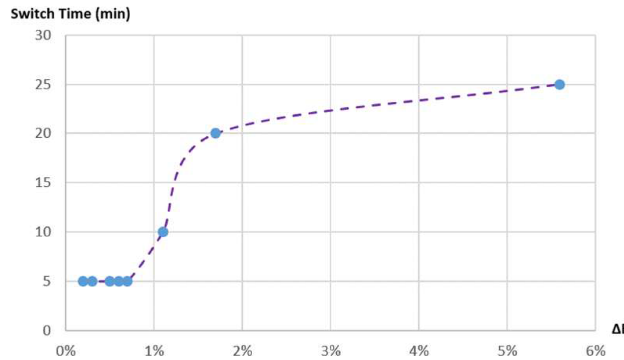

Figure 12: Switch time evolution according to CIME ΔB.

Means of improvement:

- Propose cocktail beams and define the settings for different energies, between 12 and 20 MeV/A),
- Try to produce other elements to extend the coverage of 'missing LET zones', in particular between Kr and Xe (with Ag or Rh, using a sputtering rod).

REFERENCES

[1] A.C.C. Villari, C. Eleon, R. Alves-Condé, J.C. Angelique, C. Barué, C. Canet, M. Dubois, M. Dupuis, J.L. Flambard, G. Gaubert, P. Jardin, N. Lecesne, P. Leherissier, F. Lemagnen, R. Leroy, L. Maunoury, J.Y. Pacquet, F. Pellemoine, M.G. Saint-Laurent, C. Stodel, and J.C. Thomas, "SPIRAL at GANIL: Latest results and plans for the future", *Nucl. Phys. A*, vol. 787, pp. 126–133, 2007. doi:10.1016/j.nuclphysa.2006.12.023

[2] P. Chauveau, J. Angot, V. Bosquet, S. Damoy, P. Delahaye, M. Dubois, R. Frigot, S. Hormigos, P. Jardin, L. Maunoury, C. Michel, and J.-C. Thomas, "Radioactive ion-beam development at SPIRAL1", *J. Phys.: Conf. Ser.*, vol. 2743, p. 012068, 2024. doi:10.1088/1742-6596/2743/1/012068

[3] P. Delahaye, L. Maunoury, and R. Vondrasek, "Charge breeding of light metallic ions: Prospects for SPIRAL", *Nucl. Instrum. Methods Phys. Res., Sect. A*, vol. 693, pp. 104–108, 2012. doi:10.1016/j.nima.2012.07.016

[4] L. Maunoury, P. Delahaye, M. Dubois, J. Angot, P. Sole, O. Bajeat, C. Barton, R. Frigot, A. Jeanne, P. Jardin, O. Kamalou, P. Lecomte, B. Osmond, G. Peschard, T. Lamy, and A. Savalle, "Charge breeder for the SPIRAL1 upgrade: Preliminary results", *Rev. Sci. Instrum.*, vol. 87, p. 02B508, 2015. doi:10.1063/1.4935215

[5] O. Kamalou *et al.*, "GANIL Operation Status and Upgrade of SPIRAL1", in *Proc. Cyclotrons'13*, Vancouver, Canada, Sep. 2013, paper FR1PB04, pp. 470–472.

ISBN: 978-3-95450-257-8 ISSN: 2222-5692 doi:10.18429/JACoW-ECRIS2024-MOP15

STUDY OF NOBLE GAS MEMORY EFFECT OF ECR3 AT ATLAS*

R. Scott†, J. McLain, R. C. Vondrasek, Argonne National Laboratory, Lemont, IL, USA
S. Bhattacharya, M. Paul, Racah Institute of Physics, Hebrew University, Jerusalem, Israel

Abstract

Over the past three decades a portion of the accelerated beam time at the Argonne Tandem Linac Accelerator System (ATLAS) has been reserved for ultra-sensitive detection of argon radioisotopes. A unique noble-gas accelerator mass spectrometry (NOGAMS) technique at ATLAS combines electron cyclotron resonance ion source (ECRIS) positive ion production, acceleration up to ~6 MeV/u and detection methods for separating isobars and other m/q contaminants. The ECR3 ion source was recently chosen for such experiments due to the limited scope of material introduced into the plasma chamber, inferring a lower background production compared to ECR2. A recent ^{39,42}Ar NOGAMS experiment has highlighted a need to understand the beam production of material that is no longer being actively introduced into the ECRIS, known as memory effect. A quantitative study of source memory was performed to determine the decay characteristics of argon in the ECR3 ion source. Results of this study as well as details of setup and operation of ECR3 for NOGAMS experiments are presented.

INTRODUCTION

The ATLAS facility at Argonne National Laboratory has provided heavy ion beams for nuclear physics experiments for over 40 years. ATLAS runs experiments 24 hours a day, 7 days a week with a typical ion beam species change once per week and maintenance time dispersed throughout. The ultra-sensitive noble-gas accelerator mass spectrometry NOGAMS [1,2] technique has been developed and improved at ATLAS over the past 30 years. The technique differs from conventional accelerator mass spectrometry (AMS) which, based on negative ion injection, cannot analyze noble-gas ions. Positive ions are produced from an electron cyclotron resonance ion source (ECRIS) followed by mass/charge (m/q) selection with a dipole magnet, acceleration to ~6 MeV/u using linear accelerator sections and delivery to the gas-filled Enge split-pole spectrograph [3] for ion detection, as well as isobaric and background separation (see Fig. 1).

The first detection of low concentrations of ^{81}Kr and ^{39}Ar at ATLAS occurred in 1992 [4] using the now retired ECR1 [5]. In 2002, ECR2 [6] was used to provide ion beams for ^{39}Ar detection in ocean samples for the study of ocean circulation, allowing smaller sample sizes than those required for low level counting (LLC) [7]. ECR2 was used again in 2015-16 to provide ion beams of low concentration ^{37,39}Ar for a measurement of ^{36}Ar(n,γ)^{37}Ar and ^{38}Ar(n,γ)^{39}Ar neutron-capture cross sections [8]. ECR3 [9] was used for the most recent NOGAMS detection of ^{39,42}Ar in a study of neutron induced reactions at the National Ignition Facility (NIF) [1,10,11]. Parameters of ECR3 operation are discussed later. Table 1 provides a summary of a few of the ion source operating parameters of the mentioned NOGAMS experiments.

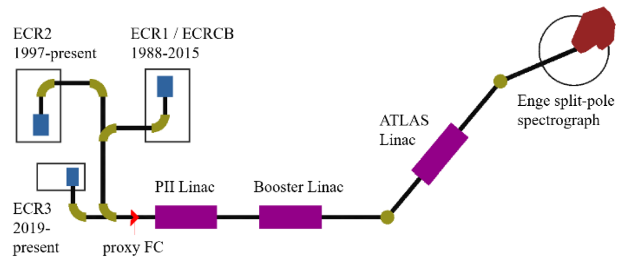

Figure 1: ATLAS accelerator NOGAMS layout.

Part of the recent ECR3 NOGAMS experiment was devoted to detection of ^{42}Ar in a NIF shot gas sample. Prior to running the NIF sample, a sample with a high concentration of ^{42}Ar [12] was used in ECR3 for identification and calibration with the detection system. Unexpected, but verified ^{42}Ar counts were observed with the NIF sample following the calibration run. Ion source memory of the calibration gas was suspected to produce those counts. A study of the ion source memory was performed, replicating the same ion source operating conditions. These results are provided within.

NOGAMS BEAM CONTAMINATION

Early NOGAMS experiments were predicated on a high sensitivity ^{39}Ar/Ar measurement, below naturally occurring Ar (8.1 × 10^{-16}), of multiple samples in ~ one week. A 100 eμA ^{40}Ar^{8+} beam, with a ^{39}Ar/^{40}Ar concentration of 1 × 10^{-17} at the ion source would yield 1 count/hr, assuming a typical 35% transmission from ECRIS Faraday cup (FC) to experimental station. At these low rates, m/q beam contaminants, such as the isobar ^{39}K, can limit the measurement due to pile up at the detector. The work done to reduce ^{39}Ar m/q contamination in ECR2, including quartz liners and cleaning methods, has been presented here [13]. In 2015, higher ^{39}Ar concentration samples ≥ 1 × 10^{-13} were to be measured. Therefore, a lower beam intensity at the ion source could achieve sufficient detection. ECR2 was run at low RF power (22 W) without support gas. With a weaker plasma and less electron interaction with the plasma chamber surfaces, this operation resulted in significantly lower contamination rates of ^{39}K^{8+}, without using any of the previous experiments mitigation methods (see Tables 1, 2).

Based on these results, ECR3 was chosen for the 2021 ^{39}Ar and ^{42}Ar series of experiments. ECR3, which was commissioned at ATLAS in 2019, has no history of solid

*This work was supported by the U.S. Department of Energy, Office of Nuclear Physics, under Contract No. DEAC02-06CH11357 and used resources of ANL's ATLAS facility, an Office of Science User Facility.
† rscott@anl.gov

ISBN: 978-3-95450-257-8 ISSN: 2222-5692 doi:10.18429/JACoW-ECRIS2024-MOP15

Table 1: NOGAMS Operational History at ATLAS

Year Measured	Ion Source	RF Power (W)	Support Gas	Ar Source Intensity (pnA)	Ar Cons. Rate (cc-STP/hr)	Isotopes Detected	Sample Detection Limit
1992	ECR1	105	oxygen	1312	1	^{39}Ar, ^{81}Kr	8×10^{-16}
2003	ECR2	300	nitrogen	13500	0.2	^{39}Ar	4×10^{-17}
2015	ECR2	22	none	250		^{39}Ar	9×10^{-16}
2016	ECR2	50	none	1500		^{37}Ar	
2021	ECR3	6	none	37.5	0.007	^{39}Ar,^{42}Ar	1×10^{-15}
2023	ECR3	7	none	29.4	0.007	^{39}Ar,^{42}Ar	

material introduction, and was expected to have similar or less $^{39}Ar^{8+}$ m/q contamination than ECR2. ECR3 was operated at 7 W in 2023 for the NIF ^{39}Ar and ^{42}Ar detection experiments. Even though ECR3 was run at lower RF power, $^{39}K^{8+}$ contamination rates were twice as high, and $^{34}S^{7+}$ contamination rates were over 100 times higher than when using ECR2 (see Table 2). In both 2015 and 2023, the full contaminant rates were measured with no blocking at the detector. In 2023, with further blocking put in place, 0 cps/µA for ^{39}K and 74 cps/µA were observed with no decrease in the ^{39}Ar rate. Perhaps the larger volume (1.37 l), diameter (7.6 cm) and radial pumping of the plasma chamber of ECR2 compared to ECR3 (0.53 l), (6.4 cm) with pumping only through the extraction hole, play a role in the lower raw potassium rates of ECR2. The larger ECR3 $^{34}S^{7+}$ ($M_0/\delta M$ = 1:270) contamination rates can mostly be explained by the inherently higher m/q discrimination of the ECR2 low energy beamline, when compared to that of ECR3. For ^{42}Ar detection, the isobar ^{42}Ca rate was easily separated at the detector, while $^{63}Cu^{12+}$ was considerably higher but still separated at the detector to provide a clean ^{42}Ar rate.

ECR3 NOGAMS OPERATION

As described for contamination reduction, the ECR3 ion source is run at low RF power, about 7 W, shifting the charge distribution lower than usual operation. The source peaks at 8+ with helium support and 62 W RF power, but peaks at 5+ at 7 W without support gas. Ideally, the charge state with the highest intensity would be used for faster sample concentration measurements. The first accelerating section of ATLAS has a m/q acceptance below 7/1 and the masses to be used for the NIF experiments are 38,39,40, and 42. The charge state $^{42}Ar^{6+}$ falls out of this acceptance, and $^{42}Ar^{7+}$ is inseparable in the accelerator from $^{12}C^{2+}$. This leaves 8+ as the lowest charge state without high intensity m/q contaminants.

Figure 2 shows the simple gas handling system used to feed a sample of interest into the ECR3 ion source. The gas of interest is fed directly into the plasma chamber through the injection side of ECR3 with an Agilent model 9515106 [14] variable leak valve with fine motor control. Gas sample sizes as low as 5 cc-STP can be expected with some samples containing a mixture of known proportions of ^{38}Ar and ^{40}Ar. The smallest sample size can be run multiple hours without a significant enough pressure decrease in the gas line to require a leak valve adjustment to maintain beam intensity, with a maximum consumption rate of 0.007 cc-STP/hr measured for Ar^{8+} at 300 enA.

The sample cylinder change sequence, intended to limit cross contamination of samples is as follows: leave RF on, stop extraction of beam, shut leak and sample cylinder valves, pump-out gas volume with independent pump to millitorr range, and stop pump-out. Then, while continuously purging the volume with boil-off nitrogen from the ATLAS cryogenic system, remove sample cylinder, attach new sample cylinder, stop continuous purge, perform pump-purge cycle on gas volume 10 times ending on pump-out, shut valve leading to pump and purge valves, open leak valve to ECR3 while maintaining a maximum ion source pressure of 2×10^{-7} Torr until leak valve is fully open. When source pressure is below 1.4×10^{-8} Torr (after about 15 min), shut leak valve, open new sample cylinder valve, resume beam extraction, and open leak valve to achieve desired total Ar^{8+} intensity.

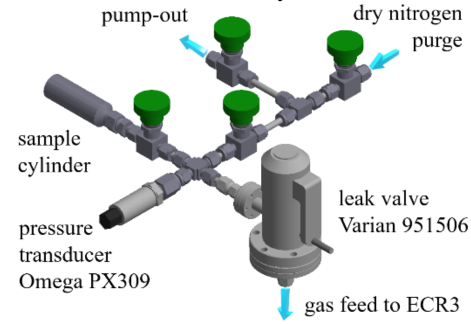

Figure 2: ECR3 NOGAMS gas handling system.

ECR3 ARGON GAS MEMORY EFFECT

ECR ion source memory is described as the continued ion beam production resulting from previous feeding of materials which are no longer being actively introduced into the plasma chamber. For argon gas, the beam intensity will follow a decay curve as residual material is consumed after the leak valve is shut. At the end of a recent NOGAMS experiment, two series of measurements were taken looking for the presence of ^{42}Ar in a sample resulting from neutron-induced reactions on ^{40}Ar seeds at the National Ignition Facility (NIF) [11]. In between these meas-

ISBN: 978-3-95450-257-8 ISSN: 2222-5692 doi:10.18429/JACoW-ECRIS2024-MOP15

Table 2: NOGAMS ^{39}K and ^{34}S Contamination at ATLAS

Ref	Date	Ion Source	ECR Source Ar8+ Intensity (eμA)	39K Detector Rate/Ar Intensity (cps/eμA)	34S Detector Rate/Ar Intensity (cps/eμA)	Configuration
[13]	Jun 2007	ECR2	83	50602		no treatment
[7,13]	Aug 2001	ECR2	75	17333		open quartz liner
[7,13]	May 2002	ECR2	76	129		closed quartz liner
[13]	Jun 2007	ECR2	98	459		ultrapure alum. thin liner
[13]	Apr 2008	ECR2	55	27273		ultrapure alum. coated PC + open quartz + cleaning
[8]	Oct 2015	ECR2	5.5	30	3	low rf power, no support gas
	Oct 2023	ECR3	0.16	66	355	low rf power, no support gas

-urements, a calibration sample with a concentration of 1.6 × 10^{-12} ^{42}Ar/Ar was fed into ECR3 for 4.9 hours to confirm the setting of the spectrograph magnetic field. While the first series detected no presence of ^{42}Ar, the second series detected 4 legitimate ^{42}Ar counts. Even though an added purge with UHP ^{nat}Ar was performed between the calibration and NIF sample change, the four counts can be suspected to be a result of memory effect from running the calibration sample. Investigating the origin of the ^{42}Ar counts was considered important since they would imply a fast two neutron capture process if they originated from the NIF sample.

A quantitative study of source memory was conducted following the experiment, replicating its operating conditions and run sequence. The spectrograph and accelerator were unavailable for this study, so measurement was limited to the FC after m/q separation using the dipole magnet following extraction from ECR3. Highly enriched ^{38}Ar (99.96%) [15] was used as a surrogate for the ^{42}Ar calibration sample, ^{40}Ar (99.99%,^{38}Ar 0.004%) [15] was used to replicate the NIF sample, and the FC was used as a proxy (see Fig. 1) for the detection system. If the ^{38}Ar enriched sample is run with same total Ar beam intensity, running conditions and period as the ^{42}Ar calibration sample, then their decay curves would be the same. The ratio of total ^{42}Ar/^{38}Ar memory ions over a specific period will equal the ratio of the total ions ^{42}cal/^{38}enr measured (normalized for time) prior to decay. This relationship can be expressed as

$$\frac{\Sigma 42_{mem}}{\Sigma 38_{mem}} = \frac{\Sigma 42_{cal}}{\Sigma 38_{enr}} * \frac{t_{38\,enr}}{t_{42cal}} ,$$

where $\Sigma 42_{cal}$ is the number of counts detected from the calibration sample over 4.9hours, and $\Sigma 42_{mem}$ is the expected detector counts from memory after running the calibration sample. Solving for $\Sigma 42_{mem}$ we get

$$\Sigma 42_{mem} = \Sigma 38_{mem} * \frac{\Sigma 42_{cal}}{\Sigma 38_{enr}} * \frac{t_{38\,enr}}{t_{42cal}} .$$

For the memory test, enriched $^{38}Ar^{8+}$ was run and monitored for 4 hours with a beam intensity of 235 enA, equalling the total Ar^{8+} intensity achieved during the experiment. The number of ^{38}Ar ions $\Sigma 38_{enr}$ was derived from the charge current on the FC and the run time. The cylinder sample change sequence described earlier was performed, installing next ^{40}Ar (99.99%) and opening the leak valve to achieve 235 enA of $^{40}Ar^{8+}$. The $^{38}Ar^{8+}$ intensity decay (see Fig. 3) and stable $^{40}Ar^{8+}$ intensity were monitored for the same period as the NIF sample. The number of ^{38}Ar memory ions $\Sigma 38_{mem}$ was derived from the integral sum of beam intensity over the decay period. Assuming no memory effect or background Ar contribution, the enriched ^{40}Ar would yield $^{38}Ar^{8+}$ intensity of 9.4 epA. For the FC measurement a Keithley 6485 digital picoammeter with zero correction was used [16].

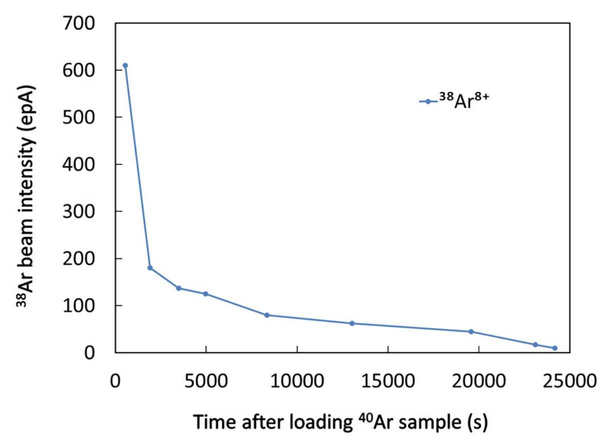

Figure 3: Decay curve of ^{38}Ar on the proxy FC following ECR3 operation with enriched 99.96% ^{38}Ar gas at 235 enA on the same FC.

The resulting value of expected memory counts $\Sigma 42_{mem}$ was 0.8. Based on this estimate (three valid ^{42}Ar counts and one memory count) the ^{42}Ar yield in the NIF sample could be higher than expected. With such low statistics, all 4 counts coming from memory cannot be strictly ruled out, but a proposal for a repeat experiment is justified.

CONCLUSION

NOGAMS experiments at ATLAS have seen a large reduction in beam contamination from background materials using lower RF power from the ECR ion sources with a

ISBN: 978-3-95450-257-8 ISSN: 2222-5692 doi:10.18429/JACoW-ECRIS2024-MOP15

reduced Ar beam intensity that does not affect measurement of ^{39,42}Ar samples with concentrations > 1 × 10^{-15}. ECR3 has recently been used for NOGAMS and has demonstrated higher ^{39}K and ^{34}S contamination rates per eμA of Ar^{8+} ions when compared to ECR2, but rates were still low enough for the ^{39}Ar detection levels needed. Live ^{42}Ar was detected for the first time using NOGAMS at ATLAS from a calibration sample with a ^{42}Ar/Ar concentration of 1.6 × 10^{-12}. A NIF sample installed in ECR3 following the calibration sample resulted in unexpected ^{42}Ar counts. A study was conducted to see if these counts were from source memory, with results indicating some could have come from a higher yield in the NIF sample. ATLAS beam time dedicated to a longer measurement of ^{42}Ar yield in the NIF sample has been requested and approved for November 2024.

ACKNOWLEDGEMENTS

M. Paul gratefully acknowledges support from USA-Israel Binational Science Foundation (grant 2020136) and from Pazy Foundation (Israel) under grant ID231-2020.

REFERENCES

[1] M. Paul *et al.*, "^{40}Ar proposed as probe of neutron-induced reactions in a high-density stellar-like plasma at the National Ignition Facility," *EPJ Web of Conferences*, vol. 279, 13004, 2023. doi:10.1051/epjconf/202327913004

[2] M. Paul *et al.*, "Positive-ion accelerator mass spectrometry at ATLAS: Peaks and pits," *Nucl. Instrum. Methods B*, vol. 456, pp. 222-229, 2019. doi:10.1016/j.nimb.2019.04.003

[3] M. Paul *et al.*, "Heavy ion separation with a gas-filled magnetic spectrograph," *Nucl. Instrum. Methods A*, vol. 277, pp. 418-430, 1989. doi:10.1016/0168-9002(89)90771-7

[4] W. Kutschera *et al.*, "Long-lived noble gas radionuclides," *Nucl. Instrum. Methods B*, vol. 92, pp. 241-248, 1994. doi:10.1016/0168-583X(94)96013-5

[5] R. Pardo, "Operating experience of an ECR ion source on a high voltage platform," *Nucl. Instrum. Methods B*, vol. 40-41, Part 2, pp. 1014-1019, 1989. doi:10.1016/0168-583X(89)90529-6

[6] M. Schlapp *et al.*, "A new 14 GHz Electron-Cyclotron-Resonance Ion Source (ECRIS) for the Heavy Ion Accelerator Facility ATLAS" *Review of Scientific Instruments*, vol. 69, pp. 631-633, 1998. doi:10.1063/1.1148725

[7] P. Collon *et al.*, "Development of an AMS method to study oceanic circulation characteristics using cosmogenic ^{39}Ar," *Nucl. Instrum. Methods B*, vol. 223-224, pp. 428-434, 2004. doi:10.1016/j.nimb.2004.04.081

[8] M. Tessler *et al.*, "Stellar ^{36,38}Ar(n,γ)^{37,39}Ar Reactions and Their Effect on Light Neutron-Rich Nuclide Synthesis," *Phy. Rev. Lett.*, vol. 121, p. 112701, Sep. 2018. doi:10.1103/PhysRevLett.121.112701

[9] R. Scott, R. C. Vondrasek, "ECR3 commissioning and planning for C-14 ion beams at the Argonne Tandem Linac Accelerator System," in *Proc. of the 24th Int. Workshop on ECR Ion Sources (ECRIS2020)*, East Lansing, Michigan, USA, Sep. 2020, pp. 157-159. doi:10.18429/JACoW-ECRIS2020-WEZZO03

[10] L. Callahan *et al.*, "Initial tests of Accelerator Mass Spectrometry with the Argonne Gas-Filled Analyzer and the commissioning of the MONICA detector," *Nucl. Instrum. Methods B*, vol. 532, pp. 7-12, 2022. doi:10.1016/j.nimb.2022.09.009

[11] National Ignition Facility Discovery Program, 2019 Awarded Campaigns, https://lasers.llnl.gov/nif-users/prior-year-awards/2019-awarded-campaigns

[12] R. N. Sahoo *et al.*, "The ^{41}Ar(n,γ)^{42}Ar reaction," *EPJ Web of Conferences*, vol. 284, 01037, 2023. doi:10.1051/epjconf/202328401037

[13] P. Collon, *et al.*, "Reducing potassium contamination for AMS detection of ^{39}Ar with an electron-cyclotron-resonance ion source," *Nucl. Instrum. Methods B*, vol. 283, pp. 77-83, 2012. doi:10.1016/j.nimb.2012.04.020

[14] Agilent Technologies, Inc. Santa Clara, California, USA, http://www.agilent.com

[15] Isoflex USA Ltd., San Francisco, California, USA, http://www.isoflex.com

[16] Tektronix, Inc., Beaverton, Oregon, USA, http://www.tek.com/en/products/keithley

ISBN: 978-3-95450-257-8 ISSN: 2222-5692 doi:10.18429/JACoW-ECRIS2024-TUA1

DESIGN OF A NEW IRON PLUG FOR THE TRIUMF ECRIS CHARGE STATE BOOSTER CONFERENCES*

J. Adegun, F. Ames†, O. Kester, TRIUMF, Vancouver, BC, Canada

Abstract

This paper presents a solution to address the issue of asymmetric dipole fields in the injection region of the TRIUMF electron cyclotron resonance ion source PHOENIX booster. The asymmetric fields arise from a wide gap in the injection soft iron plug of the booster, which allows the connection of the RF waveguide to the plasma chamber. Simulations and experimental measurements have revealed that singly charged ions, injected for charge breeding, experience deflection and get lost due to the asymmetric magnetic fields instead of being effectively captured by the plasma, thereby diminishing the efficiency of the charge state booster. To address this problem, an iron plug with an enlarged inner diameter, which allows the RF waveguide to connect to the plasma chamber, was designed. This redesign necessitated modifications to the injection electrodes and plasma chamber, including repositioning the waveguide and gas-inlet windows. By implementing these changes, the TRIUMF charge state booster is anticipated to achieve efficiency levels comparable to other PHOENIX boosters.

INTRODUCTION

The Electron Cyclotron Resonance Ion Source (ECRIS) has been used at TRIUMF's Isotope Separator and Accelerator (ISAC) facility since 2010 [1] to charge-breed exotic isotopes, particularly those with an atomic mass greater than 30. This is essential to match the mass-to-charge (A/Q) ratio of the linear accelerator (LINAC) before post-acceleration, enabling the use of these isotopes in nuclear physics and astrophysics research. The ECRIS is a highly efficient ion source that operates continuously and can produce highly charged ions at high intensities. It offers several advantages over the electron beam ion source (EBIS), including low-maintenance requirements and a prolonged operational lifespan. Systematic investigations conducted at TRIUMF [2, 3] have shown that the ECRIS charge state booster (CSB) performance can be significantly enhanced by optimizing and improving various components, such as the injection optics, injection system, RF power and frequency, magnetic field, plasma parameters, extraction system and optics. Research activities have commenced at TRIUMF to improve the performance of the CSB based on the results of these investigations. The superior two-frequency heating technique using a single waveguide was recently implemented, and the associated transport optics and the extraction system were optimized. The global efficiency of the booster for cesium charge states between 20^+ and 32^+, increased from 34 % under single-frequency heating operation to 41 % under two-frequency heating [2]. While this improvement is substantial compared to previous performance results, it's important to note that the efficiency still needs to improve compared to other PHOENIX boosters. For instance, the LPSC booster has reported a remarkable global efficiency of up to 92 % [4]. This comparison highlights the potential for further enhancements of the TRIUMF booster. Furthermore, during the systematic investigations, it was discovered that the wide gap created in the injection soft iron plug to connect the waveguide to the plasma chamber creates an asymmetry in the magnetic field in the plasma chamber that steers ions to the electrodes and chamber wall during injection, thus reducing the charge breeding efficiency. To address this problem, a new soft iron plug was designed. The redesign led to modifying the injection electrodes and plasma chamber and repositioning the waveguide and gas-inlet windows. The paper presents the results of designing a new soft iron plug, magnetic field simulation of the CSB, and RF modelling of the plasma chamber without plasma.

THE TRIUMF PHOENIX BOOSTER AND EFFECT OF A GAP IN THE INJECTION SOFT IRON PLUG

The TRIUMF ECRIS PHOENIX booster, initially developed by Pantechnik for single-frequency heating operation at 14.5 GHz, has recently been upgraded to support two-frequency heating using the existing single waveguide. Refer to [2, 3] for detailed information about the two-frequency heating setup. The single charge state efficiency of the CSB under the single-frequency heating operation has been measured up to 8.8 % for $^{133}Cs^{23+}$ and up to 9.1 % for $^{133}Cs^{26+}$ under the two-frequency heating operation [3]. The source utilizes three room-temperature solenoid coils and hexapole permanent magnets to generate axial and radial magnetic field distributions for plasma confinement. ARMCO™ soft iron plugs are installed in the injection and extraction regions to enhance the injection and extraction magnetic fields. However, a wide gap was created in the injection iron plug to allow the waveguide and water cooling lines to be connected to the plasma chamber. Figure 1 shows the injection iron plug as designed by Pantechnik. To investigate the effect of the wide gap, the geometry of the CSB was modelled in OPERA 3D [5], and the trajectories of an ion beam were calculated and visualized using the ray tracing package of the software. The simulations, which considered only the magnetic fields created by the three solenoids and hexapole of the ion source (excluding plasma space charge and electric fields from the injection system), revealed significant beam deflection. Figure 2 shows the trajectories of $^{133}Cs^+$ ion beam, initially travelling parallel to the beam axis. The

* Work supported by NSERC and TRIUMF
† ames@triumf.ca

ISBN: 978-3-95450-257-8 ISSN: 2222-5692 doi:10.18429/JACoW-ECRIS2024-TUA1

beam begins to deviate from its intended path at approximately −300 mm, eventually moving perpendicular to its original direction, indicating the presence of a dipole field near the injection region.

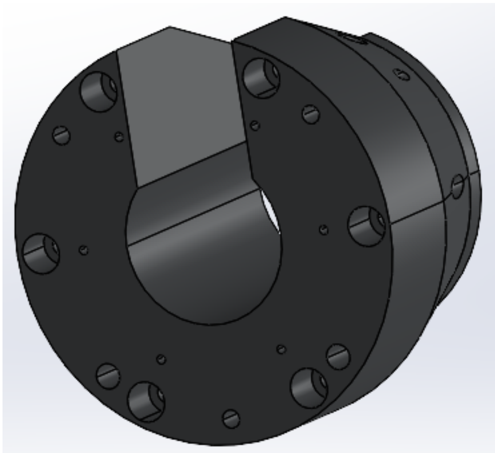

Figure 1: Injection soft iron with a gap to accommodate the RF waveguide to the plasma chamber. It has an inner diameter of 80 mm,outer diameter of 194 mm, and length of 142 mm.

The impact of the dipole field was further confirmed through experimental observations. In the experiment, the plasma was extinguished by switching off the RF power, and the magnetic field in the injection region was switched off while the center and extraction fields remained active. Subsequently, a beam of $^{133}Cs^{+}$ ions with an intensity of approximately 10 nA was injected into the booster. Downstream of the booster, the nearest Faraday cup recorded a current of about 3 nA. However, upon switching on the injection magnetic field, the measured current on the Faraday cup decreased to approximately 0.1 nA, consistent with the simulation results presented in Fig. 2.

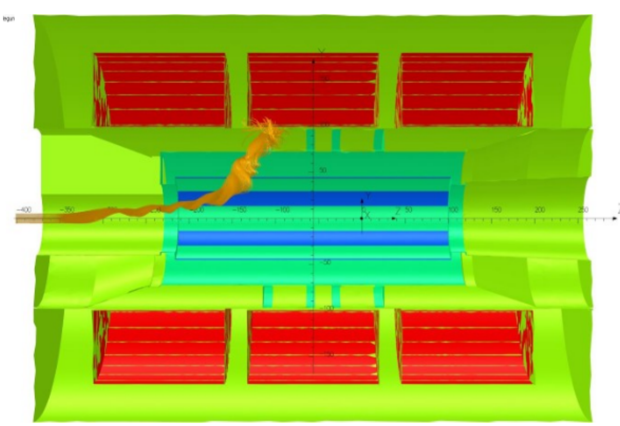

Figure 2: Simulation of ion beam deflection induced by the dipole magnetic field component at the injection region of the TRIUMF CSB. The plots in red are the solenoid coils, while the blue plots are the hexapole magnets.

Further analysis of the measured transverse magnetic fields (B_x and B_y) and the longitudinal field (B_z) around the injection region revealed that the transverse components are not zero (Fig. 3). Particularly, the B_y component (blue plot) peaked at around 1 kG at a distance of −210 mm, representing approximately 10 % of the main B_z field (10 kG). At this location, due to the deceleration caused by the injection electrodes, the injected singly charged ions had low energy (a few tens of eV). If we assume that $^{133}Cs^{+}$ beam has an energy of about 10 eV at this location, then the calculated Larmor radius for 1 kG field is 53 mm, which significantly exceeds the 20 mm aperture of the last injection electrode of the CSB. This suggests significant ion loss during injection, explaining the observed low efficiency compared to the LPSC booster.

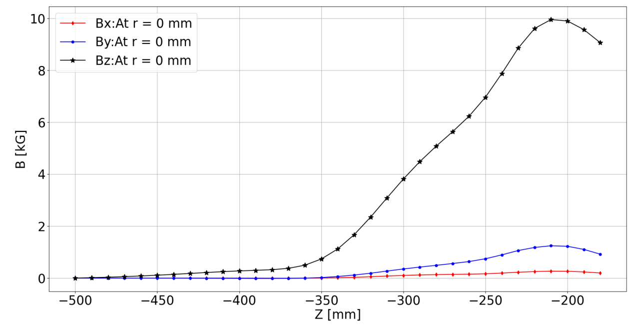

Figure 3: Spatial distribution of magnetic field components around the CSB injection region. The B_y component is up to 1 kG around −210 mm.

DESIGN OF A NEW INJECTION SOFT IRON PLUG

A new soft iron plug has been designed to address the dipole magnetic field component issue at the injection region of the CSB caused by the gap. This was achieved by increasing the inner diameter of the iron from 80 mm to 120 mm, providing sufficient space for the waveguide connection, support gas connector, and cooling line connectors without requiring a gap. Figure 4 presents a 3D drawing of the newly designed soft iron plug. Consequently, the

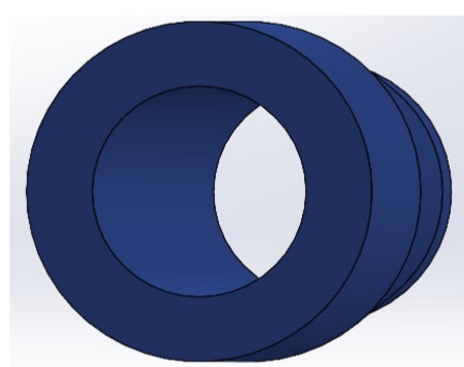

Figure 4: SolidWorks engineering drawing of the newly designed injection soft iron component. It has an inner diameter of 120 mm,outer diameter of 194 mm, and length of 142 mm.

ISBN: 978-3-95450-257-8 ISSN: 2222-5692 doi:10.18429/JACoW-ECRIS2024-TUA1

soft iron plug redesign impacted the injection system and the portion of the plasma chamber where the waveguide is connected, prompting a redesign of these components. It is worth noting that only the portion of the plasma around the injection region was modified. The main chamber where the bulk of the plasma is expected to be confined remains unchanged. The inner diameter of this injection portion of the chamber was reduced from 62 mm to 55 mm to have enough space for the waveguide. Additionally, the waveguide and gas-inlet windows were repositioned during this process. Figure 5 shows a cross-sectional view of the new soft iron plug with the injection electrodes and the injection portion of the plasma chamber.

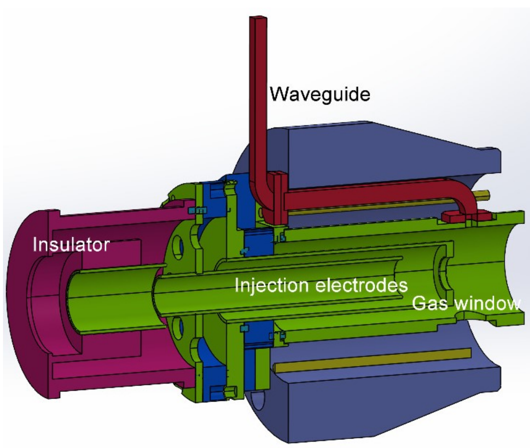

Figure 5: Cross-sectional view illustrating the newly designed injection soft iron component integrated with the redesigned injection system and a segment of the plasma chamber.

DISCUSSION

The CSB was modelled using OPERA 3D software, featuring the newly designed injection iron plug. The magnetic field was calculated, and it was found that increasing the inner diameter of the iron plug increased the air volume around it. This change impacted the magnetic field lines of the solenoid at the injection region. With the original iron plug, a current of 1050 A on the injection solenoid could produce a magnetic field strength of up to 1.0 T at the injection region. However, with the newly designed iron plug, a higher current of about 1107 A was required to achieve the same 1.0 T magnetic field. Fortunately, the power supply of the solenoid coil was rated to supply current up to 1300 A, which allowed for compensation of the reduced magnetic field. As shown in Fig. 6, removing the gap eliminated the transverse asymmetric field, thus preventing deflection of the injected ion beam, in contrast to Fig. 2. Figure 7 compares the transverse fields of the original soft iron design by Pantechnik with the new design. The results indicate that the transverse field associated with the gapped soft iron (blue plot) was eliminated in the new design (green plot).

The modification of the injection region in the plasma chamber necessitated a careful assessment of its impact on

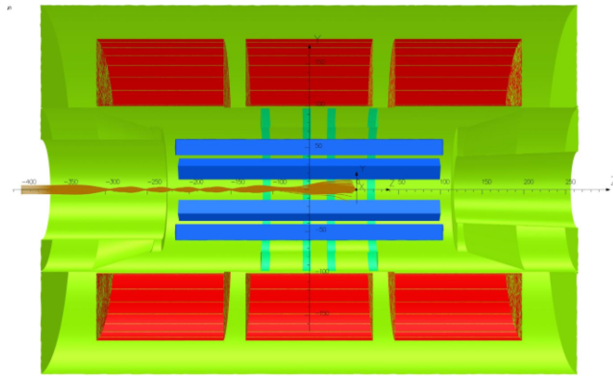

Figure 6: Ion beam trajectories at the injection region of the CSB incorporating the newly designed iron plug. The simulation illustrates how the modified plug influences the beam's path. The plots in red are the solenoid coils, while the blue plots are the hexapole magnets.

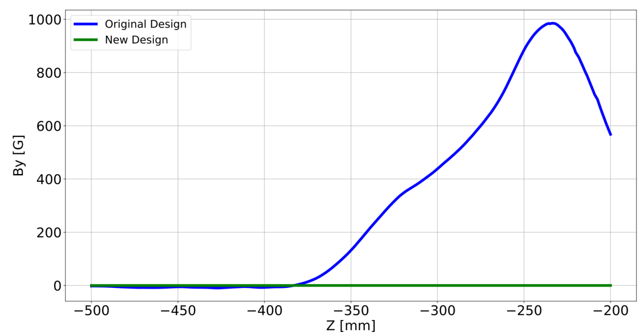

Figure 7: Comparison of the transverse magnetic field (B_y component) at the injection region for two iron plug designs. The blue curve shows the B_y component resulting from the gap in the original Pantechnik-designed iron plug. The green curve shows the elimination of this field when the gap is removed in the new design.

the RF electromagnetic modes essential for plasma heating. Despite the localized changes, their potential effects on the entire system could not be overlooked. To evaluate these effects, the redesigned plasma chamber (without plasma) was modelled using COMSOL multi-physics software [6] to simulate the electromagnetic modes. The original chamber, designed for electromagnetic waves at a frequency of 14.5 GHz, was a reference point for comparison. Simulation results, as illustrated in Fig. 8a, revealed a localized field island at the injection region (around −200 mm) in the original plasma chamber. The electric field in this region does not contribute to plasma heating. Interestingly, this field island disappeared in the modified geometry. This suggests that the changes made to the plasma chamber around the injection region improved wave propagation, resulting in more uniformly distributed modes, as shown in Fig. 8b. These findings indicate that the minor modifications avoided negative impacts on the RF electromagnetic modes and potentially enhanced the overall electromagnetic field distribution in the plasma chamber. This improvement could lead to more efficient plasma heating, which is crucial for increased efficiency.

ISBN: 978-3-95450-257-8 ISSN: 2222-5692 doi:10.18429/JACoW-ECRIS2024-TUA1

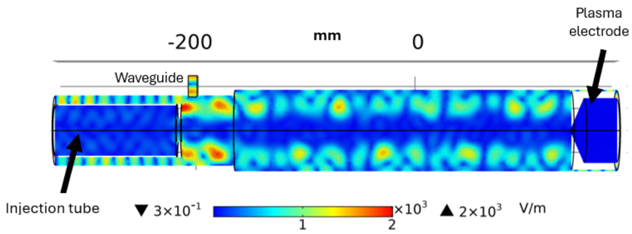

(a) Existing plasma chamber

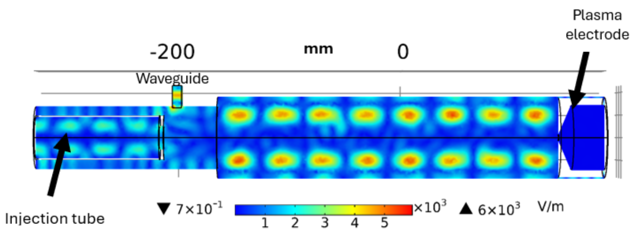

(b) Modified plasma chamber

Figure 8: These figures illustrate electromagnetic wave propagation simulations at 14.5 GHz in two plasma chamber configurations. The left portion of each figure shows the injection tube, while the right depicts the plasma electrode. Electromagnetic waves are launched from a waveguide positioned at the top of the injection tube, approximately −200 mm on the top horizontal axis. The simulations demonstrate that the modified chamber could still excite the modes required to sustain the plasma.

CONCLUSION

The new soft iron plug and other modified components have undergone a design review and are currently being manufactured by Pantechnik. After the modified components are installed, the efficiency of the TRIUMF PHOENIX CSB is expected to improve significantly, bringing the source to the same performance as its counterpart in LPSC.

ACKNOWLEDGEMENTS

The authors would like to express their gratitude for the grant from the Natural Sciences and Engineering Research Council (NSERC) of Canada and the support from TRIUMF.

REFERENCES

[1] F. Ames, R. Baartman, P. Bricault and K. Jayamanna, "Commissioning of the ECRIS Charge State Breeder at TRIUMF", in *Proc. Int. Workshop ECR Ion Sources 2010 (ECRIS'10)*, paper WECOBK01, pp. 178–180, 2010. https://jacow.org/ECRIS2010/papers/wecobk01.pdf

[2] J. Adegun, F. Ames and O. Kester, "Upgrade and Improvement of the TRIUMF ECRIS Charge State Booster", *J. Phys.: Conf. Ser.*, vol. 2743, p. 012 064, 2024. doi:10.1088/1742-6596/2743/1/012064

[3] A. J. Adegun, "Improvement of the Efficiency and Beam Quality of the TRIUMF Charge State Booster", Ph.D. dissertation, University of Victoria, 2023. http://hdl.handle.net/1828/15171

[4] J. Angot, M. Baylac, M. Luntinen, M. Migliore, O. Tarvainen and T. Thuillier, "Recent Developments and Results of the LPSC PHOENIX Type ECR Charge Breeder", *J. Phys.: Conf. Ser.*, vol. 2244, p. 012 063, 2022. doi:10.1088/1742-6596/2244/1/012063

[5] OPERA, *Electromagnetic and Electromechanical Simulation*, Dassault Systèmes, 2021. https://www.3ds.com/products/simulia/opera

[6] *RF Module User's Guide*, COMSOL Multiphysics. https://doc.comsol.com/5.4/doc/com.comsol.help.rf/RFModuleUsersGuide.pdf

ISBN: 978-3-95450-257-8 ISSN: 2222-5692 doi:10.18429/JACoW-ECRIS2024-TUA2

ECR2 PERFORMANCE UPGRADES AT ATLAS

J. McLain†, R. Scott, R. C. Vondrasek,
Argonne National Laboratory, Lemont, IL, 60439, USA

Abstract

The user requests for higher beam energies and intensities have driven the decision to upgrade the ECR2 ion source at the Argonne Tandem Linac Accelerator System. Multiple upgrades are in progress with the expected outcome of dramatically increased ECR2 beam intensities and charge state capabilities. The magnetic upgrades include integrating an improved hexapole permanent magnet array that provides the ion source radial fields, reworking the magnetic materials surrounding the plasma chamber, and installing a new cooling system for the electromagnetic solenoids that govern the ion source axial fields. The new hexapole and higher solenoid magnet operating currents will increase the ion source magnetic fields and support the use of 18GHz RF heating, further increasing the ECR2 beam capabilities. Following these improvements and subsequent source performance, simulations of beam transport devices on the ion source platform will need to be revisited for transmission of high intensity beams. Details of these upgrade projects and simulations of the ion optics are presented.

INTRODUCTION

ECR2 at The Argonne Tandem Linac Accelerator System (ATLAS) was commissioned in 1997 [1] and has since delivered the majority of the delivered ion beams for the internationally supported user facility. The electron cyclotron resonance ion source (ECRIS) has a normal running condition that includes multiple frequency heating of nominally 12 GHz and 14 GHz at powers up to 1100W using frequency generators that feed into traveling tube wave amplifiers (TWTA). The ECR2 configuration includes two water cooled solenoids to produce the axial magnetic fields, an open hexapole permanent magnet assembly to provide the radial magnetic fields in the plasma chamber, and turbomolecular pumps to pump on the plasma chamber, both axially and radially through the open ports in the plasma chamber, made possible with an open hexapole design. Lastly, gaseous material can be easily introduced to the plasma chamber through the vacuum system or solid materials can be introduced radially through the hexapole ports with either an oven or sputter rod that is biased to release material from the probe.

Since 2015, ECR2 was the exclusive ECRIS at ATLAS until the commissioning of ECR3 [2], an entirely permanent magnet ECRIS. This ion source does not have the same level of flexibility that ECR2 leverages for a few reasons. The solenoid magnets are not adjustable, the hexapole is not upgradeable, the plasma chamber has a smaller volume, and there is not radial access to the plasma chamber for material introduction. However, the performance of the ion source is sufficient for many of the requested ion beams at ATLAS, especially the requests for species that can be introduced in gaseous form. For this reason, a two-source dynamic is utilized to allow for both ion sources to be properly maintained and consistently upgraded without jeopardizing the beam hours that the facility delivers annually.

The ATLAS facility continues to make improvements, including the capabilities of the superconducting linac and target stations. The beam requests for higher energies and intensities have followed suit. Although the ion sources have been able to keep up with the requests, there are an increasing number of requests that exceed the capabilities of even ECR2 in its current configuration. It is decided to upgrade ECR2 to produce these increasingly difficult beams. The plan is to support 18 GHz operation of ECR2 while keeping a room temperature design [3]. Other facilities' results from similar upgrades [4,5,6,7] would all achieve the intensities that are needed, further justifying that this path forward will meet our operational goals of doubling the intensities that we currently produce. The upgrade projects that are needed to support this goal were a redesign of the hexapole permanent magnet array and corresponding plasma chamber, an improvement of the magnetic materials surrounding the plasma chamber, a solenoid magnet cooling upgrade, and an improvement of the transport capabilities of the ion beam directly downstream of ECR2.

MAGNETIC UPGRADES

The first and most complicated technical upgrade needed is the hexapole magnet array. The same hexapole has been used in ECR2 since 2005 and produces a simulated B_{rad} of 0.98 T. For this reason, ECR2 typically runs at 14 GHz for peak performance but would not be able to run at 18 GHz. A hexapole upgrade that could produce a B_{rad} of 1.18 T would optimize performance at 14.5 GHz and support operation of an 18 GHz driving frequency. To satisfy the ECRIS scaling laws, the axial magnetic fields must also increase. The extraction iron was modified slightly, and the injection iron was upgraded to incorporate a vanadium permendur cap and a thinner boron nitride insulation disk behind the biased disk, bringing the iron closer to the plasma chamber. Figure 1 shows the upgraded axial magnetic field from these modifications with the solenoid magnets set at 500A each.

* This work was supported by the U.S. Department of Energy, Office of Nuclear Physics, under Contract No. DEAC02-06CH11357 and used resources of ANL's ATLAS facility, an Office of Science User Facility.
† jmclain@anl.gov

ISBN: 978-3-95450-257-8 ISSN: 2222-5692 doi:10.18429/JACoW-ECRIS2024-TUA2

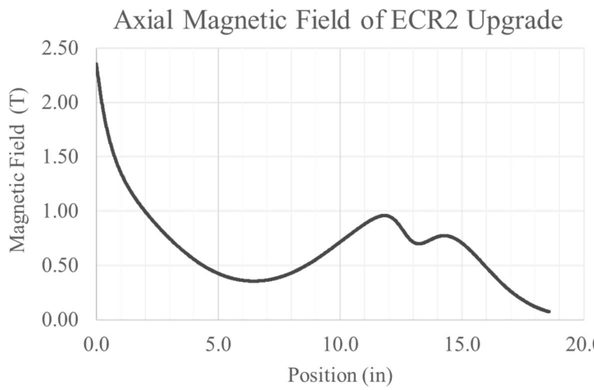

Figure 1: Axial magnetic field profile of the ECR2 upgrade.

The pre-upgrade hexapole incorporated 6 magnet bars, each with two segments. The upgrade hexapole magnet bars make use of 4 segments per bar with a new magnetization vector configuration and have a larger total volume than the previous version of the hexapole [3]. The new hexapole was originally considered using the same material as is currently used and yielded a 3D simulated B_{rad} of 1.18 T, but the risks associated with demagnetization were considered too high to move forward with the material. Additional materials were considered, and demagnetization analysis was completed for a new material, Vacodym 745 HR with a surface diffusion treatment of Vacodym 745 DHR [8]. The results yielded similar magnetic fields as the current material, but the demagnetization fields are far less concerning. Table 1 shows a comparison between the old hexapole and the upgrade hexapole.

Table 1: Magnetic Parameters of the ECR2 Upgrade

Parameter	Current	Upgrade
B_{inj}	1.85 T	2.44 T
B_{min}	0.34 T	0.36 T
B_{ext}	0.92 T	1.00 T
B_{last}	0.85 T	1.00 T
Coil currents	500 A / 500 A	525 / 525 A
B_{rad}	0.98 T	1.18 T
Plasma chamber radius	38.1 mm	38.1 mm
Plasma chamber length	297 mm	297 mm
Hexapole inner radius	42.4 mm	42.4 mm
Hexapole outer radius	74.7 mm	79.7 mm

SUPPORTING UPGRADES

To supplement the magnetic redesign work, components surrounding the plasma chamber needed to be revisited and redesigned. The first modification that was made accommodated a larger magnet volume. The plasma chamber outer diameter was expanded by 0.5 inches. Next, the cooling channels within the plasma chamber were updated. After having difficulty with consistent hermetic welds on the aluminum plasma chamber base, it was decided to explore alternative options that would decrease the risk of a leaking aluminum weld. The plasma chamber design retained the aluminum construction for the plasma facing surface and through the bulk of the material that was designed to conductively cool the plasma chamber and the magnet bars. The decision that would yield a higher success rate for these hermetic welds was the application of explosion bonding the aluminum body of the plasma chamber to a stainless-steel endcap. The stainless-steel endcap encompasses all the welds to ensure a high success rate of hermeticity, leveraging the experience of the machinists with stainless steel welding. Figure 2 highlights the transition region between the aluminum and stainless steel after explosion bonding the two materials.

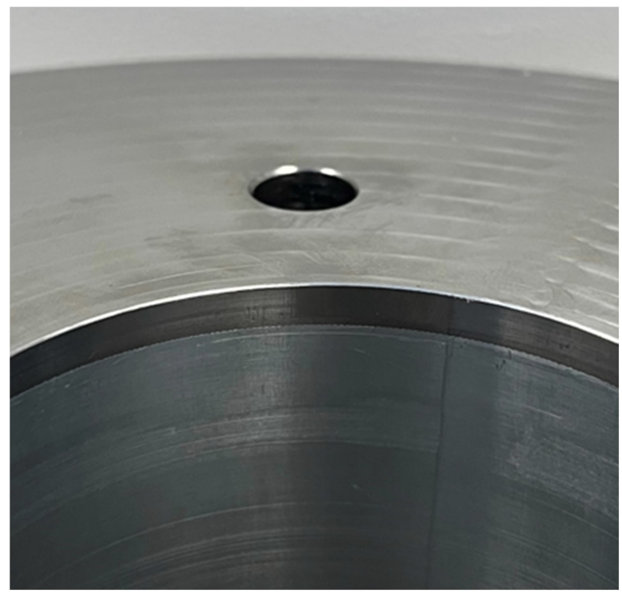

Figure 2: Aluminum and stainless-steel explosion bonded together.

With this new plasma chamber that is slightly larger than the original design, the high voltage insulation must be revisited. ECR2 has incorporated CPVC as a main insulating material since its inception and will continue to use it for its standoff capabilities and mechanical strength. A new CPVC tube and ring will be used around the extraction assembly to support the extraction region hardware as well as serve as the main high voltage standoff between the plasma chamber and the ground potential electrodes of ECR2. Additionally, an aluminum oxide insulator will be used to similarly standoff the plasma chamber potential from other nearby components at ground potential, as well as provide a vacuum sealing surface with two o-rings.

Finally, to support operation of the solenoid electromagnets on the injection and extraction sides of the ion source at higher currents than we are currently capable of, a deionized water system upgrade is being installed. The solenoid magnets are actively water cooled, but do not receive sufficient cooling to operate higher than 475A with their present cooling system. The upgraded water skid will be capable of supplying the required cooling for the upgrade

26th Int. Workshop Electron Cyclotron Resonance Ion Sources ECRIS2024, Darmstadt, Germany JACoW Publishing
ISBN: 978-3-95450-257-8 ISSN: 2222-5692 doi:10.18429/JACoW-ECRIS2024-TUA2

that will require the solenoids to run up to 550A to achieve the fields needed for 18GHz operation.

ION BEAM TRANSPORT

The present ECR2 intensities do not pose any beam transport issues with the use of a glaser solenoid optical device and simple magnetic steerers in the beamline directly downstream of the extracted ion beam. Simulations of the ion beam transport were carried out in IGUN and show that up to 100% of the ion beam is transported to the first faraday cup after the analyzing dipole magnet for 100uA of 16/4+. An additional simulation at 1 mA, seen in Fig. 3, showed 81% transmission to the faraday cup with much of the lost beam being lost in a long drift space after the analyzing magnet but before the faraday cup. From top to bottom shows the simulation from extraction to the faraday cup.

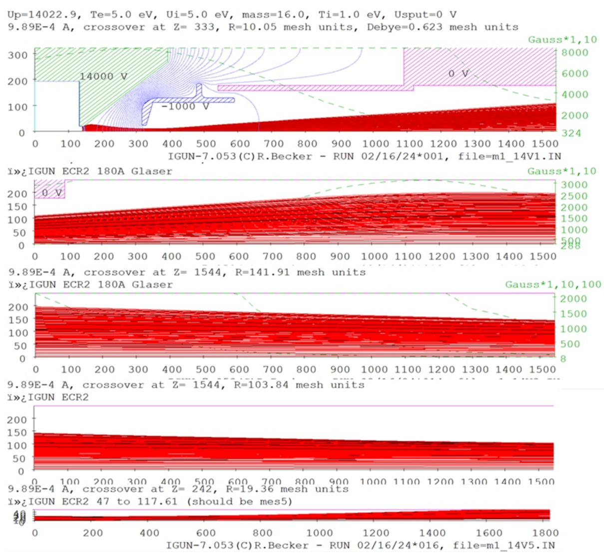

Figure 3: Beam transport from source to the first faraday cup after the analyzing magnet.

A simple solution of adding an einzel lens in the drift space before the analyzing magnet allowed for the 81% transmission to increase to 100%. Then, the extraction voltage was increased from 14 kV to 20 kV, and the beam current was increased to 3mA. Without the use of the einzel lens at 11 kV, the transmission was 44%. However, this increased to 100% with the einzel lens contribution. With the intensity improvements of this ECR2 upgrade, it is expected that the extraction potential will need to increase and the einzel lens will need to be added to the beamline to maximize the deliverable intensities for the ATLAS program. Figure 4 shows the simulation with the expected operational conditions after the ECR2 upgrade.

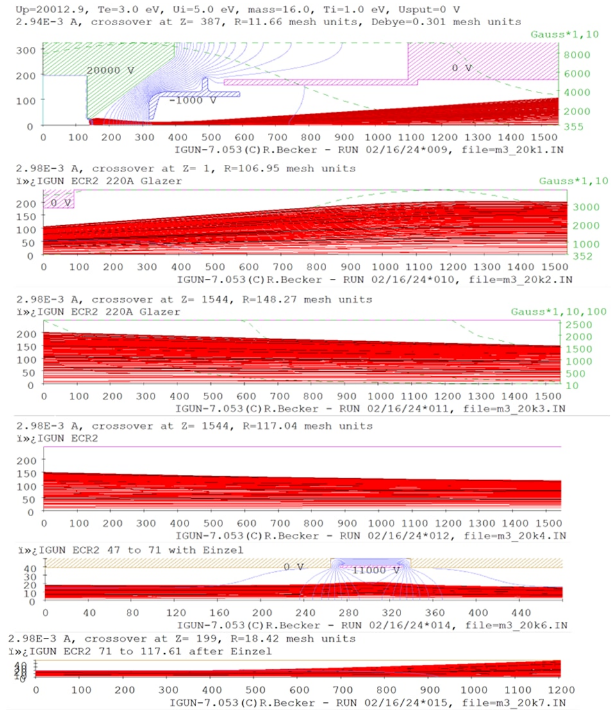

Figure 4: Beam transport from source to the first faraday cup after the analyzing magnet with the added einzel lens, increased intensity, and increased extraction potential.

CONCLUSION

ATLAS is continuing to improve the experimental areas and linac capabilities, which in turn attracts new users and experiments. These new experiments require higher beam intensities and energies, which demand higher charge states than ECR2 can produce. To provide these intensities and charge states for the facility's future, ECR2 must undergo an upgrade. This upgrade will increase the operating frequency of the ECRIS to 18 GHz, which has yielded sufficient increases in intensity and charge state at other facilities. The radial and axial magnetic fields are redesigned to accommodate 18 GHz operation. A completely new hexapole is designed for the radial fields, whereas the axial fields leverage vanadium permendur's high magnetic permeability and saturation flux density to produce the 18 GHz fields. The supplemental subsystems of ECR2 were all reevaluated and modified as needed including the plasma chamber, the cooling water skid, the high voltage insulation, and beam transport. This upgrade is expected to be capable of producing all the ion beams that are required for the upcoming experiments at ATLAS.

REFERENCES

[1] M. Schlapp, R. C. Pardo, R. C. Vondrasek, J. Szczech, P. J. Billquist, J. Vieregg, Z. Q. Xie, C. M. Lyneis, R. Harkewicz, "A new 14 GHz electron-cyclotron-resonance ion source for the heavy ion accelerator facility ATLAS", *Rev. Sci. Instrum.*, vol. 69 (2), p. 631–633, 1 February 1998. doi:10.1063/1.1148725

ISBN: 978-3-95450-257-8 ISSN: 2222-5692 doi:10.18429/JACoW-ECRIS2024-TUA2

[2] R H Scott *et al.*, "Production of C-14 and stable ion beams at the Argonne Tandem Linac Accelerator System with the ECR3 ion source", *J. Phys.: Conf. Ser.*, vol 2244, p. 012068, 2022. doi:10.1088/1742-6596/2244/1/012068

[3] R. C. Vondrasek *et al.*, "Design for an 18 GHz Open Hexapole Electron Cyclotron Resonance Ion Source", *J. Phys.: Conf. Ser.*, vol. 2743, p. 012044, 2024. doi:10.1088/1742-6596/2743/1/012044

[4] D. Hitz, A. Girard, K. Serebrennikov, G. Melin, D. Cormier, J. M. Mathonnet, J. Chartier, L. Sun, J. P. Briand, M. Benhachoum; "Production of highly charged ion beams with the Grenoble test electron cyclotron resonance ion source (plenary)", *Rev. Sci. Instrum.*; vol 75 (5), p. 1403–1406, 1 May 2004. doi:10.1063/1.1675930

[5] A. Kitagawa, M. Muramatsu, S. Yamada, T. Okada, M. Yamamoto, K. Uno, S. Biri, J. Vamosi, X. H. Zhou; "Development of 18 GHz electron cyclotron resonance ion source with high-voltage extraction configuration", *Rev. Sci. Instrum*, vol 69 (2), p. 674–676, 1 February 1998. doi:10.1063/1.1148589

[6] S. Biri, T. Nakagawa, M. Kidera, Y. Miyazawa, M. Hemmi, T. Chiba, N. Inabe, M. Kase, T. Kageyama, O. Kamigaito, A. Goto, Y. Yano, "Production of highly charged ions in the RIKEN 18 GHz ECR ion source using an electrode in two modes", *Nuclear Instruments and Methods in Physics Research Section B.*, vol. 152, p. 386-396, May 1999. doi:10.1016/S0168-583X(98)00971-9

[7] H. Koivisto, A. Ikonen, T. Kalvas, S. Kosonen, R. Kronholm, M. Marttinen, O. Tarvainen, V. Toivanen; "A new 18 GHz room temperature electron cyclotron resonance ion source for highly charged ion beams", *Rev. Sci. Instrum.*, vol. 91 (2), p. 023303, 1 February 2020. doi:10.1063/1.5128860

[8] J. McLain, R. Scott, R. C. Vondrasek, "Demagnetization analysis of the room temperature ECR2 hexapole magnet upgrade", Manuscript submitted for publication. (2024)

ISBN: 978-3-95450-257-8 ISSN: 2222-5692 doi:10.18429/JACoW-ECRIS2024-TUB1

PROGRESS IN 3D SELF-CONSISTENT FULL WAVE-PIC MODELLING OF SPACE RESOLVED ECR PLASMA PROPERTIES

A. Pidatella*, G. S. Mauro, B. Mishra, E. Naselli, G. Torrisi, D. Mascali
Istituto Nazionale di Fisica Nucleare - Laboratori Nazionali del Sud, Catania, Italy
A. Galatà, C. S. Gallo
Istituto Nazionale di Fisica Nucleare - Laboratori Nazionali di Legnaro, Legnaro, Italy

Abstract

We present updates of a simulation suite to model in-plasma ion-electron dynamics, including self-consistent electromagnetic (EM) wave propagation and population kinetics to study atomic processes in ECR plasmas. The EM absorption is modelled by a heuristic collisional term in the cold dielectric tensor. The tool calculates steady-state particle distributions via a full-wave Particle-In-Cell code and solves for collisional-radiative process giving atomic and charge state distributions (CSD). The scheme is general and applicable to many physics' cases of interest for the ECRIS community, including the build-up of the CSD and the plasma emitted X-ray and optical radiation. We present the code's last updates and future perspectives, using as a case-study the PANDORA scenario. We report about studying in-plasma dynamics of injected metallic species and radioisotopes ionisation efficiencies for different injection conditions and plasma parameters. The code is capable of reconstructing space-resolved plasma emissivity comparable to measurements and modelling plasma-induced modification of radioactivity.

INTRODUCTION

Electron cyclotron resonance ion sources (ECRIS) are widely used in accelerator facilities around the world to provide high current ion beams with charge states tuned according to experimental requirements. They operate on the dual concept of resonance heating with microwaves and magnetic confinement using a min-B profile that generates a compact and dense plasma composed of energetic electrons and multi-charged ions. In a complementary way, ECR ion trap can be also serve as a facility resembling stellar plasma conditions, useful for performing interdisciplinary experiments interesting for nuclear physics, atomic physics and astrophysics [1]. While operational ECRIS are often designed using empirical scaling laws [2], the physics of plasma leading the ion generation process as well as the charged particles' dynamics in it is really intricate due to the multi-physics interactions between static and dynamic electromagnetic fields and particles. Simulations are a powerful tool to investigate the microscopic structure of ECR plasma and improve our fundamental understanding of these devices thereof. In the following, various aspects of space-resolved 3D full-wave Particle-In-Cell (PIC) model developed to study the ECR plasma properties and therein particle interactions are presented in detail. The description of the code will follow a schematic simulation pipeline: a first-level high-precision input given in terms of steady-state electrons distributions in the simulation domain; in cascade, a second-level input will be given by computing steady-state ion charge distribution in plasma imposed by the pre-simulated electron dynamics; finally, external neutral/charged particles interaction with the electron/ion distributions is studied aiming at reconstructing their in-plasma reactions.

PLASMA ELECTRONS DYNAMIC SIMULATIONS

The ground level of the 3D full-wave electron PIC code is a set of routines employing MATLAB© as a particle pusher and COMSOL Multiphysics© as a FEM solver to generate 3D profiles of electron density (n_e) and average energy (E_e) self-consistent with EM field distribution [3, 4]. The electrons simulation implies a looped scheme where initial macro-particles are first moved and energised by the EM field distribution of the microwaves injected into the vacuum chamber, generating a first density profile based on the dielectric tensor treatment in *cold* plasma approximation. Then, fields are recalculated based on the updated electron density, including long-range Coulomb collisions for catching both particles' deterministic frictions and random diffusion, till convergence between the particle and field profiles is reached. A flowchart representing the simulation scheme is shown in Fig. 1(a). The algorithm has been applied to various types of ECRIS configurations [5–8], and is an excellent tool to produce space- and energy-resolved distributions of n_e and E_e. Figure 1(b-c) shows a comparison of E_e obtained from the simulations of a 14.28 GHz, 200 W ECRIS operational at ATOMKI, Debrecen and of a 14.428 GHz, 100 W ECRIS operations at INFN-LNL, Legnaro, hereafter LEGIS. In both ECRIS distributions are strongly space-dependent, owing to differences in shape and size of the plasma chamber, microwave frequency and power. The data in these plots represent the source maps which form the basis of ion dynamics calculations. We have recently attempted to overcome the *cold* plasma approximation in the EM wave damping in plasma. Preliminary results of the developed 1D semi-analytical model of EM wave propagation including a *hot* tensor plasma response have been presented. The study allowed to investigate on the coupling of antenna-generated 60 MHz fast X-waves to realistic plasma fusion scenario within the Divertor Tokamak Test (DTT) project. Considering linearised Vlasov-Maxwell equations, stationary and

* pidatella@lns.infn.it

ISBN: 978-3-95450-257-8 ISSN: 2222-5692 doi:10.18429/JACoW-ECRIS2024-TUB1

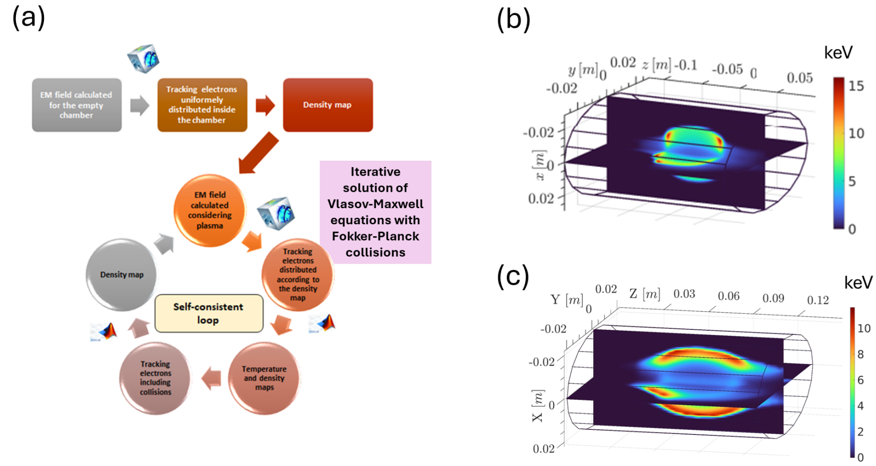

Figure 1: Schematic PIC loop for electrons (a). Electron mean energy [keV] 3D distributions for the ATOMKI ECRIS (Debrecen, Hungary) at 14.28 GHz and 200 W of RF power (b) and the LEGIS ECRIS (Legnaro, Italy) at 14.428 GHz and 100 W of RF power (c).

homogeneous plasma, with no strong EM perturbations, and in a collision-less scenario, we could model the electron Landau damping of the wave imposed by the expected plasma profile. Details can be found in Ref. [9]. Efforts to adapt the hot tensor description in ECR plasma-based devices are ongoing.

PLASMA IONS DYNAMIC SIMULATIONS

The second level of simulations allows to model ECR plasma ions properties using a PIC Monte Carlo (MC) code which takes as input steady state n_e and E_e maps from electron PIC outputs to compute the corresponding steady-state ion maps, based on the following ion balance equation:

$$\frac{\dot{n}_i}{n_e} = n_{i-1}\gamma_{i-1,i} - n_i\gamma_{i,i+1} + n_{i+1} n E_{i+1,i} - n_i n E_{i,i-1} - \frac{n_i}{n_e \tau_i} ,$$

with n_i the ion number density of charge state i, γ the electron impact (EI) ionisation rate, $n = n_0/n_e$ the neutral gas over electron density ratio, E the single-electron charge exchange (CEX) rate, and τ_i the characteristic confinement time of the charge state.

The flowchart representing the PIC-MC simulation scheme is shown in Fig. 2. For each charge state i, N representative macro-particles are sampled according to an ionisation map and moved in a collisional plasma. During their transport, EI and CEX ionisation are considered via MC routine, and the trajectories of remaining particles mapped to occupation maps. At intermediate time steps, accumulated maps are extracted, properly scaled to charge density maps, solving via the Poisson equation for the local charge unbalance imposed by the self-built up electron and charge-state distribution (CSD). The solution will provide the self-generated electric potential map, thus the related electrostatic field components acting to equilibrate the charge unbalance and serving to the formation of the well-known *double-layer* (DL) confinement close to the ECR surface. At the end of the PIC simulation for each i, occupation maps are converted into density maps using charge neutrality and

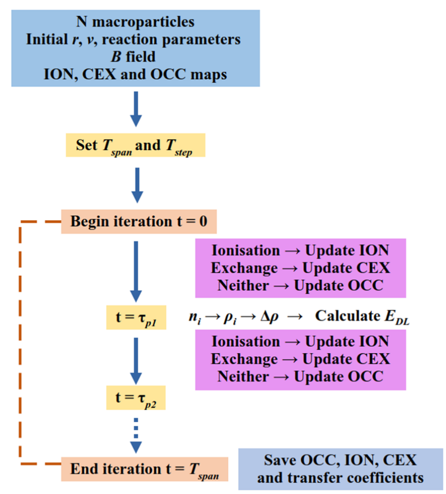

Figure 2: Schematic of PIC-MC loop for ions.

a proper scaling accounting for all the forward (backward) atomic processes in the CSD built-up.

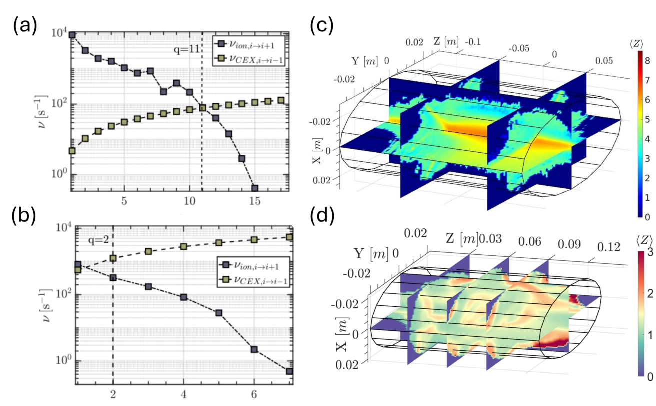

Figure 3: Volume averaged reaction frequencies for EI and CEX process as function of the charge state q for ATOMKI (a) and Legnaro (b) ECRIS. Mean charge distributions for Argon (c) and Oxygen (d) buffer ions in ATOMKI and Legnaro, respectively.

ISBN: 978-3-95450-257-8 ISSN: 2222-5692 doi:10.18429/JACoW-ECRIS2024-TUB1

This allows to generate the CSD which converges to the true steady-state value as more charge states are simulated. An example of the utility of the PIC-MC code can be seen in Fig. 3(a-b) which shows the EI/CEX average reaction frequencies vs. q charge state for Ar (O) buffer ions for ATOMKI (LEGIS) ECR sources, respectively, corresponding to E_e shown in Fig. 1(b-c). Not only the different gas species plays a role in a different trend of reactions as a function of q, but also the different operative conditions (RF power, gas pressure, geometry, frequency) impact on the q where one of the processes overcomes the other. Such predictions might help ECRIS operators in fine-tuning the CSD accordingly to the expected atomic physics occurring in plasma. In Fig. 3(c-d) the different mean-charge distributions are shown for ATOMKI and LEGIS, respectively. More details on the algorithm, its various components and conclusive results are present in Ref. [4]. Experimental benchmark of the ion dynamics from PIC-MC simulations can be provided by comparing the predicted ion current as a function of charge state (current profile) with its counterpart read at the Faraday cup. The ion density n_i is the given input, then the simulated extracted current is given by:

$$I_i = \kappa \frac{LS\langle n_i \rangle q_i e}{\tau_i}\ , \tag{1}$$

with κ the transmission factor, L is the semi-plasma length and S is the area of the extraction hole. A critical parameter in Eq. (1) is the confinement time τ_i given as the reciprocal sum of *ambipolar diffusion* and *electrostatic confinement* time. The latter arises from the electrostatic DL

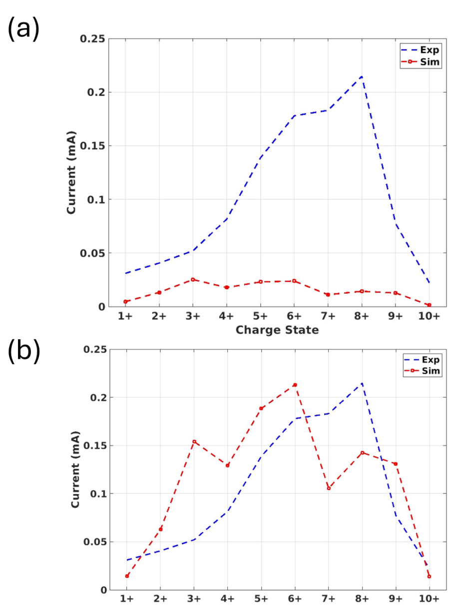

Figure 4: Experimental vs. simulated extracted ion beam current for the ATOMKI ECRIS, including only ambipolar diffusion (a) or both ambipolar and electrostatic confinement (b).

self-generated in the PIC-MC simulation and predicted to exist in ECR plasma [10]. Figure 4 shows a comparison of the current profile extracted from the ATOMKI ECRIS and that simulated using the PIC-MC code and Eq. (1). As can be observed, the general trends and overall magnitude of the current are decently reproduced only if the electrostatic confinement (in Fig. 4(b) is included in the confinement time, underlining the reliability of the model usable to predict ion beam currents in other ECRIS designs.

IN-PLASMA DYNAMICS OF INJECTED RADIOISOTOPES: STUDY OF IONISATION AND NUCLEAR DECAY RATES

In the upcoming years a new facility currently under construction at the INFN-LNS in Catania, Italy, will be available to perform in-plasma inter-disciplinary experiments. The PANDORA facility [1] aims to use a compact and high-energy density ECR magnetoplasma as a stellar emulator for in-plasma measurement of nuclear decay rates and heavy element opacity. Both these quantities depend on ion CSD and electron properties [11, 12] and which are expected to vary strongly in the plasma. Here we present two applications of interest for the PANDORA physics cases of the PIC-MC simulation tool described in the previous sections. Plasma-induced decay rate modification is a cornerstone of the PANDORA facility. In-plasma β-decay rates are given by $\lambda^* = (\ln 2/ft) f^*$ where ft is related to the nuclear matrix element of the decay, according to the Fermi theory of the nuclear decay, and f^* is the lepton phase volume calculated in the plasma. Accordingly to Ref. [11], the in-plasma decay rate can be strongly influenced by the presence of empty atomic inner shells, entering in the so-called *bound-state* β decays (e^- emitted in a bound free shell) or decaying via *orbital electron capture* (picking up e^- from bound electrons in the inner shells).

Such dependency is therefore strongly connected to the in-plasma CSD and atomic level population, biased by the thermodynamics of the radioactive isotope in plasma and the ongoing atomic processes (ionisations and excitations). The probability distribution of the radioactive ions in the plasma and can be calculated using the ion PIC-MC code with an extended balance equation including all collisional and radiative processes [13]. The application of this method can be seen in Fig. 5(c-d) which shows the ^{7}Be mean-charge distribution following the ionisation dynamics after injection of ^{7}Be^{1+} in the LEGIS plasma oxygen at 5×10^{-5} mbar pressure (c) and the related 3D variation (up to 50 %) in the electron capture half-life $t_{1/2}$ of ^{7}Be ions (terrestrial $t_{1/2} \sim 55$ days), as expected from theoretical calculations [14]. The ^{7}Be decay into ^{7}Li via electron capture is one of the PANDORA physics cases, interesting for the cosmological lithium problem and for its impact on the primordial nucleosynthesis. Another interesting case is the ^{134}Cs isotope (terrestrial $t_{1/2} \sim 2$ years), as being a key nuclei in a branching point of s-process nucleosynthesis in massive stars. Its β^--decay rate change in plasma could be observed in PANDORA via a dedicated HPGe detectors

ISBN: 978-3-95450-257-8 ISSN: 2222-5692 doi:10.18429/JACoW-ECRIS2024-TUB1

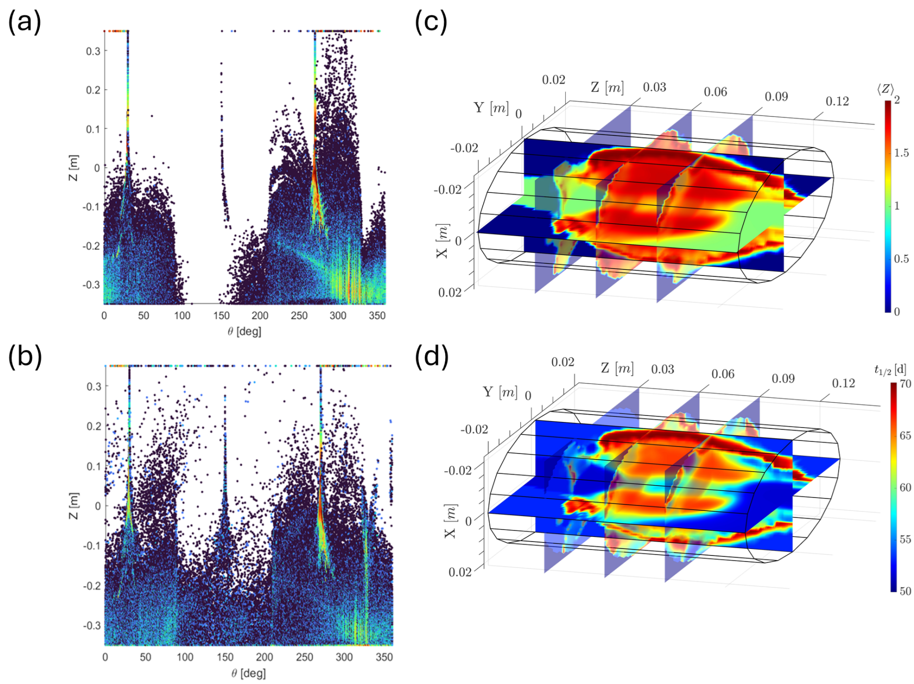

Figure 5: Deposition rate maps of caesium isotope (^{134}Cs) thermal evaporation (420 K) via resistively heated ovens and after in-plasma ionisation, with (a) and without (b) hot screen (liner, simulated at 800 K) at the plasma chamber wall. Mean-charge distribution of ^{7}Be in the plasma trap following ^{7}Be^{1+} injection (c) and related half-life time accordingly to the in-plasma nuclear decay modelling in Ref. [14] .

array surrounding the trap, looking for the daughter nuclei EM de-excitation via γ emission. However, the γ signal arising from the decay in plasma must be disentangled from the overwhelming γ noise self-generated by the plasma and Bremsstrahlung emission. Moreover, neutral isotopes condensing at the cold plasma chamber wall decay too, and such signal represents and additional source of noise to the detection system. A MC simulation has been recently performed looking at the dynamics of injected Cs particles in plasma via thermal evaporation, studying the ionisation efficiency of the PANDORA non-axisymmetric injection system and at the same time the expected amount of depositing neutral metallic atoms. The latter aspect turned to be useful in estimating the γ noise arising from the Cs deposition at the wall in the detection system [15]. In Fig. 5(a-b) the deposition maps at the PANDORA chamber wall (unfolded in the longitudinal z-axis and azimuth θ coordinates) are shown, where the recycling effects of low-melting Cs imposed by the usage of a hot screen (b) is contrasted to the case where no hot screen is used (a). The results underlines the relevant role played by the plasma and magnetic field in the isotope dynamics.

CONCLUSION

This paper presented an outline of coupled 3D full-wave PIC and PIC-MC codes capable of describing space-resolved properties of electrons and ions in an ECR plasma self-consistently. The results of the simulations are fundamental inputs to various physical processes, which can be used to validate the models while simultaneously underlining their predictive power. The simulation schemes are currently being updated in various ways including substitution of the cold electron approximation with the corrected hot electron dielectric tensor, addition of more reactions and improvement of previous ones for better modelling of ion dynamics and full implementation of the collision-radiative model for NLTE plasma-induced decay rate evaluation. The updated simulations will be compared with suitable experimental data from other ECRIS and the results will be reported in future works.

ACKNOWLEDGEMENTS

The authors acknowledge the financial support from the MUR-PNRR project PE0000023-NQSTI and the MUR-PNRR project SAMOTHRACE (ECS00000022), financed by the European Union (NextGeneration EU). The authors also wish to thank INFN for the support through the project PANDORA Gr3 funded by third Nat. Sci. Comm.

REFERENCES

[1] D. Mascali *et al.*, "A Novel Approach to β-Decay: PANDORA, a New Experimental Setup for Future In-Plasma Measurements", *Universe*, vol. 8. p. 80, 2022. doi:10.3390/universe8020080

[2] R. Geller, *Electron cyclotron resonance ion sources and ECR plasmas*, Institute of Physics, Bristol, UK, 2018.

[3] D. Mascali *et al.*, "3D-full wave and kinetics numerical modelling of electron cyclotron resonance ion sources plasma: steps towards self-consistency", *Eur. Phys. J. D*, vol. 69, p. 27, 2015. doi:10.1140/epjd/e2014-50168-5

ISBN: 978-3-95450-257-8 ISSN: 2222-5692 doi:10.18429/JACoW-ECRIS2024-TUB1

[4] B. Mishra *et al.*, "Modeling space-resolved ion dynamics in ECR plasmas for predicting in-plasma β-decay rates", *Front. Phys.*, vol. 10, p. 932448, 2022. doi:10.3389/fphy.2022.932448

[5] A. Galatà *et al.*, "On the Numerical Determination of the Density and Energy Spatial Distributions relevant for in-Plasma β-Decay Emission Estimation", *Front. Phys.*, vol. 10, p. 947194, 2022. doi:10.3389/fphy.2022.947194

[6] A. Galatà *et al.*, "Self-consistent modeling of beam-plasma interaction in the charge breeding optimization process", *Rev. Sci. Instrum.*, vol. 91, p. 013506, 2020. doi:10.1063/1.5130704

[7] R. Rácz *et al.*, "Electron cyclotron resonance ion source plasma characterization by energy dispersive x-ray imaging", *Plasma Sources Sci. Technol.*, vol. 26, p. 075011, 2017. doi:10.1088/1361-6595/aa758f

[8] A. Galatà *et al.*, "A new numerical description of the interaction of an ion beam with a magnetized plasma in an ECR-based charge breeding device", *Plasma Sources Sci. Technol.*, vol. 25, p. 045007, 2016. doi:10.1088/0963-0252/25/4/045007

[9] C. Salvia *et al.*, "Simulations of RF waves propagation in hot magnetized (^{2}H) plasma in DTT Scenario", *Il Nuovo Cimento C*, no. 5, p. 271, 2024. doi:10.1393/ncc/i2024-24271-0.

[10] D. Mascali *et al.*, "A double-layer based model of ion confinement in electron cyclotron resonance ion source", *Rev. Sci. Instrum.*, vol. 85, p. 02A511, 2014. doi:10.1063/1.4860652

[11] K. Takahashi and K. Yokoi, "Nuclear β-decays of highly ionized heavy atoms in stellar interiors", *Nucl. Phys. A.*, vol. 404, p. 3, 1983. doi:10.1016/0375-9474(83)90277-4

[12] A. Pidatella *et al.*, " Angelo Pidatella [HTML] da frontiersin.org Experimental and numerical investigation of magneto-plasma optical properties towards measurements of opacity relevant for compact binary objects", *Front. Astron. Space Sci.*, vol. 9, p. 225, 2022. doi:10.3389/fspas.2022.931744

[13] B. Mishra, "Overview of Numerical Simulations for Calculating In-Plasma β-Decay Rates in the Framework of PANDORA Project", *Eur. Phys. J. Web Conf.*, vol. 275, p. 02001, 2023. doi:10.1051/epjconf/202327502001

[14] B. Mishra *et al.*, "Plasma Induced Variation of Electron Capture and Bound-State β Decays", *arXiv*, 2024. doi:10.48550/arXiv.2407.01787

[15] A. Pidatella *et al.*, "Metal evaporation dynamics in electron cyclotron resonance ion sources: plasma role in the atom diffusion, ionisation, and transport", *Plasma Phys. Control. Fusion*, vol. 66, p. 035016, 2024. doi:10.1088/1361-6587/ad2428

ISBN: 978-3-95450-257-8 ISSN: 2222-5692 doi:10.18429/JACoW-ECRIS2024-TUB2

SIMULATION OF SURFACE X-RAY EMISSION FROM THE ASTERICS ECR ION SOURCE

T. Thuillier*, B. Cheymol, A. Cernuschi, M. Kusulja, E. Lagorio, C. Peaucelle, F. Vezzu
Université Grenoble Alpes, CNRS-LPSC, INP Grenoble, Grenoble, France
M. Dubois, F. Lemagnen, Université Normandie, GANIL, Caen, France
T. Cadoux, H. Felice, D. Simon, Université Paris-Saclay, CEA-Irfu, Saclay, France

Abstract

The bremsstrahlung x-ray emission induced by the impact of plasma electrons deconfined on the chamber wall of the ASTERICS ion source is investigated by a suite of two simulations. First, the electron velocity and density distribution of lost electrons is calculated by a dedicated Monte-Carlo code. The specificity of the electron velocity, energy and spatial distribution function on the walls is presented and discussed. Second, the electron information is used as an input for the Fluka Monte-Carlo code, used to investigate the surface induced bremsstrahlung x-ray emission. The electron distribution temperature at the wall is found to be anisotropic and increases with B_{min}. The electrons impinge the walls with large angles values with respect to the local normal surface, which has consequences on the emission direction of the x-ray. The x-ray dose is mapped inside and around the ion source for two cases: (i) for a low B_{min} magnetic confinement and an electron temperature set to 50 keV; and (ii) for a large B_{min} and an electron temperature artificially increased to 120 keV. The latter configuration gives a dose in the cave at 5 m from the source of ∼100 µSv/h per kW of impacting electrons. A set of internal tungsten shielding placed inside the source have been modelled to investigate the dose attenuation inside the cave. This shielding is very effective and significantly reduces the need for external x-ray shielding to spatially limited solid angles located on the injection side of the ion source, facilitating the source maintenance and associated safety processes.

ASTERICS ION SOURCE

The ASTERICS ion source is currently under development as part of the new GANIL injector (NEWGAIN) project [1], aiming at designing and building a second injector for the SPIRAL2 linear accelerator, able to manage heavy ion beams up to a mass over charge ratio equal to 7. ASTERICS is a 28 GHz ECR ion source using a superconducting magnet system, composed of a cos 3θ hexapole coil and 3 axial solenoids to generate the minimum-B confinement magnetic field [2, 3]. A cutaway view of the (work in progress) ion source design is proposed in Fig. 1. The superconducting magnet system is very close to the VENUS-FRIB design, except for the plasma chamber dimension which is enlarged to 600 mm length and 91 mm radius, in order to enhance the achievable ion beam intensities during operation. The goal is to produce steadily 10 pµA beams of U^{34+} for nuclear physics experiments lasting several weeks.

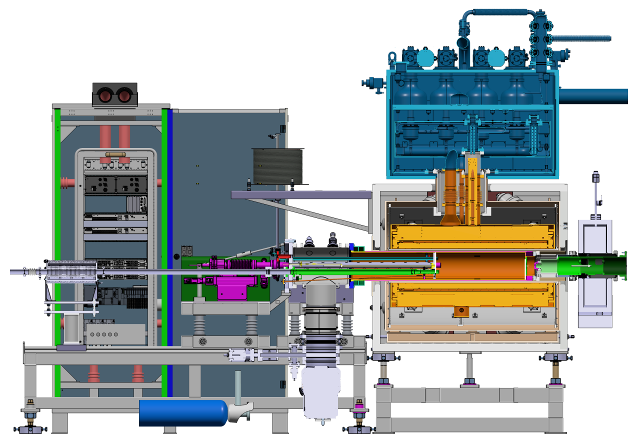

Figure 1: Cutaway view of the ASTERICS ion source design.

ELECTRON LOSSES TO THE WALL

An existing Monte-Carlo code was adapted to study the electron dynamics inside the ASTERICS ion source plasma chamber [4]. The 28 GHz radio-frequency (RF) electric field considered in the simulation is modelled with a transverse travelling plane wave with a circular polarization and a constant electric field intensity E = 10 kV/m (corresponding to 7 kW of injected RF power). Electrons are randomly generated inside the ECR volume with a random velocity direction in space. The initial electron energies are randomly sampled using a set of Gaussian distributions centered on each argon ionization potential energies IP with a standard deviation of 10 % × IP, with a relative abundance following a typical argon ion spectrum having a mean charge state number of 8. The electrons are tracked until they touch the 3 possible walls: injection at $z_{\mathrm{inj}} \approx -0.3$ m, extraction at $z_{\mathrm{ext}} \approx 0.3$ m and radial wall at $r_W = 0.091$ m. Two static electric fields are modelled in the Monte-Carlo simulation. One for the injection biased disk with a voltage of 100 V and a diameter of 20 mm. The second for the accelerating electric field of the ion source on the extraction, being 10 kV/cm, extending for 4 cm right after the extraction electrode hole of 10 mm diameter. The electrons are propagated up to 1 ms and are stopped above this time limit. Coulomb collision and electron impact are considered in the simulation to model at best the electron deconfinement. The plasma density considered is 15 % of the cut-off density at 28 GHz. A set of 1.25×10^6 electrons was simulated for each magnetic configuration.

* thomas.thuillier@lpsc.in2p3.fr

ISBN: 978-3-95450-257-8 ISSN: 2222-5692 doi:10.18429/JACoW-ECRIS2024-TUB2

The electron final positions and velocities on the plasma chamber wall were stored and analysed.

The electron particle distribution at the plasma chamber wall was studied for two axial magnetic field configurations: 3.7-0.3-2.2 T and 3.7-0.8-2.2 T, deemed representative of the actual ion source operation. The hexapolar radial magnetic field intensity at wall is fixed at 2.4 T. The B_{min} = 0.3 T configuration, suitable for double frequency operation (18+28 GHz), is known to generate a low output flux of energetic x-rays [5]. On the contrary, the B_{min} = 0.8 T configuration experimentally maximises the production of high energy x-rays [5–7]. The aforementioned magnetic configurations are used to probe the minimum and maximum x-ray dose in the accelerator cave, respectively. The electron energy distribution function (EEDF) of the electrons impacting the walls are plotted in Fig. 2(a) and Fig. 2(b) for the magnetic configurations B_{min} = 0.3 and 0.8 T respectively. The EEDF for the injection, radial and extraction walls are reported in each subplot in black, blue and red respectively. The high energy part of individual EEDF have been fitted with a Maxwell-Boltzmann distribution, and the temperature obtained with the fit are reported in the Table 1 for each surface and magnetic configuration. It is interesting to note that the EEDF both varies on the wall surface location and with the intensity of B_{min}. The normalized counts per wall surface associated with B_{min} = 0.3 and 0.8 T are proposed in Table 2. One can note a transfer of the flux of electrons from the radial (76 to 52 %) to the extraction wall (17 to 41 %) when B_{min} is changed from 0.3 to 0.8 T.

Table 1: Estimation of the EEDF high energy tail temperature obtained on the injection, radial and extraction plasma chamber walls for B_{min} = 0.3 and 0.8 T.

Axial profile	T_{inj}	T_{rad}	T_{ext}
3.7-0.3-2.2 T	19.8 ± 1.6	41.7 ± 1.5	44.0 ± 7.4
3.7-0.8-2.2 T	36.0 ± 8.6	52.0 ± 3.1	63.2 ± 7.9

Table 2: Distribution of the final position of the electrons for the two magnetic axial profiles considered. The subscripts $\%_{\text{inj}}$, $\%_{\text{ext}}$ and $\%_{\text{rad}}$ refer respectively to the particles deconfined at the injection, extraction and radial walls. $\%_{\text{conf}}$ stands for the amount of electrons still confined at the time limit of 1 ms.

Axial profile	$\%_{inj}$	$\%_{ext}$	$\%_{rad}$	$\%_{conf}$
3.7-0.3-2.2 T	3.2	17.3	76.0	3.6
3.7-0.8-2.2 T	5.8	41.5	52.1	0.6

The reason for this shift is a change of the minimum magnetic field intensity at the plasma chamber wall, which passes from 2.03 to 2.29 T, making the weakest magnetic point the extraction peak field (2.2 T) for the latter case (see [8] for details). The increase of B_{min} is coming along with a temperature increase of the hot electrons (T_{rad} from 41 to 52 keV, T_{ext} from 44 to 63 keV). This specific topic is thoroughly discussed in another paper dedicated to the ASTERICS plasma x-ray volume emission [8]. It is also worth noting that, for B_{min} = 0.8 T, the 3 EEDF feature a visible hump for E ≈ 15-20 keV, which is known to cause plasma instabilities and has been confirmed experimentally for such a high B_{min} [9]. Figure 3 presents the distribution of angle of incidence θ of electrons hitting the plasma chamber wall ($\theta = \widehat{(\vec{v},\vec{n})}$, $\vec{n}$ local normal to the surface) for (a) B_{min} = 0.3 and 0.8 T. The color plot convention in Fig. 3 is identical to the one adopted in Fig. 2. One can observe how the magnetic field intensity strongly influences the distribution shape. While the distributions for the injection are almost identical for (a) and (b), one can observe a stronger peaking of the extraction wall distribution when B_{min} is increased from 0.3 to 0.8 T,

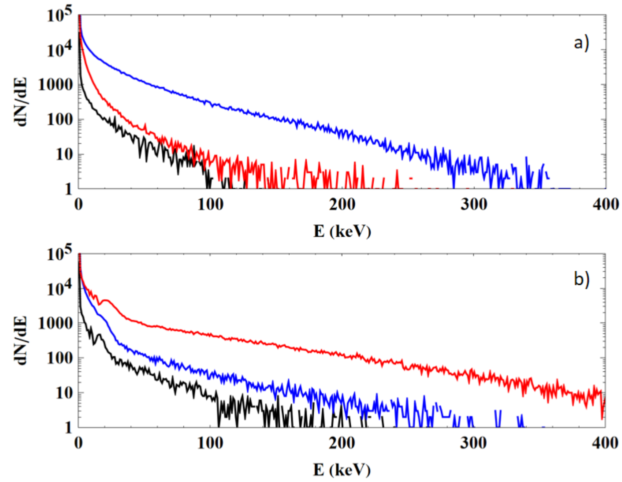

Figure 2: EEDF of the electrons hitting the plasma chamber wall for **(a)** B_{min} = 0.3 T and **(b)** B_{min} = 0.8 T. The black, blue and red plots are respectively recorded on the injection (z=z_{inj}), radial (r=r_{wall}) and extraction surfaces (z=z_{ext}).

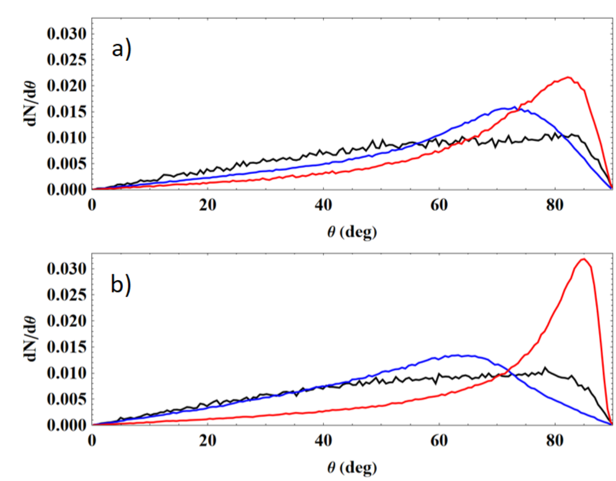

Figure 3: Distribution of the angle of incidence of electron impacting the plasma chamber walls ($\theta = \widehat{(\vec{v},\vec{n})}$), $\vec{n}$ normal to the surface) **(a)** for B_{min} = 0.3 T and **(b)** for B_{min} = 0.8 T. The black, blue and red curves correspond to the injection, radial and extraction surfaces respectively.

ISBN: 978-3-95450-257-8 ISSN: 2222-5692 doi:10.18429/JACoW-ECRIS2024-TUB2

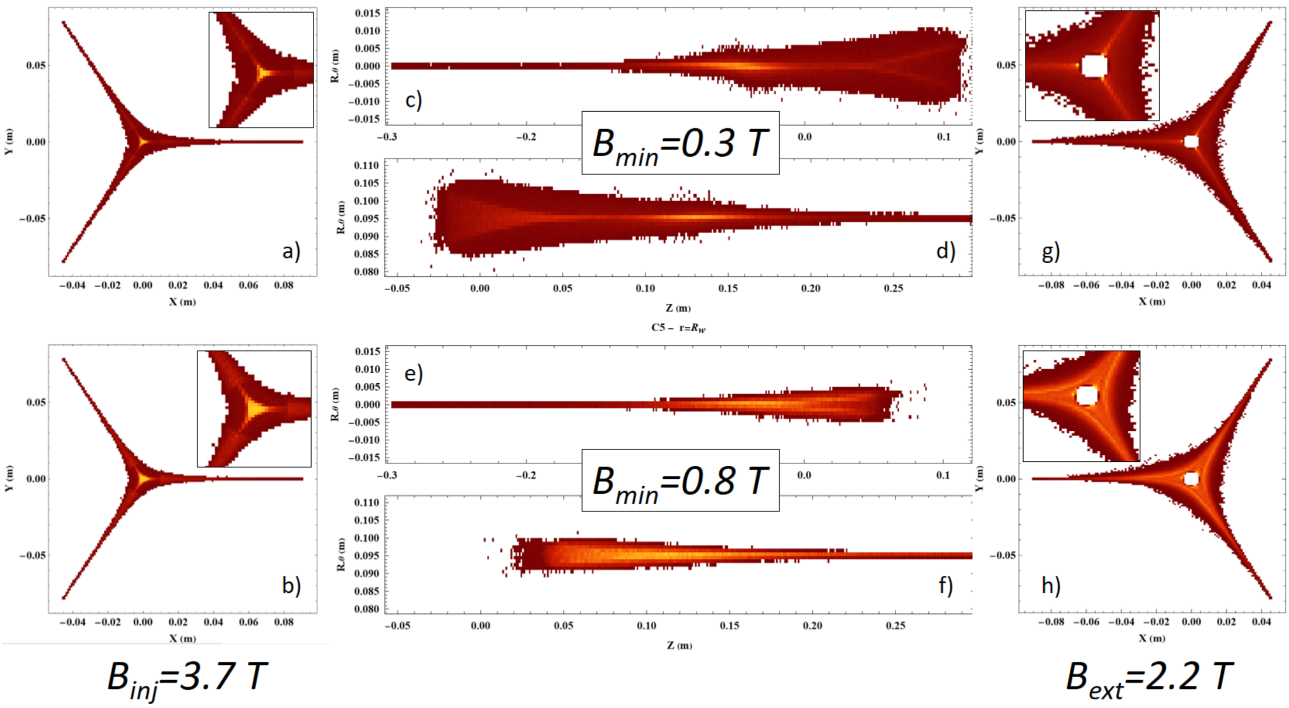

Figure 4: Electron density distribution at the injection ((a) and (b)), radial ((c), (d), (e) and (f)) and extraction ((g) and (h)) surface of the plasma chamber wall for B_{min} = 0.3 T (top plots) and B_{min} = 0.8 T (bottom plots). The dimension scale of images between the top and the bottom is conserved.

with a most probable angle of ≈ 85°. And on the other hand, a concomitant reduction of the most probable impact angle at the radial wall is found, from 72° to 65°. The high values of θ are a consequence of the magnetic mirror effect, which converts the electron parallel velocity (to the local magnetic field vector) into transverse velocity. The direction of impact of electrons on the wall influences the direction of emission of bremsstrahlung photons and must be considered in the bremsstrahlung simulation. The electron distribution of electrons on the injection, radial and extraction wall is proposed for B_{min} = 0.3 and 0.8 T in Fig. 4. While the injection electron distribution is marginally affected on the injection surface (with a triangular core centered on the axis which is twice larger when B_{min} = 0.8 T), one can observe how the distribution is significantly re-balanced between the radial and the extraction walls. At B_{min} = 0.8 T, the radial electron distribution is concentrated on a much smaller surface, while the place where high flux of electron hit the extraction wall is largely enhanced, showing by the way a distribution shape that is usually observed in ECRIS when they are dismounted.

X-RAY FLUX SIMULATION

A simplified version of the ASTERICS source's geometry, its extraction system and the first meter of its low energy beam transfer line have been modelled with Fluka [10], as can be seen in Fig. 5. The output of the MC electron simulation (position and velocity direction) was used as an input for the Fluka code. The electron energy was independently cast assuming a Maxwell-Boltzmann distribution with temperatures of 50 keV for B_{min} = 0.3 T and 120 keV for B_{min} = 0.8 T respectively. The boost of the electron temperature with respect to the one given by the MC simulation is necessary to enhance the rate of primary high energy electrons, required to produce energetic bremsstrahlung photons able to exit the source and contribute to the external dose in a reasonable simulation time. The 50 keV temperature is selected to represent a typical example of operation which minimizes the x-ray dose emitted from the source, while the 120 keV value presents an over-estimation by 20 % of the highest temperature expected during the safe and stable ion source operation [5–7]. The latter configuration is used to dimension the x-ray shielding of the ASTERICS source. In Fluka, the secondary particles showers (mainly photons and electrons) generated by each primary electron are followed until they are fully stopped by matter. The local electron position and velocity distribution of each of the three plasma chamber surface (injection, radial and extraction walls) is used to start an independent Fluka simulation.

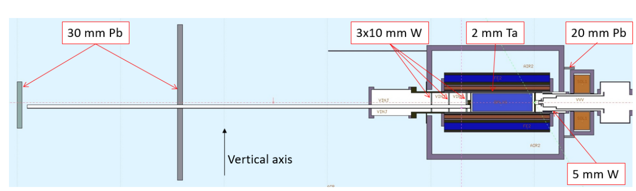

Figure 5: Sectional view of the ion source geometry modelled with Fluka. Detail of the materials geometry used to shield the x-ray emission from the source are provided. See text for details.

ISBN: 978-3-95450-257-8 ISSN: 2222-5692 doi:10.18429/JACoW-ECRIS2024-TUB2

The 3 simulations results are next merged to obtain the full x-ray spectrum of the ion source. Preliminary investigations have shown that a non-negligible amount of initial electrons impinging the walls bounce back toward the plasma chamber, especially when θ is getting close to 90°. A bouncing electron would follow a magnetic field line and hit the chamber wall elsewhere, following the initial distribution condition rules provided as input to Fluka. It is deemed unnecessary to track further such electrons (which is highly time-consuming in Fluka), since it is approximately equivalent to cast a fresh electron instead. The riddance of these parasitic electrons is achieved by defining a volume area inside the source composed of gas with a hard rule to stop any electron below 3 MeV, while the gas remain quasi-transparent to secondary x-ray photons crossing it.

Figure 6 presents the x-ray fluence per electron generated impinging (a) the injection surface, (b) the radial wall and (c) the extraction surface when $B_{\rm min}/kT_e$ = 0.8 T/120 keV. One can see that the dominant x-ray photon leak able to exit the source occurs on the source injection side, at the place where the material thickness is the lowest. The whole photon flux incoming towards the superconductor cold mass is stopped in the first radial centimeters. The 5 cm thick iron yoke surrounding the superconducting magnet cryostat also strongly attenuates the x-ray flux passing through it. On the other hand, the x-rays exiting on the extraction side are either directed along the beam pipe axis or channelled radially in the gap between the source and the first focusing solenoid yoke.

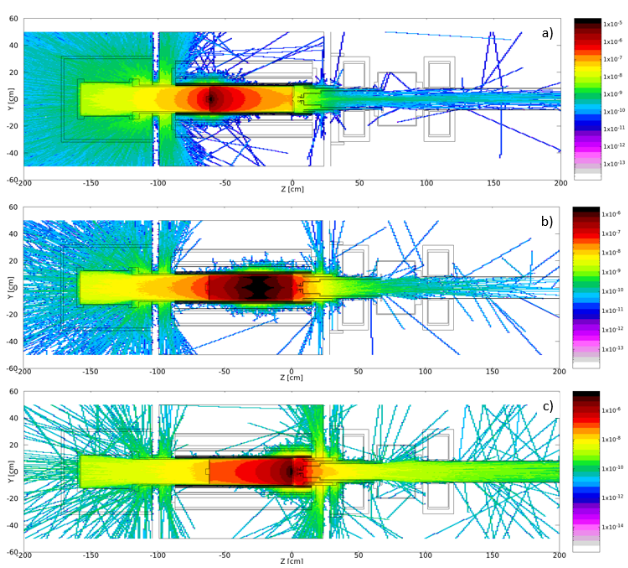

Figure 6: Averaged x-ray fluence generated by the impact of a single electron on injection (a), radial (b), and extraction walls (c) when $B_{\rm min}$ = 0.8 T and kT_e = 120 keV.

Table 3 presents the total x-ray yield per electron generated for $B_{\rm min}/kT_e$ = 0.3 T/50 keV and 0.8 T/120 keV. It is striking to note that the configuration 0.8 T/120 keV favours the leak of photons toward the injection and extraction walls (27 and 62 % respectively) rather than the radial direction (11 % only). This counterintuitive effect is likely a consequence of the following facts: (i) an increase of the electron yield on the extraction wall for $B_{\rm min}$ = 0.8 T (see Table 2), (ii) a high rate of electrons bouncing the walls and (iii) x-ray traversing thick material layers are subject to diffusion and back-scattering, favoring the remaining photons to escape toward the direction with the lesser matter (injection and extraction). On the other hand, one should remember that Fluka propagates all the secondary particles generated by the incident electron until the particle shower ends. The yields presented in Table 3 also include numerous lower energy photons subject to high scattering probability, which would finally not be detected outside the ion source.

Table 3: Total x-ray photon to electron yield passing through the injection, radial and extraction wall surfaces, for $B_{\rm min}$ = 0.3 and 0.8 T.

Axial profile	photon / e^-	%Inj	%rad	%ext
3.7-0.3-2.2 T	5.7×10^{-5}	15 %	60 %	25 %
3.7-0.8-2.2 T	1.6×10^{-4}	27 %	11 %	62 %

The ion source cave was added to the simulation to study the dose around the source without extra x-ray shielding. The result is displayed in Fig. 7(a). One can see that the local dose can be as high as ~100 µSv per kW of injected electrons in the corridor located on the left (Z<−600 cm) along the ion source axis, on its injection side. Because a maximum dose rate of 7.5 µSv is allowed in this corridor, a local shielding of the source was studied with Fluka. The shielding presented here includes a set of three 10 mm thick tungsten screens, located under vacuum inside the ion source core, installed behind the plasma injection flange, as can be seen in Fig. 5.

The shields modelled are hollowed by a set of three 40 mm diameter holes, mimicking the passage of two metallic ovens and the 28 GHz oversized waveguide. Since the latter is pointing axially toward the plasma, the copper wave guide was also modelled to study the x-ray dose distribution. The x-ray escaping the three holes are next stopped by a 30 mm thick lead shield located in the cave at the end of the injection system frame and set to ground potential. This shield dimension is limited to a small solid angle and is located far away from the place where the daily maintenance of the source is done. A second local 30 mm lead shield (not represented) was added at the waveguide bend to stop any x-ray channeled in the waveguide. Finally, a 5 mm thick lead shield is fixed along the fences closing the ion source high voltage zone. On the extraction side, the x-rays are blocked by a 5 mm thick cylinder around the extraction system and by a 20 mm thick cylinder closing the radial gap between the source yoke and the extraction solenoid yoke. The resulting x-ray dose after filtering is displayed in Fig. 7(b), showing only places where the dose is higher than 5 µSv/h per kW of electrons. One can check that the modelled compact shielding screens efficiently prevent the x-ray dose to extend outside the cave. The dose in the corridor on the left is lower than 1 µSv/h.

ISBN: 978-3-95450-257-8 ISSN: 2222-5692 doi:10.18429/JACoW-ECRIS2024-TUB2

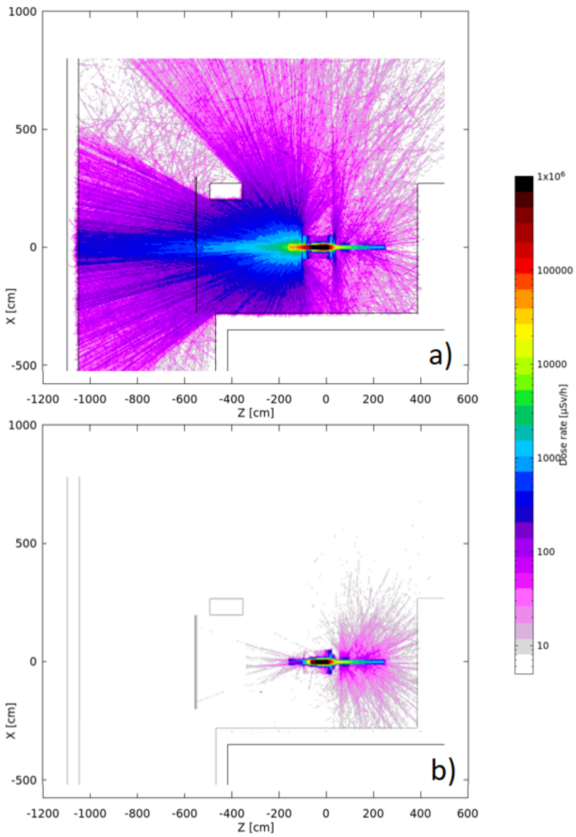

Figure 7: X-ray dose per kW of electron simulated in the cave (a) without and (b) with shielding when $B_{\mathrm{min}} = 0.8\,\mathrm{T}$ and $kT_e = 120\,\mathrm{keV}$.

CONCLUSION

The x-ray dose exiting the ASTERICS ion source has been studied with Fluka, using as input the results of a MC electron code simulating the hot electron dynamics in the ECRIS. The MC code results indicate a strong spatial electron temperature anisotropy at the three plasma chamber walls: injection, radial and extraction. An increase of the electron temperature at the three walls is obtained when B_{min} increases. The distribution of electron flux to these surfaces is also found to be strongly dependent on the value of B_{min}: electron flux leaks preferentially toward the place where the magnetic field of the Minimum-B structure is minimum. This behaviour is a consequence of the electron Coulomb scattering in the plasma. The distributions of angle of incidence of the electrons with respect to the normal to the local surface present a peak above 60° and 80° for the radial and extraction walls respectively. These distribution angles are a consequence of the magnetic mirroring effect happening in the strongly magnetized ECRIS. The large angle of incidence of electron to the wall results in a large amount of them being bounced back toward the plasma. It also results in specific solid angles of photon emissions that must be considered to appropriately simulate the x-ray spatial emission distribution from ECRIS. Without shielding, a dose higher than ~100 µSv/h per kW of electrons is obtained in the corridor located at a distance of 5 m from the injection side of the ECRIS in the NEWGAIN cave. A preliminary shielding composed of several plates of tungsten placed inside the source, under vacuum and as close as possible to the plasma chamber, are used to attenuate the x-ray dose in the cave. Such a solution allows reducing dramatically the places where x-ray shielding must be placed around the ECRIS, which results in a simplified ion source maintenance and a simpler and cheaper radiation safety design.

ACKNOWLEDGEMENT

This work is supported by Agence Nationale de la Recherche, with the contract # 21-ESRE-0018 EQUIPEX+ NEWGAIN.

REFERENCES

[1] M. Moscatello *et al.*, "NEWGAIN project at GANIL-SPIRAL2: design of the new heavy ion injector for the superconducting LINAC", in *Proc. 14th Int. Part. Accel. Conf. (IPAC'23)*, Venice, Italy, pp. 1747–1749, 2023. doi:10.18429/JACoW-IPAC2023-TUPA193

[2] D. Simon *et al.*, "Design of ASTERICS: A superconducting 28 GHz ECR ion source magnet for GANIL", *IEEE Trans. Appl. Supercond.*, vol. 33, no. 5, p. 4 002 905, 2023. doi:10.1109/TASC.2023.3260779

[3] T. Thuillier *et al.*, "ASTERICS, a new 28 GHz electron cyclotron resonance ion source for the SPIRAL2 accelerator", *J. Phys. Conf. Ser.*, vol. 2743, no. 1, p. 012 059, 2024. doi:10.1088/1742-6596/2743/1/012059

[4] T. Thuillier *et al.*, "Investigation on the electron flux to the wall in the VENUS ion source", *Rev. Sci. Instrum.*, vol. 87, no. 2, p. 02A736, 2015. doi:10.1063/1.4935989

[5] J. Benitez, C. Lyneis, L. Phair, D. Todd, and D. Xie, "Dependence of the Bremsstrahlung Spectral Temperature in Minimum-B Electron Cyclotron Resonance Ion Sources", *IEEE Trans. Plasma Sci.*, vol. 45, no. 7, pp. 1746–1754, 2017. doi:10.1109/TPS.2017.2706718

[6] D. Neben *et al.*, "X-ray investigation on the Superconducting Source for Ions (SuSI)", *J. Instrum.*, vol. 14, no. 02, p. C02008, 2019. doi:10.1088/1748-0221/14/02/C02008

[7] J. B. Li *et al.*, "Effects of magnetic configuration on hot electrons in a minimum-b ecr plasma", *Plasma Phys. Controlled Fusion*, vol. 62, no. 9, p. 095 015, 2020. doi:10.1088/1361-6587/ab9d8f

[8] A. Cernuschi and T. Thuillier, "Effect of magnetic configuration on hot electrons in a minimum-B ECR plasma", *To be submitted to Phys. Rev. Accel. Beams*.

[9] O. Tarvainen *et al.*, "Limitations of electron cyclotron resonance ion source performances set by kinetic plasma instabilities", *Rev. Sci. Instrum.*, vol. 86, no. 2, p. 023 301, 2015. doi:10.1063/1.4906804

[10] G. Battistoni *et al.*, "Overview of the fluka code", *Ann. Nucl. Energy*, vol. 82, pp. 10–18, 2015. doi:10.1016/j.anucene.2014.11.007

ISBN: 978-3-95450-257-8 ISSN: 2222-5692 doi:10.18429/JACoW-ECRIS2024-TUD1

TIME-RESOLVED MEASUREMENT OF ION BEAM ENERGY SPREAD VARIATION DUE TO KINETIC PLASMA INSTABILITIES IN CW AND PULSED OPERATION OF AN ECRIS

V. Toivanen*, H. Koivisto
Accelerator Laboratory, Department of Physics, University of Jyväskylä, Jyväskylä, Finland
J. Huovila
Department of Technical Physics, University of Eastern Finland, Kuopio, Finland
O. Tarvainen
STFC ISIS Pulsed Spallation Neutron and Muon Facility,
Rutherford Appleton Laboratory, Harwell, OX11 0QX UK

Abstract

The energy spread of ion beams extracted from Electron Cyclotron Resonance (ECR) ion sources is influenced by plasma conditions such as the plasma potential, and effects taking place in the beam formation region. Kinetic plasma instabilities have a significant impact on the plasma properties, and consequently on the ion beam energy spread. We present experimental results of time-resolved energy spread behaviour when kinetic plasma instabilities are present in CW and pulsed operation of the JYFL 14 GHz ECR ion source. It is shown that the instability-induced energy spread variation corresponds to a momentary plasma potential increase up to several kV from the steady-state value of 5–30 V. The method for measuring the time-resolved energy spread variation is presented, and the consequences of the energy spread and the underlying plasma potential variation for ECRIS operation are discussed.

INTRODUCTION

Energy spread is a relevant parameter when assessing the quality of ion beams produced with ECR ion sources, both for the beam transmission considerations and the eventual application the beam is used for. Recently, a comprehensive simulation and experimental study has been performed to determine the influence of different factors on the energy spread of ion beams extracted from ECR ion sources [1]. The study concludes that with stable plasma conditions the electrostatic focusing effects taking place during beam formation, i.e. extraction geometry and plasma beam boundary, are the dominant factors determining the beam energy spread, and exceed the contributions from magnetic field induced beam rotation, ion temperature and plasma potential.

ECR-plasmas are prone to kinetic instabilities driven by the anisotropy of the electron velocity distribution (see e.g. [2, 3]). The onset of the instability is characterised by a sudden expulsion of electrons from the plasma, resulting in a strong increase in net positive charge in the plasma volume as the heavier and less mobile ions are left behind. As a consequence, the plasma potential experiences a significant momentary (a few μs) increase, until the situation is balanced by the losses of positive ions, which restores the plasma quasi-neutrality. Because the potential has a spatial profile, this leads to a significant increase in the longitudinal energy spread of the extracted beam during the instability event.

The growth rate and broadly speaking the trigger point for the onset of the instabilities is determined by the ratio of the hot and cold electron densities in the plasma [4, 5]. As such, the instabilities can occur both in CW and pulsed operation of ECRIS. In CW operation the plasma heating and confinement leads to build-up of the hot electron population, until a threshold is reached resulting to the instability onset. In pulsed operation, following the switch-off of the plasma heating microwaves, the loss rates of the hot and cold electron populations are different as the plasma decays. The hot electrons are better confined by the magnetic trap compared to the more collisional cold electrons, hence the ratio of hot to cold electrons increases as the plasma decay progresses, eventually leading to the trigger point for the instability [6]. Several instability events can be observed during the plasma decay.

Previous studies [3, 7] have shown that the plasma potential can reach values in excess of 1 kV during a kinetic instability event, i.e. two orders of magnitude higher than the 5–30 V values typically measured in stable plasma conditions [1, 8, 9]. Consequently, in the presence of kinetic instabilities the plasma potential becomes the dominating contributor to the longitudinal energy spread of the extracted beam. As such, temporally resolved measurement of the energy spread allows determining the plasma potential during the instability. A proof-of-principle of this approach has been demonstrated for CW operation in Refs. [3, 7], where the magnetic spectrometer of an ECRIS was utilized as an ion energy analyzer. Here, this work is expanded to pulsed ECRIS operation, studying the properties of the kinetic instabilities during the plasma decay following the microwave switch-off where the instabilities are stronger than in the CW mode.

The following section describes the experimental setup to measure the variations in ion beam energy spread (and plasma potential) during the plasma instabilities. The experimental results section collates the main observations in CW operation from earlier measurement campaigns [3, 7],

* ville.a.toivanen@jyu.fi

ISBN: 978-3-95450-257-8 ISSN: 2222-5692 doi:10.18429/JACoW-ECRIS2024-TUD1

and complements them with new results in pulsed operation with varied ECRIS magnetic field. Finally, the results and their implications for ECRIS operation are discussed.

EXPERIMENTAL SETUP AND PROCEDURE

The experimental setup to study the ion beam energy spread variation in pulsed operation is presented in Fig. 1. All measurements presented in this paper were performed on the JYFL 14 GHz ECR ion source [10]. A dedicated computer was used to control the measurement procedure and for data acquisition through a Picoscope 5000-series digital oscilloscope. The computer communicates with the signal generator driving the klystron to control the microwave pulse pattern. The klystron output power monitoring signal is used to trigger and synchronize the data acquisition to the trailing edge of the microwave pulse. The computer also controls the power supply of the dipole magnet to vary the dipole B field, which was monitored with a Hall probe. The beam current downstream from the dipole was measured with a Faraday cup through a SRS SR570 transimpedance amplifier (TIA). The ion source potential was monitored with a high voltage probe to ensure it doesn't vary during the measurement.

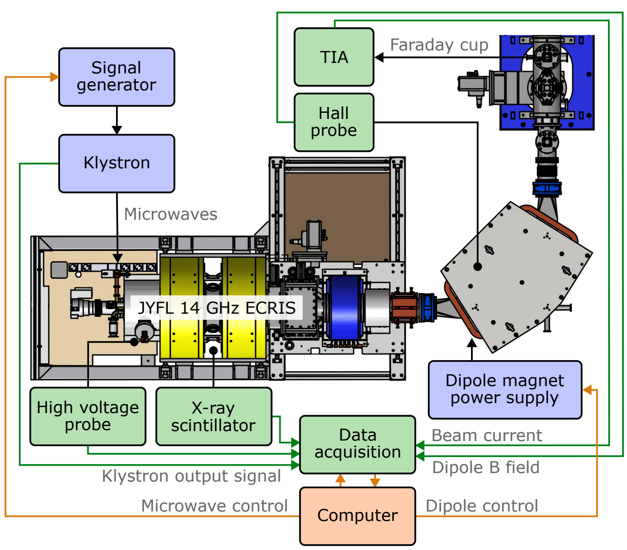

Figure 1: A schematic of the experimental setup.

A BGO x-ray scintillator coupled with a photomultiplier tube was used to monitor the x-ray emissions from the ion source plasma. Sudden bursts of x-rays are a well-established indication of kinetic plasma instabilities [2, 3], and the x-ray diagnostic was used to verify that the observed variations in the beam current during plasma decay are caused by the onset of these intabilities. Figure 2 shows an example of simultaneously measured He^+ beam current and x-ray signal following the microwave switch-off, demonstrating the correlation between the sudden discontinuities in the beam current (a sharp peak followed by a dip as the plasma recovers from the instability) and the instability-induced x-ray bursts.

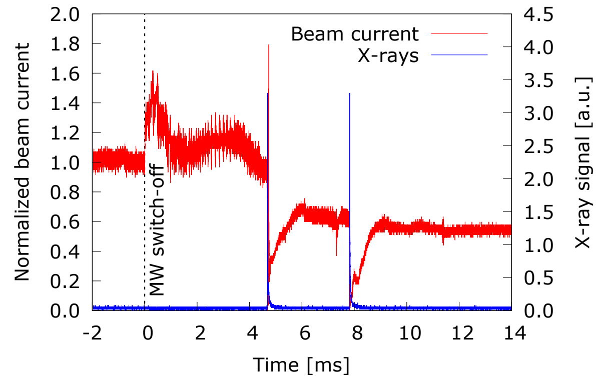

Figure 2: An example of the correlation between the $^4He^+$ beam current and the instability-induced x-ray bursts following the microwave switch-off at $t = 0$.

The measurement procedure is based on recording the temporal evolution of the beam current following the microwave switch-off, i.e. during the plasma decay, at different dipole magnetic fields, effectively scanning the B field region around the magnetic field value that corresponds to the steady-state magnetic rigidity of the ion species of interest. These individual (t, I_{beam}) traces are then combined to create a three dimensional $\left(t, B_{\mathrm{dipole}}, I_{\mathrm{beam}}\right)$ colormap plot. This is demonstrated in Fig. 3. The sudden increase of the plasma potential at the onset of a plasma instability event causes a corresponding increase in the energy spread of the extracted ions. As such, the ions of a given species are "spread" momentarily to higher dipole B field values, forming distinct lines in the $\left(t, B_{\mathrm{dipole}}, I_{\mathrm{beam}}\right)$ plot, as the dipole magnet acts as an energy analyzer and the timing of the instability events from pulse-to-pulse is very repeatable. The increase in the relative energy spread $\Delta E/E$ can be determined using the dipole field value of the beam before the instability, B_0, and the field value at the maximum extent of the spreading, B_{max}, as $\Delta E/E = \left(B_{\mathrm{max}}^2 - B_0^2\right)/B_0^2$. It was verified by careful monitoring of the ion source potential that the extraction voltage remains unchanged during the instability event, and thus the increase in the beam energy spread is dictated by the increased plasma potential. As the plasma potential before instability is much lower than the source potential, the increase in plasma potential can be estimated as $\Delta V_{\mathrm{p}} = (\Delta E/E)V_{\mathrm{s}}$, where V_{s} is the ion source potential. The experimental procedure and data analysis was automated with a custom Python based program [11].

The duration of the instability-induced beam current variations (peaks) observed during the plasma decay in a single temporally resolved current measurement is in the order of microseconds (see subplots (a)-(c) in Fig. 3), which agrees well with the time scales reported also for the CW operation [3, 7]. The delay time from the microwave switch-off to the onset of the instability is very repeatable in consecutive measurements, with variation within ± 0.5 ms (see the right side subplot in Fig. 3).

The onset of kinetic instability influences the whole plasma ion population. This gives freedom in choosing

ISBN: 978-3-95450-257-8 ISSN: 2222-5692 doi:10.18429/JACoW-ECRIS2024-TUD1

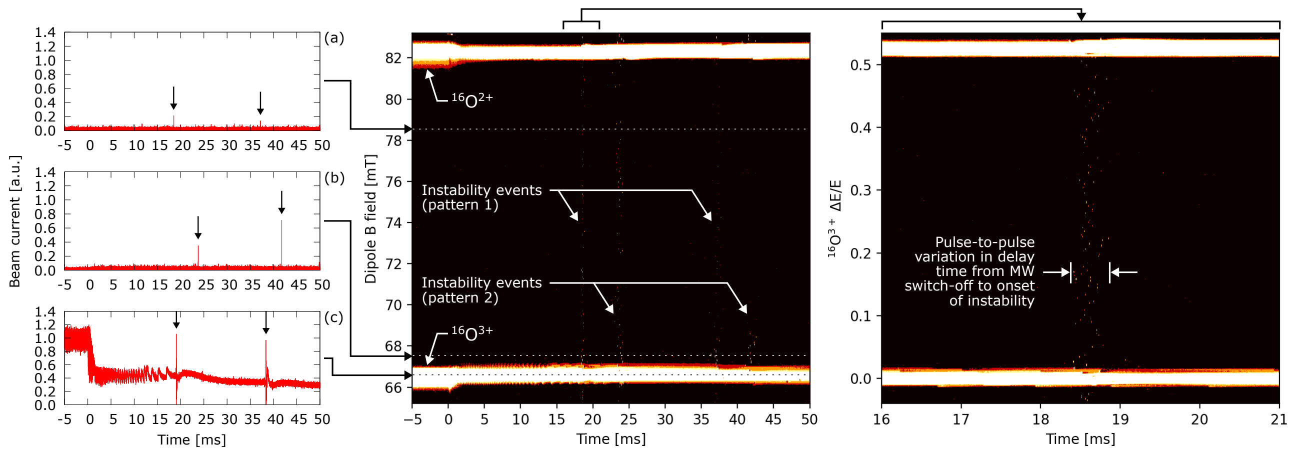

Figure 3: An example of the analysis of $^{16}O^{3+}$ beam with $B_{min}/B_{ECR} = 0.67$ during the first 50 ms of the plasma decay following the microwave switch-off at $t = 0$. Instability events are observed to take place at four discrete times: 18.6 ms, 23.6 ms, 37 ms and 42 ms. These represent a combination of two distinct instability patterns exhibited by the individual plasma decays, as is seen from the individual traces (a)-(c), each of which only show two instability events.

the extracted ion species for the studies. Especially, this provides the possibility to choose such an ion species that is well separated in dipole B field (i.e. in the q/m spectrum of extracted ions) from the neighboring species at higher magnetic field values. This separation can be considered as the most significant challenge of this method. If the beam energy spread increase causes a dipole field shift larger than the separation between consecutive ion species, the beam currents of these species overlap during the instability event, and it is not possible to determine the absolute value of the energy spread increase. In these cases only lower limit estimates for the energy spread increase can be obtained. Such situation is demonstrated in Fig. 3; out of the four observed instability events, only in the last one neighboring ion species do not overlap. This point is especially relevant, if impurity elements are present in the plasma which will further limit the available dipole B field regions. Also, during the instability event the ion optics in the beam line are no longer optimal which does impact the transmission efficiency of ions from the ion source to the Faraday cup.

As previous studies have shown (see e.g. Refs. [2, 3]), the plasma confining magnetic field has a significant impact on the occurrence and characteristics of the kinetic instabilities in CW mode. As such, the pulsed operation results presented here focus on the effect of the ECRIS magnetic field on the instability-induced change observed in the energy spread of extracted ion beams during the plasma decay. The measurements were performed with oxygen plasma (4×10^{-7} mbar plasma-off oxygen partial pressure), 300 W of microwave power pulsed at 1 Hz with 50 % duty factor, −70 V biased disc voltage and 10 kV beam extraction. The magnetic field, characterized with the B_{min}/B_{ECR} ratio, was varied between 0.63 and 0.81. The magnitude of the energy spread increase of $^{16}O^{3+}$ and the corresponding increase in plasma potential were determined, as well as the delay time from the microwave switch-off to the onset of the first plasma instability.

$^{16}O^{3+}$ was chosen instead of $^{16}O^{2+}$ or $^{16}O^{+}$, which would have larger separation in dipole B field, because they would have required lowering the extraction voltage, resulting to worse transport efficiency through the low energy beamline.

EXPERIMENTAL RESULTS

CW Operation

The first temporally resolved results for energy spread and plasma potential variations due to kinetic plasma instabilities, measured with the method described here, were published in Ref. [3] and later expanded in Ref. [7]. In these experiments the energy spread variation was studied with helium, oxygen and argon plasmas. The ECRIS was operated in CW mode with strong solenoid field to drive the plasma into unstable regime. In all cases an increase in energy spread was observed at the onset of kinetic instability. An energy spread increase of up to 15 %, corresponding to plasma potential increase of 1.5 kV at 10 kV source potential, was measured. However, in all studied cases the measured change was limited by the overlap with neighboring ion species in the q/m spectrum, and thus only lower limit estimates were obtained. Regardless, these results show that the magnitude of plasma potential increase during the instabilities can be significant. In addition, an increase in impurities, e.g. carbon, was observed in the q/m spectrum following the instability events. These were attributed to the adsorption/sputtering from the plasma chamber walls by the energetic ions expelled by the increased plasma potential.

Pulsed Operation

The results of the pulsed operation experiments are presented in Fig. 4. Figure 4(a) shows the relative energy spread of $^{16}O^{3+}$, and the corresponding plasma potential, during the instability-induced transient with varied ECRIS magnetic field. Up to $B_{min}/B_{ECR} = 0.74$ the plasma re-

ISBN: 978-3-95450-257-8 ISSN: 2222-5692 doi:10.18429/JACoW-ECRIS2024-TUD1

mains stable during the microwave pulse. In these cases the increase in energy spread during the plasma decay instability is ≥51 %, implying that the plasma potential momentarily reaches values ≥5.1 kV. Unfortunately, these are only lower limit estimates, as the actual values are obscured by the overlap with the adjacent $^{16}O^{2+}$ beam, which was revealed during the offline data reconstruction. With higher B_{min}/B_{ECR} values the plasma becomes unstable already during the microwave pulse, and significantly lower energy spread variations are measured during plasma decay; 15 % (1.5 kV plasma potential) with B_{min}/B_{ECR} = 0.77 and 4 % (0.4 kV) with B_{min}/B_{ECR} = 0.81. This implies that the instabilities provide a channel for the plasma to expel energy during the microwave pulse, which then mitigates the energy released in instability events during the plasma decay.

Figure 4(b) presents the delay time from microwave switch-off to the occurrence of the first instability event during the plasma decay. It is seen that the delay decreases with increasing B_{min}/B_{ECR} ratio. This behavior agrees with the results obtained from other kinetic instability experiments, where the onset of instabilities has been studied in pulsed operation using x-ray and microwave emissions from the ECRIS plasma [6], and is associated with the increased density and anisotropy of the hot electrons due to enhanced heating with lower magnetic field gradients at higher B_{min}/B_{ECR} values. The fact that the decrease in delay time continues when the plasma becomes unstable during the microwave pulse implies that the instability onset is driven by the ratio of hot to cold electron densities, not the actual plasma energy content.

Multiple consecutive instability events are typically observed during the plasma decay. Furthermore, certain discrete patterns of instability onsets are identified when consecutive microwave pulses are compared. This is seen in Fig. 3, where subplots (a) and (c) show one pattern and subplot (b) a different one. These patterns are combined in the colormap plot, giving the illusion that the plasma exhibits four instabilities during the first 50 ms of the plasma decay, when in reality each individual decay only has two instability events. It was also observed that consecutive events tend to become weaker as the decay progresses, in terms of beam intensity and $\Delta E/E$ variation.

DISCUSSION AND CONCLUSIONS

The experimental results presented here show that kinetic instabilities lead to drastic momentary increase in plasma potential and energy spread of the extracted beam both in CW and pulsed operation of ECRIS. The results obtained so far show that this plasma potential increase can be in excess of 5.1 kV, which is an immense increase from the typical values of some tens of volts measured for stable plasmas. It is emphasized, that this value is still a lower limit estimate for the potential increase, as the actual absolute values still remain elusive due to the overlap issue associated with this measuring technique.

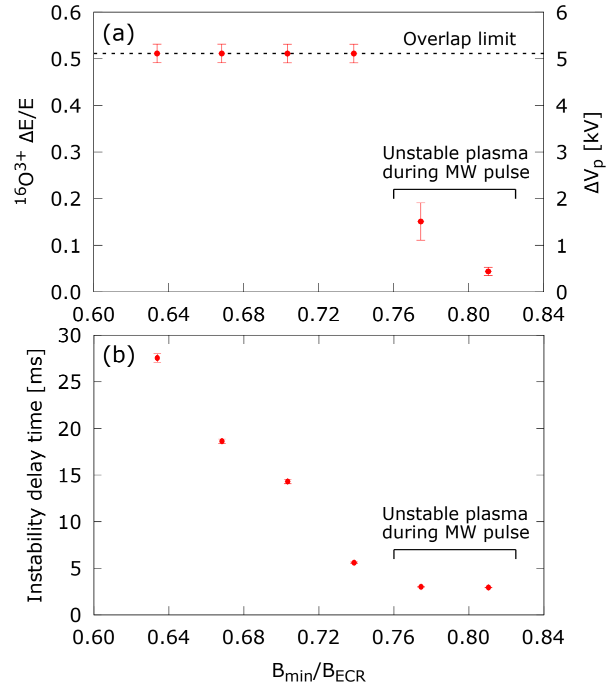

Figure 4: (a) The measured $\Delta E/E$ of $^{16}O^{3+}$ and the corresponding plasma potential increase during instability event with varied ECRIS magnetic field. The dashed horizontal line denotes the maximum $\Delta E/E$ that can be measured until the results are obscured by an overlap with the next ion species. (b) The measured delay time from the microwave switch-off to the appearance of the first instability event during the plasma decay.

The significant increase in plasma potential during the instabilities has consequences for ECRIS operation. Especially in CW operation the instability disturbs the plasma confinement, which consequently disturbs the ion production leading to degraded beam performance, especially for the high charge states. The increased plasma potential also expels high energy ions from the plasma to the chamber walls. This can have at least two undesired consequences; firstly, the flux of energetic ions cause adsorption of impurity elements from the walls, which are then ionized in the plasma, leading to beam impurities. This effect, and the consequent impact on the efficiency of ECRIS charge breeders, has been reported in Refs. [12, 13]. Secondly, the increased sputtering by the energetic ions can lead to chamber erosion. In Ref. [14] structural chamber degradation due to heavy sputtering and metal coating of extraction system insulators was reported following a six month period of pulsed afterglow operation of the GTS-LHC ECRIS with argon plasma. In the experiments presented here instability events were observed in pulsed operation with all ECRIS settings, which implies that these effects can be always present when ECRIS is operated in pulsed mode.

REFERENCES

[1] J. Angot, O. Tarvainen, P. Chauveau, S.T. Kosonen, T. Kalvas, T. Thuillier, M. Migliore and L. Maunoury, "The longitudi-

ISBN: 978-3-95450-257-8 ISSN: 2222-5692 doi:10.18429/JACoW-ECRIS2024-TUD1

nal energy spread of ion beams extracted from an electron cyclotron resonance ion source", *JINST* 18 (2023) P04018. doi:10.1088/1748-0221/18/04/P04018

[2] O. Tarvainen, I. Izotov, D. Mansfeld, V. Skalyga, S. Golubev, T. Kalvas, H. Koivisto, J. Komppula, R. Kronholm, J. Laulainen and V. Toivanen, "Beam current oscillations driven by cyclotron instabilities in a minimum-B electron cyclotron resonance ion source plasma", *Plasma Sources Sci. Technol.* 23 (2014) 025020. doi:10.1088/0963-0252/23/2/025020

[3] O. Tarvainen, T. Kalvas, H. Koivisto, J. Komppula, R. Kronholm, J. Laulainen, I. Izotov, D. Mansfeld, V. Skalyga, V. Toivanen and G. Machicoane, "Limitation of the ECRIS performance by kinetic plasma instabilities", *Rev. Sci. Instrum.* 87 (2016) 02A703. doi:10.1063/1.4931716

[4] S.V. Golubev and A.G. Shalashov, "Cyclotron-resonance maser with adiabatic magnetic pumping in a low-density plasma", *JETP Lett.* 86 (2007) 91–97. doi:10.1134/S0021364007140056

[5] A.G. Shalashov, S.V. Golubev, E.D. Gospodchikov, D.A. Mansfeld and M.E. Viktorov, "Interpretation of complex patterns observed in the electron-cyclotron instability of a mirror confined plasma produced by an ECR discharge", *Plasma Phys. Controlled Fusion* 54 (2012) 085023. doi:10.1088/0741-3335/54/8/085023

[6] I. Izotov, T. Kalvas, H. Koivisto, J. Komppula, R. Kronholm, J. Laulainen, D. Mansfeld, V. Skalyga and O. Tarvainen, "Cyclotron instability in the afterglow mode of minimum-B ECRIS", *Rev. Sci. Instrum.* 87 (2016) 02A729. doi:10.1063/1.4935624

[7] O. Tarvainen, R. Kronholm, T. Kalvas, H. Koivisto, I. Izotov, V. Skalyga, V. Toivanen and L. Maunoury, "The biased disc of and electron cyclotron resonance ion source as a probe of instability-induced electron and ion losses", *Rev. Sci. Instrum.* 90 (2019) 123303. doi:10.1063/1.5126935

[8] O. Tarvainen, P. Suominen, T. Ropponen, T. Kalvas, P. Heikkinen and H. Koivisto, "Effect of the gas mixing technique on the plasma potential and emittance of the JYFL 14 GHz electron cyclotron resonance ion source", *Rev. Sci. Instrum.* 76 (2005) 093304. doi:10.1063/1.2038647

[9] O. Tarvainen, P. Suominen, T. Ropponen and H. Koivisto, "Emittance and plasma potential measurements in double-frequency heating mode with the 14 GHz electron cyclotron resonance ion source at the university of Jyväskylä", *Rev. Sci. Instrum.* 77 (2006) 03A309. doi:10.1063/1.2162850

[10] H. Koivisto, P. Heikkinen, V. Hänninen, A. Lassila, H. Leinonen, V. Nieminen, J. Pakarinen, K. Ranttila, J. Ärje and E. Liukkonen, "The first results with the new JYFL 14 GHz ECR ion source", *Nucl. Instr. and Meth. in Phys. Res. B* 174 (2001) 379-384. doi:10.1016/S0168-583X(00)00615-7

[11] J. Huovila, *MSc thesis*, University of Jyväskylä (2023). doi:http://urn.fi/URN:NBN:fi:jyu-202305022805

[12] O. Tarvainen, J. Angot, I. Izotov, V. Skalyga, H. Koivisto, T. Thuillier, T. Kalvas and T. Lamy, "Plasma instabilities of a charge breeder ECRIS", *Plasma Sources Sci. Technol.* 26 (2017) 105002. doi:10.1088/1361-6595/aa8975

[13] O. Tarvainen, J. Angot, I. Izotov, V. Skalyga, H. Koivisto, T. Thuillier, T. Kalvas, V. Toivanen, R. Kronholm and T. Lamy, "The effect of plasma instabilities on the background impurities in charge breeder ECRIS", *AIP Conf. Proc.* 2011 (2018) 070006. doi:10.1063/1.5053348

[14] D. Küchler, J. Ferreira Somoza, A. Michet and V. Toivanen, "Never run your ECR ion source with argon in afterglow for 6 months!", in *Proc. ECRIS'16*, Busan, Korea, Aug. 2016, p. WEPP03, ISBN 978-3-95450-186-1.

ISBN: 978-3-95450-257-8 ISSN: 2222-5692 doi:10.18429/JACoW-ECRIS2024-TUP01

OPERATION WITH THE LAPECR3 ION SOURCE FOR CANCER THERAPY ACCELERATORS*

J. Q. Li†,1, Y. Cao, X. Z. Zhang, J. D. Ma, C. Qian, L. T. Sun1, H. W. Zhao1
Institute of Modern Physics, Chinese Academy of Sciences, Lanzhou, China
1also at School of Nuclear Science and Technology,
University of Chinese Academy of Sciences, Beijing, China
G. Jin, Lanzhou Ion Therapy co., Ltd (LANITH), Lanzhou, China

Abstract

An all-permanent magnet electron cyclotron resonance ion source-LAPECR3 (Lanzhou All Permanent magnet Electron Cyclotron Resonance ion source No.3) had been developed as the C^{5+} ion beam injector of Heavy Ion Medical Machine (HIMM) accelerator facility since 2009 in China. The first HIMM demo facility was built in Wuwei city in 2015, which had been officially licensed to treat patients in early 2020. The facility has been proven to be very effective, and more than 1400 patients have been treated so far. In order to prevent ion source failure, each facility employs two identical LAPECR3 ion sources. At present, there are eight HIMM facilities are under construction or in operation, and more than 16 LAPECR3 ion sources were built. In order to improve the performance of the ion source for long term operation, some techniques were employed to optimize source performance and to avoid the damage of key equipment. This paper will introduce the operation status of LAPECR ion sources at these HIMM facilities and present the latest results of carbon beam production.

INTRODUCTION

Carbon ion radiotherapy, with its unique Bragg peak, good Relative Biological Effect (RBE) and higher Liner Energy Transfer (LET), is considered to be one of the best tumour treatment methods and has developed rapidly in recent 30 years. Since the heavy ion medical accelerator in Chiba (HIMAC) at the National Institute of Radiological Sciences (NIRS) was constructed as the first medical dedicated heavy ion accelerator in 1994[1], many countries began to developed their own medical accelerator as a high-tech medical instrument. Researchers at Institute of Modern Physics (IMP) in China started carbon irradiation research since 1996. The first medical carbon ion irradiation accelerator in China, which was named Heavy Ion Medical Machine (HIMM), was constructed in Wuwei city in 2015[2]. The schematic layout ot HIMM facility as showed in Fig. 1. Since the first HIMM facility was officially permitted to clinical treatment in March 2020, more than 1400 patients have received carbon ion radiotherapy.

So far, there are 8 HIMM facilities either in operation or under construction in China, and more than 16 LAPECR3 ion sources were built. These facilities are distributed in Wuwei, Lanzhou, Putian, Wuhan, Hangzhou, Nanjing, Changchun and Jinan separately.

Although the first demonstration facility in Wuwei city has achieved remarkable results in the past 7 years, there were some problems which affected the routine operation of the accelerator. For example, the carbon contamination leads the instability of the beam, short the lifetime of the ion source. In the early operation of HIMM facility, the performance of the ion source has degraded significantly after one mouth operation. The beam intensity and the beam stability were decreased. Besides, the insulator ceramics of the ion source could damage sometimes and the ion sources could not sustain any more. In order to solve the problems, continuous work had been carried out. This paper will illustrate the operation status of LAPECR ion sources in the HIMM facilities and present the latest results of carbon beam production.

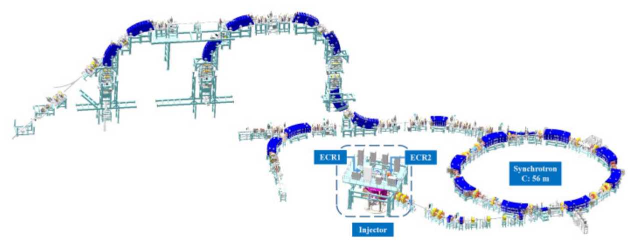

Figure 1: Schematic layout of HIMM facility.

LAPECR3

According to the requirements of ion source applications, the LAPECR series ion sources were developed successfully at IMP [3], including the LAPECR1 ion source for light ion application, the LAPECR2 for atomic physics research and the LAPECR3 ion source which was dedicate designed for carbon irradiation. Table 1 presents the key parameters of these ion sources. The LAPECR series ion sources were designed to operate at 14.5 GHz, and the magnetic field was generated from permanent magnet to lower the power consumption and easy to maintain. The LAPECR3 ion source features as compact size and high performance, the requirements of the ion source are to produce intense carbon beams with better beam emittance, such like more than 100 eμA of C^{5+} and more than 300 eμA of C^{4+}. So, an iron plug was adopted in injection side of the LAPECR3 ion source to enhance the injection field. To optimize the microwave coupling, a movable bias disc was designed with adjusting distance of ±5 mm. Moreover, a movable extraction puller electrode, which consists of a Mo head and a stainless-steel base, was employed to optimize the beam extraction. It is necessary to use a bigger ceramic to improve the gas flow conductance at the extraction region. Besides, the plasma chamber was made from stainless-steel with good water cooling, which allowed

* Work supported by NSFC with contact No. E111561GJ0
† Email address: lijiaqing@impcas.ac.cn

26th Int. Workshop Electron Cyclotron Resonance Ion Sources ECRIS2024, Darmstadt, Germany JACoW Publishing
ISBN: 978-3-95450-257-8 ISSN: 2222-5692 doi:10.18429/JACoW-ECRIS2024-TUP01

maximum power feeding of 650 W. Microwave was directly feed into plasma chamber with WR62 wave guide. Figure 2 gives the structure of the LAPECR3 ion source.

Table 1: Key Parameters of LAPECR Series Ion Sources

Species	LAP-ECR1	LAP-ECR2	LAP-ECR3
RF	14.5	14.5	14.5
B_{inj}	1.4	1.25	1.8
B_{min}	0.35	0.42	0.4
B_{ext}	0.7	1.07	0.9
B_{rad}	0.9	1.2	1.14
L_{mirror}	78	255	170
L_{ecr}	46	100	64
$D_{chamber}$	40	67	50
Dimension	Φ202*210	Φ650*560	Φ450*380
Applica-tion	Light ions	Multiple i-ons	Carbon th erapy

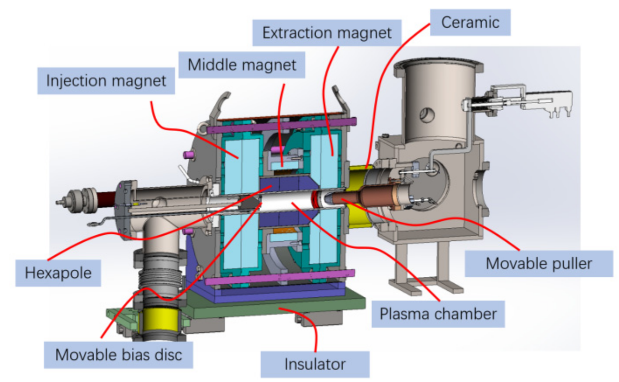

Figure 2: Structure of the LAPECR3 ion source.

There are totally 16 LAPECR3 ion sources was built to employed in 8 HIMM facilities so far, and the new ion source was upgrade from the old version according to the experience of operation.

OPERATION STATUS

The first HIMM facility has been used to treat patient for about 4 years. There were many failures were found in the early operation, including the shutdown of the microwave generator and high voltage supply, also frequent discharges in the extraction area were found. The failure was finally verified to be caused mainly by two reasons. Firstly, some equipment of the ion source system is easy to be affected by the others. For example, due to the interference caused by the other equipment, sometime the microwave signal interrupt abrupt resulting in the microwave amplifier fault. Another is the imperfect interlock between the high voltage power source and the vacuum gauge, which lead to occasional shut-down of the high voltage power supply.

Some methods were taken to avoid these malfunctions. An improved microwave signal generator has been employed to resist electromagnetic interference. And a time delay has been adopted to judge the reality of interlock signal. The recent operation status of the ion source indicates that the main problems of the equipment has been resolved.

In addition, the clear gas CH_4 was fed to the plasma chamber as working gas to enhance the stability of the plasma, which also reduced the pollution of the chamber significantly and consequently increase the operation time of the ion source. Since the employment of methods above, LAPECR3 ion source could remain stable operation for 3 months and no malfunction occurred.

Moreover, with the help of a signal generator to modulate the time structure of microwave, the LAPECR3 ion source has successfully tested with afterglow mode, which was hoped to decrease the duty cycle of the ion source operation while with comparable or even higher output ion current and hence reducing the carbon pollution in the plasma chamber. The test results as shown in Fig. 3, the maximum peak current of C^{5+} reached to 180 eμA while the beam current of 24 eμA at the steady stage. The pulse repetition rate was set to 10 Hz with the duty cycle of 50% for the microwave. The result demonstrates the possibility of the afterglow mode applied in the routine operation of LAPECR3.

In order to extend the lifetime of the ion sources in HIMM facility, the afterglow mode operation was adopted in 2021 year in HIMM-WUWEI, the lifetime of the ion source was extended significantly. Now, the maintenance interval of the ion source exceeds 200 days, and the LAPECR3 ion sources could supply ion beam for more than 8500 hours per year.

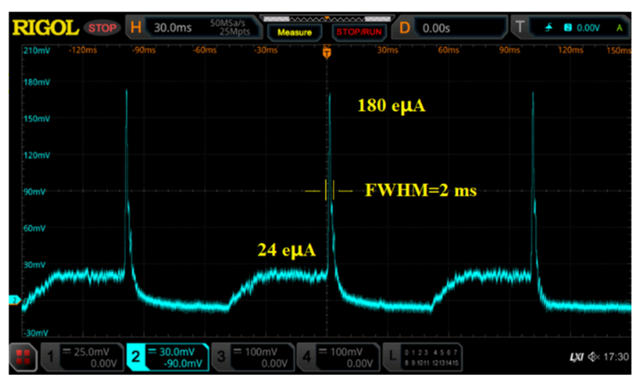

Figure 3: Afterglow mode test on C^{5+} ion beam.

LATEST RESUTLS

In 2023, China 's 2nd generation carbon ion radiotherapy accelerator start to designs, which requiring the ion source to provide more than 1 emA of C^{4+} ion beam for accelerator injection. In order to meet the requirements of the new facility, the production of intense current C^{4+} ion beam was systematically studied on a dedicated test bench.

In order to improve the extraction current of the ion source, a high extraction voltage needs to be applied. Figure 4 shows the dependence of the extraction high voltage and the extraction gap on C^{4+} beam current. It can be seen that C^{4+} beam current increases with the extraction voltage improving; In addition, the extraction beam intensity can also be well adjusted by changing the extraction electrode gap. Finally, more than1 emA of C^{4+} ion beam was obtained at 32 kV extraction voltage and a 26 mm extraction gap.

ISBN: 978-3-95450-257-8 ISSN: 2222-5692 doi:10.18429/JACoW-ECRIS2024-TUP01

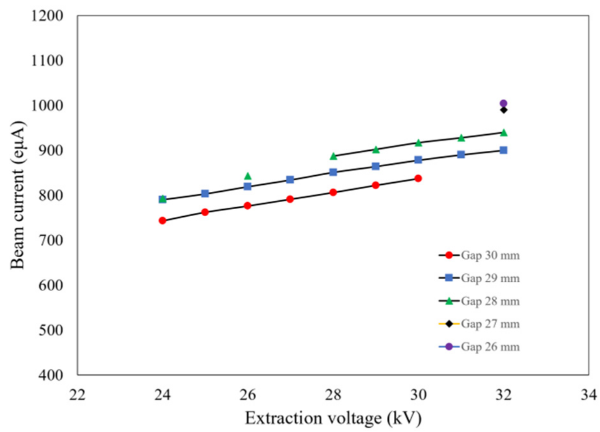

Figure 4: C^{4+} beam current versus extraction high voltage with different extraction gap.

With the purpose of investigating the impact of the extraction high voltage on the beam emittance, the C^{4+} beam emittance versus the extraction high voltage has been measured as shown in Fig. 5. Easy to see that with the in-crease of the extraction voltage, the emittance of the C^{4+} beam does not growth, which indicates that the high voltage extraction mode is beneficial to the beam transportation.

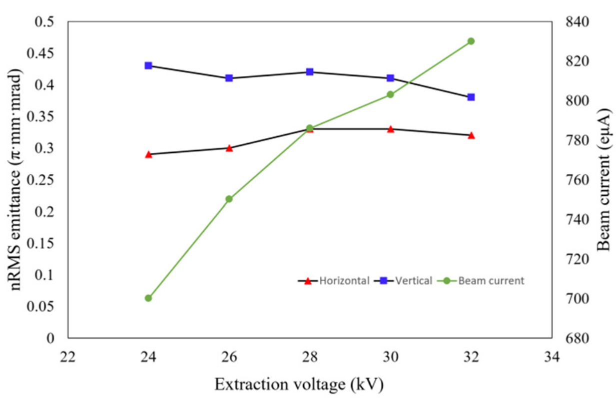

Figure 5: C^{4+} beam emittance versus extraction high voltage.

The beam emittance go against the requirement of the ion source in the 2nd generation carbon therapy accelerator, works should be carried out to reduce the growth of the beam emittance. It is better to use a higher performance ion source to supply such intense carbon beam, a hybrid superconducting ion source should be a good candidate. There will be enough space to design a highly efficient beam extraction system for intense carbon beam, it could be expected that the beam emittance could be limited to an optimal value.

CONCLUSION

Based on the 10 years development of the LAPECR3 ion source, the lifetime and the performance of the ion source has improved significantly. Continuous work should be carried out to reduce the carbon contamination and to im prove the beam stability.

ACKNOWLEDGEMENT

This work supported by the National Science Found for Distinguished Young Scholars (No. E111561GJ0).

REFERENCES

[1] A.Kitagawa, A.G. Drentje, T. Fujita, *et al.*, “Recent developments of ion sources for life-science studies at the Heavy Ion Medical Accelerator in Chiba (invited),” *Rev. Sci. Instrum.* vol. 87, p. 02C107, 2016. doi:10.1063/1.4934843

[2] J.Q. Li, Y. Cao, L.T. Sun, *et al.*, “Intense carbon beams production with an all permanent magnet electron cyclotron resonance ion source for heavy ion medical machine,” *Rev. Sci. Instrum.*, vol. 91, p. 013307, Jan. 2020. doi:10.1063/1.5128488

[3] L.T. Sun, H.W. Zhao, H.Y. Zhao, *et al.*, “Overview of high intensity ion source development in the past 20 years at IMP,” *Rev. Sci. Instrum.*, vol. 91, p. 023310, Feb. 2020. doi:10.1063/1.5129399

ISBN: 978-3-95450-257-8 ISSN: 2222-5692 doi:10.18429/JACoW-ECRIS2024-TUP04

TESTS OF A LOW-ENERGY PEPPERPOT BASED ON A MICRO-CHANNEL PLATE FOR HIGH CURRENT PROTONS SOURCES 4D-EMITTANCE CHARACTERIZATION*

A. Thézé†, B. Bolzon, A. Dubois, G. Ferrand, O. Tuske
Commissariat à l'Energie Atomique et aux Energies Alternatives (CEA-Irfu),
Institut de Recherche sur les lois Fondamentales de l'Univers, Gif-sur-Yvette, France

Abstract

In the scope of high current protons sources characterization, the CEA is working on a 4D-emittancemeter based on the pepperpot technology. After some unsuccessful developments with phosphorous scintillators, we decided to test micro-channel plates (MCP) for measurements of proton beams at very low energy (typically between 50 and 100 keV). MCP are supposed to resist to proton beams at very low energy better than scintillators. This work presents some results for MCPs with an Advanced Light Ions Sources Extraction System (ALISES) on the Banc d'Etude et de Test de Sources d'Ions (BETSI).

INTRODUCTION

In recent years, there has been a growing interest in accelerator instrumentation, particularly emittancemeter. Beam characterization through emittance measurement is a key factor in improving the efficiency of beam transport systems.

Nowadays, most emittancemeters are 2D emittancemeters, measuring the [x-x′] or [y-y′] phase space. Although studies on 4D-emittancemeter (given in a single shot the six projections: x-x′, y-y′, x-y, x′-y′, x-y′, y-x′) have become increasingly numerous in recent years, one problem re-mains: projection resolution. The fundamental principle of the 4D-emittancemeter (pepperpot) is described as the re-construction of position and angular distribution of the beam as like the slit-scan method but in a single shot by applying a metallic mask which has equidistant pinholes with the same diameter [1].

In this way, the angular and position resolutions of the projections depends on the diameter of the holes, the distance between them, and the resolution of the imaging device. Thus, the resolution will in most cases be lower compared to e. g. a slit-grid-assembly [2].

To achieve better resolution, the Accelerator Research and Development Laboratory (LEDA) at CEA Saclay has rethought the principle of the 4D-emittancemeter by proposing a pepperpot that scans the beam as an Allison scanner emittancemeter. Measurement is no longer performed in a single shot, enabling more data to be acquired. The first 4D-emittancemeter was designed in 2016 for low-energy (some keV) and intermediate-energy (some MeV) beams [3].

Due to unsuccessful developments with phosphorous scintillators for characterization of ion sources, the specifications were reduced.

Today, the laboratory focuses its studies on a 4D-emittancemeter with a MCP. The diagnostic is designed to be tested on an ALISES source producing a 50 keV beam of 28 mA, on BETSI [4] since this source is easily available for the experiments. Results are presented in this paper.

PREVIOUS WORK

The first version of the emittancemeter built in 2016 was made of a pepperpot with an integrated cooling system, a scintillator and a synchronized CCD camera. The entire diagnostic is linked to a displacement system consisting of two stepper motors (along the x and y axes).

When the pepperpot was manufactured, the assembly welds failed to withstand hot isostatic pressing, resulting in deformation, loss of thermal conductivity and loss of flatness, making it difficult to drill the sampling holes. In addition, several scintillators were studied and tested [5] but no one satisfied the need for ion sources characterization because of the first atomic layers of the scintillators quick degradation. Even with MeV beams, the scintillators degradation was too quick for precise measurements.

Combining the pepperpot defects and the scintillator heterogeneous light signal degradation (due to certain areas more exposed to the beam), the results obtained for a beam on the Injecteur de Protons à Haute Intensité (IPHI) (3 MeV, 9 mA, 1 Hz, 1 ms pulse time) were not those ex-pected (see Fig, 1).

The data obtained could not be processed, and none of the six projections gave an accurate and precise emittance value [3]. At lower energy (around 60 keV), scintillators were destroyed after a single pulse.

UPDATED EMITTANCEMETER

The pepperpot was redesigned without the cooling system making the manufacturing easier. Thermal simulations were carried out using COMSOL software. An aluminium plate with the dimensions of the pepperpot was tested in front of the ALISES 3 source beam (1 Hz, 29 mA and 65 kV) [6]. Various operating cycles were tested in order to measure the maximal local temperature and to avoid dam-aging the pepperpot before measuring the emittance. For a 10 % duty

* Work supported by the Commissariat à l'Energie Atomique et aux Energies Alternatives (CEA, France)
† anna.theze@cea.fr

ISBN: 978-3-95450-257-8 ISSN: 2222-5692 doi:10.18429/JACoW-ECRIS2024-TUP04

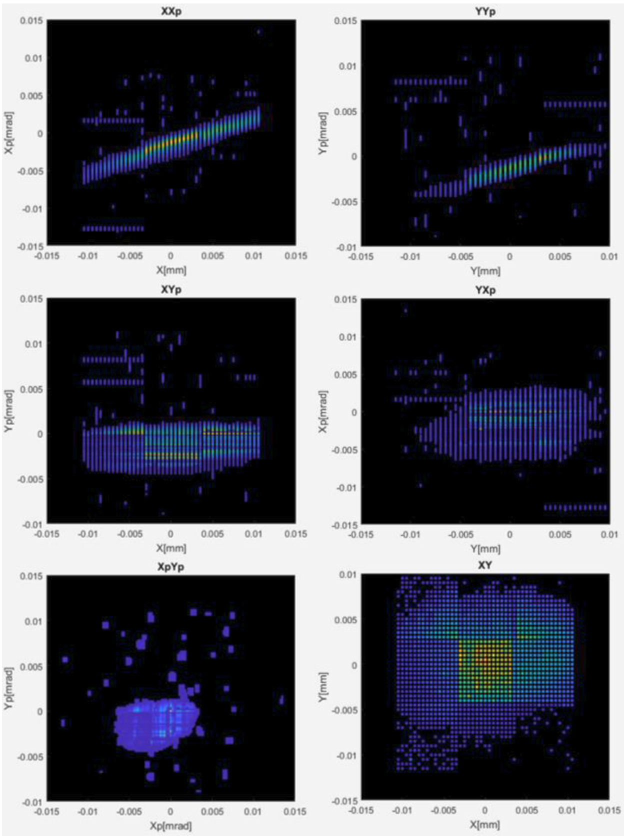

Figure 1: The 6 emittance projections obtained by the 4D-emittancemeter designed in 2016.

cycle, the maximum temperature measured was 81 °C. At this duty cycle, no water cooling system is required.

The scintillator has been replaced by a MCP. Most recent 4D-emittancemetters use them due to their good temporal resolution [7]. When the ion beam enters a channel and strikes the wall, several secondary electrons are emitted due to the electric potential between electrodes. They then strike the opposite channel wall, emitting further secondary electrons. The electrons thus move towards the end of the MCP while repeatedly striking the inner wall of the channel. The phosphor screen behind the MCP receives electrons rather than protons, limiting its degradation.

The MCP used is a Hamamatsu MCP F2225-21P with the small channel diameter (12 µm), large effective surface diameter (42 mm) and an integrated phosphor screen.

The displacement system has been retained. It was described in [3]. The available 2D-displacement increases greatly the spatial resolution (x and y) of the measurement. The operator can define the step size of the acquisition.

The spatial resolution of each shot of a pepperpot 4D-emittancemeter is determined by the distance between the holes. This resolution is limited by the size of the spots on the imaging plane, which must not overlap. Angular resolution is determined by the spatial resolution of the position-sensitive detector and by the pepperpot-MCP distance.

By adding a displacement system that scans the entire beam along the x and y axes, spatial resolution depends essentially on the step size, which can be far lower than the single shot resolution. In this case, the measurement is no longer instantaneous, the number of required shots is given by the square of the ratio between the single shot resolution and the step size.

Main design parameters are listed in Table 1.

Table 1: Main Design Parameters

Parameters	Value	Unit
Number of holes	69	—
Hole-to-hole distance	4	mm
Holes diameter	⌀ 0.06	mm
Pepperpot to MCP distance	60	mm
MCP active diameter	⌀ 42	mm
Materials of mask	Al	—

The camera uses for the acquisition is an AV MAKO G-419B POE bought in 2013 with 12 bit colour depth (monochrome) and a 2048 × 2048 pixel resolution.

RESULTS

The emittance projections presented in this part were obtained with the new version of the 4D-emittancemeter on ALISES 2 on BETIS. The source parameters are as fol-lows: 1 Hz, 28 mA, 40 keV beam, with a pulse time of 10 ms.

These values are a compromise to obtain a fully formed beam and minimize the energy absorbed by the pepperpot. A LabVIEW™ program controls the system. It moves along a trajectory known as a “vertical comb”. For a chosen distance and number of points, the acquisition system collects images with the camera, with the defined step size. The acquisition system recorded data at regular intervals of 0.5 mm over 4 mm along the x and y axes. This gives a final spatial resolution of 72 × 72. 81 acquisitions were made for one emittancemeter measurement. A python program has been written to reconstruct the phase-space distributions from these acquisitions (see Fig. 2).

Each hole in the pepperpot has a different dimension due to the precision of the manufacturing process. Therefore, the quantity of particles incoming (beam sampling) differs from hole to hole.

To overcome this problem, a calibration process was carried out: At time t, an acquisition is made for a known pepperpot position. A second acquisition is then made under the same conditions, with the pepperpot offset by 4 mm along the X or Y axis (inter-hole distance).

Assuming that the beam profile does not vary over time, beam sampling should be the same.

By comparing the two acquisitions, it is possible to calibrate the sensitivity of each hole. By convention, the calibration of the central hole is 1. After calibration, emittance projections are shown in Fig. 3.

To evaluate the MCP and the phosphor screen response over time and demonstrate that its reliability is better than that of a scintillator, a first acquisition was made and then a

ISBN: 978-3-95450-257-8 ISSN: 2222-5692 doi:10.18429/JACoW-ECRIS2024-TUP04

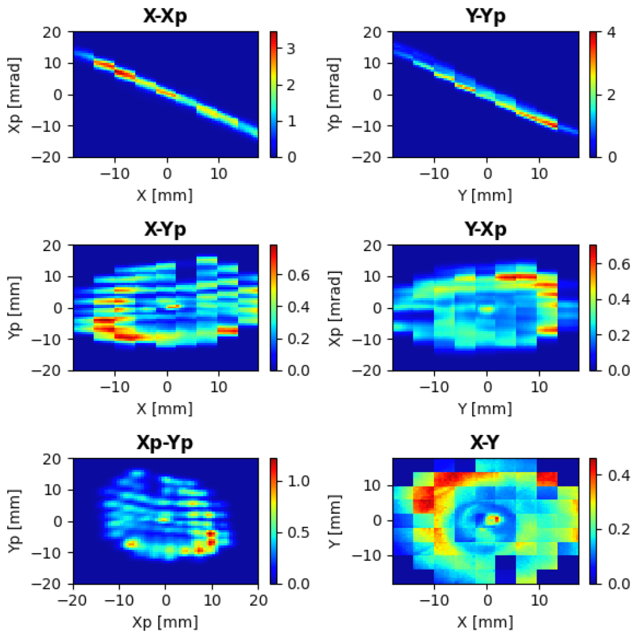

Figure 2: The 6 emittance projections obtained before calibration.

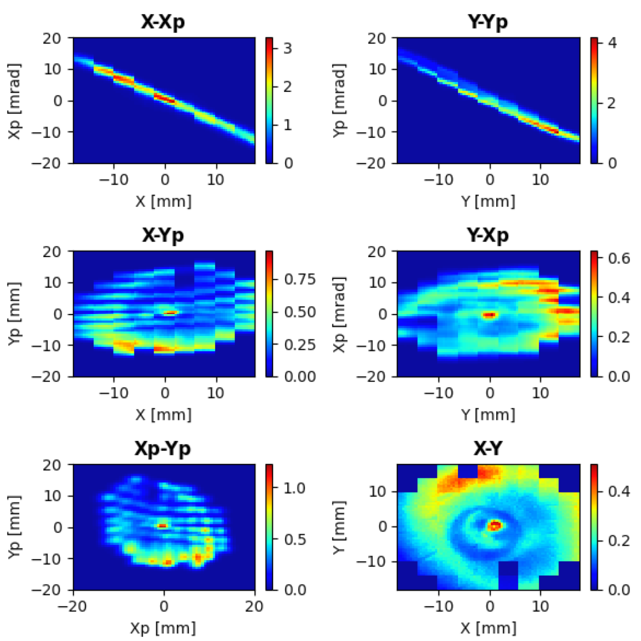

Figure 3: The 6 emittance projections obtained after calibration.

second acquisition was carried out under the same conditions a few moments later (see Fig. 4). The MCP response did not seem to deteriorate in the face of the proton beam, unlike the scintillator used in the first version.

CONCLUSION

In conclusion, this article presents the progress made in the first development of a moving 4D-emittancemeter based on pepperpot technology.

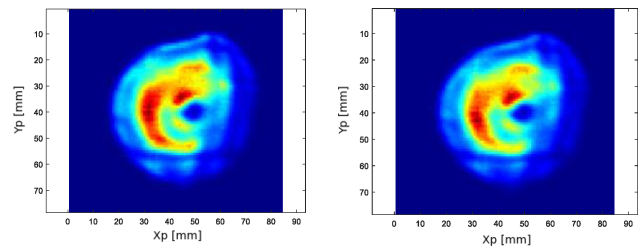

Figure 4: First (on the left) and second (on the right) x'-y'emittance projections.

Initially faced with difficulties with phosphorus scintillators, the study turned to the use of microchannel plates (MCP), because of their reliability over time.

The 4D-emittancemeter displacement system has enabled more accurate and detailed measurements of proton beam emittance projections. In addition, the results obtained validated the MCP as a better alternative to scintillators for such applications.

However, MCP have limitations. They require several elements that are not easy to integrate on a beam line (MCP + P-screens + camera) and cannot differentiate ions and atoms or molecules. Other acquisition methods will be studied and developed in the near future.

REFERENCES

[1] G. Hahn and G.G. Hwang, "Development of a precision pepper-pot emittance meter", in *Proc. Int. Beam Instrum. Conf. 2019 (IBIC'19)*, Malmö, Sweden, pp. 369-372, 2019. doi:10.18429/JACoW-IBIC2019-TUPP027,

[2] R. Cee, C. Dorn, E. Feldmeier, T. Haberer, A. Peters, J. Schreiner, and T. Winkelmann, "Development of a pepper pot emittance measurement device for the HIT-LEBT", in *Proc. Int. Beam Instrum. Conf. 2021 (IBIC'21)*, Pohang, Rep of Korea, pp. 214-217, 2021. doi:10.18429/JACoW-IBIC2021-TUPP12

[3] A. Dumancic, "Conception et réalisation d'un émittancemètre 4D", Ph.D. thesis, Université Paris Saclay (COmUE), Oct. 2019. https://theses.hal.science/tel-02506617

[4] O. Tuske, O. Delferrière, Y. Gauthier, F. Harrault, and Y. Sauce, "Preliminary results of BETSI test bench upgrade at CEA-Saclay", *Rev. Sci. Instrum.*, vol. 90, p. 113305, 2019. doi:10.1063/1.5126634

[5] C. Simon, F. Harrault, F. Senee, and O. Tuske,, "Scintillating screens investigations with proton beams at 30 keV and 3 MeV" in *Proc. IBIC'16*, Barcelona, Spain, Sep. 2016, pp. 273–276. doi:10.18429/JACoW-IBIC2016-MOPG79

[6] A. Dubois, O. Delferriere, Y. Gauthier, Y. Sauce and T. Thibeau, "Evolution of ALISES 3 Light Ion Source at CEA Saclay", *J. Phys.: Conf. Ser.*, vol. 2743, p. 012058, 2024. doi:10.1088/1742-6596/2743/1/012058

[7] H. Kremers, J. Beijers, and S. Brandenburg, "A pepper-pot emittance meter for low-energy heavy-ion beams", *Rev. Sci. Instrum.*, vol. 84, p. 025117, 2013. doi:10.1063/1.4793375

ISBN: 978-3-95450-257-8 ISSN: 2222-5692 doi:10.18429/JACoW-ECRIS2024-TUP05

RF AND MULTIPACTOR SIMULATIONS IN THE PLASMA CHAMBER OF THE SILHI PROTON SOURCE

Mathias Barant†, Augustin Dubois, Guillaume Ferrand, Juliette Plouin, Olivier Tuske
Commissariat à l'Energie Atomique et aux Energies Alternatives (CEA-Irfu),
Institut de Recherche sur les lois Fondamentales de l'Univers, Gif-sur-Yvette, France

Abstract

In the scope of high current protons sources simulations, we tried to simulate the plasma chamber of the SILHI proton source with HFSS. This work focuses on the RF and multipactor simulation close to the boron nitride window.

INTRODUCTION

The CEA Saclay develops and produces ECR sources for various projects. In particular, several sources have been developed for high-intensity proton and/or deuteron beams, as the SILHI and ALISES sources. Currents typically vary between 5 mA (Spiral 2) to 125 mA (IPHI, IFMIF), and several test benches have been assembled, BETSI and PACIFICS, to analyse these sources [1].

ECR sources, in general, require the production of electrons, which, by interacting with the molecules and ions of the gas, produce the ions beam. Part of these electrons are produced by a dielectric window, (here made of boron nitride), possessing very high primary and secondary electron emission coefficients [2].

Electron production is certainly mainly due to secondary emission. Among the different processes that generate secondary emission, the multipactor, under certain conditions, can be one of them. It has been widely described for example on the ceramic windows of high-power RF couplers [3]. The objective for RF couplers is in principle to minimize this phenomenon. Here, we try to show that the multipactor can affect the production of electrons at the ceramic level of an ECR source.

For this, we have simulated the RF field on the boron nitride, in order to describe the field at the dielectric level. Then, we tried, based on some analytical calculations, to estimate the best conditions to get (or to do not get) multipactor.

ABOUT MULTIPACTOR

The multipactor is a potential source of secondary electrons in ECR sources, and Boron Nitride (BN) has a high secondary emission coefficient [2]. So, the primary electrons produced by the BN ceramic can themselves produce new electrons, if their trajectory brings them back on the ceramic.

The primary and secondary electrons follow a trajectory defined by the RF electromagnetic field at 2.45 GHz, at the time of their appearance (or their initial phase), as well as by the external magnetic field. If the kinetic energy of the primary electron acquired thanks to the RF field is sufficient, secondary electrons can be produced.

The ionization energy (or gap energy) of 5.8 eV for H-BN (Hexagonal) [4] gives an estimate of the minimum energy to produce secondary electrons.

Moreover, if an electron comes back after an whole number of RF periods, the secondary electron starts with the same phase, and thus, follows the same trajectory, and the phenomenon continues indefinitely. The number of electrons increases exponentially until reaching saturation, which depends on the available electrons, the available RF power, and the space charge generated. This phenomenon was known as multipactor.

To test our hypothesis, we modeled the distribution of electromagnetic fields in the cavity with HFSS software and identified potential areas producing multipactor. An analysis of the electron trajectory near the window is proposed.

HFSS SIMULATION

These simulations were realised with the HFSS software. We reproduced the cavity of the plasma chamber of the SILHI source, measuring 45 mm in radius and 100 mm in length, and the boron nitride plate with a thickness of 2 mm. The coupler of SILHI was simulated with its three ridges.

The waveguide was modelled by a 550 mm long line. The ATU (Automatic Tunning Unit) was modelled by a single piston that modifies the coupling of the ECR cavity.

We have calculated the electric field on the BN for several position of piston. For each position of the piston, we have modified its penetration to adapt the cavity by minimizing the reflected power. The frequency remained close to 2.45 GHz ± 100 MHz.

To realize the simulation, we defined a port in TE10 mode at the extremity of the waveguide. In a perfect cylinder in the TE mode theory, the electric field is only axial. Here, due to the coupler, the electric field on the longitudinal axis is not zero on the boron nitride window.

The simulation was made for different distances between the piston and the RF cavity, to observe how the piston position affects the RF field on the window. All field patterns are presented at the resonance frequency of the ensemble, which always remains close to 2.45 GHz.

Figures 1 and 2 show that the electric field at the center of the window is very intense (281 kV/m) at 335 mm, but becomes less intense (11.4 kV/m) when the piston position was at 410 mm, for an injected power of 50 W at the extremity of the waveguide. It seems reasonable to imagine that the multipactor acts differently in both cases.

† mathias.barant@cea.fr

ISBN: 978-3-95450-257-8 ISSN: 2222-5692 doi:10.18429/JACoW-ECRIS2024-TUP05

During our experiments with SILHI, we observed that the minimal power to see some "pink" light in the H source was around 50 W. It shows that there are interactions between electrons and gas, even without current emission

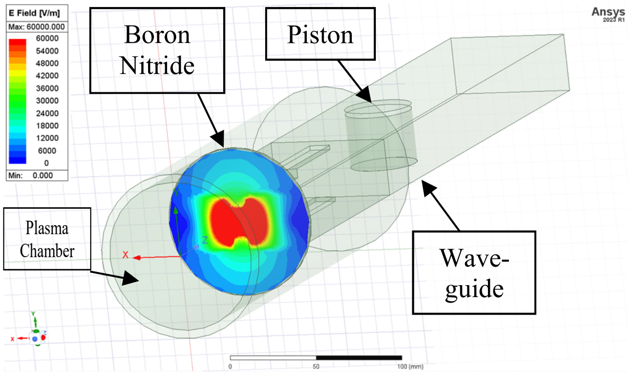

Figure 1: Visualization of E-field at the center of the window for a piston position of 335 mm.

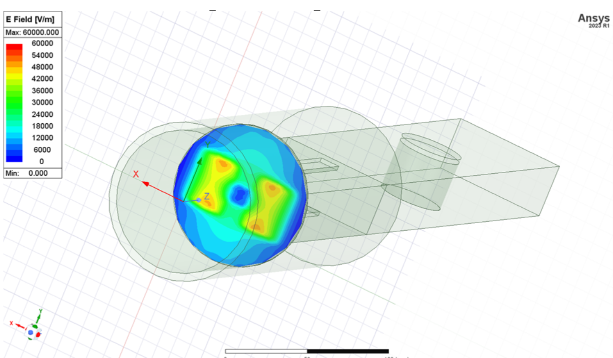

Figure 2: Visualization of E-field at the center of the window for a piston position of 410 mm.

SIMULATION OF THE ELECTRON TRAJECTORY CLOSE TO THE CERAMIC

The general equation of motion of an electron of mass m and charge q in presence of an electromagnetic field is

$$m\frac{d^2}{dt^2}\begin{bmatrix}x\\y\\z\end{bmatrix} = q\left(\begin{bmatrix}E_{rf,x}\\E_{rf,y}\\E_{rf,z}\end{bmatrix} + \begin{bmatrix}0 & B_z & -B_y\\-B_z & 0 & B_x\\B_y & -B_x & 0\end{bmatrix}\frac{d}{dt}\begin{bmatrix}x\\y\\z\end{bmatrix}\right),$$

in our case, the magnetic field $B_{x,y,z}$ includes a DC and an RF component: $B_{x,y,z} = B_{0,x,y,z} + B_{rf,x,y,z}$. While the electric field has only an RF component $E_{x,y,z} = E_{rf,x,y,z}$. The z axis is the longitudinal axis, and the x axis is the radial axis where E_{rf} is maximal in average. φ defines the initial phase between the electron and the electric RF fields in the resonant cavity

$$E_{rf,i} = E_{1,i}\cos(\omega t + \varphi),$$
$$B_{rf,i} = -B_{1,i}\sin(\omega t + \varphi).$$

We therefore have a first-order differential equation in $\frac{d}{dt}\begin{bmatrix}x\\y\\z\end{bmatrix}$, with constant and sinusoidal terms. The general analytical solution to this type of equation is not developed here.

If B_0 is oriented along the z axis, and E_1 along the x axis, if $\omega \neq \omega_c = \frac{qB_z}{m}$, and the initial speed is zero, the analytical solution is given by

$$\frac{d}{dt}\begin{bmatrix}x\\y\\z\end{bmatrix} = \begin{bmatrix}\cos(\omega_c t) & \sin(\omega_c t) & 0\\-\sin(\omega_c t) & \cos(\omega_c t) & 0\\0 & 0 & 1\end{bmatrix}\begin{bmatrix}C_x\\C_y\\C_z\end{bmatrix} +$$
$$\frac{a_c}{\omega^2-\omega_c^2}\begin{bmatrix}\omega\sin(\omega t+\varphi)\\\omega_c\cos(\omega t+\varphi)\\1\end{bmatrix},$$

with $a_c = \frac{q\cdot E_0}{m}$, and C_x, C_y, C_z are integration constant.

In normal conditions, at $t = 0$, the velocity is close to the electron's thermal velocity, which is given by

$$\sqrt{< V_{th}^2 >} = \sqrt{\frac{3k_BT}{m}} = 115\,000\ \mathrm{m.s^{-1}}.$$

The corresponding kinetics energy is 0.038eV.

In this specific case, the speed along the z axis is constant, thus, primary electrons cannot go back and there is no multipactor. This is the "perfect case", where the B field is longitudinal and the E field is transverse.

However, in an imperfect case, where the longitudinal electric and transverse magnetic fields are different from zero, the multipactor phenomenon can appear.

In this case, the longitudinal electric field tends to accelerate electrons on the z-axis, and the rotation plan of the electrons is not parallel to the window anymore.

The magnetic field for simulations is $B_{0,z} = 78.75$ mT (90% of the ECR magnetic field, 87.5 mT @ 2.45 GHz). The value of the electric field $E_x = 300$ kV/m corresponds to figure 1. Then we applied an x component to the magnetic field $B_{0,x} = 23.3$ mT and a small z component to the electric field $E_z = 10$ kV/m to force multipactor.

Figure 3(abc) shows the results along x, y and z axes at different phases. Figure 3c shows that, for a phase $\varphi = 1.1220$ rad, the electron hits the wall after exactly one RF period. The dotted lines represent also the trajectory of electron. Figure 4 shows that the speed of the electrons after one period was around 10 000 km/s. This correspond to an energy about 310 eV, enough for secondary emission.

This demonstrates that, in these conditions, multipactor is likely to appear.

EXPERIENCES WITH SILHI [5]

We have carried out some experiments with the SILHI source to observe the influence of the pistons position on the beam generation.

We have used the following components (see Figure 5): a 2.45 GHz magnetron (1) and its circulator (2), several waveguides with different lengths (3), a bidirectional coupler (4), a 3-pistons ATU (5), a 3-pistons MTU (6) and the SILHI source (7).

ISBN: 978-3-95450-257-8 ISSN: 2222-5692 doi:10.18429/JACoW-ECRIS2024-TUP05

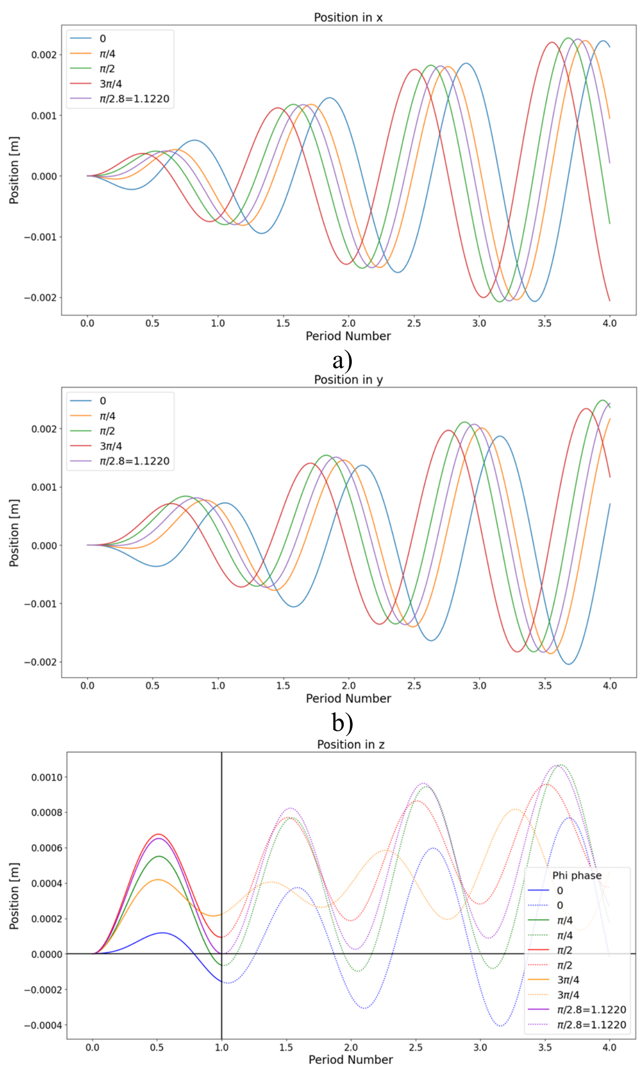

Figure 3: Electron positions in x, y and z as a function of the number RF periods. If the electron hits the window after 1 period, multipactor can appear.

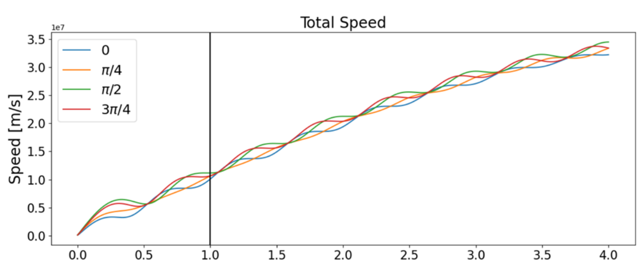

Figure 4: Total speed as a function of period number.

We minimized the reflected power with presence of plasma with the ATU for different configurations of the MTU (Manual Tunning Unit). Figure 6 shows an example of beam current exiting the cavity.

We observed that the required power to launch the source could vary significantly from one configuration to another – from 450 W to 900 W, to get a stable beam – for the same reflected ratio. In some configurations, the source did not work at all.

We also observed that, in some cases, having an inhomogenous B field (there are two coils that can be separately driven with current sources), with a radial component, reduced the required input RF power.

This does not demonstrate that the multipactor comes into play, but it at least shows that the shape of the RF field on the boron nitride wall could be critical.

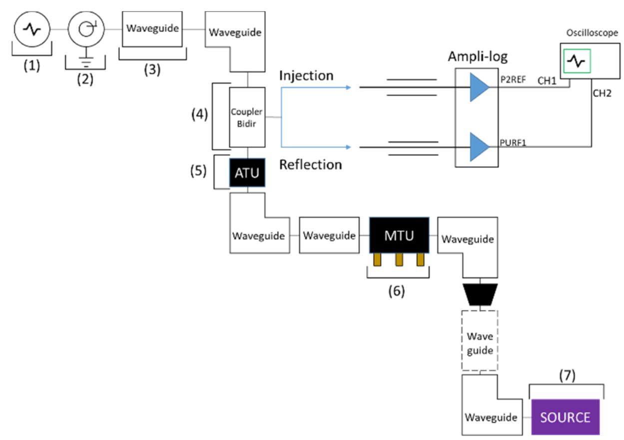

Figure 5: Diagram of the SILHI source test.

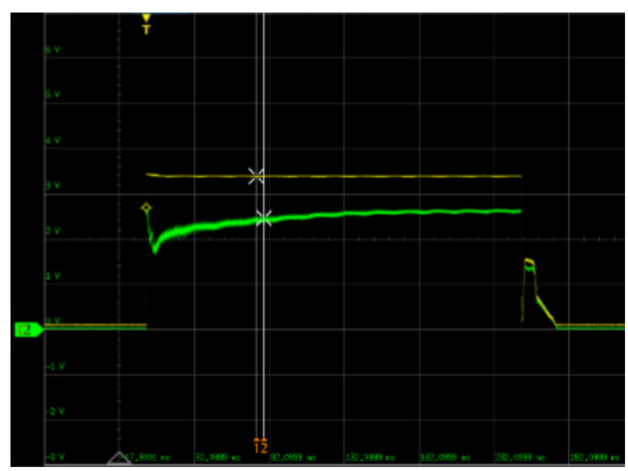

Figure 6: Magnetron pulse gate (yellow signal). Beam current (green signal). Time abscissa is 50 ms per division. Arbitrary ordinate unit.

CONCLUSION

Thanks to the simulations realised with HFSS, we were able to show that the electric field on the boron nitride can greatly vary with the source settings. The analysis showed that this could affect the appearance of multipactor on the window.

Indeed, we observed experimentally with the SILHI source that the position and adjustment of the ATU and MTU have a significant impact on the required RF power.

The next step will be to develop a source, with potentially different window geometries, targeting to maximize the multipactor in simulation and observe the effect on the ion beam.

ISBN: 978-3-95450-257-8 ISSN: 2222-5692 doi:10.18429/JACoW-ECRIS2024-TUP05

REFERENCES

[1] O. Tuske, G. Adroit, O. Delferrière, D. De Menezes, Y. Gauthier, "BETSI, a new test bench for ion sources optimization at CEA SACLAY," *Rev. Sci. Instrum.*, vol. 79, no. 2, Feb. 2008. doi:10.1063/1.2805625

[2] L. Huang and Q. Wang, "Study on Secondary Electron Yield of Dielectric Materials," *J. Phys. Conf. Ser.*, vol. 2433, no. 1, p. 012002, Feb. 2023. doi:10.1088/1742-6596/2433/1/012002

[3] G. Devanz, "Multipactor simulations in superconducting cavities and power couplers," *Phys. Rev. Spec. Topics - Acc. Beams*, vol. 4, no. 1, Jan. 2001. doi:10.1103/physrevstab.4.012001

[4] M. J. Powers and M. C. Benjamin, "Observation of a negative electron affinity for boron nitride," *Appl. Phys. Lett.*, vol. 67, no. 26, pp. 3912–3914, Dec. 1995. doi:10.1063/1.115315

[5] R. Gobin, P.-Y. Beauvais, D. Bogard, G. Charruau, O. Delferrière, D. De Menezes, A. France, R. Ferdinand, Y. Gauthier, F. Harrault, J.-L. Jannin, J.-M. Lagniel, P.-A. Leroy, P. Mattéi, A. Sinanna, and J. Sherman, "High intensity ECR ion source ($H+, D+, H-$) developments at CEA/Saclay," *Rev. Sci. Instrum.*, vol. 73, no. 2, pp. 922–924, Feb. 2002. doi:10.1063/1.1428783

ISBN: 978-3-95450-257-8 ISSN: 2222-5692 doi:10.18429/JACoW-ECRIS2024-TUP06

WIEN FILTER UPGRADE AND MEASUREMENT FOR BETSI TEST BENCH*

A. Dubois†, O. Tuske‡, O. Delferrière, Y. Gauthier, Y. Sauce
Commissariat à l'Energie Atomique et aux Energies Alternatives (CEA-Irfu),
Institut de Recherche sur les lois Fondamentales de l'Univers, Gif-sur-Yvette, France

Abstract

During first operation of SILHI in 1995 at CEA Saclay, a velocity filter diagnostic (Wien Filter) was installed on the LEBT (Low Energy Beam Transport), analysing the 100 mA of protons at 95 keV. The device was used many years providing beam proportion measurements on the beam axis. Unfortunately, it was damaged while handling and was no longer working as intended. This paper describes the maintenance and upgrade of the diagnostic as well as the first beam proportion figures with ALISES v2 ion source.

INTRODUCTION

A velocity filter or also called a Wien Filter combines a constant dipole with a varying electric field, perpendicular to the magnetic forces. When a sample of the beam enters the dipole, the particles are naturally deviated thanks to the magnetic field. By applying an electrostatic force, these particles are brought back on the beam axis and can be collected on an isolated wire. Depending on the mass of the species, there is a specific value of bias to counter act the dipole effect. For the same energy, the lighter the particle, the stronger the electric field is required. So with the Wien Filter it is possible to estimate the proton fraction of the beam of an ion source. This value is an important value for ion source characterization. The second question that was never discussed before: does this proton fraction uniform all over the transverse plane?

This Wien Filter was developed in the 90s for SILHI ion source [1, 2], to analyse the proportion of H^+, $H_2{}^+$ and $H_3{}^+$ as well as measuring the total beam intensity. It was later installed on BETSI test bench [3] to characterize the new sources developed at Saclay, especially the ALISES ion source family [4, 5]. However, the clearance between the diagnostic and the vacuum chamber is very tight and it got stuck during the removal of the Wien Filter from BETSI test bench, damaging the actuator and the measurement system.

DESCRIPTION

This Wien Filter (see Fig.1) is composed of a water cooled beam-stopper (A) that can handle 10 kW beam power. It is equipped with a removable tantalum diaphragm (B) drilled with a ø 250 µm diameter hole and 0.2 mm in length to let a very small part of the beam through.

Right behind this diaphragm, the measurement unit is composed of a Permanent Magnet structure (C), two electrodes (D), a charge collecting wire (E) and a negative polarized electron repeller (F). All these elements are enclosed in a box constructed of 4 mm thick ARMCO plates (G) bolted together to create a magnetic shield. The side panels of this box are hollowed with an array of holes to allow the pumping of the inside.

The (C) dipole is formed by six permanent magnets, distributed equally over and under the beam, originally designed to create a 0.19 T magnetic field on the beam axis. During the reassembly of the measurement unit, it was measured at 0.183 T with a Hall probe, which remains acceptable to separate Proton from molecular $H_2{}^+$ and $H_3{}^+$ at 95 keV energy.

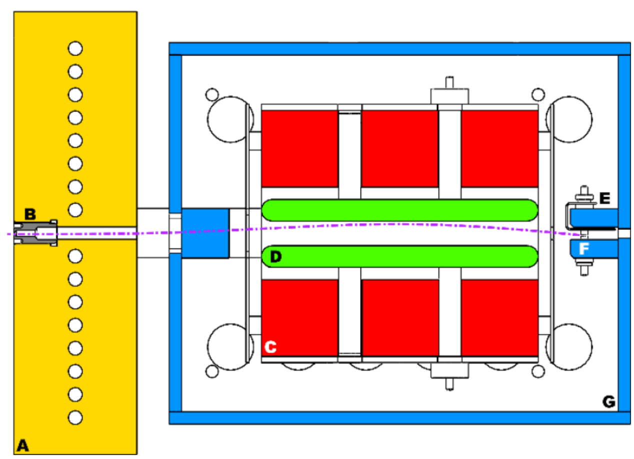

Figure 1: SILHI Wien Filter cross section.

The two stainless steel electrodes (D) are placed inside the magnetic system with the following dimensions, 90 mm along the beam axis, 36 mm in width, 7 mm thick and spaced 8 mm apart. Both of them are connected to SHV 10 kV feedthrough with Kapton insulated wire.

Coming after the deviation structure, an isolated ø 0.25 mm Tungsten wire (E) collects the particles, measuring their intensity. A thin stainless steel (F) sheet connected to another SHV feedthrough sits over the Tungsten wire to act as an electron repeller electrode.

In order to measure the beam intensity on the beam stopper (A), it must be isolated from the measurement unit and the actuator. Moreover, the measuring unit has to be mechanically mounted on the beam-stopper to ensure a good alignment of the sampling pinhole (B) and the collecting wire (E). The size of the measuring unit (see Fig. 2) left very little space to design a stiff assembly. Therefore, the mechanical attachment of the iron box to the shield was not sturdy

* Work supported by the Commissariat à l'Energie Atomique et aux Energies Alternatives (CEA, France)
† augustin.dubois@cea.fr
‡ olivier.tuske@cea.fr

ISBN: 978-3-95450-257-8 ISSN: 2222-5692 doi:10.18429/JACoW-ECRIS2024-TUP06

enough to withstand the bound, creating a great misalignment of the wire with the sampling pinhole. To repair the Wien filter, it was compulsory to change the actuator and the system supporting the measurement unit to the diaphragm.

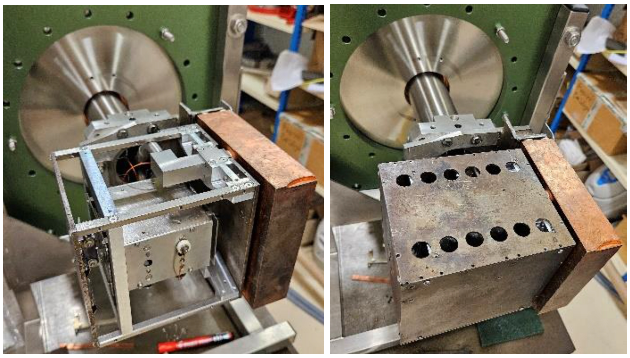

Figure 2: Measuring unit assembly.

MODIFICATIONS

The LEDA (*Laboratory of Study and Development for Accelerators*) developed its own motorized actuator, which was designed to accept the heavy-duty diagnostics such as Emittancemeter [6] or Faraday Cup or in this case a Wien Filter. With this device, the bellow is now outside of the vacuum chamber and the mounting interface of the diagnostic is close to the CF250 actuator flange. In parking position, and thanks to the improved stroke, from 150 mm to 250 mm, the distance between the permanent magnets and the beam is increased by 100 mm, reducing the perturbation induced by the permanent magnets on the beam.

The Stögra stepper motor SM56 used on the first actuator was upgraded with a Neugart PL40 planetary gearbox, compatible with the LEDA actuator motor interface.

The ability of measuring the total beam intensity with the collimator is not required any more, enabling the design of a new frame to hold the measurement unit. In the previous design, the ARMCO plates were bolted together with small screws and were attracted by the magnet during assembly. Each maintenance tasks were quite tedious with a risk of damaging a part or a cable inside of the measurement system. The new frame follows the exact internal dimensions of the box, each plate are independently positioned and bolted on the new structure. This support is made out of aluminum for its amagnetic properties and lightweightness.

MEASUREMENTS SETTINGS

The measurement campaign was performed with the ALISES v2 source biased at different voltage, from 35 kV to 50 kV [7]. The extracted intensity is around 30 mA reduced to 18 mA on the beam dump after going through two solenoids and a diaphragm. The beam pulse is set up at 10 ms and 7 Hz. The first measure is done in the center of the beam, then the diagnostic is moved up 5 mm for each 9 other positions. The diagnostic is 850 mm away from the extraction point of the ion source because the diagnostic chamber is located after the first solenoid. This magnet stayed off not to alter the trajectories of the measured species extracted from the ion source.

As for the deviation plates, one is connected to the Trek amplifier (Trek 10/10B-HS) for ±10 kV and the other one grounded with a special connector plugged on the feedthrough.

SIGNAL TREATMENT AND DATA ANALYSIS

A Labview program developed specifically for this diagnostics operates the Wien Filter. It communicates with the servomotor and the Trek amplifier to respectively move the diagnostic in the beam in the transverse plane and variate the HV voltage ie the electric field between the deflecting plates to make the mass selection. The collecting wire current is amplified by a front-end electronic and is acquired and synchronized with the beam timing trigger. The sampling frequency is set 100 kHz for a 11 ms windows, giving a list of 110 points to describe the pulse behaviour over time. This list of points are saved for each HV voltage value within the range of the HV ramp at each position of the Wien filter position inside the beam. Then they are averaged and subtracted to each pulse to remove the measure noise and obtain “filtered data”.

In order to reconstruct the mass spectrum (see Fig. 3) at a set transverse position, all these filtered data are averaged and the raw spectrum obtained is corrected with a second degree polynomial baseline fit. From the 10 ms initially measured, 3 ms are cropped at the beginning of the pulse to remove the beam formation phenomenon. In the following graph, the beam current on the wire is plotted over the HV value of the biased plates. The negative signal seen after each peak is always present even with a -1kV bias voltage on the electron repeller.

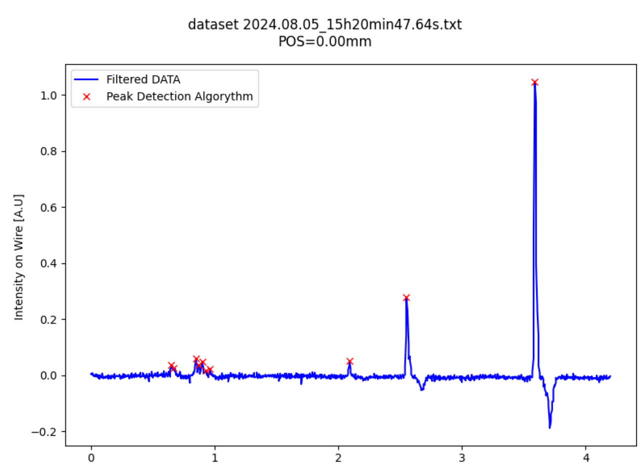

Figure 3: Mass spectrum of ALISES v2 at 35 keV.

A simple algorithm was used to detect the peak position of 10 different masses extended from one to 32 amu. The list of detected mass was determined by the position of the peak with respect to most intense proton peak and the squareroot of the mass ratio when the Wien filter stands on the beam axis (Eq. (1)).

$$V(ion) = V(H^+) * \sqrt{\frac{m_{H^+}}{m_{\text{ion}}}}\,. \qquad (1)$$

Table 1 shows all the detected peak associated to their mass. Most of them are related to oxygen and nitrogen molecules, presuming a leak in the ion source. As for the peak number 15, it could be either CH_3 or NH, but it is assumed to be NH since there is no C(amu = 12) peak detected. A measure with a RGA (Residual Gas Analyzer) on the LEBT is planned to confirm this hypothesis.

Table 1: Mass of Elements

Element	H	H_2	H_3	N	NH	O	OH	H_2O	N_2	NO
AMU	1	2	3	14	15	16	17	18	28	30

RESULTS

The intensity of all peak allows calculating the fraction of all element and more particularly the proton fraction of the ion source.

At different extraction energy (35, 40, 45 and 50 kV) on beam axis, the proton fraction is found to be around 65 and 70 %, 18 % for H_2^+, 3 % for H_3^+ and 9 % for the remaining heavier elements (Fig. 4). The proton fraction value is very close to what is expected: when adjusting the LEBT solenoids to transport the proton species, the normalized transmitted intensity collected on the LEBT beam Stopper over the power supply drain current at the same moment, respectively 20 and 30 mA gives around a 66 % proton fraction. It is possible to assume that the bias of the source does not affect the plasma formation and the type of particles created.

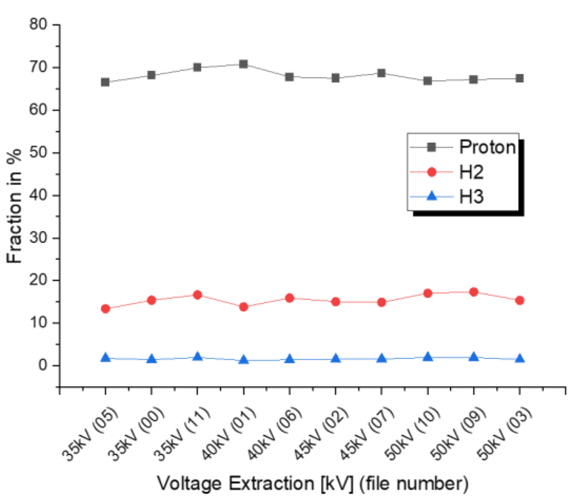

Figure 4: Evolution of the proton proportion with respect to the beam energy.

The next series of measures were done at different height in the beam transverse plane within the same range of beam energy as previously done. The following Fig. 5 only represents the interesting value, the proton fraction. At 35 kV and 40 kV, this fraction stays constant over the transverse plane. However, at higher beam energy, the value is decreasing after a certain radius, 25 mm for 45 kV and 15 mm for 50 kV. This phenomenon is directly related to the extraction conditions of the ion source. Since the bias is higher, the particles extracted are less divergent and the beam transversal size is therefore smaller at the diagnostic position. When the measurement is done far from the beam center, the wire collects less particles, and so the signal over noise ratio is decreasing making the result difficult to analyze in term of ratio.

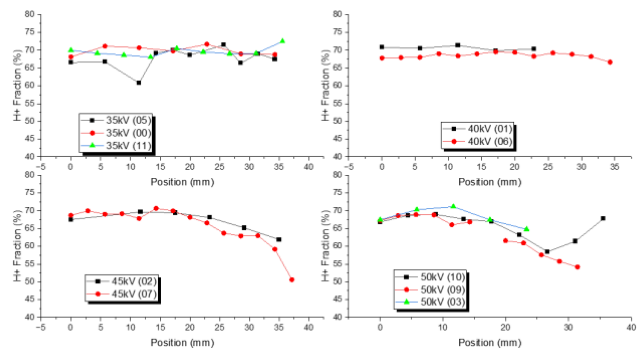

Figure 5: Evolution of the proton proportion along the beam transversal plane at different source bias.

CONCLUSION

The upgrade of the Wien Filter allowed us to measure the proton fraction at the exit of ALISES v2 ion source. At first, the proton fraction obtained on the axis is coherent with measured transmission in the LEBT with a 65 % value for both cases. Secondly, thanks to the motorized actuator, the proton fraction along transverse plane seems to be uniform, as long as beam exists. This Wien Filter is operational and ready to be compared to a Doppler shift measure, and a RGA to confirm the species detected.

REFERENCES

[1] J.-M. Lagniel *et al.*, “Status and new developments of the high intensity electron cyclotron resonance source light ion continuous wave, and pulsed mode”, *Rev. Sci. Instrum.*, vol. 71, no. 2, pp. 830–835, 2000. doi:10.1063/1.1150306

[2] R. Gobin *et al.*, “Last results of the continuous-wave high-intensity light ion source at CEA-Saclay”, *Rev. Sci. Instrum.*, vol. 69, pp. 1009–1011, 1998. doi:10.1063/1.1148546

[3] O. Tuske, O. Delferrière, Y. Gauthier, F. Harrault, and Y. Sauce, “Preliminary results of BETSI test bench upgrade at CEA-Saclay”, *Rev. Sci. Instrum.*, vol. 90, p. 113305, 2019. doi:10.1063/1.5126634

[4] O. Delferriere, Y. Gauthier, R. Gobin, O. Tuske, and F. Harrault, “Development of a Compact High Intensity Ion Source for Light Ions at CEA-Saclay”, in *Proc. ECRIS’16*, Busan, Korea, Aug.-Sep. 2016, pp. 73–75. doi:10.18429/JACoW-ECRIS2016-WECO02

ISBN: 978-3-95450-257-8 ISSN: 2222-5692 doi:10.18429/JACoW-ECRIS2024-TUP06

[5] O. Tuske *et al.*, "For intense proton beam production with compact ion sources: the ALISES ion source family developed at CEA Saclay", *J. Phys.: Conf. Ser.*, vol. 2743, p. 012057, 2024. doi:10.1088/1742-6596/2743/1/012057

[6] O. Tuske *et al.*, "ESS Emittance Measurements at INFN CATANIA", in *Proc. Int. Part. Accel. Conf. (IPAC'17)*, Copenhagen, Denmark, May 2017, pp. 123–125. doi:10.18429/JACoW-IPAC2017-MOPAB023

[7] O. Delferriere *et al.*, "ALISES II source is still alive", in *Proc. ECRIS'24*, Darmstadt, Germany, Sep. 2024, p. MOP03. doi:10.18429/JACoW-ECRIS2024-MOP03

ISBN: 978-3-95450-257-8 ISSN: 2222-5692 doi:10.18429/JACoW-ECRIS2024-TUP07

MODIFICATION OF THE FLEXIBLE PLASMA TRAP FOR HIGH-INTENSITY METAL ION BEAMS PRODUCTION

C. S. Gallo*, A. Galatà, G. R. Mascali, INFN-Laboratori Nazionali di Legnaro, (Padova), Italy
S. Marletta, D. Mascali, G. S. Mauro, S. Passarello, A. Pidatella, A. D. Russo, G. Torrisi
INFN-Laboratori Nazionali del Sud, Catania, Italy

Abstract

NQSTI (National Quantum Science and Technology Institute) is the enlarged partnership on QST established under the National Recovery and Resilience Plan (NRRP) funded by the European Union – NextGenerationEU. In this framework, there is a growing interest in the availability of mA beams of singly charged (1+) metallic ions to realise quantum devices. To satisfy this request, the joint INFN Laboratories LNS and LNL proposed to modify the Flexible Plasma Trap (FPT), installed at LNS, thus transforming it into a simple mirror Electron Cyclotron Resonance Ion Source (ECRIS). This contribution describes the various technical solutions that will be adopted, foreseeing novel radial RF and gas/metal injection systems, focusing particularly on the design and simulations of a flexible extraction system capable of handling different beam intensities and ion species. Specifically, the project targets the production of high-intensity beams of singly charged ions such as Fe^{+}' and Ba^{+}, highlighting the versatility and innovation of the proposed modifications.

INTRODUCTION

Within the NextGeneration EU project NQSTI (National Quantum Science and Technology Institute), the scope of the Task 3.1 of Spoke 3 is to develop novel atomic/molecular systems to extend coherence time in quantum system. In fact, there is an active field of research in the quantum technologies concerning the measure of the permanent electric dipole moment of specific molecules' electrons in a solid matrix, looking for evidence of CP violation [1]. This atomic-embedding in low-temperature solid matrix conventionally resorts to glow discharge chamber and electrostatic elements to select and transport ions to be embedded [2]. The two INFN Laboratories LNL and LNS have studied novel techniques to produce isotopically enriched metallic ion beams (iron, barium), with intensities in the mA range end energies of tens of keV. This will be accomplished by proper modifications of the Flexible Plasma Trap (FPT) [3], installed at LNS and used to date for fundamental studies of magnetically confined plasmas, thus turning it into a simple mirror Electron Cyclotron Resonance Ion Source (ECRIS) [4]. This contribution describes the innovative technical solutions adopted, with greater emphasis to the design of the extraction system through numerical simulations. Finally, preliminary results of the beam optics studies will be also reported.

* carmelo.gallo@lnl.infn.it

UPGRADES OF THE FLEXIBLE PLASMA TRAP

The Flexible Plasma Trap (FPT) is an ECR plasma-based facility present at the INFN-LNS to trap ionised particles in plasma and perform in-plasma interdisciplinary measurements. The FPT magnetic field is provided by means of three solenoids, which allow the tuning of the field profile. The plasma can be generated in both simple mirror and quasi-B-flat configuration, adequately tuning the coils currents. The RF power up to 500 W is injected through a WRD 350 waveguide entering radially the trap [5], at frequencies from 3 to 7 GHz, leaving the longitudinal axis to the access of plasma diagnostics. As being a trap, ions' extractions have never been attempted and thus no extraction system has been developed so far. The modifications to the Flexible Plasma Trap (FPT) have been focused on implementing innovative metal/radiofrequency injection and beam extraction systems, which are crucial for upgrading FPT to an ion source and optimizing the production of singly charged metallic ion beams. With reference to Fig. 1, the key upgrades include the following listed below.

Radial RF and Gas/Metal Injection

The FPT will be equipped with a radial injection of radiofrequency (RF) through a WRD 475, working at 5-7 GHz, and a radial gas/metal injection system. This will improve the power coupling to the plasma, as well as the efficiency of metals ionisation, thus increasing the intensity of the extracted beam.

Advanced Diagnostic Systems

Plasma and extraction conditions will be monitored through a Langmuir probe and an optical emission spectroscopy (OES) quartz window. These diagnostic tools will allow for precise assessment of plasma parameters, thus facilitating the optimization of the source.

Flexible Extraction System

A three-electrode (accel-decel) extraction system has been designed to produce beams with suitable quality for isotopic selection. We conceived a flexible design that enables the extraction gap to be adjusted without breaking the vacuum, adapting the system to the specific requirements of the produced beam (a more detailed description will be given in the next section).

DESIGN OF THE EXTRACTION SYSTEM

The requirements to fulfil the goal of task 3.1, Spoke 3 of the NQSTI project concern the production of a currents

ISBN: 978-3-95450-257-8 ISSN: 2222-5692 doi:10.18429/JACoW-ECRIS2024-TUP07

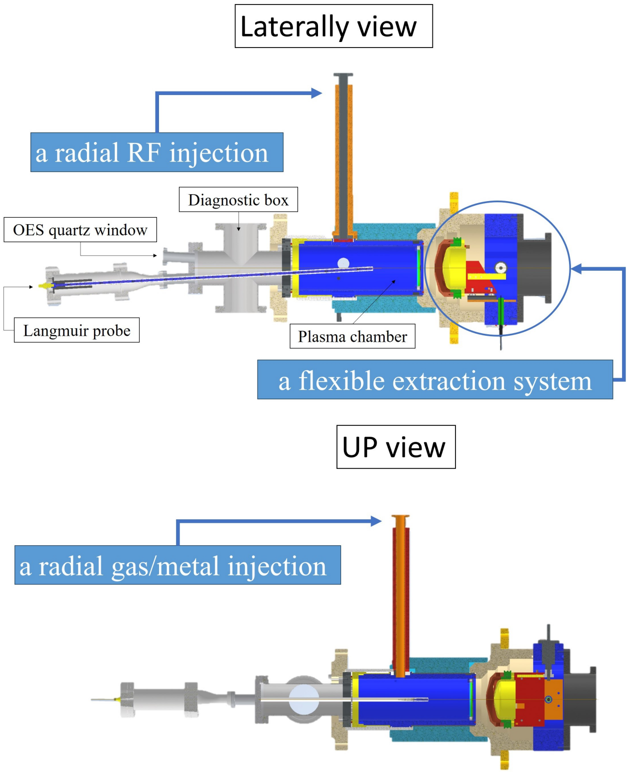

Figure 1: Schematic view of the Flexible Plasma Trap (FPT) highlighting the radial RF injection system and the advanced diagnostic components, the radial gas/metal injection system and the flexible extraction system designed for optimal beam extraction.

≥1 mA of singly charged medium/heavy metallic ions (iron in the first experimental phase, barium in the second one). This level of intensity in known to be a challenge, due to the high contribution of the space charge to the beam quality. This last aspect is very relevant for the project because it influences the ability to reach the desired resolution for isotopes separation, especially for heavy elements (~1/200 for Barium). In the first experimental phase, we plan to verify the ability of FPT to produce the required intensity by proceeding through a preliminary step, that is the extraction of 5 mA of protons. In that case the FPT will produce a plasma of pure hydrogen. Then, iron will be extracted by creating a helium plasma where iron vapours produced by a resistive oven will flow and be ionized. By keeping the same total extracted current as in the case of hydrogen, it has been reasonably estimated a beam ratio of 80 %–20 % between helium and iron (this last one including all the stable isotopes). The design and construction of an extraction system able to handle the above-mentioned intensities is part of the modification of FPT. Such system should be able to:

- Extract beams with different masses/intensities by employing a common design;
- Produce beams with a quality suitable to reach the required resolution for isotopic separation;
- Employ an extraction voltage not higher than 35 kV to ensure proper high voltage insulation.

The choice fell on a common three electrodes (accell-decel) extraction system, with the possibility to vary the extraction gap without breaking the vacuum to adapt it to the extracted intensity. The design has been validated using the numerical code IBSsimu [6], a Vlasov solver able to solve the Poisson equation including the potentials applied to the electrodes and the space charge generated by the extracted beam, then tracing the motion of a given number of particles resembling the whole beam.

The extraction hole has been fixed to 3 mm in radius, a good compromise between the expected extracted current density and initial beam dimensions. Before proceeding to the design, some preliminary evaluations has been carried out, the first being the contributions to the beam emittance. In fact, the beams of interest for NQSTI will be extracted from a magnetized plasma, so two possible contribution could be expected: the ion temperature and the trap magnetic fringing field at extraction. The latter is a trap's parameter (0.3 T maximum in the case of FPT), while the former is quite difficult to be measured but reasonable values could be guessed. With the use of two handy formulas [7], a comparison between the two contribution has been done considering ion temperatures ranging from 0.1 eV to 10 eV: except for the highest value of the magnetic field and the lowest of ion temperature, the major contribution comes from this last parameter. This made easier the second preliminary evaluation, that is the main extraction system parameters starting from considerations concerning the Child-Langmuir (CL) limit [8]. Normally, it is a good practice to configure the extraction system in order the beam perveance to be a half of the one foreseen by the CL limit: considering the limitations on the voltage applicable and starting from an extraction gap around 30 mm (in order not to have a too high electric field leading to possible sparks), this limit was evaluated for the two steps foreseen for the first experimental phase. For protons, a CL limit of 10 mA is obtained with an extraction voltage of 30 kV, a puller voltage of −3 kV and an extraction gap of 30 mm. For iron, extracting 4 mA of He^+ and 1 mA of Fe^+ (supposed consisting entirely of the mass 54) is equivalent to a proton current of around 15 mA: unfortunately, in this case the CL limit gives an extraction voltage higher than 60 kV for an extraction gap of 27.5 mm, being above the limit of FPT. It has to be pointed out that the CL limit strictly holds for particles generated by a fixed emitter with zero velocity: in the case of the extraction from a plasma particles are emitted with several eV of longitudinal energy, having to satisfy the Bohm criterion [9]. This leads to an increase of the CL limit because the condition of zero electric field at the emitter does not prevent necessarily ions form exiting the plasma. In light of all this, we launched systematic numerical simulations by varying, in the case of hydrogen: the extraction voltage (V_s), the puller voltage (V_p) and the extraction gap (d). All the simulations considered a beam space charge compensation of 90 %.

With the aim at optimizing the beam transport downstream the extraction system, the criteria adopted to choose a proper configuration have been:

ISBN: 978-3-95450-257-8 ISSN: 2222-5692 doi:10.18429/JACoW-ECRIS2024-TUP07

- A RMS emittance (ϵ_{rms}) as low as possible;
- A RMS maximum divergence (x'_{rms} for the x axis, z being the axis of propagation) not higher than 40 mrad;
- The highest beam percentage within four times the rms emittance.

Table 1 shows all the simulated configurations. It has been found that, for voltages equal to or higher than the evaluated CL limit, the beam appeared to be over-focused with a dense core and a rarefied halo: a direct view of this effect is visible in Figs. 2 and 3, showing the 2D plots of the extracted beam for 37 kV/−1 kV/37 mm and 30 kV/−1 kV/30 mm (V_s, V_p, d).

Table 1: Configurations of the Extraction System Simulated for H^+ Extraction

Extraction voltage [kV]	Puller voltage [kV]	Gap [mm]
35	−1	37
30	−1	37
30	−1	35
30	−1	30
20	−1	30

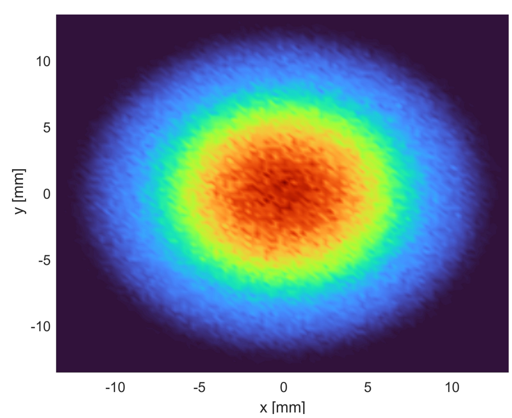

Figure 2: 2D plot of the proton beam extracted at V_s=35 kV, V_p= −1 kV and d=37 mm.

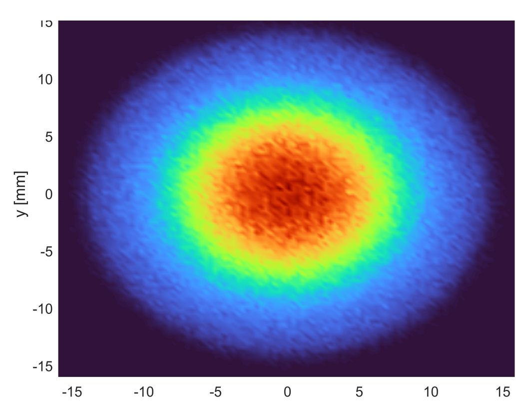

Figure 3: 2D plot of the proton beam extracted at V_s=30 kV, V_p= −1 kV and d=30 mm.

The optimization of the parameters proceeded, with the best results given by the configuration 20 kV/−1 kV/30 mm (V_s, V_p, d): figure 4 shows the beam distribution along the x axis.

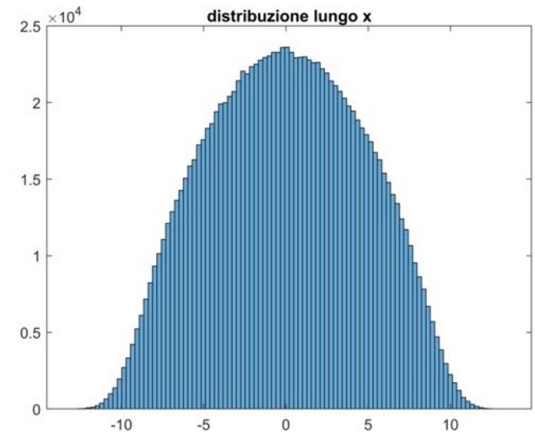

Figure 4: Proton beam distribution along the x axis at V_s=20 kV, V_p= −1 kV and d=30 mm.

It is worth noticing that the beam is very well distributed, resembling almost a Gaussian shape. Concerning the selection criteria, this configuration gave ϵ_{rms} ~8 mm·mrad, x'_{rms}= 26.6 mrad and the 88 % of the beam within 4*ϵ_{rms}. Once the best configuration to extract a proton beam has been found, the numerical study proceeded on the composed beam He^+-Fe^+ starting from V_s=35 kV (the highest possible value) and optimizing V_p and d. Despite the allowed value for V_s was considerably lower than the expected CL limit, good beam properties where found by setting V_p=−5 kV and d=27.5 mm: Figure 5 shows the total beam emittance along the x axis for the Fe^+ beam. It can be clearly seen that both the beam dimension and divergence are fairly small, with a x'_{rms} even smaller than in the case of hydrogen (20.6 mrad) and almost the same percentage within 4*ϵ_{rms}.

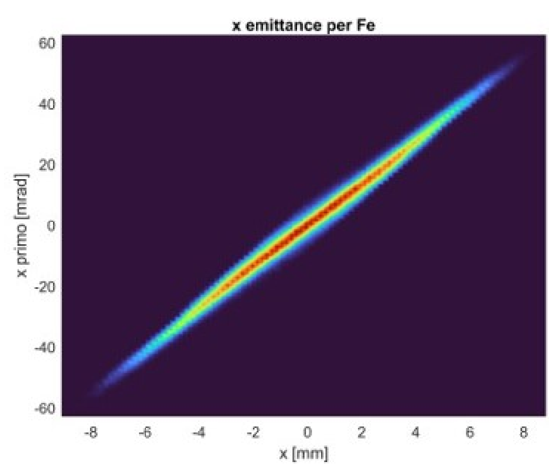

Figure 5: Total emittance along the x axis of a 1 mA Fe^+ beam at V_s=35 kV, V_p= −5 kV and d=27.5 mm.

Starting from the beam parameters found for protons extraction, a preliminary study of the beam optics in the downstream beamline started, to verify the feasibility to reach the

ISBN: 978-3-95450-257-8 ISSN: 2222-5692 doi:10.18429/JACoW-ECRIS2024-TUP07

required resolving power. The first results (not including the beam space charge) show that, by implementing a magnetic solenoid and an electrostatic quadrupole between FPT and the magnetic selection, the beamline turn out to be flexible enough to handle beams with different characteristics, ensuring a high enough resolving power (1/660 calculated for protons against 1/200 necessary for barium). Further optimizations including the beam space charge will follow and lead to the final design.

ACKNOWLEDGEMENTS

The authors acknowledge the financial support from the MUR-PNRR project PE0000023-NQSTI, financed by the European Union (NextGeneration EU).

REFERENCES

[1] ACME Collaboration, "Improved limit on the electric dipole moment of the electron", *Nature*, vol. 562, pp. 355-360, 2018. doi:10.1038/s41586-018-0599-8

[2] A. F. Borghesiani, G. Carugno, G. Messineo, and J. Pazzini, "Electron thermalization length in solid para-hydrogen at low-temperature", *J. Chem. Phys.*, vol. 159, p. 104501, 2023. doi:10.1063/5.0163776

[3] S. Gammino *et al.*, The Flexible Plasma Trap (FPT) for the production of overdense plasmas, *J. Instrum.*, vol. 12, no. 7, p. P07027, 2017. doi:10.1088/1748-0221/12/07/P07027

[4] R. Geller, *Electron Cyclotron Resonance Ion Sources and ECR Plasmas*. Bristol, UK: Institute of Physics Publishing, 1996.

[5] D. Mascali *et al.*, "Modelling RF-plasma interaction in ECR ion sources", *Eur. Phys. J. Web Conf.*, vol. 157, p. 03054, 2017. doi:10.1051/epjconf/201715703054

[6] IBSimu, https://ibsimu.sourceforge.net/

[7] D. Leitner and C. Lyneis, "ECR Ion Sources", in *The Physics and Technology of Ion Sources*, I.G. Brown, Ed. John Wiley & Sons, Ltd, pp. 203-231, 2004.

[8] A. T. Forrester, *Large Ion Beams: Fundamentals of Generation and Propagation*. USA: John Wiley and Sons Inc, 1987.

[9] K.-U. Riemann, "The Bohm criterion and sheath formation", *J. Phys. D: Appl. Phys.*, vol. 24, no. 4, p. 493, Apr. 1991. doi:10.1088/0022-3727/24/4/001

26th Int. Workshop Electron Cyclotron Resonance Ion Sources ECRIS2024, Darmstadt, Germany JACoW Publishing
ISBN: 978-3-95450-257-8 ISSN: 2222-5692 doi:10.18429/JACoW-ECRIS2024-TUP08

PLANNED OPTIMIZATION OF THE ION SOURCES ON THE HIT TEST BENCH

T. Winkelmann, R. Cee, T. Haberer, B. Naas, A. Peters
Heidelberger Ionenstrahl-Therapie Center (HIT), D-69120 Heidelberg, Germany

Abstract

The Heidelberg Ion Beam Therapy Center (HIT) is a hospital-based treatment facility in Germany. Since the first treatments in 2009, more than 8,500 patients have been irradiated with protons or carbon ions and since July 2021 with helium ions. At HIT, three supernanogan ion sources from Pantechnik are in operation 24/7 for therapy up to 335 days a year. A fourth supernanogan ECR ion source is installed at the HIT test bench. The test bench is currently being prepared for a measurement campaign that will start in October. The aim of the investigations is to obtain more beam current for the carbon ions used in the therapy by feeding two microwave frequencies in parallel. We expect this experiment to lead to a better understanding of the ionization process in the ion source. In the first step, we will feed 14.5 GHz and an additional frequency close to the resonance frequency of 14.5 GHz ± 0.5 GHz and in the second step 14.5 GHz and 18 GHz are injected.

To characterize and evaluate the beam quality in this setup, we use the Pepperpot as a 4D emittance meter. In addition, it is possible to measure the beam current and the beam profile on the test bench.

INTRODUCTION

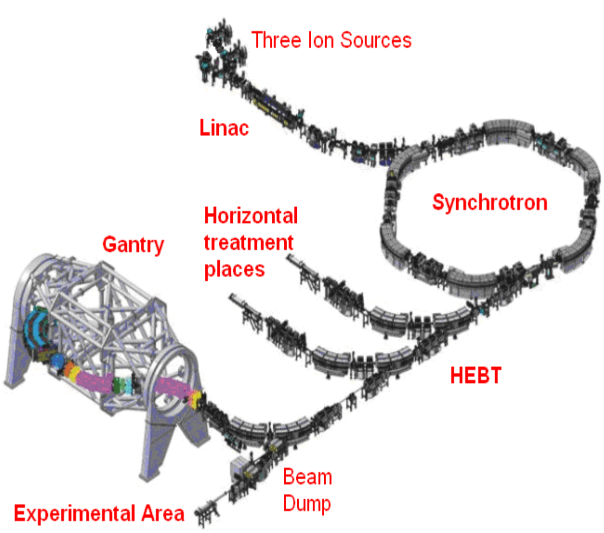

Figure 1: Overview of the HIT facility.

The beam production at HIT (see Figure 1) consists of three ECR Supernanogan ion sources [1] for the routine operation of proton, carbon and helium beams at 8 keV/u.

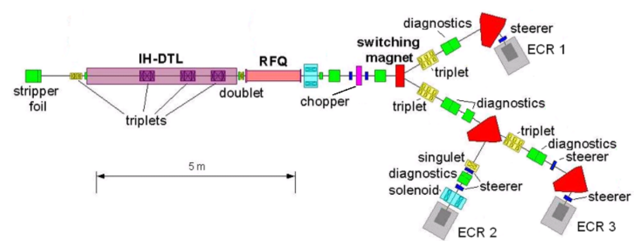

Figure 2: Low energy beam line (LEBT) and the linear accelerator (LINAC).

The compact 217 MHz linear accelerator (LINAC) consists of a radio frequency quadrupole accelerator (RFQ) and an IH-type drift tube linac (IH-DTL) with the end energy of 7 MeV/u for all ions; a foil stripper directly located behind these cavities produces fully stripped ions (see Figure 2). A synchrotron of 65 m circumference accelerates protons, helium, carbon and oxygen to predefined end energies e.g. for carbon ions from 89 to 430 MeV/u in 255 steps.

In order to minimize the already very short downtimes at the ion source (Figure 3), we started testing the 14.5 GHz solid-state amplifier (R&S PKU100) some years ago [2]. Until then, only tube amplifiers were used in clinical operations at HIT. After testing and checking the beam quality, the tube amplifiers were gradually replaced by solid-state amplifiers.

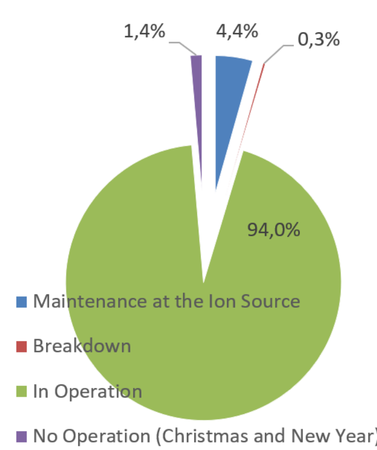

Figure 3: Statistics of the three ion sources in 2023.

ISBN: 978-3-95450-257-8 ISSN: 2222-5692 doi:10.18429/JACoW-ECRIS2024-TUP08

The future use of multi-energy operation [3] requires the synchrotron to be filled as quickly as possible. In order to achieve this efficiently, the existing RFQ will be replaced by a newly designed and optimized version [4]. By increasing the transmission of the linac from the current 30% to about 70% - 80%, efficient fast filling of the synchrotron can be ensured.

In order to achieve a stable source setting with an extracted beam current of 250 eμA C^{4+}, we will begin testing the coupling of two frequencies [5,6,7] on the test bench in autumn this year.

An increase in output would be particularly desirable for the therapeutically used carbon ion. For protons (H_3^+) and helium ($4He^{2+}$), the intensity and stability are sufficient with the mechanical changes to the plasma lens made to the ion source in the past [8].

COUPLING OF TWO FREQUENCIES

The plasma chamber of the ECR ion source has multiple excitations of different modes in the presence of non-magnetized homogeneous plasma. This leads to the generation of different resonance modes when electromagnetic waves are injected into the chamber.

Due to the complex magnetic field topology generated by hexapole and solenoid magnetic fields, plasma electrons are also heated outside the intended resonance surfaces. To achieve this, they must oscillate at the frequencies of the excited modes within the plasma chamber [9].

Since multiple modes are generated in the plasma chamber when heated at one frequency, it is suspected that superimposed multimodes are excited when the ECR ion source is operated in heating mode at different frequencies.

To investigate this phenomenon, we start with the following setup (Figure 5): A TWT amplifier capable of delivering 13.75 GHz to 14.75 GHz is connected to one of the RF ports, while a solid-state amplifier capable of delivering 13.75 GHz to 14.75 GHz is connected to a second RF port (see Figure 4).

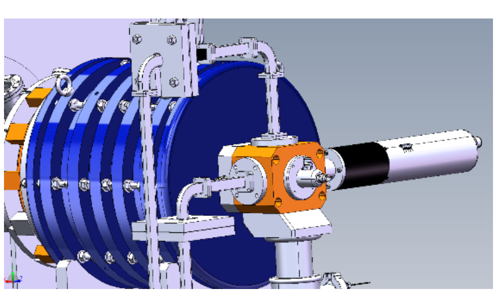

Figure 4: 3D model of the ion source with two waveguide connections on the copper cube.

Both RF systems are equipped with circulators, vacuum windows, dummy loads and high voltage insulators. Finding the two optimal frequencies that provide the highest stable current for C^{4+} will certainly require some iterations given the strong dependence on the tuning bulb position.

In a second setup (Figure 6) we will investigate how to increase and improve the beam intensity and beam quality for C^{4+} by using two far apart frequencies (14.5 GHz and 18 GHz).

The coupling is also done via the second flange in the copper cube of the SuperNanogan ion source, as in the experiment with the nearby frequencies, see Figure 4.

It is expected that the interference of two microwaves with far apart frequencies will lead to complex phenomena and the highly charged ion currents will generally tend to increase. Despite this complexity, we hope that the second frequency will increase plasma stability and thus improve beam quality for C^{4+}.

The beam quality is measured on the test bench using a pepperpot [10]. In addition, we have an RFQ on the test bench (see Figure 7), with the help of which the measured transmission also allows conclusions to be drawn about possible beam-improving properties.

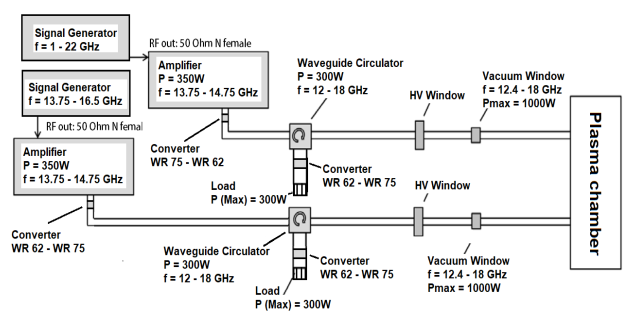

Figure 5: Schematic drawing of the two-frequency heating system (14.5 GHz & 14.5 GHz).

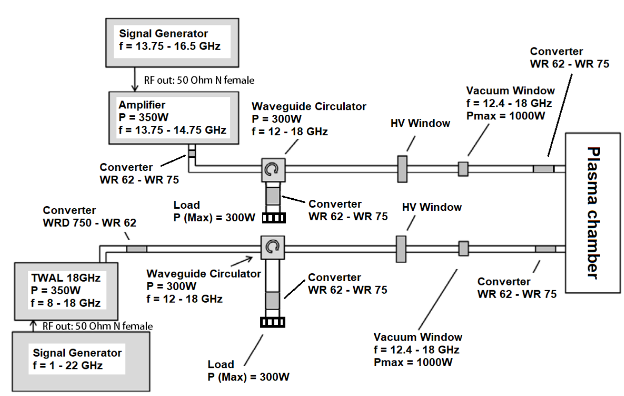

Figure 6: Schematic drawing of the two-frequency heating system (14.5 GHz & 18 GHz).

ISBN: 978-3-95450-257-8 ISSN: 2222-5692 doi:10.18429/JACoW-ECRIS2024-TUP08

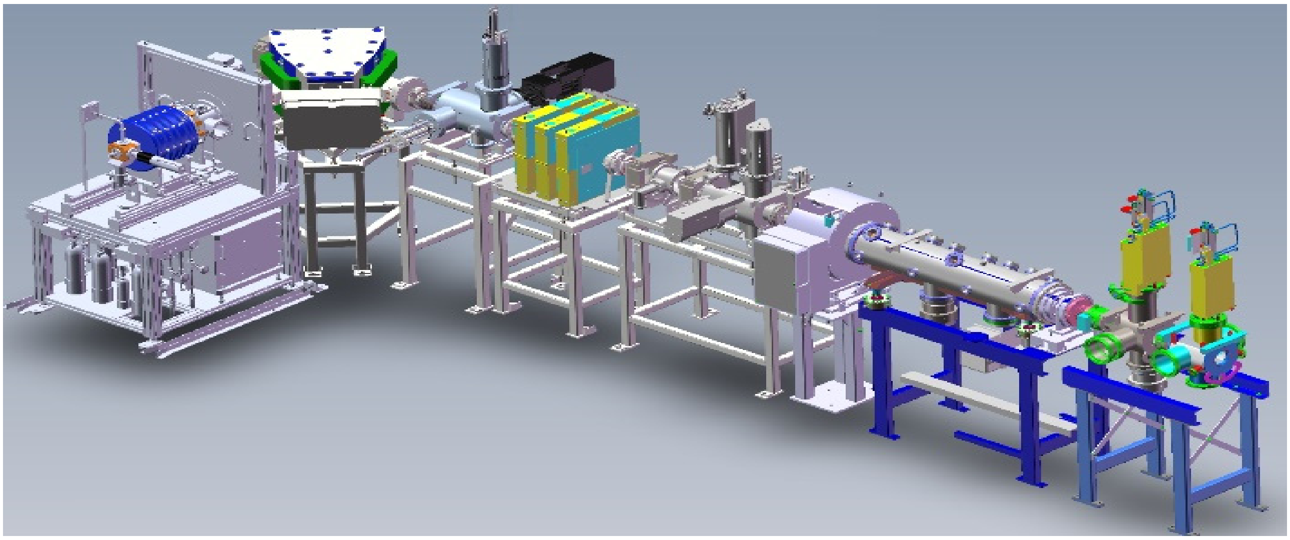

Figure 7: 3D CAD model of the testbench with the Supernanogan ion source (from left: ion source, dipole analyzing magnet, diagnostic chamber one with profile grid 1, analyzing slits, and Faraday cup 1, quadrupole triplet, diagnostic chamber two with pepper pot, profile grid 2, and Faraday cup 2, solenoid magnet, RFQ accelerator, diagnostic chambers three and four with a set of 3 phase probes, profile grid 3, and Faraday cup 3).

ACKNOWLEDGMENT

We would like to thank Siemens Healthcare GmbH for the support of this work by providing essential parts of the beamline such as the ion source, beam diagnostics and beam optical equipment for the HIT testbench.

REFERENCES

[1] Pantechnik | Boost your physics, `https://www.pantechnik.com/`

[2] R&S®PKU100-I Satellite uplink amplifier | Rohde & Schwarz, `https://www.rohde-schwarz.com/de/produkte/broadcast-und-medientechnik/satelliten-uplink-verstaerker/rs-pku100-i-satellite-uplink-amplifier_63493-528997.html`

[3] C. Schoemers, E. Feldmeier, M. Galonska, Th. Haberer, J. T. Horn, and A. Peters, "First Tests of a Re-accelerated Beam at Heidelberg Ion-Beam Therapy Centre (HIT)", *in Proc. 8th Int. Particle Accelerator Conf. (IPAC'17)*, Copenhagen, Denmark, May 2017, pp. 4647-4649. `doi:10.18429/JACoW-IPAC2017-THPVA083`

[4] U. Ratzinger at al., "A new RFQ for the Carbon Therapy Injector at HIT Heidelberg", presented at LINAC 2024, Chicago, USA,paper TUPB023.

[5] V. Toivanen *et al.*, "Effect of electron cyclotron resonance ion source frequency tuning on ion beam intensity and quality at Department of Physics, University of Jyväskylä," *Rev. Sci. Instrum.*, vol. 81, 02A319, Feb. 2010. `doi:10.1063/1.3267287`

[6] D. Mascali *et al.*, "Plasma ion dynamics and beam formation in electron cyclotron resonance ion sources," *Rev. Sci. Instrum.*, vol. 81, 02A334, Feb. 2010. `doi:10.1063/1.3292932`

[7] F. Maimone *et al.*, "Influence of frequency tuning and double-frequency heating on ions extracted from an electron cyclotron resonance ion source," *Rev. Sci. Instrum.*, vol. 82, 123302, Dec. 2011. `doi:10.1063/1.3665673`

[8] T. W. Winkelmann *et al.*, "Status Report at the Heidelberg Ion-Beam Therapy (HIT) Ion Sources and the Testbench", *in Proc. 21st Int. Workshop on ECR Ion Sources (ECRIS'14)*, Nizhny Novgorod, Russia, Aug. 2014, paper MOPPH004, pp. 49-51.

[9] L. Celona *et al.*, "Observations of the frequency tuning effect in the 14GHz CAPRICE ion source," *Rev. Sci. Instrum.*, vol. 79, 023305, Feb. 2008. `doi:10.1063/1.2841694`

[10] R. Cee *et al.*, "Development of a Pepper Pot Emittance Measurement Device for the HIT-LEBT", *in Proc. 10th Int. Beam Instrumentation Conf. (IBIC'21)*, Pohang, Korea, Sep. 2021, pp. 214-217. `doi:10.18429/JACoW-IBIC2021-TUPP12`

ISBN: 978-3-95450-257-8 ISSN: 2222-5692 doi:10.18429/JACoW-ECRIS2024-TUP09

CHARACTERIZATION OF AN PROTON ECR ION SOURCE FOR LOW BEAM CURRENT*

P. Usabiaga†,1, I. Arredondo[1], J. Feuchtwanger[1,2], J. Vivas[1],
J. Portilla[1], V. Etxebarria[1], I. Ariz[3], J. M. Seara Eizaguirre[3]
[1]University of the Basque Country, Bilbao, Spain
[2]Ikerbasque, Basque Foundation for Science, Bilbao, Spain
[3]Fundación TEKNIKER, Elbr, Spain

Abstract

In this paper we analyze the behavior of a low beam current proton ECR ion source for linac. During the operation of the source, as a function of the operating parameters we have observed a complex behavior. The state of the plasma is highly dependent on the input parameters, and in some cases even bi-stable conditions can be achieved showing abrupt changes in the state. To try to understand this behavior we carried out a series of experiments varying the input parameters both sequentially and randomly to avoid following the same path every time. Thanks to these experiments we have been able to observe the change in the luminosity of the plasma, which is an indirect measure of the degree of ionization in the plasma, along with the changes in reflected and transmitted RF power delivered to the source. We also characterized the relation between the outer temperature of the ion source chamber walls and the plasma. In addition to this we have analyzed the resulting extracted ion beam using a pepperpot and a faraday cup. We have observed that our beam does not have one dominant species and has three species that are found in comparable quantities.

INTRODUCTION

The LINAC 7 project is a research project that aims to create a compact low intensity proton accelerator with an energy of 7 MeV. As detailed in Ref. [1], while some accelerator stages are still in design, this work focuses on characterizing the Ion Source where positively charged particles are generated, the beam extraction to create the particle beam, and the Low Energy Beam Transport (LEBT) stage, which focuses the beam to go onto the next accelerating stage. A good understanding and control of the first stages of a LINAC is essential, because this is where many of the most important properties of the beam are determined. Among them, the most important are the current of the beam, which mostly depends on the performance of the Ion Source and the beam extraction [2], and the emittance of the beam, which once the beam is generated keeps constant through all the path of the accelerator [3].

To better understand the Ion Source and the extracted beam, various experiments have been conducted, exciting different behaviors in the plasma and beam and measuring relevant parameters. By analyzing the results of the experiments, it is possible to better understand the behavior of the first stages of the LINAC 7 accelerator.

Between the instruments used to manage and measure the parameters of the accelerator, many are of common use, like gas flow control, pressure measurement, a pepperpot and a Faraday cup to measure the characteristics of the beam, and luminosity measurements to determine the ignition degree of the plasma on the Ion Source. In addition to those, there is a specialized instrument developed for the LINAC 7 project that allows to measure the amplitude and phase of the incident and reflected RF signals used to excite the Ion Source, allowing calculation of the reflection coefficient, which varies with plasma state [4].

Some of those experiments deal with the effects of the temperature on the inner walls of the Ion Source, which increases during its operation, affecting the plasma [5]. The rest of the experiments are about better understanding different states on the plasma, which are believed to be linked with the chemical reactions on the ionized plasma, where different states belong to different predominant chemical species generated inside [6]. By better understanding this phenomena, it is intended to prioritize a state on the plasma where H^+ is the main generated element, and to maximize the amount of generated H^+.

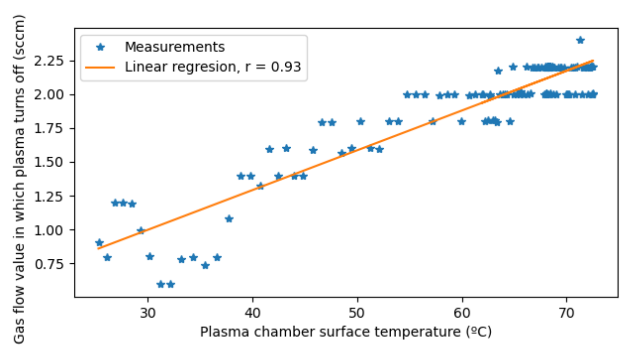

Figure 1: The relation between the temperature on the surface of the Ion Source, and the value of gas flow in which the plasma turns off.

PLASMA EXTINCTION AND TEMPERATURE RELATION

Since during the operation of the ion source a considerable amount of energy is used to generate the plasma, the temperature of the resonant cavity increases over time. This

* Work supported by Basque Government Department of Industry Grants KK-2024/00065 and KK-2022/00026
† pellousabiaga@gmail.com

26th Int. Workshop Electron Cyclotron Resonance Ion Sources ECRIS2024, Darmstadt, Germany JACoW Publishing
ISBN: 978-3-95450-257-8 ISSN: 2222-5692 doi:10.18429/JACoW-ECRIS2024-TUP09

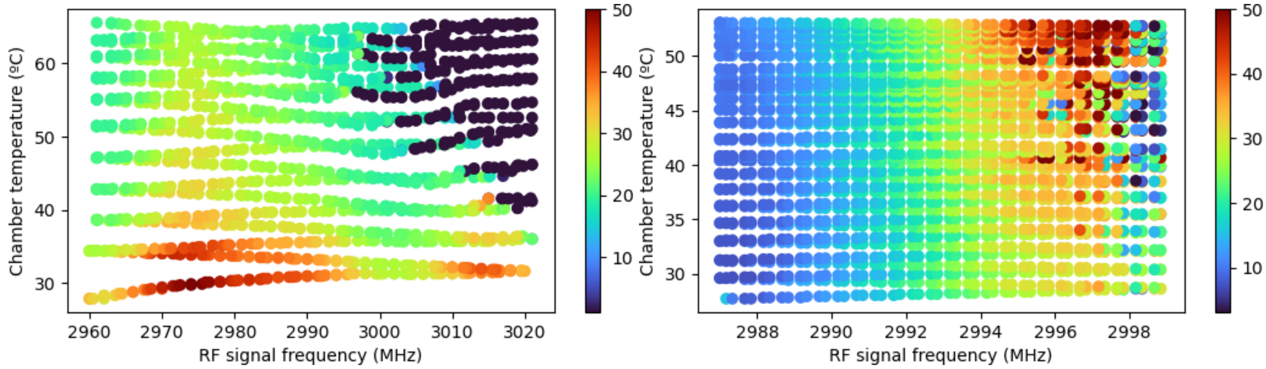

Figure 2: Up, the relative luminosity of the plasma depending on the frequency of the incident RF signal, and the temperature on the surface of the Ion Source. The dark zone on the high frequency high temperature area corresponds to measurements where the plasma was off. Down, the same experiment, with the effect of the temperature compensated. Note that the measurement of the luminosity is done in a. u., and that the different measurements are scaled differently along different experiments.

temperature has an effect on the behavior of the plasma, which can be measured on the moment the plasma turns off. By keeping a constant RF power incident onto the Ion Source, and decreasing the gas flow so that the plasma turns off, it is possible to measure at which gas flow value turns off the plasma. By comparing these measurements with the temperature of the surface of the Ion Source at each moment, it is possible to obtain the graphic shown in Fig. 1. It can be seen that there is a clear relation between the two values, one that appears to be linear.

The higher the temperature on the Ion Source, the higher the amount of gas flow required to keep the plasma on. There are many possible explanations for this phenomenon, and two hypothesis have been raised on our team:

On the one hand, it is possible that the temperature increase is affecting the permanent magnets that create the magnetic field for our Ion Source. With the increase in the temperature, it is possible that they generate a different magnetic field, and that this changes the ECR resonant frequency of the cavity. By changing the resonant frequency, it is possible that the frequency of the RF signal is closer to it on low temperatures than in high ones, and therefore the effect would be due to the generally lower stability of the plasma at high temperatures.

On the other hand, this effect can also be linked to gas expansion inside the Ion Source. If the gas inside the cavity behaves like an ideal gas, and its temperature is linked to the temperature on the surface of the Ion Source, at higher temperatures it would expand, reducing the density of H_2. If the relevant magnitude for the plasma generation is the H_2 density inside the cavity, and not the incident gas flow, the observed effect would be again explained.

FREQUENCY CYCLES WITH TEMPERATURE INCREASE

To see if the first of the previous hypothesis holds, a simple experiment has been performed. The frequency of the incident RF signal has been changed, and how the relative luminosity varies with the frequency and temperature changes have been measured. The results of the experiment can be seen in Fig. 2.

It can be seen that the luminosity for the same frequency generally decreases with the increase in the temperature, but that the frequency with highest luminosity always stays the same, around 2975 MHz. Hence, the ECR resonant frequency does not highly change with the increase of the temperature on the surface of the Ion Source.

DENSITY MODEL WITH IDEAL GAS EQUATION

Discarding the first hypothesis, let us analyze the second one, according to which the density of the gas inside the ion source changes with the temperature of the chamber. In order to try to test this approach, a model of the density has been created, and it has been used to try to compensate for the effect of the temperature on the gas density inside the ion source.

For the model, some assumptions have been done. First of all, let us assume that the gas inside the ion source behaves like an ideal gas. Also, let us assume that the temperature of the gas inside the cavity is proportional to the temperature on the surface of it, so that $(T_{\mathrm{surface}} - T_{\mathrm{amb}}) = K_1(T_{\mathrm{gas}} - T_{\mathrm{amb}})$ is fulfilled. Finally, it is assumed that the plasma shutdown shown in Fig. 1 always happens at a constant density. With these assumptions, the density of the gas on the ion source can be calculated as:

$$\rho \propto \frac{P}{K_1(T_{\mathrm{gas}} - T_{\mathrm{amb}}) + T_{\mathrm{amb}}} . \qquad (1)$$

Given that the volume is constant. ρ is the density of gas, P is the pressure, T_{gas} and T_{amb} are the temperature of the gas and of the ambient and K_1 is a constant.

With this, the relation between the temperature and the plasma shutdown density derived from the values on Fig. 1 can be calculated, and K_1 can be fitted until the relation is null. The optimum value for K_1 has been estimated at 6.308, so that the normal range of temperatures for the gas inside the chamber would be between 22 °C (ambient temperature)

ISBN: 978-3-95450-257-8 ISSN: 2222-5692 doi:10.18429/JACoW-ECRIS2024-TUP09

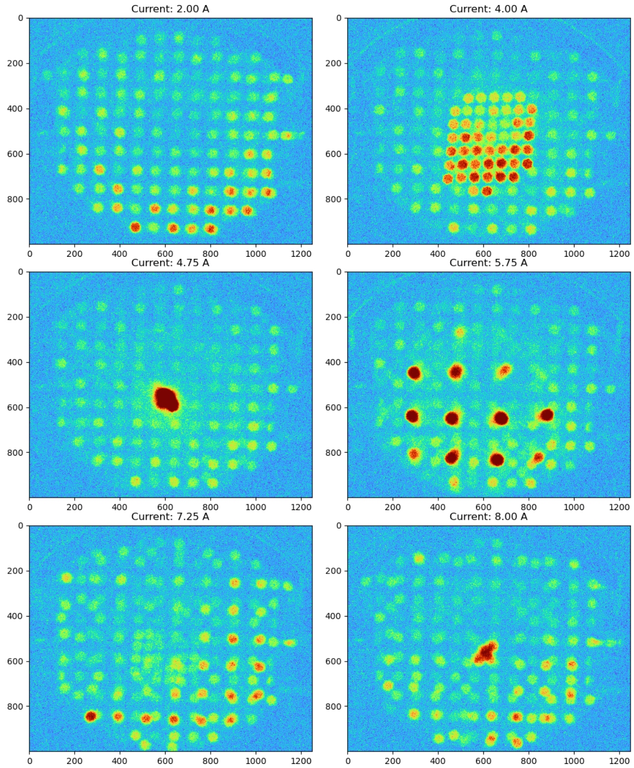

Figure 3: Images taken from the pepperpot camera with different currents on the focusing solenoid. The color represents the intensity of each pixel, in arbitrary units.

and 440 °C. This range is reasonable, because the steel of the chamber has suffered no damage, but in a previous experiment a piece that was soldered with tin came off, due to the tin melting (about 232 °C).

With this model, a simple controller has been created to maintain a constant density inside the ion source varying the gas flow depending on the temperature. With this controller, the experiment of the frequency cycles has been repeated, obtaining the results shown in Fig. 2 down. It can be seen how the effect of the temperature is largely compensated.

ANALYSIS OF ELECTRICAL PROPERTIES OF THE PLASMA

Continuing with the analysis of the behavior of the ion source of the LINAC 7 accelerator, there are a couple of experiments that appear to show different states on the plasma of the ion source. It is believed that those states can be linked with the generation of different species on the ion source plasma, which have been studied on previous works on the team [6]. Thanks to the new instrument that can measure the reflection coefficient of the ion source at the frequency of the incident RF signal, it has been possible to perform the experiment shown in Fig. 4.

In this experiment, it can be seen how the luminosity of the ion source changes abruptly with smooth changes on the gas flow. These changes happen between states where it is hard to distinguish the plasma from one that is off (blue and dark blue) and states where the luminosity appears to change more smoothly with the gas flow at high luminosity values (red).

DIFFERENT SPECIES ON THE PEPPERPOT

As have been mentioned before, there are multiple species being generated on the ion source and extracted on the beam to the LEBT. It is believed that those species are H^+, H_2^+ and H_3^+. Due to their different mass-charge relationships, each species responds differently to electric and magnetic field applications. Those which have more mass will reach smaller velocity when electrostatically accelerated on the beam extraction, and they will be curbed less when under a magnetic field, like on the solenoids that focus the beam.

This effect is measurable using the pepperpot in the LEBT. An experiment was designed where the beam extracted from the ion source is focused using solenoids. By changing the current that goes through the solenoids, it is possible to apply more or less curvature to the beam, focusing it more or less. Thus, an experiment was conducted where solenoid current was varied, and a photo was taken of the pepperpot for each current setting.

In Fig. 3 some of the resulting images of the experiment can be seen. With low currents, it is not possible to distinguish the different species, and none of them is focused. With the increase of the current to 4.75 A, one of the species gets focused on the pepperpot, and the rest stays at the same place. If the current is further increased, it can be seen that the beam becomes divergent for one of the species, and when getting close to 7-8 A another species starts to focus too. In the final image at least three species can be seen, one diverging, the other focused, and the rest not focused at all.

FARADAY CUP CURRENT MEASUREMENTS

The Faraday cup in the LEBT has a limited radius, so it only measures the current of particles near the center of the beam. As a result, different focusing conditions yield different current measurements. In the previous experiment it has been seen that by varying the current on the LEBT solenoids it is possible to focus certain species, while keeping unfocused others. Hence, using appropriate parameters on the different stages, it should be possible to measure the current of each different species separately on the Faraday cup. This way, by knowing how each species reacts against the parameters on the accelerator (specially the Ion Source), it would be possible to favor the generation of the desired species for the LINAC 7, the H^+.

An experiment has been done to try to measure this, in which the same parameters of the previous experiment have been used, setting the solenoids current to 4.75 A. This way, the first of the species (which is believed to be H^+) is focused while the rest are unfocused, and the current on the Faraday cup should be mainly proportional to this species. Then, the power of the RF signal going to the Ion Source has been

ISBN: 978-3-95450-257-8 ISSN: 2222-5692 doi:10.18429/JACoW-ECRIS2024-TUP09

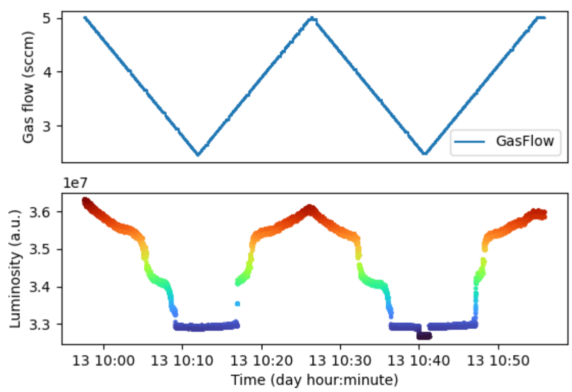

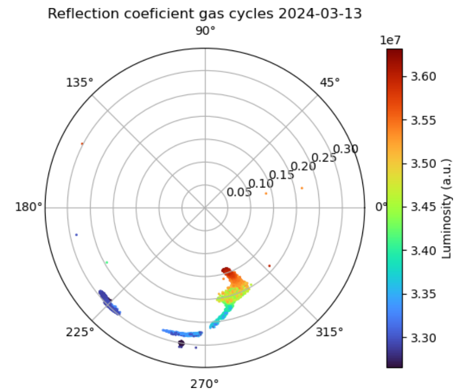

Figure 4: On the left, gas flow cycles and measured luminosity at each moment. On the right, the polar plot of the reflection coefficient of the ion source.

changed on cycles, increasing and decreasing it. In the Fig. 5 the results of this experiment can be seen.

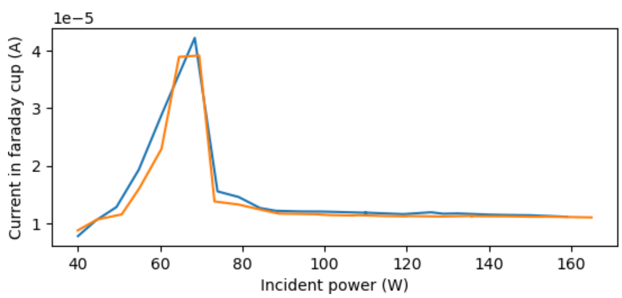

Figure 5: The current measured on the Faraday cup with 4.75 A on the focusing solenoid in function of the power going through the Ion Source. The blue is the result of increasing the power, and the orange of decreasing it.

While in previous experiments it has been seen that the luminosity of the Ion Source always increases with both the gas flow and the power of the RF signal that goes to the Ion Source, it can be seen how in the current of the beam the same is not true. We found that there is a certain RF power where the current of the species selected by the focusing is optimum, and further increasing the RF signal power rather than increasing it decreases its intensity.

Currently, this experiment has not been repeated using different focusing currents on the solenoids so that other species can be analyzed. But when those experiments have been done, it can be possible to determine the composition of the plasma for different parameters on the Ion Source, and how each of its components affects to the luminosity of the Ion Source, to see if the measurements on the Faraday cup can be somehow correlated to those of the luminosity.

CONCLUSIONS AND FUTURE WORK

Thanks to the experiments shown in this work, the team now has a much better understanding about the behavior of the Ion Source of the LINAC 7 accelerator, and it is hence more prepared to optimize its performance and the overall performance of the accelerator. It also provides some clear points where future work have to be put in:

- The temperature of the Ion Source is an important factor on the charged particles generation. It has to be included in the control of the system, by taking into account the changes in the temperature, or by introducing a cooling system to keep it constant after a thermal conditioning step.
- Thanks to the analysis of the photos on the pepperpot scanner, we have experimental proof of different species being formed on the Ion Source and accelerated. How each of those species behaves and how the generation of H^+ can be maximized has to be further explored, in order to get the maximum current on the particle beam, and to apply the correct magnetic fields on the LEBT to focus the desired species only.
- Regarding this, the next experiments can be to perform more measurements using the Faraday cup and different focusing currents on the solenoids, so that how the current of different species answer to the parameters on the Ion Source can be explored.

REFERENCES

[1] J. Feuchtwanger *et al.*, “New generation compact linear accelerator for low-current, low-energy multiple applications”, *Appl. Sci.*, vol. 12, p. 4118, 2022. doi:10.3390/app12094118

[2] S. Anishchenko *et al.*, “Cumulation of high-current electron beams: Theory and experiment”, *IEEE Trans. Plasma Sci.*, vol. 45, no. 10, pp. 2739–2743, 2017. doi:10.1109/TPS.2017.2707591

[3] M. Reiser, *Theory and design of charged particle beams*. John Wiley & Sons, 2008.

[4] J. Vivas, *Sistema de adquisición de datos de la onda incidente y reflejada en una fuente de iones de resonancia ciclotrónica*, Bachelor’s thesis, 2023. http://hdl.handle.net/10810/67871

[5] G. Torrisi *et al.*, “Investigation of radiofrequency ion heating in the magnetoplasma of an ecr ion trap”, in *Int. Conf. Electromagn. Adv. Appl. (ICEAA’19)*, pp. 1203–1207, 2019. doi:10.1109/ICEAA.2019.8879288

[6] M. Elorza, *Global model for the study of the hydrogen plasma generated at an ecr ion source*, Master’s thesis, 2022.

ISBN: 978-3-95450-257-8 ISSN: 2222-5692 doi:10.18429/JACoW-ECRIS2024-TUP10

OPTICAL DIAGNOSTIC STUDIES TO ANALYSE ELECTRON CYCLOTRON RESONANCE PLASMA PRODUCED IN THE GTS-LHC ION SOURCE

B. S. Bhaskar*, D. Küchler, CERN, Geneva, Switzerland
T. Kövener

Abstract

The GTS-LHC electron cyclotron resonance (ECR) ion source is an integral part of the chain of accelerators at CERN. It produces the heavy ion beams which are accelerated using a series of accelerators from LINAC up to the LHC. The ion beams are extracted from an ECR plasma generated at the GTS-LHC ion source, however, there has not yet been a non-invasive diagnostic device to study the plasma. This research focuses on the implementation of an optical diagnostics and studies the optical emission spectra (OES) as a monitor of the performance of the ion source. Furthermore, we explore the correlation between spectral properties and changing source parameters, offering insights into the behaviour of the ion source, which in turn helps in fine-tuning of the source. Specifically, the study concentrates on long-term OES analysis spanning several weeks, focusing on the production of magnesium and lead ions using the GTS-LHC ion source.

INTRODUCTION

The production of ion beams at CERN is crucial for a wide range of research activities, particularly in the field of heavy-ion physics, where specific ion species are required for diverse experimental needs. The GTS-LHC 14.5 GHz Electron Cyclotron Resonance (ECR) ion source [1], located at the start of the Linac3 accelerator, is essential to this process. It has been predominantly used for producing lead ions, which are vital for many of CERN's high-energy physics experiments.

A new working group was formed recently "Future Ions in the CERN Accelerator Complex" to define future ion operations based on requests from LHC and other fixed target experiments at North Area (NA) of CERN. One light ion selected is magnesium. Mg Highly Charged Ions (HCIs) can be produced by the GTS-LHC ion source, the magnesium atoms are introduced into the source by a micro-oven, which evaporates the metal samples by controlling the oven power based on the required vapour pressure. Helium is injected as a buffer gas to enhance magnesium ion production.

The study of new ions at CERN is limited because there is only one ECR ion source, which is used for both current experiments and developing new ion beams. Due to the complex accelerator setup and long experimental periods (up to six months), only two types of ions can typically be studied each year. These long periods require the ion source to remain stable for extended times, which is an additional challenge for metal ion beams made with oven-based evaporation. Maintaining stability over time is often harder than achieving high beam intensity.

To address these challenges, recent research has focused on optimising the ion source's performance using Optical Emission Spectroscopy (OES). OES is a non-invasive diagnostic tool that allows for the analysis of plasma by examining the emitted light, providing insights into parameters like electron density, electron temperature (T_e), ion temperature (T_i), and the densities of both neutral atoms and ions [2, 3]. These parameters are crucial for fine-tuning the ion source to ensure efficient and stable ion beam production.

The installation of a new OES setup has further enhanced the diagnostic capabilities of the ECR ion source, enabling continuous monitoring of the plasma. This study is focused on finding a correlation between the optical emissions with ion source parameters and thereby helping to optimise the production of HCIs.

EXPERIMENTAL SETUP AND PROCEDURE

The experiment is performed on the 14.5 GHz GTS-LHC ECR ion source at CERN. The HCIs are generated based on stepwise ionisation of neutral atoms. The neutral atoms are primarily introduced to the source by means of evaporation using a micro oven [4]. The resultant ions are extracted via a suitable extraction system [5] and is directed through a dipole magnet, which is employed to isolate and select the specific charge state of interest, a Faraday cup for direct measurement of beam current by blocking the ion beam, and a beam current transformer (BCT), which enables non-invasive beam current measurements. Subsequently, the ions are accelerated through a series of accelerators.

The experimental setup includes an optical spectrometer system designed to observe the optical emissions from the plasma through the port on the first dipole magnet as shown in Fig. 1. A concave mirror is placed at this point which collects and focuses the light onto the entrance of an optical fiber. The other end of the optical fiber is connected to the optical spectrometer (Ocean Optics USB4000 Spectrometer). A vacuum valve is positioned between the concave mirror and the dipole magnet, providing the flexibility to change or adjust the optical components without needing to vent the entire low-energy beamline thereby maintaining the vacuum. This valve also serves as an external shutter for measuring the background spectrum.

The experiments were performed by simultaneously collecting optical spectra and monitoring the total beam current using the BCT. An OES measured during magnesium pro-

* bichu.bhaskar@cern.ch

ISBN: 978-3-95450-257-8 ISSN: 2222-5692 doi:10.18429/JACoW-ECRIS2024-TUP10

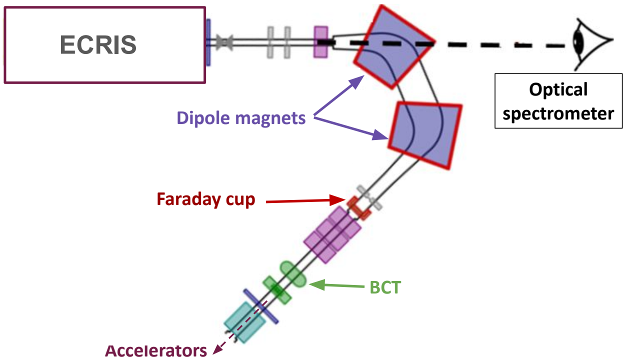

Figure 1: Schematics of the experimental setup show the ECR ion source, followed by dipole magnets, the newly installed optical spectrometer, along with a faraday cup and beam current transformers positioned downstream from the dipole magnet.

duction is shown in Fig. 2 where emission peaks of neutral Mg (i.e. Mg I), singly ionised Mg (Mg II), neutral helium (He I) and singly ionised He (He II) have been detected. The subsequent analysis is focused on isolating the emission peak of interest, quantifying its integrated intensity and correlating it with the beam current, as recorded by the BCT.

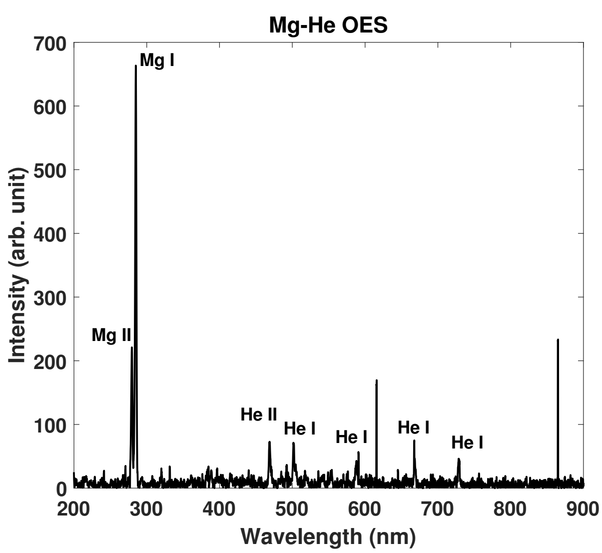

Figure 2: Recorded optical emission spectra of magnesium, where helium is used as a buffer gas. The spectrum shows emissions lines corresponding to neutral and singly ionised magnesium and helium.

A series of optical emission spectra of magnesium was recorded and one such representative of the recorded spectrum is shown in Fig. 2. It should be noted that in all cases, the source was operated in afterglow mode with an RF pulse duration of 50 ms and a repetition rate of 10 Hz. The optical spectrometer collected sufficient light with an integration time of 1 second, and the spectra for magnesium were averaged over 50 acquisitions.

A dedicated experimental campaign to study the influence of various source parameters on the spectrum was conducted for magnesium, with the results detailed in the following sections. The term *'intensity'* is used to refer the integrated signal from one particular transmission line in the OES spectrum (i.e. for Mg I at ~285 nm and He I at ~668 nm). Throughout the measurements, Mg^{7+} was selected using the dipole magnet spectrometer and is accelerated downstream from the dipole magnet. Furthermore, the reader should note that the optical notation “I” indicates optical emission from a neutral atom, while “II” denotes emission from 1^+ ion and so on.

EXPERIMENTAL RESULTS AND DISCUSSION

Optical Emission Studies on Magnesium

This study of intensities of Mg I with the simultaneous measurement of BCT current resulted in identifying a linear correlation with the intensity of neutral magnesium optical emission spectra with BCT current (which measures Mg^{7+} beam current).

The temporal behaviour of the optical intensity of Mg I and He I is shown in Fig. 3, along with the beam current of Mg^{7+} measured on the BCT. The correlation of the optical emission from Mg I with the current measured in the BCT are shown in Fig. 4. This data was taken over a span of

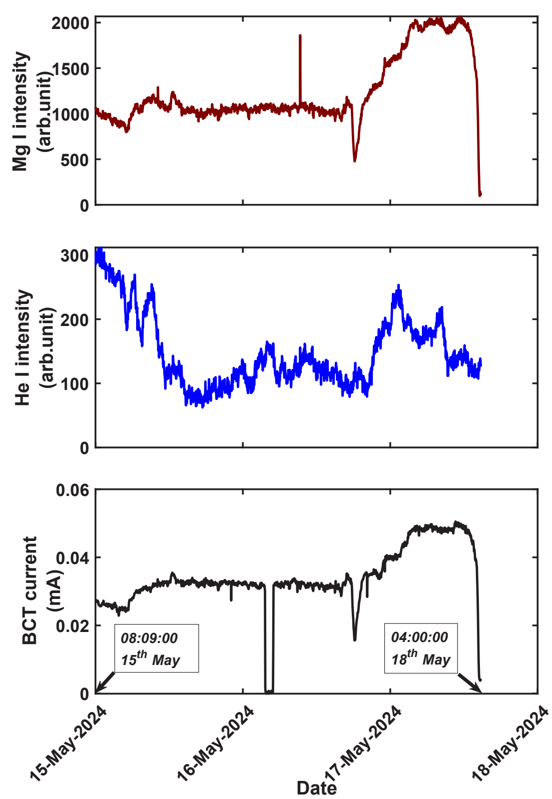

Figure 3: Figure showing the temporal evolution of the optical spectral intensities of neutral magnesium (top plot), neutral helium (middle plot) and the total beam current measured in the BCT (bottom plot) for Mg^{7+} ions.

115 hours 50 minutes from May 15th, 2024 (08:09:00 CEST) to May 18th, 2024 (04:00:00 CEST). During this period, the only source tuning parameter that was increased was the oven power (by 2 W), while all other source tuning parameters

ISBN: 978-3-95450-257-8 ISSN: 2222-5692 doi:10.18429/JACoW-ECRIS2024-TUP10

remained nearly constant, (with variations of less than ±1 %). Additionally, the optical spectrometer settings also remained the same throughout the measurement.

Another observation is the linear increase in the optical emission from Mg II with the increase in intensity of neutral magnesium optical emission (Fig. 5). These two relationships suggest that the increase in Mg^0 intensity increases the intensity of Mg^{1+}, with a high fraction of ions possibly being further ionised to Mg^{7+} in the ECR plasma. However, it is important to emphasise that this observation is based on a specific measurement and therefore cannot be generalised to all conditions especially because of the the complex ionisation mechanism in ECR ion source. A similar observation was reported by Kronholm et al. [6], where an increase in the optical emission intensity of Ar^{13+} correlated with an increase in Ar^{13+} ion beam current (as a function of microwave power), while no such correlation was observed for Ar^{9+}.

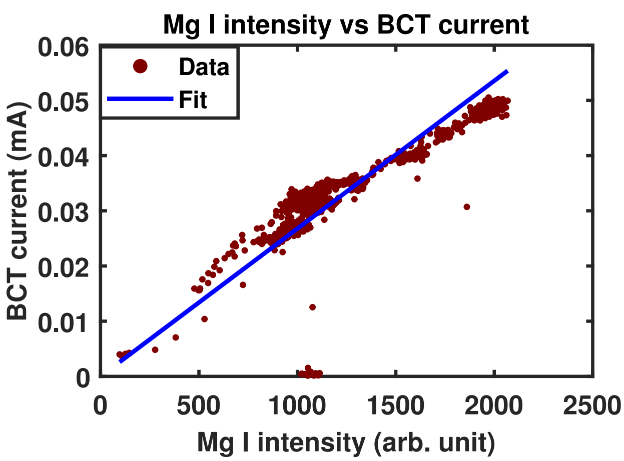

Figure 4: Figure showing the linear correlation between the measured beam current using BCT and the intensity of optical emission spectrum from the neutral magnesium.

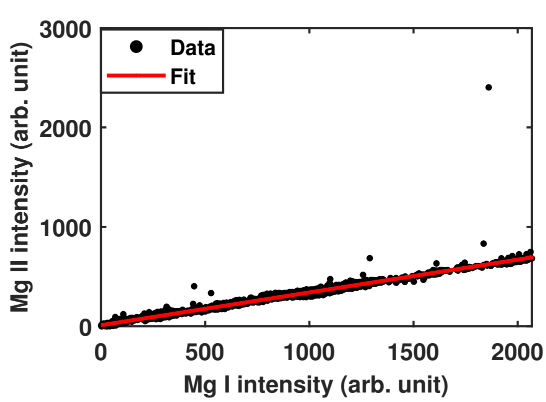

Figure 5: Figure showing the linear correlation between the optical emission from neutral magnesium and singly ionised magnesium.

Consequently, the study was further extended to systematically investigate the effects of source parameters such as microwave heating power, biased disk potential (a negatively biased electrode placed axially at the injection end of the source), and neutral buffer gas pressure (adjusted by adjusting the valve control value ranging from 0 to 10 V). The microwave power and biased disk potential were held constant for two-minute during the experiment. For the gas valve control settings, a four-minute interval was chosen to allow sufficient time for the changes to be fully reflected in the plasma conditions.

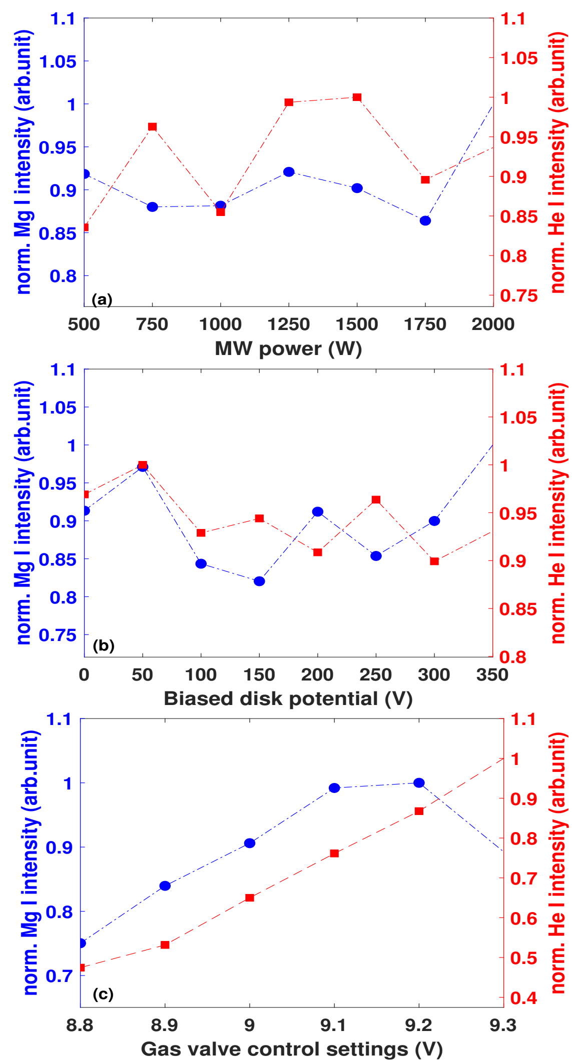

Figure 6: Systematic study of optical emission from neutral magnesium and helium is studied by varying (a) the input microwave power, (b) the biased disk potential, and (c) the gas valve settings, while keeping all other parameters constant throughout the measurements (i.e the nominal settings of the source for this experiment are: microwave power at 1700 W, biased disk potential at 200 V and gas valve control settings at 8.89 V).

It has been observed that increasing the neutral buffer gas pressure (using helium) resulted in a higher optical emission intensity from neutral helium, whereas no significant changes were noted with variations in microwave power or biased disk potential (see Fig. 6). Additionally, as helium neutral gas pressure increased, the intensity of Mg I also increased, reaching a peak at a gas valve setting of 9.2 V and

ISBN: 978-3-95450-257-8 ISSN: 2222-5692 doi:10.18429/JACoW-ECRIS2024-TUP10

subsequently decreasing. This behaviour indicates the role of the buffer gas in the production of highly charged Mg ions (HCIs).

Preliminary Optical Emission Studies on Lead

The optical spectrum produced by evaporating lead using micro-ovens was recorded at a later stage (refer Fig. 7) with oxygen as the buffer gas. In this case, adequate light was only obtained for lead after integrating for 10 seconds and averaging over 15 acquisitions. However, unlike the case with magnesium, no systematic measurements of the source parameters for lead ions were performed, as the source was no longer available for further experimental studies. In

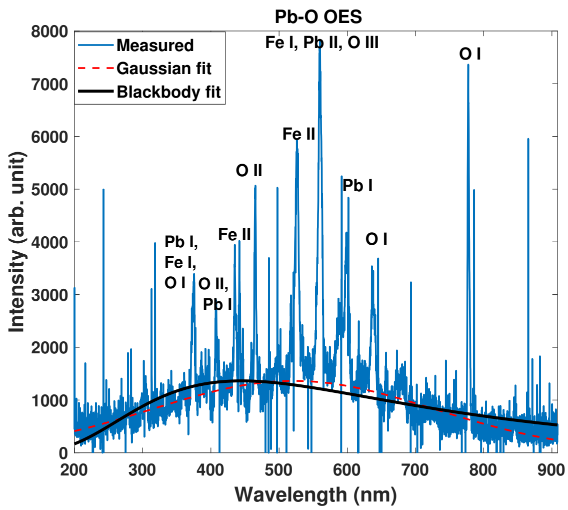

Figure 7: Recorded optical emission spectra during lead operation, where oxygen is used as a buffer gas. The spectrum shows emission lines from lead, oxygen and iron.

analysing the spectrum, it was observed that, in addition to the expected emission lines from lead and oxygen, there are also distinct emission lines from iron present. Moreover, the spectrum exhibits a continuous background signal that spans across the wavelength range, which is not accounted for by the discrete emission lines alone. To investigate this background continuum more thoroughly, two different fitting techniques are employed (i.e. Gaussian and blackbody). The fitting results, shown in Fig. 7, could provide insights into the characteristics of the background and may help to identify its underlying cause. The blackbody fit resulted in a temperature of ~0.44 eV. However, this result does not match with any known energy or temperature in the source indicating the need for further investigation into other possible mechanisms that could be contributing to the broad signal in the spectrum.

CONCLUSION AND FUTURE SCOPE

The study demonstrates the successful implementation of a new optical diagnostic setup for continuous plasma monitoring. Optical spectra were collected for two ion beam operations at CERN (i.e. Mg and Pb). The Mg spectra showed a linear relationship between the optical emission from neutral magnesium and the extracted HCI beam current, indicating that OES could play a role in optimising the ion source. Further analysis with other source parameters also showed a clear correlation between neutral buffer gas pressure and the optical emission spectra. Measurement with lead ion plasma displayed a background continuum requiring further investigation.

The future work will focus on investigating the origin of the background continuum observed in the optical spectrum measured for the lead run, as understanding this will improve understanding of the physics of ECR ion sources. Additionally, the study will explore the correlation between optical spectra and different charge states of the ion beams, which could simplify and optimise the operation of the ion source. Both tasks aim to enhance the efficiency and control of ion sources in future applications.

ACKNOWLEDGEMENTS

We sincerely thank Dr. Richard Scrivens from CERN for his valuable insights and suggestions, which greatly improved this manuscript. We are also grateful to Mr. Michael O'Neil from CERN for his essential technical support, and to Ms. Naida Ustavdić of the University of Sarajevo for her contributions to the data analysis.

REFERENCES

[1] L. Dumas *et al.*, "Operation of the GTS-LHC Source for the Hadron Injector at CERN", CERN, Technical Report LHC-PROJECT-REPORT- 985, 2007. `https://cds.cern.ch/record/1019180`

[2] U. Fantz, "Basics of plasma spectroscopy", *Plasma Sources Sci. Technol.*, vol. 15, no. 4, p. S137, 2006. `doi:10.1088/0963-0252/15/4/S01`

[3] R. Kronholm *et al.*, "Spectroscopic study of ion temperature in minimum-B ECRIS plasma", *Plasma Sources Sci. Technol.*, vol. 28, no. 7, p. 075 006, 2019. `doi:10.1088/1361-6595/ab27a1`

[4] T. Kövener, D. Küchler, and V. A. Toivanen, "Lead evaporation instabilities and failure mechanisms of the micro oven at the GTS-LHC ECR ion source at CERN", *Rev. Sci. Instrum.*, vol. 91, no. 1, p. 013 320, 2020. `doi:10.1063/1.5126084`

[5] V. Toivanen and D. Küchler, "Studies of the beam extraction system of the GTS-LHC electron cyclotron resonance ion source at CERN", *Rev. Sci. Instrum.*, vol. 87, no. 2, p. 02B923, 2015. `doi:10.1063/1.4934211`

[6] R. Kronholm *et al.*, "The effect of microwave power on the Ar^{9+} and Ar^{13+} optical emission intensities and ion beam currents in ECRIS", *AIP Conf. Proc.*, vol. 2011, no. 1, p. 040 014, 2018. `doi:10.1063/1.5053288`

26th Int. Workshop Electron Cyclotron Resonance Ion Sources ECRIS2024, Darmstadt, Germany JACoW Publishing
ISBN: 978-3-95450-257-8 ISSN: 2222-5692 doi:10.18429/JACoW-ECRIS2024-TUP11

EFFICIENT INJECTION OF HIGH-INTENSITY LIGHT IONS FROM AN ECR ION SOURCE INTO AN RFQ ACCELERATOR

Chuan Zhang [#, 1, 2, 3], Eduard Boos [†, 1, 2]
[1] GSI Helmholtz Center for Heavy Ion Research, Planckstr. 1, Darmstadt, Germany
[2] Institute for Applied Physics, Goethe-University, Frankfurt am Main, Germany
[3] Helmholtz Research Academy Hesse for FAIR (HFHF), Frankfurt am Main, Germany

Abstract

This study investigates an efficient injection of high-intensity light ions from an Electron Cyclotron Resonance (ECR) ion source into a Radio Frequency Quadrupole (RFQ) accelerator. An often-adopted solution for the beam matching between an ion source and an RFQ is to apply two solenoids as a Low Energy Beam Transport (LEBT) section. There are also other solutions which skip the LEBT section and inject the ion-source output beam directly into an RFQ e.g. the so-called Direct Plasma Injection Scheme (DPIS). For this study, a compact electrostatic LEBT using an einzel lens as well as an efficient RFQ based on a special design method have been developed to achieve high transmission of a 60 mA proton beam. Additionally, the RFQ design has been also checked with the LEBT removed. The design and simulation results will be presented.

INTRODUCTION

Usually a particle beam extracted from an Ion Source (IS) is defocused in both transverse (*x* and *y*) planes. At the entrance to an RFQ accelerator, however, an input beam focused in both *x* and *y* planes are desired. To transport a particle beam from an IS to an RFQ accelerator, there are different approaches:

- Using a magnetic LEBT (M-LEBT) typically consisting of two solenoids, e.g. [1].
- Using an electrostatic LEBT (E-LEBT) with one or two einzel lenses, e.g. [2].
- Using a zero-length LEBT (Z-LEBT) i.e. direct injection, e.g. [3].

An M-LEBT often needs more space than an E-LEBT and a Z-LEBT solution usually causes high beam losses at the injection due to lake of beam matching, this study focuses on the R&D of a compact einzel lens for an efficient injection of a 50 keV, 60 mA proton beam into an RFQ.

EINZEL-LENS DESIGN

For the design of the aimed einzel lens, a particle distribution with 10000 macro particles (see the left graphs of Fig. 1) generated at the extractor exit of an ECR-IS was taken as the input beam. This generated 50 keV, DC input beam has a transverse size of ~5 mm in diameter and it is defocused in both transverse planes. The task of the aimed einzel lens is to convert the particle beam to be focused in both transverse planes, whereby the beam energy should be kept almost unchanged and the transverse beam size should not increase too much.

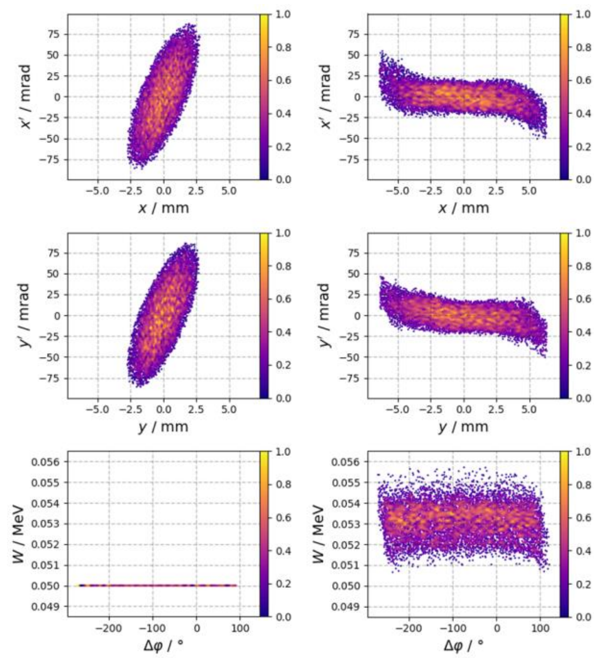

Figure 1: Particle distributions at the extractor exit of the ECR-IS (left) and at the RFQ entrance (right, obtained from the beam dynamic simulation using TraceWin [4]).

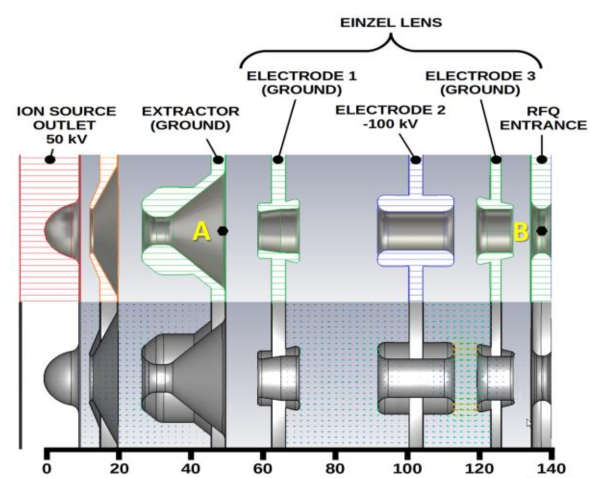

Figure 2: Schematic layout of the designed einzel lens, where Points A and B represent the start and end positions of the beam transport simulation through the einzel lens, respectively (the electrostatic field calculated using the CST Studio Suite [5] is shown in the bottom graph).

c.zhang@gsi.de
† e.boos@gsi.de

ISBN: 978-3-95450-257-8 ISSN: 2222-5692 doi:10.18429/JACoW-ECRIS2024-TUP11

As shown in Fig. 2, a defocusing-focussing scheme has been chosen for designing a ~8 cm long einzel lens. The defocussing part of the lens system (between the first and second electrodes) tries to smoothly increase the transverse beam size, the transverse diverging angles, and the beam energy. The focussing part (between the second and third electrodes) will then try to reduce the above-mentioned parameter values, whereby the position and shape of the electrodes as well as the applied potential were optimized to obtain a particle beam focused in both x and y planes with minimum emittance growth and energy spread. The resulted particle distribution at the exit of the einzel lens can be found in the right graphs of Fig. 1, which shows that the einzel-lens output beam has a transverse size of ~12 mm in diameter and ±4% of energy spread. The beam dynamics simulation through the einzel lens was performed using the TraceWin code with electrostatic field calculated by the CST Studio Suite.

EZ-LEBT RFQ DESIGN

Due to the relatively large transverse size and energy spread of the input beam for the downstream RFQ, the following RFQ design parameters have been decided:

- A relatively low working frequency i.e. 176.1 MHz was taken to allow a relatively large electrode aperture for the beam transport.
- The RFQ output energy was chosen to be 1.5 MeV in order to keep the structure length below 4 m.

In addition, for such an RFQ input beam, the ratio of longitudinal to transverse emittance $\frac{\varepsilon_l}{\varepsilon_t}$ will be very likely beyond the optimal emittance-ratio range ($0.9 \leq \frac{\varepsilon_l}{\varepsilon_t} \leq 1.4$) required by the MEGLET (Minimizing Emittance Growth via Low Emittance Transfer) method [6–8] after the pre-bunching, so another method so-called SEGLER (Small Emittance Growth at Large Emittance Ratios i.e. $2.0 \leq \frac{\varepsilon_l}{\varepsilon_t} \leq 4.0$) [7, 8], which provides a "safe ¼ ellipse" (the orange-marked area with $\frac{\sigma_l}{\sigma_t} = 0.0 \sim 1.0$ and $\frac{\sigma}{\sigma_0} = 0.25 \sim 1.0$ in Fig. 3) for the tune footprints of the beam motion on the corresponding Hofmann Chart, has been adopted.

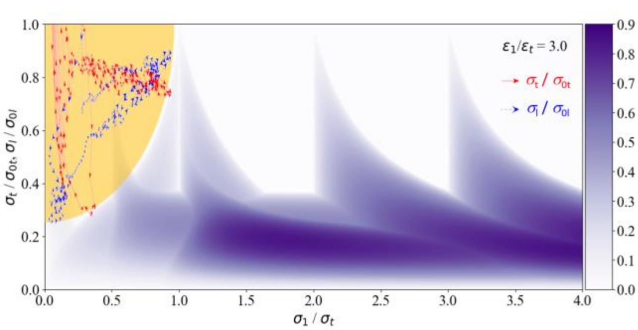

Figure 3: Hofmann chart for $\frac{\varepsilon_l}{\varepsilon_t} = 3.0$ with the "safe ¼ ellipse" (and the tune footprints of the EZ-LEBT RFQ from the beam beam dynamics simulation mentioned later).

For this study, a SEGLER-style RFQ (hereafter also referred to as the EZ-LEBT RFQ, because this RFQ has been designed for an E-LEBT and later will be checked for the Z-LEBT case) has been designed. The main parameters of the EZ-LEBT RFQ are given in Fig. 4.

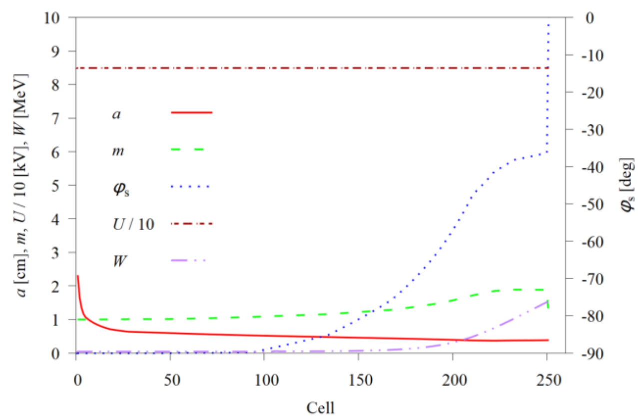

Figure 4: Main design parameters of the EZ-LEBT RFQ, where a is the minimum electrode aperture, m is the electrode modulation, φ_s is the synchronous phase, U is the inter-vane voltage, and W is the beam energy.

The beam dynamics simulation performed with the RFQGen code [9] tells that that the pre-bunching ends at around Cell 90 (see Fig. 5) where $\frac{\varepsilon_l}{\varepsilon_t} \approx 2.0$ and afterwards $\frac{\varepsilon_l}{\varepsilon_t}$ is still increasing up to $\frac{\varepsilon_l}{\varepsilon_t} \approx 4.0$ (see Fig. 6, the average $\frac{\varepsilon_l}{\varepsilon_t}$ for the main RFQ is ~3.0). As the transverse emittance keeps relatively constant after the pre-bunching, it indicates that the increase of the longitudinal emittance was not caused by emittance transfer, but because of the particles that were not well captured by the pre-bunching and were moving further and further away from the bunch center (see Fig. 5). The tune footprints of the EZ-LEBT RFQ are plotted on the $\frac{\varepsilon_l}{\varepsilon_t} = 3.0$ Hofmann Chart in Fig. 3. It is clear that most of the footprints are well located in the "safe ¼ ellipse" and only touch the resonance peaks very briefly, which explains the low emittance transfer.

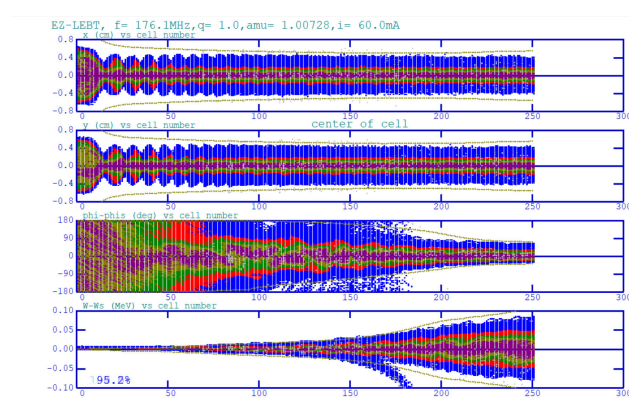

Figure 5: Beam transport simulation along the EZ-LEBT RFQ.

ISBN: 978-3-95450-257-8 ISSN: 2222-5692 doi:10.18429/JACoW-ECRIS2024-TUP11

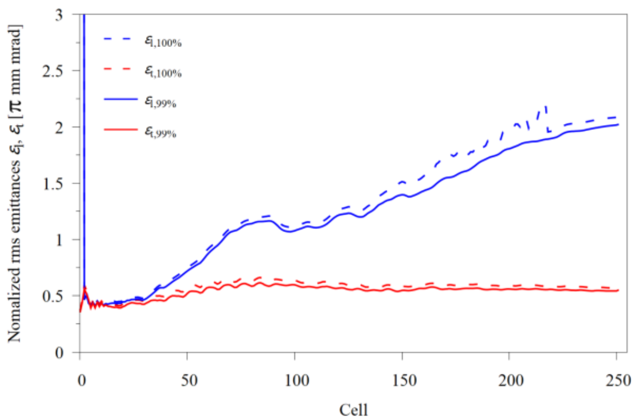

Figure 6: Evolution of emittances along the EZ-LEBT RFQ.

Z-LEBT (NO LEBT) CASE

The EZ-LEBT RFQ was also checked in case the Einzel-Lens LEBT is removed namely the IS output beam (see the left graphs of Fig. 1) will be injected into the RFQ directly. Obviously, the orientations of the transverse emittance ellipses for both the Einzel-Lens LEBT case and the Z-LEBT (i.e. no LEBT) case are quite different. To improve the matching at the entrance, the RFQ design shown in Fig. 4 has been slightly adjusted in the beginning part for the Z-LEBT case.

In Fig. 7, one can see that with a defocused input beam, the oscillation of the transverse beam envelopes becomes much stronger (compared with that shown in Fig. 5), while the beam transmission is about 10% lower

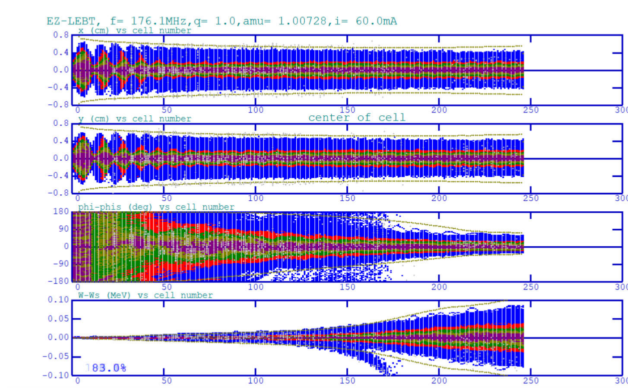

Figure 7: Beam transport simulation along the EZ-LEBT RFQ for the Z-LEBT case.

Figure 8 shows that for the Z-LEBT case, $\frac{\varepsilon_l}{\varepsilon_t}$ reaches ~1 which is actually ideal for applying the MEGLET method, but the tune footprints (see Fig. 9) are not located in the "safe rectangle" ($\frac{\sigma_l}{\sigma_t}$ = 0.5 – 2.0 and $\frac{\sigma}{\sigma_0}$ = ~ 0.25 – 1.0) [6–8] required by MEGLET.

For the Einzel-Lens LEBT case and the Z-LEBT case, the main design and simulation results are summarized in Table 1 and the corresponding RFQ output distributions are compared in Fig. 10, respectively.

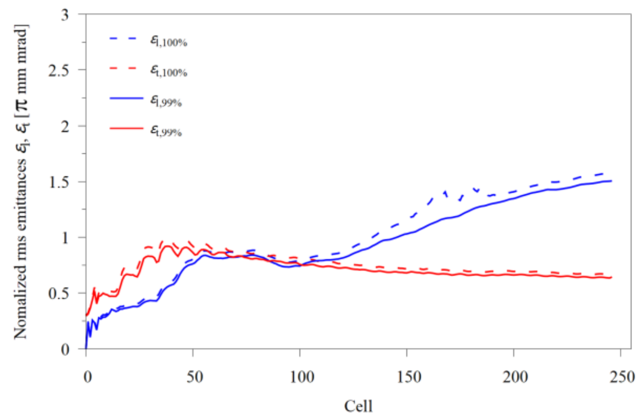

Figure 8: Evolution of emittances along the EZ-LEBT RFQ for the Z-LEBT case.

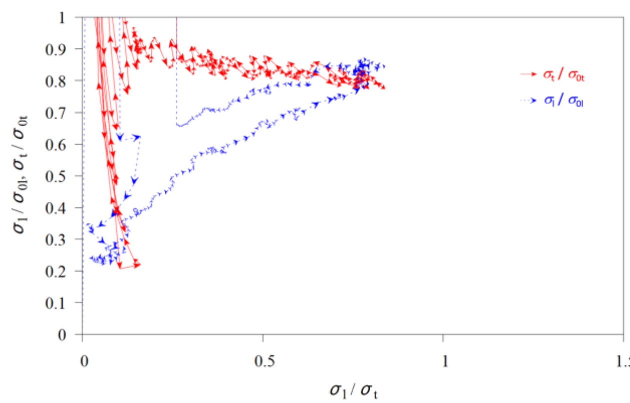

Figure 9: Tune footprints of the EZ-LEBT RFQ for the Z-LEBT case.

Table 1: RFQ Design and Simulation Results

Parameter	Einzel-Lens LEBT	No LEBT
f [MHz]	176.1	176.1
W_{in} / W_{out} [MeV]	0.053 / 1.512	0.050 / 1.511
I [mA]	60	60
U [kV]	85	85
$\varepsilon_{x, in, n., rms}$ / $\varepsilon_{x, out, n., rms}$ [π mm mrad]	0.3767 / 0.5592	0.3001 / 0.6783
$\varepsilon_{y, in, n., rms}$ / $\varepsilon_{y, out, n., rms}$ [π mm mrad]	0.3599 / 0.6068	0.3001 / 0.6726
$\varepsilon_{z, in, n., rms}$ / $\varepsilon_{z, out, n., rms}$ [π MeV deg]	4.8870 / 0.4148	0.0000 / 0.3123
N_{cell}	251	246
RFQ length [cm]	383.9	385.0
Transmission [%]	95.2	83.0

CONCLUSION & OUTLOOK

It has been demonstrated that one can use a very compact (<10 cm) einzel lens and a SEGLER-style RFQ to achieve an efficient injection of a 50 keV, 60 mA proton beam from an ECR-IS into an RFQ. With small modifications at the

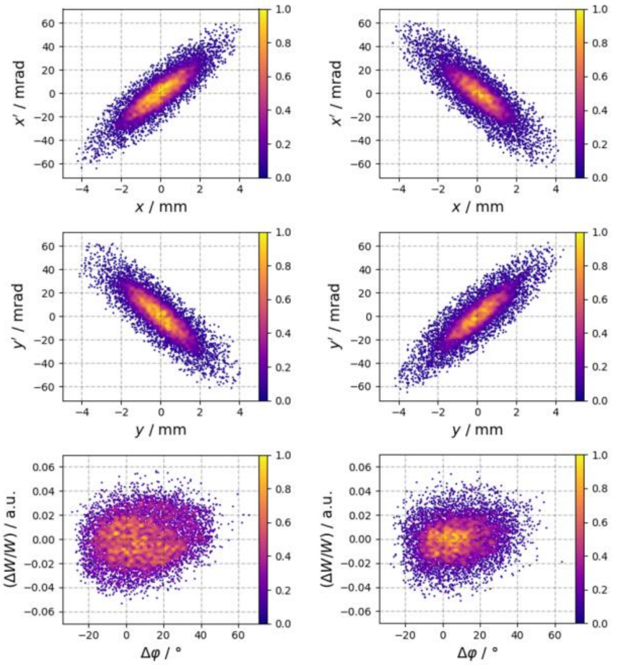

Figure 10: Output particle distributions of the EZ-LEBT RFQ for the E-LEBT case (left) and for the Z-LEBT case (right), respectively.

entrance, the SEGLER-style RFQ can still reach 83% of beam transmission even for a direct injection from the IS into the RFQ. Further improvements, e.g. to remove the "wings" in the einzel-lens output distribution (see Fig. 1) by optimizing the einzel-lens design and to change the SEGLER-style RFQ to a MEGLET-style RFQ for the Z-LEBT case, have been foreseen.

ACKNOWLEDGEMENTS

Thanks to Dr. Rustam Berezov for the discussion on output distributions of ECR proton sources as well as to Dr. Didier Uriot for his help in einzel-lens beam dynamics simulation with TraceWin.

REFERENCES

[1] R. Hollinger *et al.*, "High current proton beam investigations at the SILHI-LEBT at CEA/Saclay", in *Proc. LINAC'06*, Knoxville, Tennessee, USA, August 2006, paper TU3001, pp. 232-236.

[2] V. Dudnikov, B. Han, M. Stockli, R. Welton, and G. Dudnikova, "Low energy beam transport system developments", *AIP Conference Proceedings*, vol. 1655, no. 050003, April 2015. doi:10.1063/1.4916460

[3] M. Okamura *et al.*, "Direct plasma injection scheme in accelerators", *Rev. Sci. Instrum.*, vol. 79, no. 02B314, February 2008. doi: 10.1063/1.2821590

[4] TraceWin code, http://irfu.cea.fr/dacm/logiciels/

[5] Dassault Systems, https://www.3ds.com

[6] C. Zhang, "Minimizing Emittance Growth via Low Emittance Transfer", *Physical Review Accelerators and Beams*, vol. 25, no. 034201, March 2022. doi:10.1103/PhysRevAccelBeams.25.034201

[7] Chuan Zhang, "Beam physics and techniques towards efficient linear accelerators with space charge challenges", Habilitationsschrift, Institute of Applied Physics, Goethe University, Frankfurt, 2022.

[8] Chuan Zhang, *Radio-Frequency Quadrupole Accelerators: From Protons to Uranium Ions*, Springer Nature, Switzerland, 2023. doi:10.1007/978-3-031-40967-7

[9] L. Young and J. Stovall, "RFQGen User Guide", Los Alamos National Laboratory, 2021.

ISBN: 978-3-95450-257-8 ISSN: 2222-5692 doi:10.18429/JACoW-ECRIS2024-TUP13

TRANSPORT OF INTENSE BISMUTH AND URANIUM BEAMS INTO A RADIO FREQUENCY QUADRUPOLE ACCELERATOR

G. Rodrigues*,[1], R.W. Hamm[2]
[1]Inter University Accelerator Centre, Aruna Asaf Ali Marg, New Delhi, India
[2]R&M Technical Enterprises, Pleasanton, CA, USA

Abstract

A 48.5 MHz RFQ has been designed to transport and accelerate $^{238}U^{40+}$ (0.52 emA) and $^{209}Bi^{30+}$ (1.047 emA) beams extracted from a high performance ECR ion source. The RFQ design comprises of a pre-buncher built into the vanes to narrow the transmitted charge state distribution as much as possible. The design parameters as a function of cell length is optimised on $^{209}Bi^{30+}$. It is shown that the losses of various ions without using an inlet aperture are inevitable, but by proper coating of the vanes of the RFQ, sputtering can be minimised to a great extent. Titanium shows better results when compared with gold or copper and this has been verified using the modelling results from SRIM. The design details of matching the ECR and the RFQ and the predicted performance will be presented.

INTRODUCTION

Recent emphasis at many heavy ion accelerator facilities has been to develop, extract and transport intense beams of highly-charged, heavy ions from ECR ion sources. Assuming that these highly charged ion beams can be extracted with high intensities, the next technical challenge is to determine how to transport them without large losses of the desired ion species. All recent high performance, third generation, superconducting Electron Cyclotron Resonance (ECR) ion sources, such as the VENUS (LBNL) [1], SECRAL (IMP) [2], SUSI (MSU) [3], and the SCECRIS (RIKEN) [4], operate at higher frequencies than older sources and hence have higher plasma densities and magnetic fields. A design study of a 56 GHz source by the ECR ion source group at Berkeley shows that the source can have even higher plasma densities, since the density scales as the square root of the operating frequency [5]. A new type of ECR source has been proposed by D.Z. Xie [6] for operation at 50 GHz. Further, an upcoming new ion source, FECRAL [7], being built by the ECR group at Lanzhou, is designed to be operated at 45 GHz. The enhancement in the beam intensity for $^{209}Bi^{30+}$ at 45 GHz is expected to be greater than 1 emA at an extraction voltage of 50 kV. Considering the frequency scaling for the VENUS ion source from 28 GHz to 56 GHz with an increased volume of the plasma chamber of a factor of 10, the heavy ion beam of $^{238}U^{40+}$ produced earlier by the VENUS source [1] at an intensity of 13 eμA can be extracted with an intensity of possibly as much as 0.52 emA at the higher 56 GHz operating frequency. The extraction of these intense highly charged heavy ion beams, however, poses several problems. Generally, conventional accelerating–decelerating systems coupled to these ECR ion sources have shown inherent problems extracting intense beams of highly-charged ions due to sparking at the high voltages required and the poor vacuum conditions, which in turn limit the extraction currents. Therefore, this type of extraction system generally fails due to problems with the high voltage power supplies. This eventually keeps the ion source from functioning smoothly and increases the downtime of the accelerator.

In the applications of laser ion sources, with their much higher plasma densities, severe problems of handling intense beams due to sparking and/or beam loading are avoided by using an ingenious technique, the so-called Direct Plasma Injection Scheme (DPIS) [8]. This technique was utilized for injecting intense beams directly into an RFQ using the combined focusing of the gap between the ion source and RFQ vanes (or rods) and the focusing of the RF fields from the RFQ penetrating into this gap. In this scheme, the plasma expands to the entrance of the RFQ where the electrons are deflected by the RFQ's fringe field and only the ions get trapped by the RFQ focusing field. Hence, space charge effects are efficiently controlled, with the great advantage being the ability to transport very intense highly-charged beams. This technique was experimentally demonstrated for the acceleration of carbon (C^{3+}, C^{4+}, C^{5+}) and aluminum (Al^{9+}) ions with beam intensities greater than 60 mA [9].

In the case of the next generation ECR ion sources, the development of higher operating frequencies in superconducting ECR ion sources will result in higher plasma densities. Therefore, much higher beam intensities will not only be possible by using extraction voltages higher than the 30 kV in use today in most ECR sources, but also by changing the extraction electrode aspect ratio. Operating at these higher extraction voltages would result in operating the conventional accelerating–decelerating extraction systems at relatively higher voltages, thus increasing the probability of sparking. In order to circumvent this problem in conventional ECR ion source extraction systems, a proposed solution is to couple an RFQ directly to a high performance ECR ion source using the DPI scheme. For high performance ECR sources that use superconducting solenoids, the stray magnetic field of the source can also be used in the DPI scheme to provide more focusing in order to overcome the space charge blow-up of the beam [10].

After the correct matching is accomplished between the ion source and the RFQ, the next task is to design the RFQ to select the ion of interest for further beam transport and to

* gerosro@gmail.com

ISBN: 978-3-95450-257-8 ISSN: 2222-5692 doi:10.18429/JACoW-ECRIS2024-TUP13

discard the unwanted ions. Therefore, the RFQ is in principle be used as a filter in a charge/mass (Q/M) selective mode for a reduced bandwidth of Q/M. By matching the velocity of the desired charge state to the vane modulation in the RFQ, other unwanted charge states will not be focused or accelerated and will be lost in the RFQ. The RFQ will then resemble a Paul quadrupole filter [11] where the action of the dc voltage on the electrodes is replaced by the modulation.

This filtering can be very efficient for ions with larger Q/M, such as carbon and aluminium, but is restricted to several charge states being transported for much lower Q/M ion beams. Some initial work was reported in this direction for the case of uranium ions, which assumed an ion source configured to work at 56 GHz and scaled for currents with data taken from the VENUS ECR ion source operated at 28 GHz [12].

Work on charge state selective ion beam acceleration using a laser ion source directly coupled to an RFQ was reported in Ref. [13]. However, this was for low charge states of bismuth to be used primarily as a driver beam for heavy ion beam inertial fusion (HIF). Other studies, for example Ref. [14], report on use of a DPI scheme mainly for acceleration of C^{5+} ions.

In the present study, a high performance ECR ion source is assumed to be directly coupled to an RFQ that is designed for charge state selection of heavier ions with higher charge states and very high intensities. We have considered two ion species, uranium and bismuth ions, where the charge state distribution (CSD) data have been reported from existing ion sources for each specie, VENUS and SECRAL II respectfully. Although the 4th generation ion source being proposed by C. Lyneis et al. would be operated at 56 GHz, the FECRAL ion source being built by the ECR group at Lanzhou is designed to be operated at a modest frequency of 45 GHz to reduce the complexity as compared to 56 GHz. The beam intensity for $^{209}Bi^{30+}$ at 45 GHz is expected to be greater than 1 emA at a designed and operable extraction voltage of 50 kV [2]. It should be emphasized here that the emerging charge state distribution will be essentially narrowed down by the RFQ. This further reduces the transport problem for the beam line as well as reduces the emittance growth for the transmitted charge states as they are further accelerated.

ECR-RFQ MATCHING SECTION

It is well known that the RFQ is very efficient for acceleration in the energy range from 1 keV/u to 1 MeV/u, but space charge effects are dominant at the low energies and relatively higher beam intensities that are used for injecting beam into them. Therefore, our proposal is to operate the ECR ion source at an extraction voltage in the range of 60 to 70 kV (i. e., 10.084 keV/u) to overcome the defocusing forces in the extracted beam due to the beam's space charge. New ion sources which are under commissioning, such as FECRAL [7] have designed their extraction systems to be operable at 50 kV [2]. For example, at an extraction voltage of 50 kV, a $V^{3/2}$ enhancement factor of 2.15 in the beam intensity is expected as compared to extraction at 30 kV. Since most existing superconducting ECR ion sources operate at ~30 kV with conventional accelerating–decelerating extraction systems, the gain in the beam intensities are expected to be even higher, when the extraction voltage is further raised above 50 kV.

In the RFQ, the Twiss parameters depend on time (or radio frequency phase), but the Twiss parameters for the injected beam from the ion source are constant and do not vary with time. Although the PARMTEQ code has generally used for the design of an RFQ, it cannot be used for designing the proposed DPI matching system because it does not simulate the plasma meniscus and the static accelerating field. The full simulation of this problem requires matching a time independent beam from the ion source to a time dependent beam inside the RFQ, which poses a serious matching problem. Therefore, a symmetric beam is required which has the same Twiss parameters in both the planes. However, the design of such a combined extraction/matching section can easily be performed using the IGUN code [15]. The unique features of IGUN take into account the electrostatic field between the ion source and the RFQ, the stray magnetic field of the ECR source, the defocusing space charge of the intense beam, and the RF focusing in the fringe field between the RFQ electrodes and the RFQ flange [16]. In the matched beam condition, as shown in Ref. [16], the effective current becomes zero which is independent of the emittance to acceptance ratio, and the result is a homogenous focusing of the RFQ using unmodulated electrodes. Even in the case of a mismatched condition, the beam envelope will depict betatron oscillations that may finally get damped in the initial acceleration in the RFQ. The code allows the user to simulate the beam from the plasma meniscus of the ECR source to the position in the RFQ where the axial acceleration starts with the modulation of the electrodes. This matching technique of high current beams has been shown to be very effective [17]. An added advantage is that the Kapchinsky–Vladimirsky equations used in the IGUN code can handle axisymmetric charge density distributions of the input beam, which compared to other distributions, has only linear space charge fields and does not contribute to the emittance growth. Although, these are not fully realistic distributions, analytic computation of these fields is possible.

DIRECT INJECTION OF ECR SOURCE INTO AN RFQ

The injector design being proposed implements the matching of the beam from a high performance ECR ion source into a special matching section of an RFQ, which is a section without any vane modulation. The radial matching section of an RFQ is typically 4 to 6 cells in length and has a varying vane tip radius with a constant vane voltage along its length. However, for this design a 6-cell matching section with a constant tip radius was used with no focusing element between the ECR source and the matching section. The ECR source

ISBN: 978-3-95450-257-8 ISSN: 2222-5692 doi:10.18429/JACoW-ECRIS2024-TUP13

axial magnetic field (~4 T maximum value generated by the superconducting solenoid) is positioned at the extraction electrode for optimum extracted beam optics, and it defines the beam size at the start of the simulation.

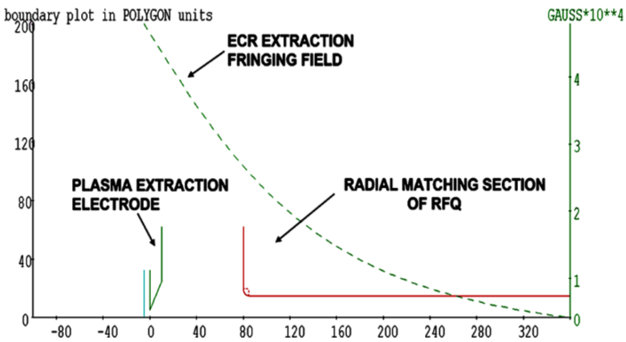

Figure 1: Model of the extraction and matching problem simulated using IGUN.

The geometry of the proposed extraction system simulated in IGUN is shown in Fig. 1. Due to the large axial magnetic field necessary in the ECR ion source, the magnetic field extends significantly into the matching section of the RFQ (shown as the green dashed line). The distance between the position of the plasma electrode and the start of the RFQ matching section was chosen to be 28 mm. The source extraction voltage defines the beam injection energy for all extracted charge states. The basic plasma parameters of the electron and ion temperatures were chosen to be 5 eV and 0 eV, respectively. Higher values may be more realistic at these higher frequencies since the electron and ion temperatures are expected to increase with frequency. However, as those values are unknown, the values chosen seem to be justified for a first approximation. In the first series of simulations for this design, the ECR stray magnetic field was varied from low to high values to determine its effect on the focusing at the entrance of the RFQ matching section. For a matched beam at the entrance of the RFQ channel, the variation of the axial magnetic field gives the smallest radius for different Q/M at different magnetic fields, and the radius and divergence decrease with increasing magnetic fields. Therefore, there is an optimal magnetic field for each charge state of the injected beam.

For injection of bismuth ions, a total beam intensity of 25 mA was assumed, consisting of 1.047 emA of $^{209}\mathrm{Bi}^{30+}$ ions, other charge states of bismuth ions, and ions of the mixing gas used in the ECR. While keeping the beam intensity constant in the simulation (i. e., the total ion current is 25 emA), IGUN adjusts the plasma density over many iteration/convergence cycles until the loss to the RFQ entrance aperture has converged. The final extraction geometry and the calculated results are shown in Fig. 2 for bismuth and oxygen ions (the mixing gas). The RF focusing parameter (%) for the RFQ is plotted as the black dashed line, with the values given on the vertical axis in the middle of the plot, and the stray magnetic field from the ECR source (the green dashed line) is labelled on the right vertical axis.

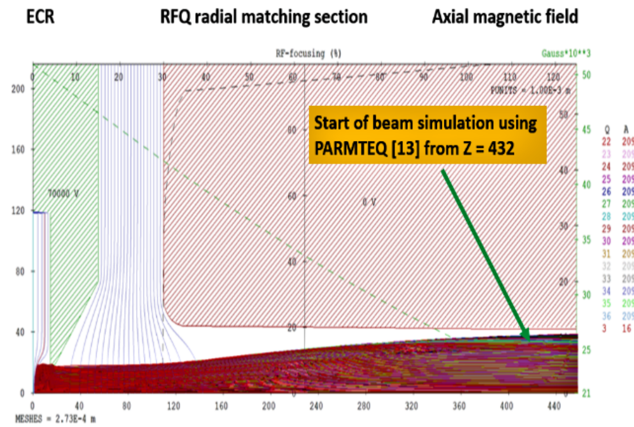

Figure 2: Optimized design using IGUN for transporting 25 emA from 45 GHz ECR ion source, consisting of $^{209}\mathrm{Bi}^{30+}$ and other charge states, including oxygen mixing gas ions directly into the RFQ.

THE RFQ AS A CHARGE FILTER

A number of RFQ beam dynamics calculations have been performed using PARMTEQ [18] in order to sharpen the output CSD for $^{209}\mathrm{Bi}^{30+}$. However, this is generally not an easy problem. In order to have a high current limit, one needs a large focusing force and large RFQ bore. This allows a wide selection of charge states to be focused. The unmodulated RFQ vanes (or rods) focus the ions with no acceleration, so all the charge states are transmitted. Selecting only $^{209}\mathrm{Bi}^{30+}$ acceleration in the RFQ is not possible, but the aim was to narrow the CSD as much as possible and eliminate the oxygen carrier gas ions.

The RFQ design proposed here is a 4-rod RFQ using the constant radius matching section described above as the first stage, which matches the input beam from the ECR as calculated by IGUN. A normal RFQ was then designed to follow this matching section. The performance of this RFQ was calculated for the matched input beam. In order to operate the RFQ as a "charge filter", the normal design of a conventional RFQ with adiabatic bunching will not serve the purpose as a charge filter, since all charge states other than the designed charge state (M/Q) will also pass through the RFQ due to the large longitudinal acceptance. Here we describe the new design of the RFQ called as a charge filter. The RFQ design was modified to use a short buncher section using few cells with modulation in the front end of the RFQ just after the IGUN matching section and then another unmodulated section (drift region) before the RFQ bunching and acceleration begins. It should be noted here, that, the various sections described here are integrated into one complete RF structure. The length of this pre-buncher and drift region was adjusted in such a way that ions with different charge states can be pre-bunched separately in longitudinal phase space. This "pre-buncher" in the beginning of the RFQ was used to reduce the width of the transmitted charge state distribution, but as noted by Fuwa et al. [19], while the pre-bunching slightly reduces the transmission in the lower charge states, it also slightly shifts the transmitted ions

ISBN: 978-3-95450-257-8 ISSN: 2222-5692 doi:10.18429/JACoW-ECRIS2024-TUP13

toward the higher charge states. A further decrease of the width of the transmitted CSD can be achieved by a slight lowering of the operating vane voltage or by decreasing the modulation. However, this action reduces the $^{209}Bi^{30+}$ transmission slightly. It should be noted that the modified design of the final resulting RFQ with the pre-buncher has the same length and RF power requirement as the original RFQ design without the modifications.

The resulting realistic 48.5 MHz 4-rod RFQ has a total length of 298 cm and an average vane bore radius of 11.5 mm. Its performance was calculated using PARMTEQ, assuming an injection beam energy of 10.084 keV/u for a beam of $^{209}Bi^{30+}$ (M/Q =6.966). The results showed that >94 % transmission could be achieved for this beam, and a total beam current of 8 mA could be accelerated to a final energy of 60 keV/u. At these energies, the short RFQ cells are advantageous since the stable phase and accelerating field change very slowly over the length. Therefore, the dc beam from the ion source is bunched by the RFQ with minimum emittance growth. Since the characteristic impedance of the structure depends on its type, design parameters, and operating frequency, a lower operating frequency of 48.5 MHz and shorter length were chosen to minimize the RF power requirements. This RFQ requires an input RF power of ~18 kW. The concept of a "variable energy" RFQ can also be easily adopted here, especially in the case of using a 4-rod RFQ as compared to using the 4-vane RFQ, since the electrodes and the driving inductances are practically separable [20].

This RFQ for $^{209}Bi^{30+}$ is almost identical to the earlier reported 48.5 MHz RFQ designed for $^{238}U^{40+}$ [12], which also had a length of 298 cm for input ions at 10.084 keV/u and output energy of 60 keV/u with an input rf power of 18 kW. The design and operating parameters of the $^{209}Bi^{30+}$ RFQ are shown in Table 1. Table 2 lists the energy and velocity levels at various sub-sections of the RFQ calculated for $^{209}Bi^{30+}$. In this table, β is defined as the ratio of the particle velocity, v to the velocity of light, c ; β = v/c. Figure 3 shows the design parameters of the RFQ as a function of cell number. This matching section replaces the normal radial matching section used in most RFQ's. For the calculations that are reported here, the emittance and rms ellipse parameters were calculated using IGUN at the position Z = 432 meshes (4.32 cm) in the matching section as indicated in Fig. 2, and these values were used as input parameters to PARMTEQ for calculation of the beam bunching and acceleration through the RFQ. The transverse and longitudinal beam parameters have been computed through the final RFQ design as a function of the cell number. These are shown in Fig. 4 for the case of $^{209}Bi^{30+}$. The RFQ beam transmission, shown in Fig. 5, has a narrower charge state distribution than the beam extracted from the ECR ion source.

Similarly, the case is shown for the $^{238}U^{40+}$ RFQ in Fig. 6, again clearly depicting the selection of a much narrower charge state distribution than the beam extracted from the ECR ion source. In both cases, as shown, the modified RFQ with the pre-buncher has a narrower charge state distribution than the original design. Finally, the two assumed ECR

Table 1: Design and Operating Parameters of the RFQ

Parameter	Value
Mass (M)	209
Input Energy	10.084 keV/u
Charge (Q)	30
Frequency	48.5 MHz
Aperture	1.15 cm
Vane voltage	94.0 kV
Electric field (surface)	11.45 MV/m
Bravery factor	1.3
Capacitance/m	75 pF/m
Power/m (at vane voltage of 90.56 kV)	0.0061 MW/m
Stored energy/m	0.3575 J/m
Quality factor	17768
Maximum vane modulation	1.45
Focusing strength	4.354
Accelerating efficiency	0.2841
Focusing efficiency	0.7566
Vane length (including IGUN matching section)	298 cm
Beam current limit	59.8 mA
Normalized acceptance	0.40 cm·mrad
Maximum capture efficiency of $^{209}Bi^{30+}$	94 %

Table 2: Energies and Velocities Through the Various Subsections of the RFQ Calculated for $^{209}Bi^{30+}$

RFQ subsection	W [MeV]	W/u	W/Q [MeV]	β=v/c
Initial (beam entry point)	2.10	0.0101	0.0600	0.0046
Shaper	6.90	0.033	0.230	0.0084
Buncher	11.19	0.0535	0.373	0.0107
Final	12.54	0.060	0.418	0.0114
Accelerator	40.	0.191	1.333	0.018

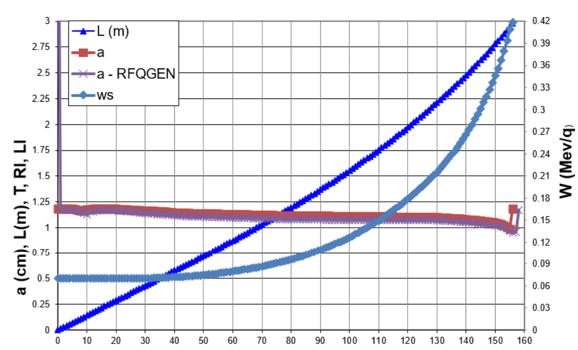

Figure 3: RFQ design parameters as a function of cell length for $^{209}Bi^{30+}$.

output current distributions are shown in Fig. 7, along with the predicted RFQ output beam current distribution for the $^{209}Bi^{30+}$ and $^{238}U^{40+}$ peaks.

ISBN: 978-3-95450-257-8 ISSN: 2222-5692 doi:10.18429/JACoW-ECRIS2024-TUP13

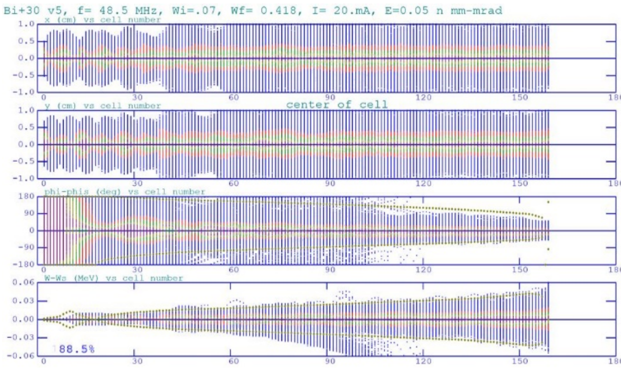

Figure 4: Transverse and longitudinal beam parameters as function of cell number in the final RFQ design for $^{209}Bi^{30+}$.

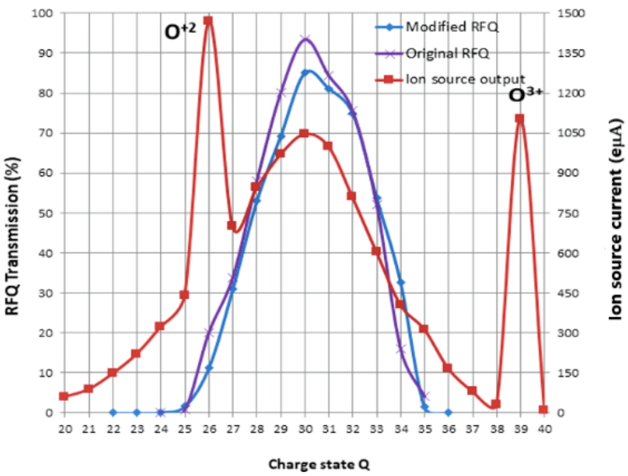

Figure 5: Transmission of ^{209}Bi ions through the modified RFQ design compared with the original design as a function of the input charge state distribution.

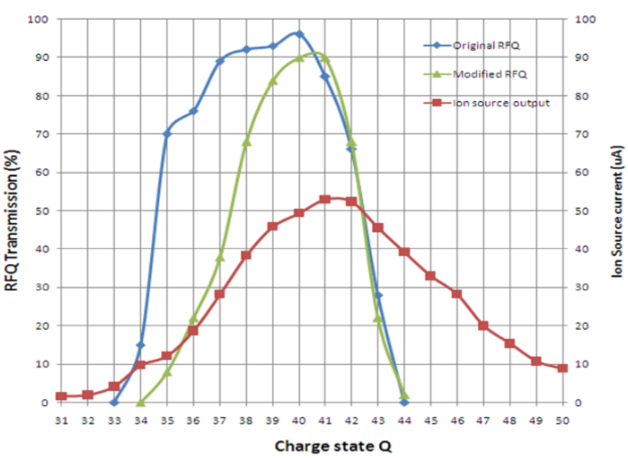

Figure 6: Transmission of ^{238}U ions through the final modified RFQ design compared with the original design as a function of the input charge state distribution.

It is to be noted here, that both the charge state distributions have been obtained from two different ion sources and the resulting widths of the emerging charge state distributions after the RFQ will be different, although the difference in their M/Q values are not substantial.

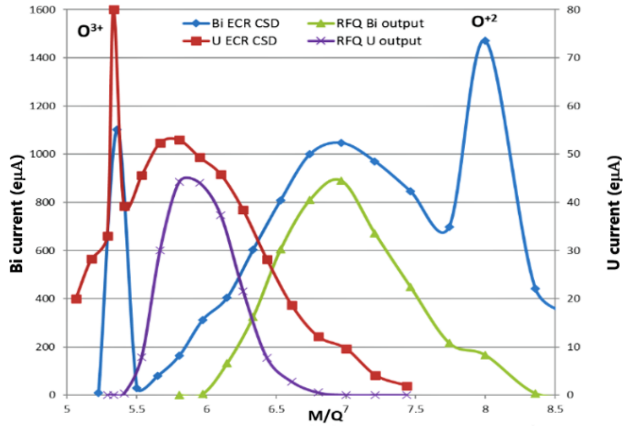

Figure 7: Input and output RFQ current distributions calculated for both bismuth and uranium beams.

BEAM LOSSES AND COOLING REQUIREMENTS

The distance between the plasma electrode of the ECR ion source and the start of the matching section of the RFQ is such that the extraction flange of the ECR extraction system can be attached to the entrance flange of the RFQ. Hence the beam power of the extracted beam, which is estimated to be a maximum of 1.5 kW assuming a total extracted ion current of 25 mA, extracted at 60 kV, is mostly deposited in the entrance of the RFQ. It is important to use an aperture at the entrance of the RFQ to avoid unwanted ions getting sputtered on the RFQ rods and further damaging them and at the same time increasing the beam transmission through the RFQ. This is a possible measure to be adopted or to be considered for improving the lifetime of the RFQ rods. Figure 8 depicts the calculated beam losses (charge states 24^+ to 35^+) all through the RFQ, considering an input of 10000 macroparticles, without using an input aperture and this may possibly result in sputtering of the RFQ rods. It is to be noted that 24^+ is predominantly lost in the first 10 cells of the RFQ and the higher charge states up to 25^+ are about 25 % of the total loss of 24^+ throughout the remaining cells

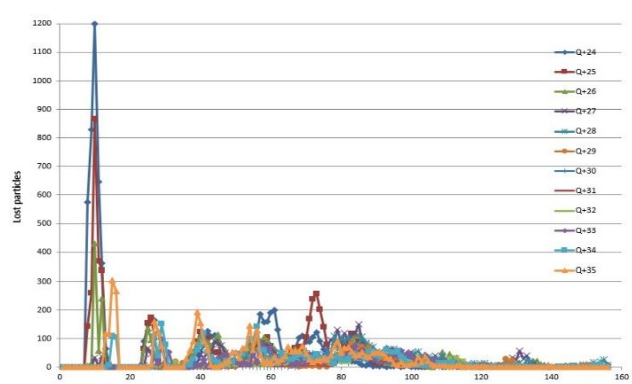

Figure 8: Beam losses calculated (charge states 24^+ to 35^+) all through the RFQ using 10000 macroparticles, without using an input aperture, and may result in sputtering of the RFQ rods.

of the RFQ. Figure 9 shows the transmission achieved for $^{209}Bi^{30+}$ as a function of cell length. It may be important to perform a hard metal coating of the RFQ rods (instead of a thin metal coating of nickel of few mils which eventually gets sputtered out [21]) to mitigate sputtering effects resulting from the use of heavy ions. High-gradient experiments [22] suggest that titanium vane tips support higher surface fields compared to copper, up to 40 MV/m, and are more resistant against beam irradiation. In the worst case scenario, the damaged RFQ rods may be replaced with new RFQ rods, which may cause downtime of the accelerator. It should be noted that sputtering of the RFQ rods is inevitable and the suggested measures mentioned above should be seriously considered.

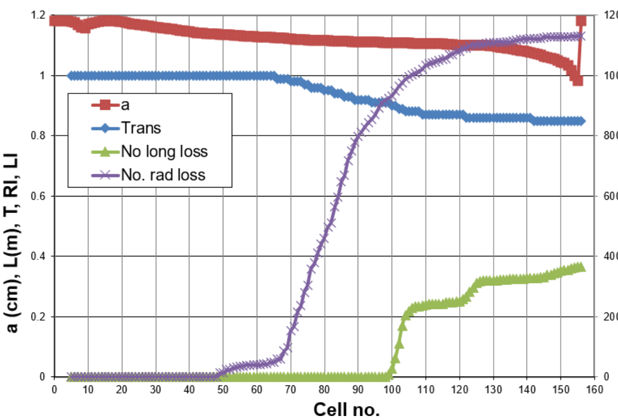

Figure 9: Transmission of $^{209}Bi^{30+}$ as a function of cell length.

The beam power of the filtered ions through the RFQ is expected to be smaller than the remaining part of the non-filtered ions. Since the beam power is very high, it is important that the RFQ entrance flange is water cooled to dissipate the heat. This will further reduce the outgassing and discharges in the extraction area. The RFQ itself will have good pumping to evacuate the gas load coming from the non-filtered ions in addition to the pumping system installed between the extraction and RFQ flanges.

DISCUSSION AND CONCLUSION

It has been shown in this study that an RFQ can be used as a charge filter to efficiently transport highly charged heavy ion beams of interest with a reduced emittance growth. It should also be obvious that the proposed RFQ structures could be designed to filter other charge states of uranium and bismuth (i. e., $^{209}Bi^{31+}$ and $^{238}U^{41+}$). It is emphasized here that the emerging charge state distributions have narrowed down. In the case of filtering a $^{209}Bi^{30+}$ beam, the transmission through the RFQ is 94 %, while the resulting charge state distribution shows a narrowed FWHM of 60 % of the original distribution. For the case of $^{238}U^{40+}$, the transmission is slightly above 90 %, and the FWHM of the resulting charge state distribution has narrowed down to ~62 % of the original distribution. This clearly demonstrates that the RFQ is acting as a charge filter by removing the unwanted ions and at the same time, preserving the transmission and improving the emittance with acceleration. The filtered ions, consisting of the unwanted charge states and the carrier gas ions, are lost inside the RFQ.

This technique has the advantage that axisymmetric forms of charge density distributions can be properly matched from the ECR directly into the RFQ. It is evident that such an RFQ channel is very effective and less M/Q sensitive for the extraction system of all high performance ECR ion sources. This technique has promising applications for injecting and transporting very intense beams into RFQ accelerators for research, Accelerator Driven Sub-critical Systems (ADSS), and more efficient, compact neutron generators [23]. The ADSS being developed at various laboratories around the world to create nuclear energy may also benefit from this technique, both in terms of transporting intense beams of protons and making the low energy segment more compact. The charge breeding concept can be utilized with a powerful ECR ion source directly coupled to this RFQ charge filter and then injected into another higher frequency LINAC for additional acceleration.

ACKNOWLEDGEMENT

The work that has been pioneered, developed and reported here is fondly devoted to the memory of the late Prof. Dr. Reinard Becker, and author of the IGUN code, and an important contributor to the concepts and simulations presented.

REFERENCES

[1] C. Lyneis, D. Leitner, M. Leitner, C. Taylor, and S. Abbott, "The third generation superconducting 28 GHz electron cyclotron resonance ion source VENUS", *Rev. Sci. Instrum.*, vol. 81, p. 02A201, 2010. doi:10.1063/1.3271135

[2] H.W. Zhao *et al.*, "Superconducting ECR ion source: From 24-28 GHz SECRAL to 45 GHz fourth generation ECR", *Rev. Sci. Instrum.*, vol. 89, p. 052301, 2018. doi:10.1063/1.5017479

[3] G. Machicoane *et al.*, "First Results at 24 GHz with the Superconducting Source for Ions (SuSI)", in *Proc. ECRIS'14*, Nizhny Novgorod, Russia, Aug. 2014, paper MOOMMH03, pp. 1-4. https://jacow.org/ECRIS2014/papers/moommh03.pdf

[4] Y. Higurashi, H. Haba, M. Kidera, T. Nakagawa, J. Ohnishi, and K. Ozeki, "Recent Developments of RIKEN 28 GHz SC-ECRIS", in *Proc. ECRIS'16*, Busan, Korea, Aug.-Sep. 2016, pp. 10–13. doi:10.18429/JACoW-ECRIS2016-MOBO04

[5] C. Lyneis, P. Ferracin, S. Caspi, A. Hodgkinson, and G.L. Sabbi, "Concept for a fourth generation electron cyclotron resonance ion source". *Rev. Sci. Instrum.*, vol. 83, p. 02A301, 2012. doi:10.1063/1.3655527

[6] D.Z. Xie, "A new structure of superconducting magnetic system for 50 GHz operations", *Rev. Sci. Instrum.*, vol. 83, p. 02A302, 2012. doi:10.1063/1.3655530

ISBN: 978-3-95450-257-8 ISSN: 2222-5692 doi:10.18429/JACoW-ECRIS2024-TUP13

[7] G. Machicoane *et al.*, "Recent Advance in ECR Ion Sources", in *Proc. NAPAC'19*, Lansing, MI, USA, Sep. 2019, pp. 31–36. doi:10.18429/JACoW-NAPAC2019-MOYBB2

[8] M. Okamura, T. Katayama, R.A. Jameson, T. Takeuchi, and T. Hattori, "Simulation of direct injection scheme for RFQ linac", *Rev. Sci. Instrum.*, vol. 73, p. 761–763, 2002. doi:10.1063/1.1430044

[9] M. Okamura *et al.*, "Simulation of direct injection scheme for RFQ linac", *Rev. Sci. Instrum.*, vol. 79, p. 02B314, 2008. doi:10.1063/1.1430044

[10] G. Rodrigues, R. Becker, R.W. Hamm, R. Baskaran, D. Kanjilal, and A. Roy, "The direct injection of intense ion beams from a high field electron cyclotron resonance ion source into a radio frequency quadrupole", *Rev. Sci. Instrum.*, vol. 85, p. 02A740, 2014. doi:10.1063/1.4861405

[11] W. Paul and H. Steinwedel, "Notizen: Ein neues Massenspektrometer ohne Magnetfeld", *Z. Naturforsch. A*, vol. 8, no 7, pp. 448–450, 1953. doi:10.1515/zna-1953-0710

[12] G. Rodrigues, R. Becker, R.W. Hamm, and D. Kanjilal, "Direct Injection of Intense Heavy Ion Beams from a High Field ECR Ion Source into an RFQ", in *Proc. ECRIS'14*, Nizhny Novgorod, Russia, August 2014, paper MOPPH006, pp. 52–56. https://jacow.org/ECRIS2014/papers/mopph006.pdf

[13] Y. Fuwa, S. Ikeda, T. Kanesue, M. Okamura, and Y. Iwashita, "Charge State Selective Ion Beam Acceleration Using the RFQ Linac", *RIKEN Accel. Prog. Rep.*, vol. 48, p. 198, 2015. https://www.nishina.riken.jp/researcher/APR/APR048/pdf/198.pdf

[14] J. Tamura, Y. Fuwa, T. Kanesue, and M. Okamura, "Charge State Selective Ion Beam Acceleration with RFQ Linac", in *Proc. HIAT2015*, Yokohama, Japan, Sep. 2015, paper WEPB11, pp. 216–218. doi:10.18429/JACoW-HIAT2015-WEPB11

[15] R. Becker and W.B. Herrmannsfeldt, "IGUN–A program for the simulation of positive ion extraction including magnetic fields", *Rev. Sci. Instrum.*, vol. 63, p. 2756, 1992. doi:10.1063/1.1142795

[16] R. Becker and R.A. Jameson, "Emittance growth as mesh artefact", *Nucl. Instrum. Methods Phys. Res., Sect. A*, vol. 558, pp. 32-35, 2006. doi:10.1016/j.nima.2005.11.009

[17] R. Becker, "RFQ Matching for Current Dominated Ion Beams", in *Proc. EPAC'92*, Berlin, Germany, Aug. 1992, pp. 816–818. https://jacow.org/e92/PDF/EPAC1992_0816.PDF

[18] K.R. Crandall and T.P. Wangler, "PARMTEQ—A beam dynamics code for the RFQ linear accelerator", *AIP Conf.Proc.*, vol. 177, pp. 22-28, 1988. doi:10.1063/1.37798

[19] Y. Fuwa, S. Ikeda, M. Kumaki, T. Kanesue, M. Okamura, and Y. Iwashita, "Beam Dynamics of Multi Charge State Ions in RFQ Linac", in *Proc. LINAC'14*, Geneva, Switzerland, Aug. 2014, paper MOPP112, pp. 317–319. https://jacow.org/LINAC2014/papers/mopp112.pdf

[20] A. Schempp, "RFQ ion accelerators with variable energy", *Nucl. Instrum. Methods Phys. Res., Sect. B*, vol. 40/41, pp. 937–942, 1989. doi:10.1016/0168-583X(89)90511-9

[21] J. Staples, "Beam dynamics and vane geometry in the LBL heavy ion RFQ", in *Proc. PAC'83*, Santa Fe, NM, USA, March 1983, pp. 3533–3535. https://jacow.org/p83/PDF/PAC1983_3533.PDF

[22] H.W. Pommerenke, G. Bellodi, A. Grudiev, S. Kumar, and A.M. Lombardi, "Beam Dynamics and RF Design Studies for the New RFQ for CERN Linac4 Upgrade", in *Proc. LINAC'22*, Liverpool, UK, Aug.-Sep. 2022, pp. 430–433. doi:10.18429/JACoW-LINAC2022-TUPOPA10

[23] R.W. Hamm and R. Becker, "The Design of a Compact RFQ Neutron Generator", *Int. J. Modern Phys. Conf. Series*, vol. 27, p. 1460126, 2014. doi:10.1142/S2010194514601252

ISBN: 978-3-95450-257-8 ISSN: 2222-5692 doi:10.18429/JACoW-ECRIS2024-TUP14

3D SIMULATIONS OF THE CAPRICE ECRIS EXTRACTION SYSTEM

M. A. Händler*[1,2], A. Andreev[1], G. Franchetti[1,2], M. Galonska[1], R. Hollinger[1], R. Lang[1], J. Mäder[1], F. Maimone[1]

[1] GSI Helmholtzzentrum für Schwerionenforschung GmbH, Darmstadt, Germany

[2] Institute for Applied Physics, Goethe University, Frankfurt am Main, Germany

Abstract

The simulation of the ion extraction from the Electron Cyclotron Resonance Ion Sources (ECRISs) is necessary for the optimization and development of the performance of ion sources. Due to the magnetic field configuration of the ECRISs the calculations need to be performed in 3D. For this reason simulations based on the C++ library "Ion Beam Simulator" (IBSimu) were developed. In this work, a physical model was implemented in IBSimu for performing detailed 3D simulations of ion extraction from a CAPRICE-type ECRIS. Simulations of multi-species Argon ion beam including Helium contribution as support gas extracted from CAPRICE are carried out. Simulation results are presented and compared to experimental findings, in particular for ion beam intensities and beam profiles measured with viewing screens.

INTRODUCTION

Understanding and optimizing the performance of the ECR ion sources, particularly in terms of beam formation and transport, is crucial for their application in scientific research and industrial processes. In this work, a study of the CAPRICE ECRIS focusing on the comparison between experimental beam profile measurements and a novel three-dimensional simulation is presented. The use of a 3D simulation model provides a more comprehensive analysis of the ion source behavior compared to a two-dimensional approach and allows for a more accurate prediction of the ion extraction from an ECRIS source. The simulation results obtained using IBSimu [1], a versatile ion beam simulation tool, have been compared with experimental measurements. For the experiment, a viewing screen was employed to capture and analyze the beam profile, providing valuable data to benchmark the simulation.

MATERIALS AND METHODS

Simulations

For the simulations, the C++ library IBSimu was utilized. This software was designed for ion beam simulations calculating the ion trajectories. However, since the library was not originally intended for simulating ion beam extraction from deep within a plasma volume, several modifications were necessary to adapt the program for this purpose. Additionally, some fundamental assumptions regarding the ion extraction process had to be made. These assumptions align with the prevailing consensus in the field of ion sources, however, their applicability to this specific type of simulation requires further validation.

In the simulation, the ions are generated from a surface located at the center of the plasma chamber (see simulation results). This position was chosen based on the assumption that the plasma occupies the majority of the chamber and by results of previous simulations, which indicate that the ions for each ion beam extracted from an ECR ion source originate from various positions within the plasma volume [2]. By placing the ion origin at this location, the simulation aims to more accurately predict the real ion production and transport dynamics. Additionally, an initial plasma had to be defined to ensure accurate results for the simulation. For this simulation the plasma potential was set to 20 V and the plasma was positioned in the area inside the plasma chamber (from $x = 0$ m to $x = 0.17$ m). A 98% space charge compensation was also applied from $x = 0.204$ m to $x = 0.5$ m.

The simulations were conducted for various charge states of argon (Ar^{3+} to Ar^{10+}) together with helium (He^{+} and He^{2+}) and hydrogen (H^{+}) ions. The initial distribution of the different charge states and different ion species used in the simulation was based on a previously conducted experiment. The magnetic field parameters and electrode geometry (STL files) utilized in the simulation were based on the results of simulations previously performed [3]. The following Table 1 presents the parameters setting used for the simulation.

Table 1: Parameters Used in the Simulation

Parameter		Value	Unit
parallel ion temperature	T_p	0.1	eV
transversal ion temperature	T_t	0.15	eV
electron temperature	T_e	5	eV
start energy of the ions	E_i	0.8	eV
screening electrode voltage		−2	kV
plasma electrode voltage		15	kV
number of ions	N	100000	
plane of ion creation		$x = 0.1$	m

The current density j at the starting plane of the ions is not included as different values for this parameter were tested, and this parameter appears to have the biggest influence of the outcome of the simulations.

Experimental Setup

The experimental setup employs a CAPRICE ECRIS (see Fig. 1), whose plasma chamber and ion extraction system are modeled in IBSmu by implementing its geometry, electric potential and internal magnetic field. This computer model is the base for all the simulations that will be presented in this proceeding.

* M.A.Haendler@gsi.de

ISBN: 978-3-95450-257-8 ISSN: 2222-5692 doi:10.18429/JACoW-ECRIS2024-TUP14

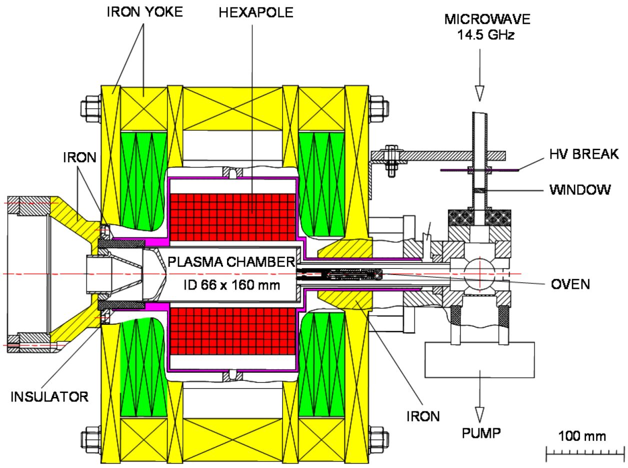

Figure 1: Schematic of the CAPRICE ECRIS.

The experimental data have been obtained from an ECR test stand. The ECR injector stand (EIS) includes an analysis system capable of measuring various parameters, including ion beam mass spectra and beam currents [4]. Figure 2 provides a schematic of the ECR test stand.

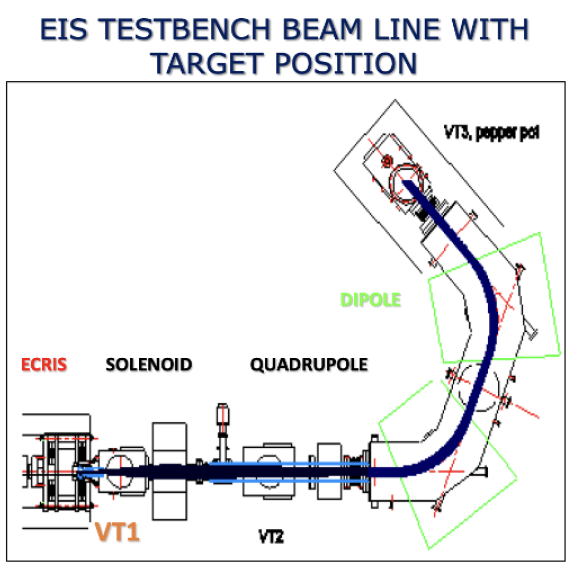

Figure 2: Layout of the EIS test bench.

During the measurement, the extraction parameters were set as in Table 2.

Table 2: Parameters during the Measurements

Parameter	Value	Unit
extraction voltage	15	kV
screening electrode voltage	−2	kV
total beam current	1.63	mA
gas pressure at source	1.75×10^{-6}	mbar
microwave power	400	W

In order to have a better comparison with the simulations, it was decided to insert a viewing screen directly behind the ion extraction (VT1 in Fig. 2, approximately 32 cm behind the plasma electrode) to obtain clearer pictures of the ion beam profile. The viewing target, i.e. the viewing screen, mounted on a feed through is shown in Fig. 3.

To visualize the ion beam profile the viewing screen was coated with potassium bromide (KBr), as KBr glows upon ion impact. The side length of the used square shape viewing screen is 80 mm and it was introduced into the beam path at an angle of 45 degrees, see in Fig. 3. The working gas for the measurements was argon together with helium as auxiliary gas.

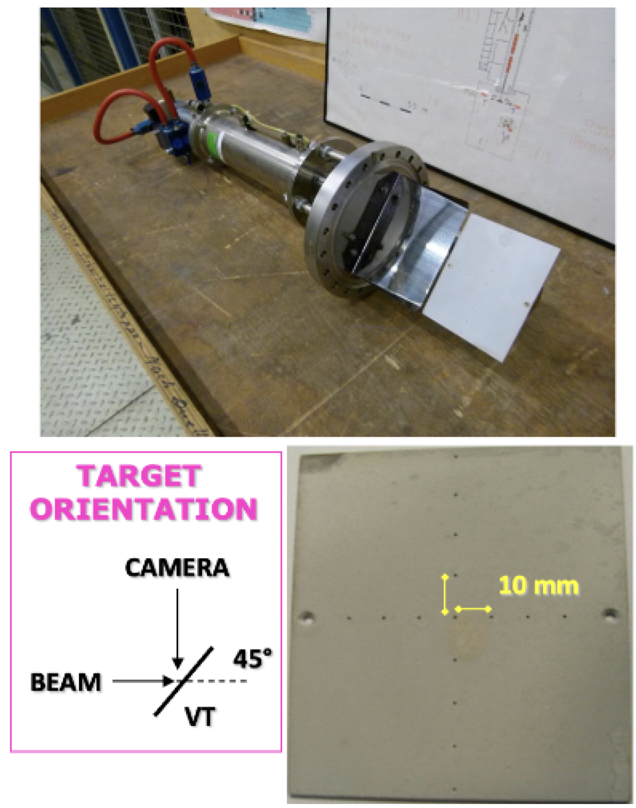

Figure 3: Top: Device for inserting the viewing screen. Bottom left: Alignment in beam path. Bottom right: Used screen with holes as distance markers.

RESULTS

Simulation

Figure 4 shows the results for the trajectories of the simulated ions for different current densities j at the creation plane of the ions. The different colours represent the different ion species, the light green lines represent the electric potential lines, while the electrodes are depicted by the dark blue surfaces. It can be observed that as the initial current density decreases, the beam spreads more significantly indicating a considerable divergence and loss of beam intensity at lower current densities.

According to the simulation, the beam currents shown in Table 3 are obtained for the different current densities j at the starting plane. Figures 5 to 7 show the beam profiles, at the end of the simulation box ($x = 0.5$ m), for the different

ISBN: 978-3-95450-257-8 ISSN: 2222-5692 doi:10.18429/JACoW-ECRIS2024-TUP14

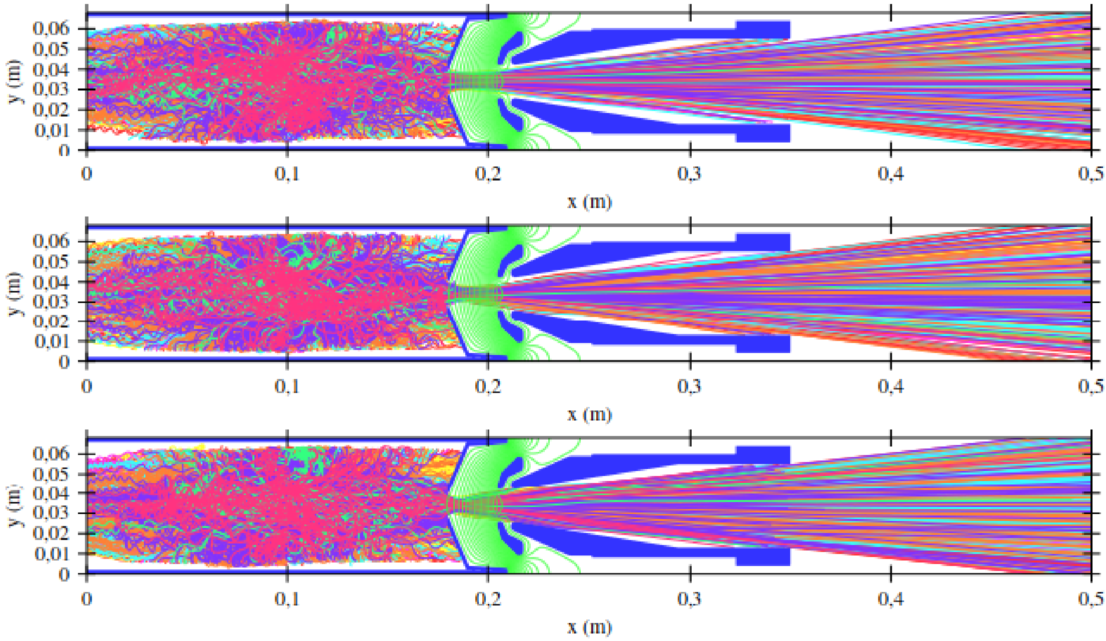

Figure 4: Ion trajectories for different current densities j at the start plane $x = 0.1$ m. From Top to Bottom $j = 5, 3, 1$ A/m^2.

current densities j. As the current density increases, the expected triangular spiral geometry of the beam profile becomes progressively clearer. Upon closer examination, it can also be observed that ions are lost at the edges of all the beam profiles, a phenomenon that is particularly pronounced in the profile corresponding to the current density of 1 A/m^2. This phenomenon originates from the boundaries of the simulation which are exceeded at the edges of the beam profiles.

Table 3: Simulated Total Beam Current at $x = 0.5$ m Dependent on the Current Density j at the Starting Plane

Current density j	**Beam current at x =0.5 m**
5 A/m^2	3.2 mA
3 A/m^2	2.1 mA
1 A/m^2	0.9 mA

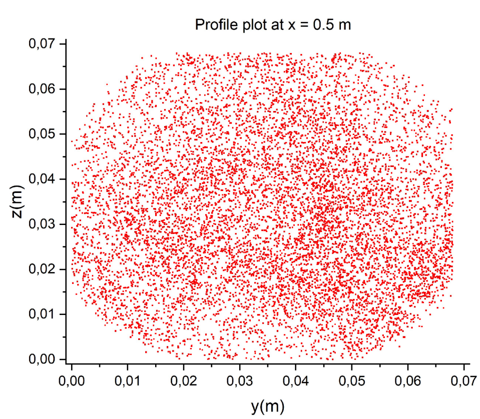

Figure 5: Beam profile for a current density j of 1 A/m^2.

The simulations also provided the emittance of the beam at the position $x = 0.5$ m. Since it was not possible to measure the emittance during the measurements, the emittances

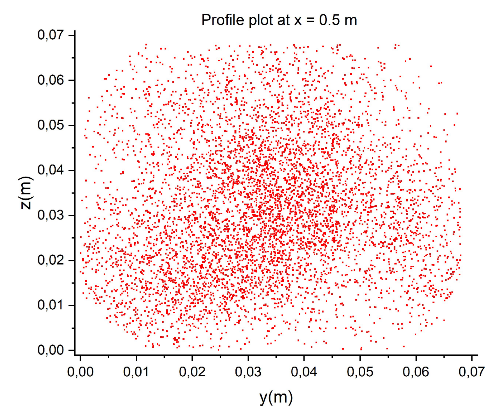

Figure 6: Beam profile for a current density j of 3 A/m^2.

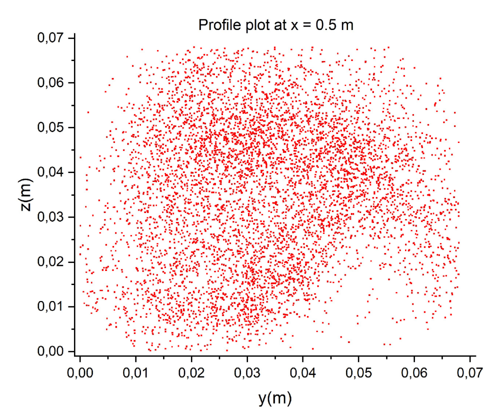

Figure 7: Beam profile for a current density j of 5 A/m^2.

were not used for the benchmarking. For the sake of completeness the simulated emittances in the (y, y') phase space are shown in Fig. 8 where also the Twiss parameters are reported. The figure shows clearly that the emittance ϵ is bigger for lower current densities, which indicate that the

26th Int. Workshop Electron Cyclotron Resonance Ion Sources ECRIS2024, Darmstadt, Germany JACoW Publishing
ISBN: 978-3-95450-257-8 ISSN: 2222-5692 doi:10.18429/JACoW-ECRIS2024-TUP14

beam is not optimized at lower current densities. However, it should be noted that the emittances considered here are only suitable for phenomenological assessments, as the beams are cut off at the simulation boundaries.

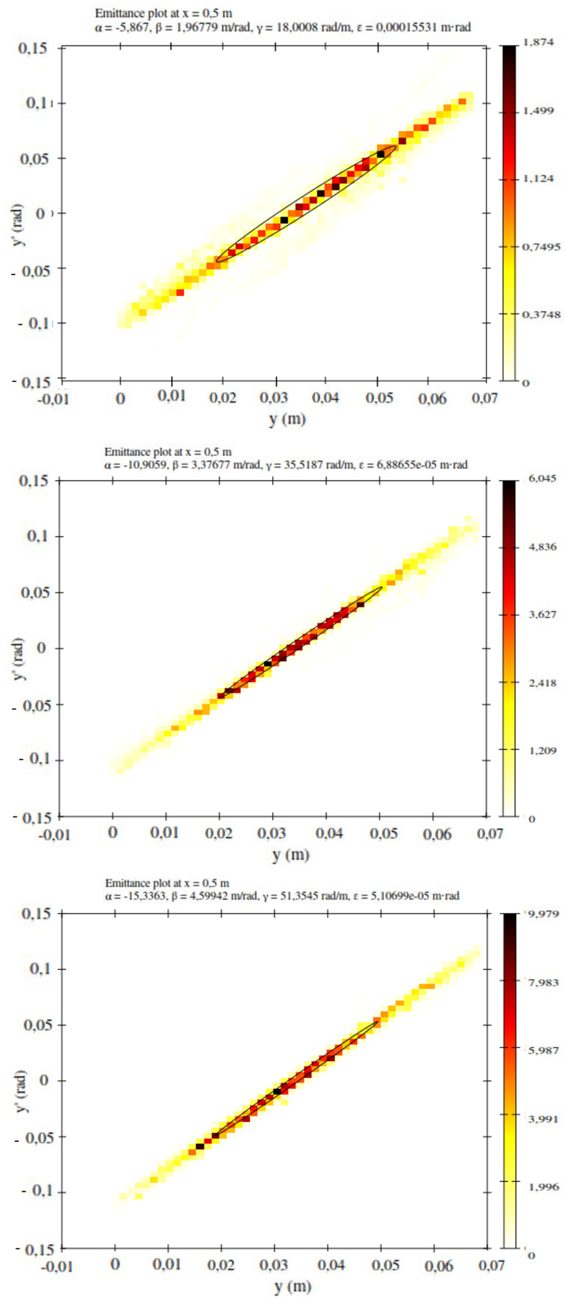

Figure 8: Beam emittances at the position $x = 0.5$ m for the different current densities j at the start plane. From top to bottom $j = 1, 3, 5$ A/m^2.

Experimental Results

Figure 9 shows a beam profile taken during the measurements. The brighter areas in the picture indicate regions where a higher concentration of ion impacts on the screen. The characteristic triangular spiral structure of the beam, originating from the hexapole used in the setup, is clearly visible. The image shown was not corrected from the distortion caused by the angle in which the screen was put into the beam. The diameter of the measured beam profile is just under 7 cm, closely matching the simulated beam diameter (of approximately 7 cm). This image was used as a reference for comparison with the simulation results to verify the accuracy and progress of this work.

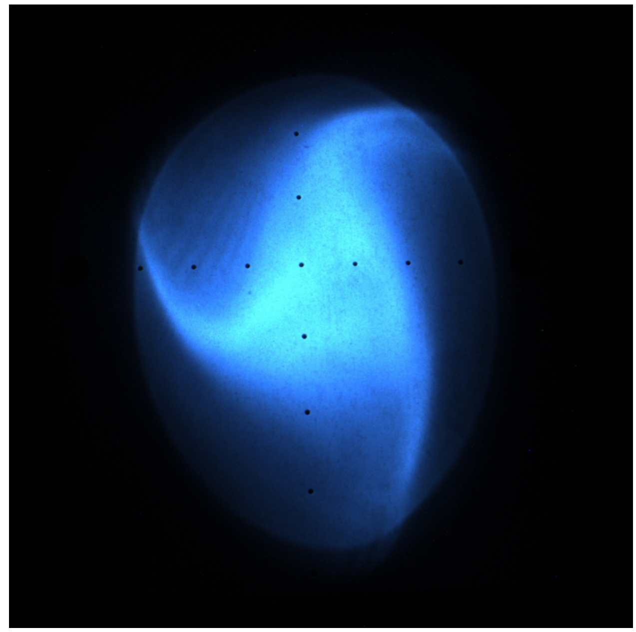

Figure 9: Picture of a beam profile.

CONCLUSION AND OUTLOOK

We find that the simulations provide a reasonable prediction of the beam profile for the CAPRICE-ECRIS, with the results already closely matching the experimental measurements. The primary difference between the simulation and the experimental measurements lies in the beam profile itself: in the experimental data, the profile appears significantly sharper and rotated by 45 degrees counterclockwise compared to the simulation. The beam current, however, shows only slight discrepancies between the two, where the simulation with the starting current density $j = 3$ A/m^2 is closest to the measurements.

Future work will focus on testing various parameter configurations until the optimal setup is found that best replicates real-world conditions, especially the beam profile. Once the correct configuration will be identified, the simulation framework will be extended to explore different plasma electrode geometries. These new simulations will also be validated against experimental measurements to ensure accuracy and consistency with observed results.

ACKNOWLEDGEMENTS

I want to thank Taneli Kalvas for his helpful feedback concerning the simulation software. Additionally, I appreciate the guidance of Alexander Engeda for his advice on programming and software-related matters, as well as the support of Annemarie Lauterbach.

ISBN: 978-3-95450-257-8 ISSN: 2222-5692 doi:10.18429/JACoW-ECRIS2024-TUP14

REFERENCES

[1] T. Kalvas, "Development and use of computational tools for modelling negative hydrogen ion source extraction systems", Ph.D. theses, University of Jyväskylä, 2013.

[2] P. Spädtke, "Simulation as a Tool for Understanding Experimental Observations - Ion Beam Extraction from an ECRIS", *Plasma*, vol. 5, pp. 540-554, Nov. 2022, doi:10.3390/plasma5040038

[3] F. Maimone and A. Andreev, "Research and development activities to increase the performance of the CAPRICE ECRIS at GSI", *J. Phys.: Conf. Ser.*, vol. 2743, no. 1, p. 012048, May 2024. doi:10.1088/1742-6596/2743/1/012048

[4] K. Tinschert, J. Bossler, S. Schennach, and H. Schulte, "Status report on ECR ion source operation at the GSI accelerator facilities", *Rev. Sci. Instrum.*, vol. 69, no. 2, pp. 709–711, Feb. 1998. doi:10.1063/1.1148558

ISBN: 978-3-95450-257-8 ISSN: 2222-5692 doi:10.18429/JACoW-ECRIS2024-WEA1

CHARACTERIZATION OF D^+ SPECIES IN THE 2.45 GHz ECRIS FOR 14-MeV NEUTRON PRODUCTION

S. Vala[†,1,2], Ratnesh Kumar[1], H. Sharma[1], M. Abhangi[1,2], H. Swami[1], M. Panda[1], Rajesh Kumar[1,2]
[1]Institute for Plasma Research, Gandhinagar, India
[2]Homi Bhabha National Institute, Mumbai, India

Abstract

The Institute for Plasma Research has set up a 14-MeV neutron generator facility. The stability, quality, and repeatability of the D^+ ion beam are critical parameters for ensuring the reliable operation of the neutron generator. Hence, a 2.45 GHz ECR ion source has been installed to produce the deuterium beam. The primary D beam characteristics are assessed by varying extraction voltage, microwave power, gas flow, and solenoid current of the ECRIS. By optimizing these parameters, the maximum design beam current is achieved. The D ion beam contains various species, including D^+, D_2^+, D_3^+, and impurities. Accurate measurement of the D^+ content within the D ion beam is the key parameter for a neutron generator. Multiple experiments were conducted to determine the D^+ species and optimise the ECRIS parameters for maximum production of D^+ species. Two beam current measurement devices, the DCCT and the Faraday Cup, were installed in the beamline to measure the total deuterium beam current and D^+ beam current, respectively. Especially, the variation in the D^+ fraction primarily depends on the operating parameters of the ECRIS, such as extraction voltage, microwave power and gas flow. This paper presents the results of the D^+ ion current as a function of extraction voltage, microwave power, and gas flow rate. Understanding and characterizing the D^+ species are essential steps toward achieving stable and efficient neutron production in fusion applications.

INTRODUCTION

The Institute for Plasma Research (IPR), India, has recently commissioned a 2.45 GHz Electron Cyclotron Resonance Ion Source (ECRIS)-based high-yield 14 MeV neutron generator. This sophisticated system is designed to produce a remarkable 10^{12} neutrons per second, both in continuous mode and pulse mode [1-3]. Deuterons, extracted from the SILHI ECRIS [4-6], are directed onto a solid titanium tritide (TiT) target. The collision of deuterons with the TiT target results in the production of fast neutrons. These fast neutrons are essential for various applications, such as benchmark experiments for the Fusion Evaluated Nuclear Data Library (FENDL), neutron spectroscopy measurements, double differential cross-section measurements, and neutron diagnostics, all aimed at the development of future fusion reactors. Additional applications of the neutron generator include neutron radiography, medical isotope production, explosive detection, and the characterization of electronic components used in space applications. The Institute for Plasma Research (IPR) has developed an accelerator-based D-T neutron generator capable of producing 10^{12} neutrons per second as shown in Fig. 1 [7].

The 2.45 GHz Electron Cyclotron Resonance (ECR) ion source is a critical component of the 14 MeV neutron source, significantly contributing to its stability, reliability, and performance. This paper details the experimental setup of the accelerator-based 14 MeV neutron generator and presents experimental results on ion beam characterization and neutron yield measurement using various diagnostic techniques.

Figure 1: Photograph of Accelerator based 14 MeV Neutron Generator.

EXPERIMENTAL SETUP

The beam characterization process begins at the ion source and is carried out in a step-by-step manner. To ensure smooth and successful beam characterization, extensive preparatory work on accelerator physics and hardware has been conducted. The beamline is evacuated to a base pressure of 10^{-7} mbar before the production of the deuterium beam. Deuterium plasma is generated in the Electron Cyclotron Resonance Ion Source (ECRIS), from which the deuterium ion beam is extracted.

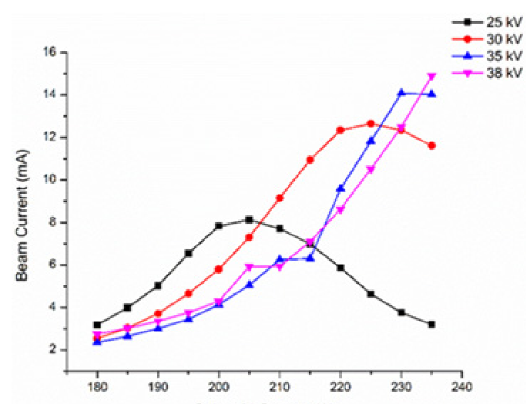

Figure 2: Beam current as function of solenoid current at different extraction voltage.

The extracted deuterium ion beam is then focused into the acceleration column via the Low Energy Beam Transport (LEBT) system and further accelerated using

ISBN: 978-3-95450-257-8 ISSN: 2222-5692 doi:10.18429/JACoW-ECRIS2024-WEA1

electrostatic acceleration. The parameters of the accelerated deuterium ion beam are measured using the Beam Diagnostic System (BDS). The primary beam was measured by varying extraction energy, microwave power, gas flow rate, and solenoid current. By tuning these parameters, the maximum design beam current was obtained. Figure 2 shows the results of beam current measurement as a function of solenoid current at different extraction voltages. Figure 3 shows the results of beam current as a function of extraction voltage and RF power. The deuterium ion beam comprises species such as D^+, D_2^+, D_3^+, and impurities. It is crucial to measure the D^+ content within the deuterium ion beam.

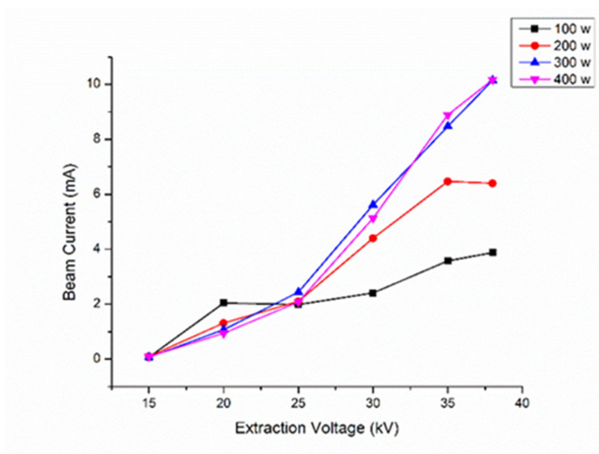

Figure 3: Measured beam current as a function of extraction voltage at different MW power.

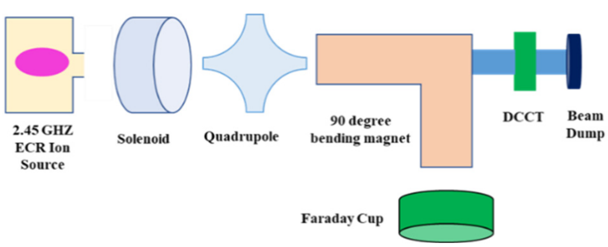

Figure 4: Schematic of the experimental setup for D^+ fraction measurement.

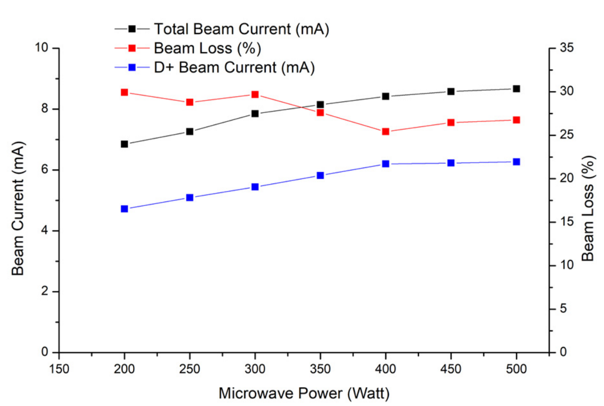

Figure 5: Measured beam loss as function microwave power at 30 kV extraction.

An experimental setup has been established to measure the D^+ ion species, as illustrated in Fig. 4. The Direct Current Current Transformer (DCCT) and Faraday Cup (FC) have been installed to measure the total beam current and the D^+ beam current, respectively, as shown in Fig. 4. Initially, the extracted beam passes through the DCCT with the bending magnet power supply turned off, allowing for the measurement of total beam currents. In the subsequent step, the bending magnet is activated, and the magnetic field is adjusted to allow only the D^+ species to pass through. The beam is then focused onto the FC for the measurement of the D^+ beam current.

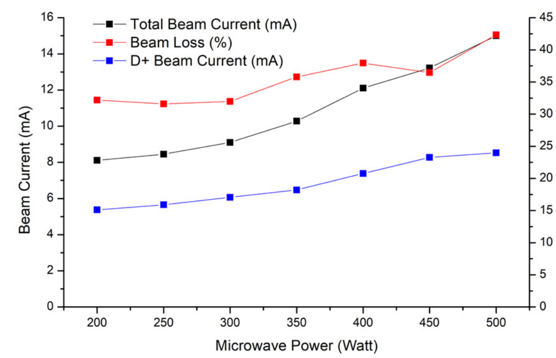

Figure 6: Measured beam loss as function microwave power at 35 kV extraction.

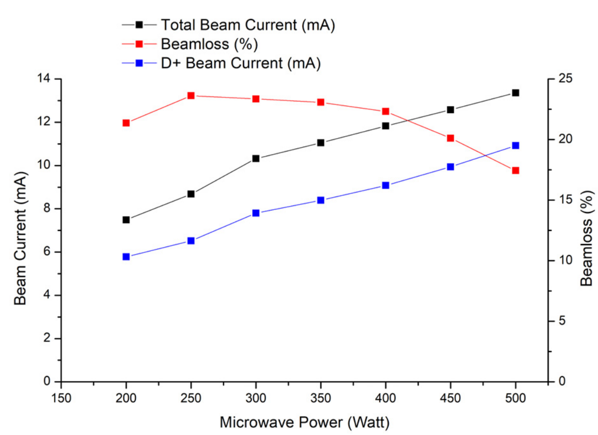

Figure 7: Measured beam loss as function microwave power at 38 kV extraction.

RESULTS AND DISCUSSION

Several experiments were conducted to measure the D^+ fraction as a function of microwave power and extraction voltage. The results of the D^+ fraction measurements as a function of microwave power are presented in Figs. 5, 6, and 7. The percentage beam fraction is calculated from the total beam current and the D^+ current. This percentage includes fractions of D_2^+, D_3^+, and impurities. It was observed that the variation in the D^+ fraction is primarily dependent on the operating parameters of the ECR ion source,

ISBN: 978-3-95450-257-8 ISSN: 2222-5692 doi:10.18429/JACoW-ECRIS2024-WEA1

such as extraction voltage and microwave power. The maximum and minimum D^+ fractions obtained are approximately 82% and 60%, respectively. Notably, the variation in the D^+ fraction primarily depends on the operating parameters of the Electron Cyclotron Resonance Ion Source (ECRIS), such as extraction voltage, microwave power and gas flow. Understanding and characterizing the D^+ species are essential steps toward achieving stable and efficient neutron production in fusion applications.

SUMMARY

An accelerator-based 14 MeV neutron generator has been successfully commissioned at IPR. The following critical aspects were thoroughly investigated. Rigorous measurements were conducted for beam current, beam profile, deuterium fraction, and emittance. The beamline underwent evacuation, achieving a base pressure of 10^{-7} mbar. Within the plasma chamber, deuterium plasma was efficiently produced. An extraction system facilitated the efficient extraction of the ion beam. Extraction performance was systematically studied, considering extraction voltage, microwave power, and mass flow rate. A robust 14 mA ion beam, containing all species, was successfully extracted from the ion source. Specifically, an 11 mA D^+ (deuterium) beam was obtained after passage through the analyzing magnet. This achievement represents a significant milestone in neutron research, with promising implications for fusion studies and practical applications.

REFERENCES

[1] S. J. Vala *et al.*, "Development and performance of a 14-MeV neutron generator", *Nucl. Inst. Method. Phys. Res., Sect. A*, vol. 959, p. 163495, 2020. doi:10.1016/j.nima.2020.163495

[2] H. L .Swami *et al.*, "Physics design of 14 MeV neutron generator facility at the Institute for Plasma Research Physics Design", *Plasma Sci. Technol.*, vol. 25, no. 12, 2023. doi:10.1088/2058-6272/ace6da

[3] H L Swami *et al.*, Occupational radiation exposure control analyses of 14 MeV neutron generator facility: A neutronic assessment for the biological and local shield design, *Nucl. Eng. Technol.,* vol. 52, no. 8, pp. 1784-1791, 2020. doi:10.1016/j.net.2020.01.006

[4] R. Gobin *et al.*, "General design of the International Fusion Materials Irradiation Facility deuteron injector: Source and beam line", *Rev. Sci. Instrum.*, vol. 81, p. 02B301, 2010. doi:10.1063/1.3257998

[5] R. Gobin *et al.*, "High-intensity ECR ion source (H^+, D^+, H^-) developments at CEA/SACLAY", *Rev. Sci. Instrum.*, vol. 73, pp. 922-924, 2002. doi:10.1063/1.1428783

[6] R. Gobin *et al.*, "Development of a permanent magnet light ion source at CEA/SACLAY", *Rev. Sci. Instrum.,* vol. 77, p. 03B502, 2006. doi:10.1063/1.2164893

[7] M. Abhangi *et al.*, "Neutron emission characterization of IPR 14 MeV neutron generator", *Fusion Eng. Des.,* vol. 204, p. 114522, 2024. doi:10.1016/j.fusengdes.2024.114522

ISBN: 978-3-95450-257-8 ISSN: 2222-5692 doi:10.18429/JACoW-ECRIS2024-WEA2

COMPACT 2.45 GHz PMECR ION SOURCES AND LEBTS DEVELOPED FOR ACCELERATOR BASED RADIATION THERAPY FACILITIES AT PEKING UNIVERSITY

Bujian Cui, Shixiang Peng†, Tenghao Ma, Wenbin Wu, Kai Li,
Yicheng Dong, Zhiyu Guo, Jiaer Chen
State Key Laboratory of Nuclear Physics and Technology & Institute of Heavy Ion Physics,
Peking University, Beijing, China

Abstract

Recently, Accelerator Based Radiation Therapy (ABRT) facilities for cancer treatment, that includes ion therapy and BNCT, have been bloomed up rapidly and are being established as a future modality to start a new era of in-hospital facilities around the world. A high current, small emittance, easy maintenance, long lifetime, high stability and reliability ion source is crucially important for those ABRT facilities. Research on this kind of ion source has been launched at Peking University (PKU) ion source group for more than 30 years and some exciting progresses, such as hundred mA beam current of $H^+/N^+/O^+$ etc., less than 0.2 π·mm·mrad emittance, a continue 300 hours operation record of CW proton beam without spark have been achieved. In recent years, our involvement in the ABRT campaign has extended to include responsibilities for ion sources and LEBT section. In this paper, we will provide a summary of two compact PKU standard 2.45 GHz permanent magnet ECR sources (PM SMIS) that were developed for a proton therapy (PT) machine and an accelerator based BNCT facility (AB-BNCT). The individual structure of the sources as well as the LEBT along with the commissioning results will be presented then.

INTRODUCTION

Cancer is a general term for a large category of diseases that can affect any part of the body. It is a leading cause of death worldwide, accounting for nearly 10 million deaths in 2020, or nearly one sixth of deaths are due to cancer [1]. Many cancers can be cured if detected early and treated effectively. Radiation therapy (also called radiotherapy) is a cancer treatment that uses high doses of radiation to kill cancer cells and shrink tumors. There are two main types of radiation therapy, external beam and internal. External beam radiation therapy comes from a machine that aims radiation at the cancer. The machine does not touch but can move around the patient, sending radiation to a part of patient's body from many directions. External beam radiation therapy is a local treatment, it treats a specific diseased part of the body. Proton therapy (PT), heavier ions therapy (HI-RT) and boron neutron capture therapy (BNCT), are new highly targeted external beam radiation therapy for cancer treatment. Accelerator Based Radiation Therapy (ABRT) facilities are compact and useful tools to generate desired particles, such as energized protons, carbon ions or neutrons, to kill the cancer cells. Therefor ABRT has been bloomed up rapidly and is being established as a future modality to start a new era of in-hospital facilities around the world [2,3].

For any ABRT type PT or BNCT facilities, a proton beam with a current of several tens of mA in pulsed or continuous wave (CW) mode is required from the ion sources by the accelerator. The 2.45 GHz Electron Cyclotron Resonance (ECR) ion source is considered to be the optimal choice for ABRT facilities due to its advantages in high beam intensity, stable performance, low emittance, good reproducibility, high stability, simple structure, convenient maintenance, low cost, long lifespan and ability to operate in both CW and pulsed modes. Ion source group of Peking University (PKU) initiated an ABRT campaign by developing compact 2.45 GHz ECR ion sources and LEBT for these facilities.

The study on permanent magnet 2.45 GHz ECR ion sources (PMECR) started at 1980's at PKU [4]. Since then, several series of 2.45 GHz PMECR ion sources have been developed, including the PKU Standard permanent magnet Microwave Ion Source (SMIS) [5], Miniaturized Microwave ion source (MMIS) [6], Surface plasma electron source (SPS) [7], H_2^+/H_3^+ ion source [8], 2.45 GHz microwave driven H- source [9], O^{3+}, Ar^{3+} multicharged ion source [10] and C^{2+} ion source for PIMS [11]. The SMIS has achieved a proton beam of more than 130 mA at 50 keV with a Φ6 mm emittance aperture [5]. In June 2016, a long-term operation of 300 hours with a continuous wave proton beam of 50 mA@50 keV was conducted using the SMIS. Throughout this period, no sparks appeared and no plasma generator failure caused any interruptions to the beam. More than ten copies of SMISs have been developed for different facilities such as SFRFQ [12], PKYNIFTY [13], C-RFQ [14], DWA [15] and Proton therapy facility [16]. To better understand the discharge ignition and plasma sustain process within a miniaturized 2.45 GHz microwave driven ion source, a hybrid discharge heating (HDH) mode has been proposed at PKU [6]. Additionally, a global model based on electronic equilibrium equations has been proposed to explain H^+, H_2^+ and H_3^+ generation [17].

This paper primarily focuses on the compact permanent magnet 2.45 GHz ECR ion sources (PMECR) along with LEBT developed for a PT machine and a BNCT facility. The ion sources belong to SMIS type. In both cases, we have followed the same structure as PKUNIFTY by designing the ion source and the LEBT as a whole. In section II, we will present the commissioning results of the Proton Injector for PT Machine. Section III will depict details of the pulsed/CW proton PMECR and two-solenoid LEBT

† sxpeng@pku.edu.cn

26th Int. Workshop Electron Cyclotron Resonance Ion Sources ECRIS2024, Darmstadt, Germany JACoW Publishing
ISBN: 978-3-95450-257-8 ISSN: 2222-5692 doi:10.18429/JACoW-ECRIS2024-WEA2

developed for a BNCT machine. A summary and discussion of next steps will be provided at the end of this paper.

PROTON INJECTOR FOR PT MACHINE

PKU involved the Proton Therapy Facility project was charged by Shanghai APACTRON Particle Equipment Company Limited and funded by the National Key Research and Development Program of China in 2018. Its LINAC mainly consists of a proton injector that includes an ion source with a Low Energy Beam Transport line (LEBT), a 3 MeV Radio-Frequency Quadrupole (RFQ) and a 7 MeV Drift Tube LINAC (DTL) [16]. The output proton current at the exit of DTL should be higher than 12 mA. This LINAC accelerator requires an 18mA pulsed proton beam with an energy of 30 keV. The repeat frequency of the beam ranges from 0.5 to 10 Hz, with a pulsed length between 40 to 100 µs, and a pulsed raising edge less than 2 µs. Further details can be found in Table 1. Figure 1 depicts this LINACS from the ion source side, while Figure 2 provides a view from behind the beam direction.

Table 1: Beam Parameters at RFQ Entrance

Parameter	Value
Ion type	H^+
Energy	30±0.1 keV
Ion source current	20~30 mA
LEBT current	>18 mA
Beam stability (LEBT)	±1 mA
Emittance (RMS, Norm)	≤0.2 π.mm.mrad
Repeat frequency	0.5~10 Hz
Pulse length	40~100µs
Raising edge	≤2.0µs

Figure 1: A photograph of PT machine taken from ion source side.

The PT SMIS source test was conducted on PKU ion test bench at the end of 2019. Test results demonstrate that the source has the ability of delivering a proton beam with current from 10 mA to 90 mA when duty factor changes from 1% to 20% (0.5 Hz - 100 Hz) with the peak RF power. Its rms emittance less than 0.1 π·mm·mrad at 30 keV. The results displayed in Figure 3 is an example obtained with SAIREM GMP 30K SM microwave power supply during ion source qualification at PKU. As depicted in Figure 3, the beam current is 34 mA at 30 keV, the beam diameter located 250 mm downstream from the particle emitting plane is about 20 mm. H^+ faction is estimated to be around 91%, while its rms emittance is about 0.1 π·mm·mrad. All the data exceed the requirements of the machine.

Figure 2: A photograph of PT machine taken from end of LINAC.

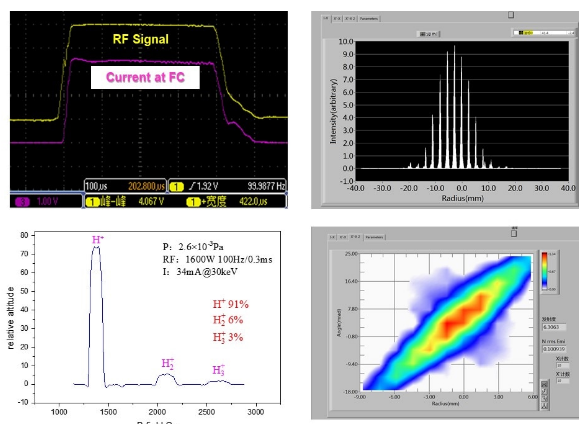

Figure 3: Result of PT SIMS proton source when RF is 1600W. (Beam current: up left, beam profile: up right, ion fraction: down left, RMS emittance: down right.)

The results of the proton injector commissioning were presented in Figure 4. This test was done using a new 2.45 GHz microwave generator produced by Xian SIGNUM High Voltage, which is a new Chinese company. The kicker power supply (No. JNHP19-01) was also provided by this company. As shown in Figure 4, the beam rise edge without/with chopper is 5 µs/2 µs. The current at ACCT equals to that reaches at FC2. This means that all proton ions that travel through ACCT can be injected into RFQ.

Figure 5 is a hard copy of LINAC commissioning result achieved at Match 2023. A proton beam with a current of 14.4 mA and energy of 7 MeV was achieved at the exit of DTL, which is much higher than the required 12 mA.

ISBN: 978-3-95450-257-8 ISSN: 2222-5692 doi:10.18429/JACoW-ECRIS2024-WEA2

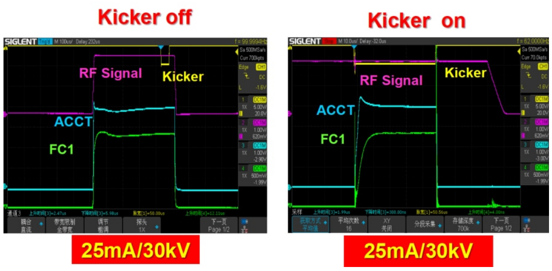

Figure 4: Beam current recorded with oscilloscope (OSC) at the end of LEBT w/o chopper.

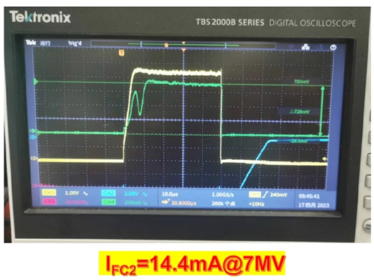

Figure 5: LINAC commissioning result. A 14.4 mA beam was obtained at 7 MV.

The PT injector has been delivering proton beams for this facility since the beginning of 2021. Up to now, no sparks have been recorded. Similar to other SMISs developed for SFRFQ, C-RFQ, PKUNIFTY, DWA, etc., no maintenance is required.

CW/PULSED PROTON INJECTOR FOR AB-BNCT FACILITY

The development of the accelerator base boron neutron capture therapy (AB-BNCT) facility, charged by the Joint Laboratory of Xi'an Jiaotong University and Huzhou Neutron Science Laboratory, is currently underway. The accelerator is a LINAC consisting of a 2.45 GHz ECR ion source, a two-solenoid LEBT, and a RFQ plus Cross-bar H-mode DTL (CH-DTL). A 20 mA proton beam should be delivered to the target for neutron production.

The required beam for this LINAC is a 30 mA@40 keV proton beam in both CW and pulsed mode. Its beam duty cycle should be adjustable from 0.5% to 100% at 200 Hz, with a normalized root mean square emittance of less than 0.2 π.mm.mrad. Parameters at the entrance of RFQ are listed in Table 2. In this framework, our group is responsible for designing and realizing both the CW and pulsed 30 mA@40 keV proton beams.

In order to provide a suitable beam for this facility, a proton injector that consisting of a standard PKU PMECR ion source (SMIS) and a two-solenoid LEBT was developed. Similar to the ones used for the PT facility, this source follows a Matryoshka doll style by embedding part of the ion source body into the extraction system and inserting the whole source into the first diagnostic box of LEBT. The dimensions of this source body are 100 mm ×Φ 100 mm, with a plasma chamber measuring 50 mm × Φ 40 mm. A well water-cooled three-electrode extraction system designed at 45 kV is also incorporated. The outside dimension of the SMIS is 160 mm × Φ 200 mm. Pictures displayed in Figure 6 show the source body, integrated source, and online source; while Figure 7 depicts the AB-BNCT proton injector (down). The total length of LEBT from plasma electrode to RFQ electrode is about 1130 mm.

Table 2: Parameters at the Entrance of RFQ for AB-BNCT Facility

Parameter	Value
Particle	H^+
Operation mode	CW (rare), pulse: 1~500Hz, 200Hz spe cific, length >200 μs
Energy	40 keV
Beam Current	> 30 mA
Normalized rms emittance at LEBT exit	< 0.20 π·mm·mrad
H^+ fraction	> 80%
Stability	24 h
Twiss parameter at RFQ entrance	α=1.484, β=5.622 cm/rad
Mismatching degree of TWISS parameter	<30%
Raise/Full edge	<1ms

Figure 6: Pictures of SMIS.

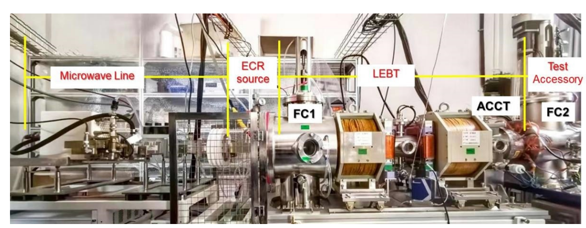

Figure 7: Picture of the proton injector for AB-BNCT.

The commissioning process for this AB-BNCT proton injector was carried out in two steps: ion source qualification and LEBT testing. Ion source qualification took place on a PKU ion test bench last year where characteristics such as beam intensity, distribution, emittance, and H^+ fraction were evaluated. With this SMIS, it was easily obtained that more than 60 mA hydron beam at 40 kV with H^+ faction higher than 80% and rms emittance less than 0.11 pi.mm.mrad when changing duty factor from 10% to CW.

The RFQ acceptance tests of this proton injector was launched at the end of 2023. A four-quadrant diaphragm with a Φ4 mm aperture that used to simulate the entrance of RFQ electrodes, and a set of slit-grid emittance unit that follow a Φ4 mm aperture were used for this test [13].

This test was conducted in pulsed mode with a duty factor ranging from 5% to 90% due to the ACCT working

ISBN: 978-3-95450-257-8 ISSN: 2222-5692 doi:10.18429/JACoW-ECRIS2024-WEA2

range. The purpose of this test is to ensure that the current at FC 2 (I_{FC2}), which represents the future current into RFQ. At the same time, I_{FC2} should be closer to that obtained at ACCT (I_{ACCT}). Additionally, its emittance should be less than 0.2 π·mm·mrad. Furthermore, its twiss parameters and mismatching degree should meet the specified criteria.

The test results demonstrate that a beam with a current greater than 50 mA can be easily obtained at the FC 2 location. Simultaneously, the currents at FC 2 are equal to that at IACCT. Its rms emittance is from 0.09 π·mm·mrad to 0.112 π·mm·mrad, α is approximately 1.285, β is about 5.788 cm/rad, and the mismatching degree is 12.5%. Figure 8 provides two examples of the beam current at FC 1, ACCT and FC 2 when the duty factors were 70% and 90%.

The proton injector has been consistently delivering a proton beam to the RFQ since January 2024. There have been no recorded sparks during RFQ operation so far. A 33-mA proton beam was achieved at the exit of the RFQ at the beginning of July. Additional data is coming soon.

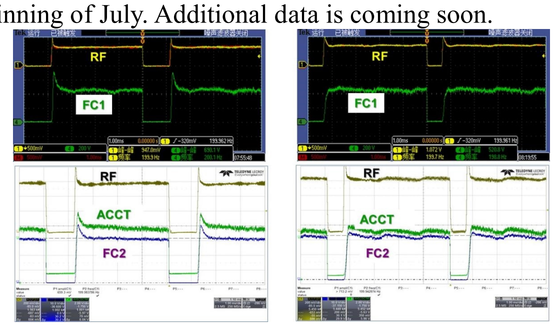

Figure 8: Beam current at FC 1, ACCT and FC 2 under different duty factor. (Left: duty factor is 70%. I_{FC1}: 45 mA, I_{ACCT}: 30 mA, I_{FC2}: 30 mA. Right: duty factor is 90%. I_{FC1}: 45 mA, I_{ACCT}: 30 mA, I_{FC2}: 30 mA.)

SUMMARY AND FUTURE PLAN

Two compact 2.45 GHz PMECR ion sources, along with their LEBT, have been developed for use in accelerator-based radiation therapy facilities at PKU. The ion sources are PKU compact standard 2.45GHz permanent magnet ECR ion sources, also known as SMIS.

The LINAC commissioning results for PT facilities demonstrate that the proton injector has met all requirements in every aspect. The LINAC has been in routine operation for over two years without any recorded sparks.

In the case of the AB-BNCT machine, results from RFQ acceptance tests confirm that the proton injector already meets the requirements for the LINAC.

Furthermore, a more compact SMIS is currently under design for use with a dynamitron type LINAC.

ACKNOWLEDGEMENTS

The authors express their gratitude to the colleagues from the Xi'an Jiaotong University-Huzhou Neutron Science Laboratory and Shanghai APACTRON Particle Equipment Company Limited for engaging in fruitful discussions. Furthermore, the authors thank State Key Laboratory of Nuclear Physics and Technology at Peking University for their valuable support.

REFERENCES

[1] J. Ferlay *et al.*, Global Cancer Observatory: Cancer Today. Lyon: International Agency for Research on Cancer, 2020 `https://gco.iarc.fr/today`

[2] A. J. Kreiner *et al.*, "Accelerator-based BNCT," *Appl. Radiat. Isot.*, vol. 88, pp. 185–189, Jun. 2014. `doi:10.1016/j.apradiso.2013.11.064`

[3] A. J. Kreiner *et al.*, "Present status of Accelerator-Based BNCT," Reports of Practical Oncology & Radiotherapy, vol. 21, no. 2, pp. 95–101, Mar. 2016. `doi:10.1016/j.rpor.2014.11.004`

[4] Zhao Kui, Song Zhizhong, Wang lifang, Zhao Weijiang, Xiao Min, "A compact Microwave Ion source with co-axis coupling type," Proceedings of The Third Symposium on Ion Sources and Beams, Lanzhou, China, Sep. ,1987

[5] Shixiang Peng *et al.*, "New progress on beam availability and reliability of PKU high intensity CW proton ECR ion source," *Chin. Phys. B*, vol. 26, no. 2, p. 025206, Feb. 2017. `doi:10.1088/1674-1056/26/2/025206`

[6] Jiamei Wen *et al.*, "A miniaturized 2.45 GHz ECR ion source at Peking University," *Chin. Phys. B*, vol. 27, no. 5, p. 055204, May 2018. `doi:10.1088/1674-1056/27/5/055204`

[7] B. Cui *et al.*, "Design and Experiment of a Slotted Antenna Surface Wave Plasma Flood Gun," *J. Phys. Conf. Ser.*, 20th International Conference on Ion Sources, vol. 2743, no. 1, p. 012088, May 2024. `doi:10.1088/1742-6596/2743/1/012088`

[8] S. Peng *et al.*, "Possibility of generating H+, or H2+, or H3+ dominated ion beams with a 2.45 GHz permanent magnet ECR ion source," *Rev. Sci. Instrum.*, vol. 90, no. 12, Dec. 2019. `doi:10.1063/1.5128019`

[9] T. Zhang *et al.*, "Practical 2.45-GHz microwave-driven Cs-free H- ion source developed at Peking University," *Chin. Phys. B*, vol. 27, no. 10, p. 105208, Oct. 2018. `doi:10.1088/1674-1056/27/10/105208`

[10] Y. Xu *et al.*, "Multiple charge ion beam generation with a 2.45 GHz electron cyclotron resonance ion source," Science China Physics, Mechanics & Astronomy, vol. 60, no. 6, p. 060021, Apr. 2017. `doi:10.1007/s11433-016-9029-y`

[11] K. Li *et al.*, "Preliminary results of positive ion mass spectrometry based on a 2.45 GHz ECR ion source and a non-metallic gas target," *J. Phys. Conf. Ser.*, vol. 2244, no. 1, p. 012093, Apr. 2022. `doi:10.1088/1742-6596/2244/1/012093`

[12] Zhang Meng, *et al.*, "Experimental results of an ECR oxygen source and a LEBT system for 1 MeV ISR RFQ accelerator upgrade project," *Chin.Phys C*, vol. 32 (S1), p. 220-222, Mar. 2008.

[13] H. T. Ren *et al.*, "Deuteron injector for Peking University Neutron Imaging Facility project," *Rev. Sci. Instrum.*, vol. 83, p. 02B711, Feb. 2012. `doi:10.1063/1.3670345`

[14] Shixiang Peng *et al.*, "Experimental results of an electron cyclotron resonance oxygen source and a low energy beam transport system for 1MeV integral split ring radio frequency quadruple accelerator upgrade project," *Rev. Sci. Instrum.*, vol. 79, no. 2, Jan. 2008. `doi:10.1063/1.2802200`

[15] S. X. Peng *et al.*, "Proton injector acceptance tests for a Dielectric Wall Accelerator (DWA):characterisation of Advanced Injection System of Light Ions (AISLI)," *Nucl. Instrum. Methods Phys. Res., Sect. A*, vol. 763, pp. 120–123, Nov. 2014. doi:10.1016/j.nima.2014.06.025

[16] S. X. Peng *et al.*, "A Low Emittance Compact Proton Injector for a Proton Therapy Facility", in *Proc. IPAC'21*, Campinas, Brazil, May 2021, pp. 1218-1221. doi:10.18429/JACoW-IPAC2021-MOPAB404

[17] W.-B. Wu *et al.*, "Global model of miniature electron cyclotron resonance ion source," Acta Physica Sinica, vol. 71, no. 14, p. 145204, 2022. doi:10.7498/aps.71.20212250

ISBN: 978-3-95450-257-8 ISSN: 2222-5692 doi:10.18429/JACoW-ECRIS2024-WEA3

A PLASMA BASED, CHARGE STATE STRIPPER FOR HEAVY ION ACCELERATORS

G. Rodrigues*,[1], Surender Kumar Sharma[2], Rishi Verma[2], Rahul Singh[4], Ramesh Narayanan[3], Marcus Iberler[5], R. Mehta[1], J. Jacoby[5], Wolfgang Quint[4], Archana Sharma[6]
[1]Inter University Accelerator Centre, Aruna Asaf Ali Marg, New Delhi, India
[2]Bhabha Atomic Research Centre, Visakhapatnam, Andhra Pradesh, India
[3]Indian Institute of Technology, New Delhi, India
[4]GSI Helmholtzzentrum fur Schwerionenforschung GmbH, Darmstadt, Germany
[5]Institute for Applied Physics, Frankfurt, Germany
[6]International Institute of Information Technology, Naya Raipur – Chhattisgarh, India

Abstract

The ionization of ions to a higher charge state is of central importance for the development of new accelerator facilities like FAIR (Facility for Antiproton and Ion Research) at GSI, Darmstadt,and the resulting cost savings. That is why the comparative analysis of the charge state stripping alternatives is a relevant topic. Currently, mainly gas and foil strippers are used for increasing the charge state even after using a high performance ECR ion source in a typical Accelerator chain. Even when the foil or/and gas efficiency or lifetime has proved to be less than optimal, as these alternatives either require great effort or are practically not suitable for smooth operation in the long term.

INTRODUCTION

Free electrons in highly ionized plasmas can be effectively used for improving the charge state of heavy ions as the rates of radiative recombination of free electrons are much smaller than those of electron capture on bound electrons, which leads to a substantial increase of the effective charge in a plasma compared to a cold-gas target of the same element. Therefore, the use of highly ionized plasmas for charge state enhancement are more effective than in the case of using gas and foil stripper mediums and are advantageous when compared to the limited lifetime of foils and lower mean charge state distributions in gaseous media. In order to realize such a plasma device, various types of pinch plasmas have been explored to look into the possibility of heavy ion stripping with an enhanced mean charge state distribution. Theta and Z pinch plasmas are possible options which have been explored and experimentally studied at IAP, Frankfurt, Germany [1]. Typical electron line densities required to be achieved are in the range of 10^{16} to 10^{19} cm^{-3} and electron temperatures of the order of few tens of eV are found to be favourable as per modelling with the FLYCHK code [2], but also challenging. Such a plasma device, the challenges to be overcome, together with their design details will be presented.

A collaboration [3] between BARC, Vishakhapatnam and IUAC, New Delhi has been initiated to further modify plasma pinch devices and optimise them for the accelerator conditions, in particular for the High Current Injector [4] programme at IUAC, New Delhi, and to plan for the beam tests as "proof of principle".

With regard to the development of new accelerator technologies for high-intensity ion beams and efficient acceleration, the transfer of beam ions into higher-charged states is a necessary prerequisite for numerous experiments. The acceleration of heavy ions is being pursued with increasing efforts and especially during the last, few ten years, acceleration techniques have been studied in detail. In reaching the goal to produce intense beams of ions as heavy as uranium and energetic enough to overcome the Coulomb barrier even for the heaviest targets, many new problems must be solved which were not important for the design of conventional light particle accelerators. One of these problems concerns the ionic charge of heavy ions which is an influential new parameter. In this paper, the variation of ionic charge due to collisions with matter ("stripping") will be discussed, as well as some associated phenomena of practical interest.

The effects of charge stripping on heavy ion acceleration are twofold, On the one hand, the passage of heavy ions through specially designed strippers can be exploited to produce a substantial increase of the ion charge which reduces the effective potential required for further acceleration, In order to find the most suitable stripper and to utilize the highest possible charge states, it is necessary to investigate the effects of strippers on heavy ion beams in great detail. On the other hand, random stripping in the residual gas of an accelerator may lead to beam losses. In order to calculate the vacuum which guarantees a satisfactory particle transmission, it is necessary to know charge changing cross sections. These cross sections are very complex quantities and they can hardly be estimated without extensive knowledge about fundamentals of charge changing processes.

BACKGROUND INFORMATION

Plasma has been discussed as a possible medium for ion strippers since the 1960s. In his paper from 1991, T. Peter calculated the achievable equilibrium charge states in cold gas and plasma for iodine ions [5,6]. The equilibrium charge states for uranium ions were calculated by V. Shevlko in 2012

* gerosro@gmail.com

ISBN: 978-3-95450-257-8 ISSN: 2222-5692 doi:10.18429/JACoW-ECRIS2024-WEA3

for the parameters and requirements of the plasma stripper of the AG Plasmaphysik. They confirm an advantage of a plasma stripper over a gas stripper. In the 1990s, experiments with a Z-pinch were carried out by D. H. H. Hoffman, J. Jacoby et al. [7] at GSI, Germany. Despite the results, the Z-pinch is not suitable for use in beam operation due to its instabilities. For this reason, the plasma physics group of the IAP at Goethe University has been working for several years on an inductively coupled theta pinch as a more stable, homogeneous solution for use as a plasma stripper. The plasma stripper built and investigated in recent years was already developed with a view to the beam intensities required at FAIR. With discharge energies of 50 kJ, electron densities of over 10^{17} cm^{-3} are achieved.

In heavy-ion accelerator facilities, solid or gaseous media are often used to strip electrons from the projectile ions between acceleration stages because higher energies for a given acceleration voltage result from higher charge states. The stripping properties of these media have been studied for many years. The charge state distribution of ions traversing a stripping medium reaches equilibrium after passage through a certain thickness of the target. Equilibrium charge states in a solid material are generally higher than those in gaseous media due to the density effect. However, owing to radiation damage, sputtering, as well as thermal and mechanical stresses due to the irradiation, lifetimes of solid media are limited. Also, the quality of ion beams from solid strippers are degraded more than that from gas strippers. The above disadvantages of conventional gaseous or solid strippers can be overcome by using a hot plasma as a new stripping medium. Not only in a plasma but also in cold matter, the charge states of projectile ions are determined by ionization and recombination processes in the target. The free electrons are captured by projectile ions less often than the bound electrons. This difference is based on the fact that in the case of free electron capture, the excess binding energy and momentum have to be removed by one of the less probable processes, such as radiative recombination.

If the projectile-ion velocity v is larger than the electron thermal velocity v_{th} in plasma, the stopping power of plasma free electrons for non-relativistic ions is determined by the Bohr formula

$$-\left[\frac{dE}{dx}\right]_{\text{plasma}} = \left(\frac{Z_{\text{eff}}\, e\, \omega_p}{v}\right)^2 ln\frac{mv^3}{Z_{\text{eff}}\, e\, \omega_p}\ , \tag{1}$$

$$v >> v_{th} = \sqrt{\frac{k_B T}{m}}\ , \tag{2}$$

where T is the plasma temperature, k_B is the Boltzmann constant, Z_{eff} is the effective charge of incident ions, and ω_p is the plasma frequency, defined as follows, where is the density of free electrons.

$$\omega_p = \left(\frac{4\pi N_e\, e^2}{m}\right)^{\frac{1}{2}}\ , \tag{3}$$

where N_e now refers to the density of bound electrons in gas.

In the case of the stopping power for non-relativistic ions propagating in a (gas) target, the following Eq. (4) can be re-written in a form similar to Eqs. (1) and (3):

$$-\left[\frac{dE}{dx}\right]_{\text{gas}} = \left(\frac{Z_{\text{eff}}\, e\, \omega_p}{v}\right)^2 \ln\frac{2mv^2}{I}\ . \tag{4}$$

Equations (1) and (4) differ from each other by the expression under the logarithm sign. This means that even if the effective charges in plasma and gas targets are the same, the stopping power of free electrons in a plasma is always greater than that in a gas due to the logarithmic term. For a partially ionized plasma, the ion energy loss is defined by the sum of expressions (Eq. (4)) for the bound electrons of atoms and ions in a plasma and Eq. (1) for free electrons, where each term has to be multiplied by the corresponding particle density in a plasma.

A comparison of ionization losses in a gas and in a fully ionized plasma is schematically shown in Fig. 1. The stopping power for a fully ionized gas is larger than for a cold gas, for example, in a plasma, free electrons are much easier to excite (plasma waves) than bound electrons in atoms and ions. This is further confirmed by experimental data shown in Ref. [7–10].

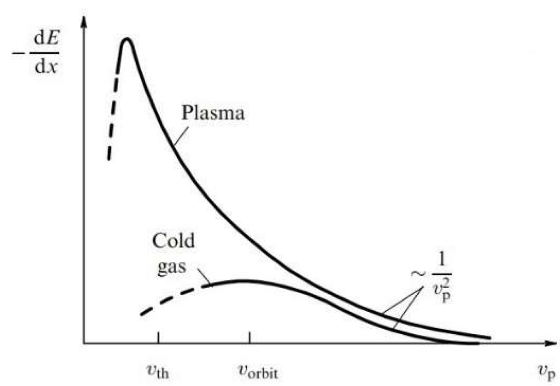

Figure 1: Stopping power in a plasma compared with a cold gas as a function of ion velocity, assuming that the effective charge is the same for both cases. Adapted from Ref. [5].

In general, while the slowing down of heavy ions in solid and gaseous targets have been studied sufficiently well and many theoretical models adequately reproduce the experimental results, the interaction of charged particles with a plasma have been investigated in less detail, and the number of available experimental data is also limited. The experiments carried out so far have been mainly using plasma pinch devices (theta pinch, Z pinch, screw pinch etc.) for studying the stopping power of heavy ions and the ultimate charge states which are achievable. However, few experimental groups have also utilised laser induced plasma devices with 'in-situ' interaction with heavy ions which is presently not discussed in this contribution.

ISBN: 978-3-95450-257-8 ISSN: 2222-5692 doi:10.18429/JACoW-ECRIS2024-WEA3

PLASMA PINCH DEVICES

The current stripper technology is only suitable to a limited extent for heavy ion beams with the desired intensity. In the proposed project, a plasma stripper with fully ionised hydrogen and simultaneously high particle densities in the range of a few 10^{17} to 10^{18} cm^{-3} is to be developed and investigated. In Ref. [10] the ionization percentages for several pressures as a function of plasma temperature are depicted using the Saha equation, and above 2 eV, ionization is larger than 80 %. In order to study the energy loss measurements, the ion stopping should not perturb the plasma thermodynamics. Considering typical plasma parameters, i.e, n_e = 5×10^{17} cm^{-3} and T_e ~20.000 K, the stored energy per unit volume is ~0.4 J·cm^{-3}. The actual projectile energy loss of the beam would be much smaller, typically few orders of magnitude, smaller than the stored energy. The plasma stripper is being designed to be positioned in the high energy part of the High Current Injector facility (where the final energy is 1.8 MeV/u) located at the object plane of the first achromatic bend. Due to the pulsed nature of the beam, the beam bunches are separated in time 82.47 ns apart, corresponding to the bunching frequency of 12.125 MHz of the multi-harmonic buncher which is placed upstream of the 48.5 MHz, RFQ and the 97 MHz drift tube LINAC accelerators. The plasma device needs to be ON for a sufficient time of at least 1 ns or even more, in order to utilise most of the bunched beam. Similar to the gas stripper, the beam ions lose the outer electrons through collisions and thus reach higher charge states. The plasma stripper is characterised by a lower recombination rate, so that higher charge states can be achieved. These higher charge states facilitate the further acceleration of the ions. The electron density to be achieved and the degree of ionisation to be achieved are of importance for the effectiveness of the plasma stripper. The frequency of the Coulomb impacts responsible for ionisation increases with density. The degree of ionisation achieved is important for the recombination process: The recombination cross-section of ions with bound electrons is a factor of 1000 larger than with free electrons. This means that even a proportion of 0.1 % of not fully ionised ions/atoms negates the advantages of the plasma stripper compared to other stripper systems. The plasma devices which have been designed, fabricated and routinely used for various applications at BARC, Vishakhapatnam [11, 12] are presently being modified to be compatible for the upcoming beam tests in the High Current Injector facility for validation as a 'proof of principle" device.

HIGH PRECISION DIAGNOSTICS

In order to be able to advance the targeted further development, high-precision diagnostic equipment is required that enables access to the parameters of the plasma [13]. For this purpose, a combination of a vibration-compensated, heterodyne laser interferometer and a polarimeter for the time- and spatially-resolved determination of the electron density including magnetic field distribution of the new stripping cell would be required to be adapted to the experimental conditions. The methods used so far by some working groups to diagnose electron density are essentially limited to spectroscopy with the observation of the broad H β-line, i.e. diagnostics with passive electromagnetic radiation. Although this type of spectroscopy is to be regarded as a standard procedure, it nevertheless has certain shortcomings, which are partly intrinsic, but are also partly caused by special experimental conditions: On one hand, the intensity of the recombination radiation is not necessarily temporally correlated with the electron density, so that at the time of highest density, little light intensity can be available for spectroscopy. This non-mandatory temporal correlation means that when using different optical recording systems, such as ICCD or streak camera, the measured temporal course of the electron density does not match. On the other hand, with regard to the necessary time resolution, a compromise must be found between the maximum resolvable time interval and the brightness of the radiation at the detector, since the light intensity available to the optical system decreases with a better time resolution. It is problematic to perform a diagnosis with only one physical method. Verification and confirmation, as well as the avoidance of systematic errors, can only be achieved by using different physical measurement methods. In order to avoid the problems mentioned above, plasma diagnostic capabilities may be considered by establishing laser interferometric diagnostics alongside spectroscopy would be required. Although laser interferometric diagnostics can be classified as complex, it nevertheless has reliability and precision when used correctly, which means that a wide density range of the plasma can be investigated with good time resolution down to the sub-nanosecond range. An interferometer can be used to directly measure and that is crucial for the interaction with an ion beam, the integrated axial electron density. The interferometer/polarimeter combination is to be so powerful that the plasma parameters that are decisive for the interaction with an ion beam, including the magnetic field distribution of the stripper cell, can be determined radially spatially resolved with a precision that has never been achieved before and at the same time with high time resolution.

CONCLUSION

Plasma based heavy ion strippers are promising candidates for use in heavy ion accelerators as they are rugged, efficient and have a long lifetime when compared to gas and foil strippers. For the upcoming FAIR project and other projects worldwide, the use of plasma strippers will benefit the projects by further lowering the operating voltages of the LINAC cavities and reducing the running costs.

REFERENCES

[1] C. Teske, J. Jacoby, F. Senzel, and W. Schweizer, "Energy transfer efficiency of a spherical theta pinch", *Phys. Plasma*, vol. 17, no. 4, Apr. 2010. doi:10.1063/1.3368795

[2] FLYCHK: Generalized Model of Atomic Processes in Plasmas, https://www-amdis.iaea.org/FLYCHK/

[3] Memorandum of Understanding, BARC, Visakhapatnam and IUAC, New Delhi, November 2023

[4] Amit Roy, "Accelerator development at the nuclear science centre", *Curr. Sci.*, vol. 76.2, p. 149-153, 1999.

[5] T. Peter and J. Meyer-ter-Vehn, "Energy loss of heavy ions in dense plasma. I. Linear and nonlinear Vlasov theory for the stopping power", *Phys. Rev. A*, vol. 43, no. 4, pp. 1998–2014, Feb. 1991. doi:10.1103/PhysRevA.43.1998

[6] T. Peter and J. Meyer-ter-Vehn, "Energy loss of heavy ions in dense plasma. II. Nonequilibrium charge states and stopping powers", *Phys. Rev. A*, vol. 43, no. 4, pp. 2015–2030, Feb. 1991. doi:10.1103/PhysRevA.43.2015

[7] D. H. H. Hoffmann, K. Weyrich, H. Wahl, D. Gardés, R. Bimbot, and C. Fleurier, "Energy loss of heavy ions in a plasma target", *Phys. Rev. A*, vol. 42, p. 2313, 1990. doi:10.1103/PhysRevA.42.2313

[8] J. Jacoby *et al.*, "Stopping of Heavy Ions in a Hydrogen Plasma", *Phys. Rev. Lett.*, vol. 74, p. 1550, 1995. doi:10.1103/PhysRevLett.74.1550

[9] M. Engelbrecht *et al.*, Numerical description and development of plasma stripper targets for heavy-ion beams", *Nucl. Inst. Meth. Phys. Res., Sect. A*, vol. 415, no. 3, pp. 621-627, 1998. doi:10.1016/S0168-9002(98)00435-5

[10] D. Gardes *et al.*, "Stopping of multicharged ions in dense and fully ionized hydrogen", *Phys. Lett. A*, vol. 46, p. 5101, 1992. doi:10.1103/PhysRevA.46.5101

[11] Rishi Verma *et al.*, "Compact sub-kilojoule range fast miniature plasma focus as portable neutron source", *Plasma Sources Sci. Technol.*, vol. 17, p. 045020, 2008. doi:10.1088/0963-0252/17/4/045020

[12] Rishi Verma *et al.*, "Miniature plasma focus device as a compact hard X-ray source for fast radiography applications", *IEEE Trans. Plasma Sci.*, vol. 38, no. 4, pp. 652–657, 2010. doi:10.1109/TPS.2010.2041558

[13] Marcus Iberler, private communication, IAP, Frankfurt

ISBN: 978-3-95450-257-8 ISSN: 2222-5692 doi:10.18429/JACoW-ECRIS2024-WEB1

MIXED CARBON AND HELIUM ION BEAMS FOR SIMULTANEOUS HEAVY ION RADIOTHERAPY AND RADIOGRAPHY: AN ION SOURCE PERSPECTIVE

M. Galonska*, A. Andreev, C. Graeff[1], R. Hollinger, R. Lang, J. Mäder, F. Maimone, L. Volz
GSI Helmholtzzentrum für Schwerionenforschung GmbH, Darmstadt, Germany
[1]also at Technical University Darmstadt, Darmstadt, Germany

Abstract

Within the framework of research on simultaneous heavy ion radiotherapy and radiography, a mixed carbon/helium ion beam with a variable He percentage has been successfully established and investigated at GSI for the first time in order to study this new mode of image guidance for carbon ion beam therapy. The mixed C / He ion beam was provided by the 14.5 GHz CAPRICE ECR ion source for the subsequent linac-synchrotron accelerator systems at GSI. Prior to that experiment, different ion combinations ($^{12}C^{3+}$/ $^{4}He^{+}$ or $^{12}C^{4+}$/ $^{3}He^{+}$) out of CH_4 or CO_2 have been investigated at the ECR test bench in terms of ion beam currents, stability, and C-to-He-fraction quantified by optical spectral lines and mass spectra. From an ion source perspective, it turned out that each of the different combinations comply with all the requirements of the experiments which successfully took place utilizing a $^{12}C^{3+}$/ $^{4}He^{+}$- ion beam with an energy of 225 MeV/u. Finally, both ions were simultaneously accelerated, extracted and characterised in the biophysics cave. This paper briefly outlines some of the measurements obtained at the test bench and during the beam time from an ion source perspective.

INTRODUCTION

Particle therapy, as a Bragg peak method of irradiation, is subject to even small range uncertainties in especially for anatomical changes like moving tumours. Mixed carbon and helium on beams have been proposed for simultaneous therapy and online monitoring [1–6].

Due to the similar mass-to-charge-ratio C^{3+} and $^{4}He^{+}$ (or C^{4+} and $^{3}He^{+}$) ions can be accelerated to the same energy per nucleon. At this same velocity the penetration depth of He in water is three times the one of carbon ions. Therefore, carbon ions stop in the tumour volume applying the dose there while helium ions exit the patient and can be detected and used for range verification and imaging. Previous works revealed that the additional dose from a small, 10 % helium percentage in the plateau of the depth-dose-profile of helium is sufficiently low [1–4].

Most recent simulation works analysed the injection and extraction process at a medical facility while the experimental exploration is still ongoing [7, 8]. Recently, such a mixed beam has been produced at GSI with an energy of 225 MeV/u, slowly extracted with a particle rate of about 10^8 particles/second [9, 10]. This paper briefly reviews the major steps of the dual isotope beam production and some of the important results achieved with an emphasis on ion source development.

MATERIALS AND METHODS

Ion Source Set Ups

In order to meet the requirement of 10^8 particles/second at the experiment an ion beam of circa 150 μA ($^{12}C^{3+}$ or $^{12}C^{4+}$) with a helium fraction of approx. 10 %, i.e. circa 5 μA ($^{4}He^{+}$ or $^{3}He^{+}$) has to be provided upstream the subsequent linac-sychrotron system UNILAC-SIS18 at GSI. The 14.5 GHz CAPRICE type ECR ion source was utilised for this purpose meeting all the requirements given.

The preliminary measurements were conducted at the ECR ion source test bench which includes a low energy beam transport line (Fig. 1). Different reasonable combinations of methane/carbon dioxide and $^{4}He^{+}$/ $^{3}He^{+}$ were checked in terms of feasibility.

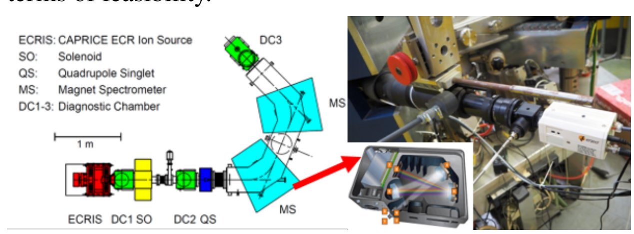

Figure 1: Sketch of the test bench: ion source and LEBT (left), camera and optical spectrometer system (right).

The helium percentage was controlled by stepwise altering the helium inflow to the plasma and by measuring a) the optical emission spectrum (OES) with an optical spectrometer (Oceaninsight QE Pro [11]) covering approx. the visible light spectrum, b) the analysed ion beam current in a Faraday cup, and c) the corresponding mass spectra. In the two latter cases, it is impossible to distinguish between the $^{12}C^{3+}$/ $^{4}He^{+}$ or $^{12}C^{4+}$/ $^{3}He^{+}$ ions, but the C-to-He ratio and its long term stability also during operation can be estimated by the optical emission lines of carbon (wavelength 465 nm) and helium I (728 nm).

Finally, a mixed ion beam of $^{12}C^{3+}$ and $^{4}He^{+}$ was provided from the high charge state injector (HLI) to the experiment (smaller deviation of the mass-to-charge ratios compared to $^{12}C^{4+}$ and $^{3}He^{+}$). After setting up the ion source, the C-to-He ratio was adjusted and constantly monitored by measuring the analysed ion beam current in a current transformer and by measuring the optical emission lines that is by non-destructive beam instrumentation.

* m.galonska@gsi.de

ISBN: 978-3-95450-257-8 ISSN: 2222-5692 doi:10.18429/JACoW-ECRIS2024-WEB1

Unfortunately, the oxygen emission lines, and therefore the evolution of the oxygen contamination of the plasma and hence, the ion beam, were not recorded in both cases.

SIS18 and Beam Instrumentation at Biophysics Cave

The sensitivity of the SIS18 even to the small difference between the mass-to-charge ratio of carbon and helium (^{4}He) ions of 0.065 % is most challenging, in especially for slowly extracted ion beams. The transverse RF Knock-Out (RFKO) extraction scheme was used with reduced horizontal chromaticity minimising the effects of r in order to get an ion beam with a constant carbon-to-helium ratio over a spill as requested [9].

Since it was impossible to obtain information of the different ion beam species helium and carbon with the accelerators´ beam instrumentation, the beam properties were measured by different set ups in the biophysics cave. The particle rates, for instance, were recorded by a stack of three ionisation chambers (IC): at the beam nozzle (IC1) and at the positions of the carbon (IC2) and helium (IC3) Bragg peak, respectively. The corresponding ion beam ranges were set by a set up of range shifters (Fig. 2) allowing for a separate measurement of the carbon and helium ion beam.

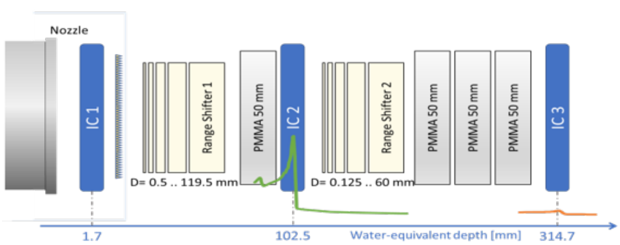

Figure 2: Scheme of the set up with an arrangement of range shifters and ICs; IC2 and IC3 are positioned at the carbon (green line) and helium (orange line) Bragg peaks.

EXPERIMENTAL RESULTS

Prior to the ion beam production at the injector beam line and accelerator, different combinations of ions have been checked at the ECR test bench (EIS) for their suitability. Those were CH_4 / ^{4}He (C^{3+}/ $^4He^+$), CH_4 / ^{3}He (C^{4+}/ $^3He^+$), and CO_2 / ^{3}He (C^{4+}/ $^3He^+$).

The charge state distributions (CSD) have been recorded for various helium fractions after setting up a C^{3+} or C^{4+} beam of approximately 150 µA out of CH_4 or CO_2. Figures 3 and 4 show different CSDs containing different helium percentages. The CSDs are shifted on the momentum axis for comparison of the various graphs. With increasing inflow of He to the plasma only those combined peaks (C^{3+}/ $^4He^+$, $^4He^{2+}$ (methane) or C^{4+}/ $^3He^+$, $^3He^{2+}$ (carbon dioxide)) are increasing at the same time while the rest of the beam composition remains nearly unaffected by adding helium. A similar result for the system C^{4+}/ $^3He^+$, $^3He^{2+}$ (methane) is reported in [12].

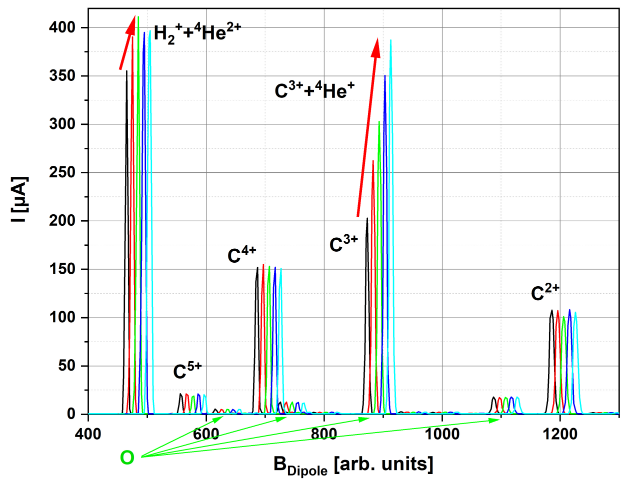

Figure 3: Charge state distributions (methane and ^{4}He) as function of the He fraction; shifted on momentum axis for illustration; green: indicating oxygen part.

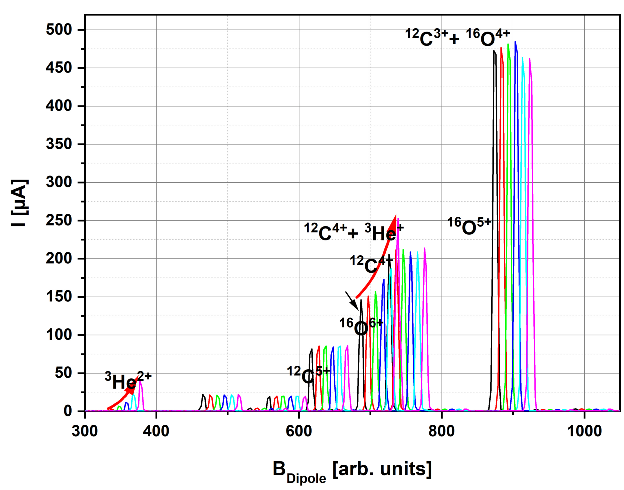

Figure 4: Charge state distributions (carbon dioxide and ^{3}He) as function of the He fraction; shifted on momentum axis for illustration.

Additionally, the number of counts of an optical emission line of He I at approximately 728 nm wavelength was read from the overall optical spectrum (see Fig. 5). This distinct He I line over some background was taken for probing the relative helium fraction in the plasma over time. By controlling the helium inflow to the plasma to different extents only the corresponding helium lines alter (insert in Fig. 5: black curve) while the residue of the spectrum remains almost unchanged. Thus, one can correlate the optical counts to the analysed current and therefore the C-to-He ratio can be elaborated (Figs. 6 and 7) while the actual particle rates of the beams' constituents helium and carbon cannot be discriminated with the accelerator's beam instrumentation; the measured actual number of particles relies on the beam instrumentation in the biophysics cave.

Finally a C^{3+}/ $^4He^+$ (methane) ion beam has been provided by the ion source (smaller mass-to-charge-ratio of ^{4}He to C).

ISBN: 978-3-95450-257-8 ISSN: 2222-5692 doi:10.18429/JACoW-ECRIS2024-WEB1

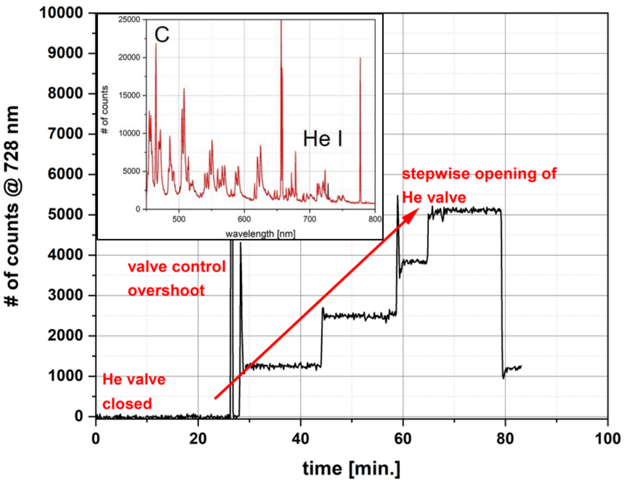

Figure 5: Number of counts at 728 nm wavelength (He I) for stepwise increase of He flow in a methane / helium plasma; insert: part of OES, number of counts over wavelength w/o He (red graph) and with He content (black graph) [10].

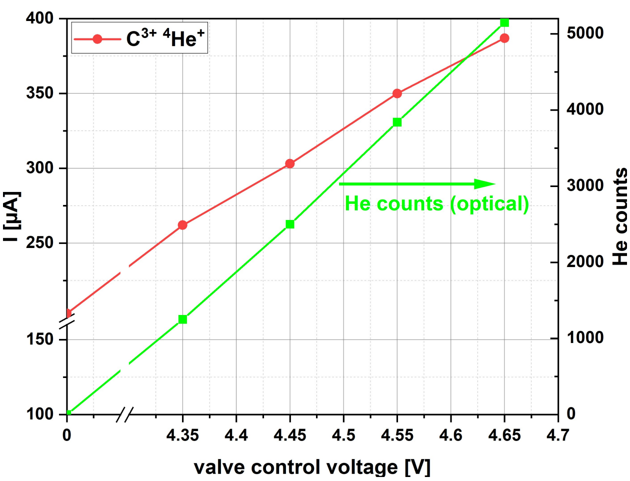

Figure 6: Correlation between current and counts; system CH_4 and ^4He.

The analysed beam current measured with a current transformer and the optical emission lines were used to adjust the relative helium fraction during operation at the injector and to monitor the overall stability of operation (Fig. 8). It shows the good stability during the whole duration of the experiment which lasted for about four days. There are two main sources of fluctuating current measurement, that is HV drops due to plasma fluctuations and partly a lack of timing of the beam instrumentation devices; none of them being of concern for the experiment.

The plasma and therefore the ion beam still contained a small part of oxygen the amount of which could be reduced (not eliminated completely) by conditioning of the ion source over weeks of operation. Thus, an O^{4+} part of less than 10 % was expected in the beam the amount of which can be roughly estimated by the height of the neighbouring peaks in the CSD. This was quantitatively confirmed by the experiments' instrumentation (see below).

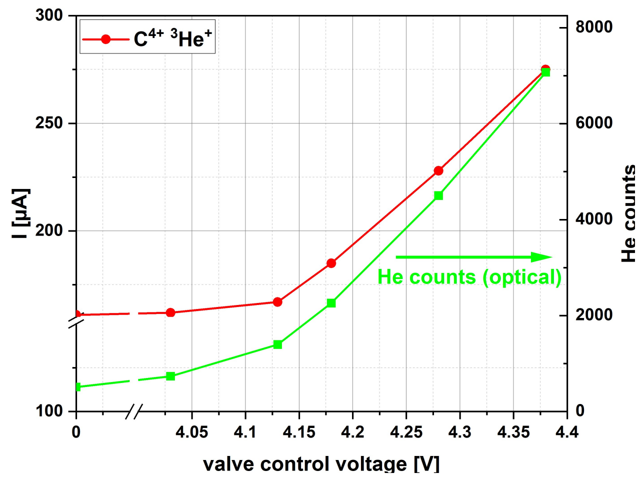

Figure 7: Correlation between current and counts; system CO_2 and ^3He.

Despite the small mass-to-charge difference, both C^{3+} and $^4He^+$ were successfully accelerated simultaneously at the UNILAC and SIS18 to the required beam energy of 225 MeV per nucleon. According to the objectives, a spill with a fairly constant ratio of helium to carbon was achieved by using the RFKO extraction scheme with adjusted, i.e. reduced chromaticity. The C-to-He-ratio varied by ±30 %, but it was, however, stable over many cycles and suitable for the exploration of this particular method of online monitoring in carbon ion beam therapy (see [9] for details).

Figure 9 shows the depth-dose profile of the dual- isotope beam with a helium fraction of 4.5 % and 20 % (related to carbon) and stable over time. The signals are normalised to IC1: the ruby graph shows the carbon Bragg peak and the oxygen Bragg peak in front (percentage of 7 % related to carbon); the light and dark green graphs show the helium Bragg peaks also containing a background of fragments. Thus, this new method of imaging was successfully investigated. Many further experimental data (utilising a dE-E telescope (particle composition), films (beam profiles), an IC array (dosimetry), and a camera/scintillator system) were collected, the results of which have yet been and will be reported elsewhere (see for instance [13, 14]).

SUMMARY

A mixed carbon-helium ion beam was produced successfully with the CAPRICE ECRIS using methane, carbon dioxide and ^3He and ^4He. C^{3+} and $^4He^+$ were accelerated and extracted simultaneously for the first time by using the transverse RFKO extraction scheme. The achieved stable conditions (inter-spill He-to-C ratio, fairly flat distribution over the spill (±30 %), and unwanted, but stable oxygen fraction) permitted to experimentally explore the potential of this new image guidance modality for carbon ion beam therapy. To further reduce the oxygen content in the plasma the ion source conditioning phase will be revised.

ISBN: 978-3-95450-257-8 ISSN: 2222-5692 doi:10.18429/JACoW-ECRIS2024-WEB1

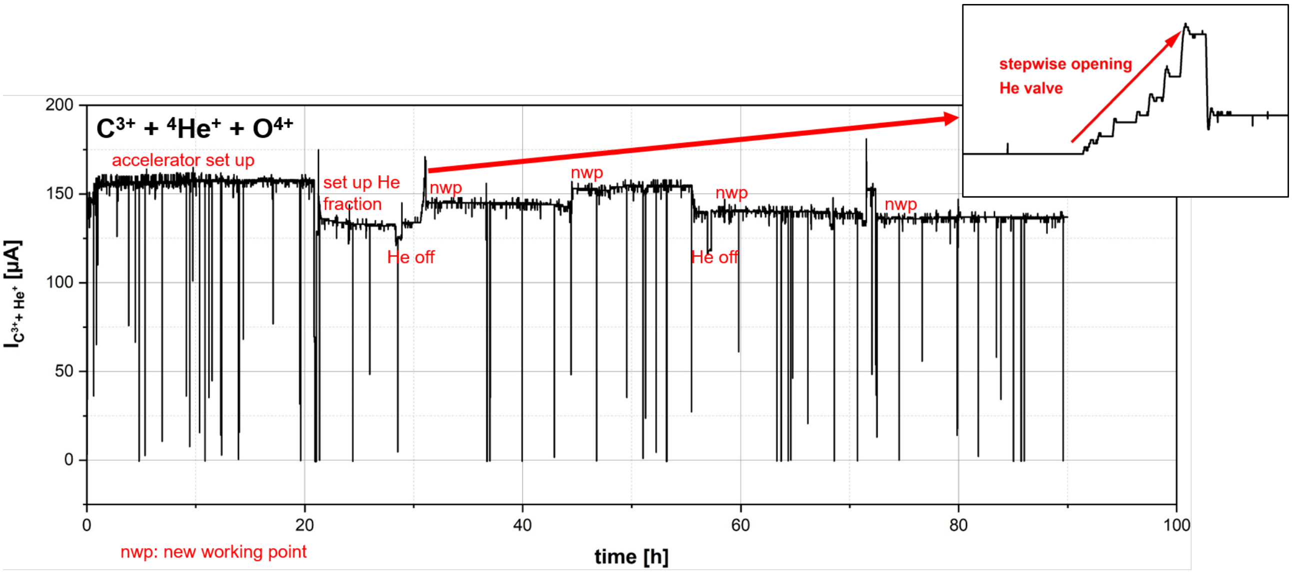

Figure 8: Ion source stability over 4 days in terms of analysed beam current; current de- and increase for different He fraction (insert).

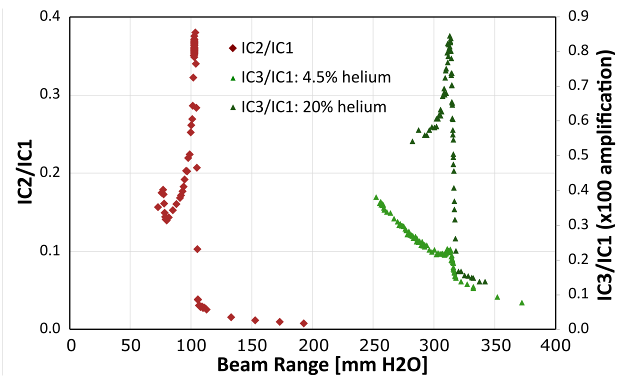

Figure 9: Depth-dose profile of carbon and oxygen (ruby) and helium (light green: 4.5 %, dark green: 20 % helium fraction over fragment's background).

REFERENCES

[1] C. Graeff *et al.*, "Helium as a range probe in carbon ion therapy", *Physica Med.*, vol. 52, p. 11 (abstract), 2018. doi:10.1016/j.ejmp.2018.06.099

[2] L. Volz *et al.*, "Experimental exploration of a mixed helium/carbon beam for online treatment monitoring in carbon ion beam therapy", *Phys. Med. Biol.*, vol. 65, p. 055002, 2020. doi:10.1088/1361-6560/ab6e52

[3] Ch. Graeff, L. Volz, and M. Durante, "Emerging technologies for cancer therapy using accelerated particles", *Prog. Part. Nucl. Phys.*, vol. 131, p. 104046, Jul. 2023. doi:10.1016/j.ppnp.2023.104046

[4] D. Mazzucconi *et al.*, "Mixed particle beam for simultaneous treatment and online range verification in carbon ion therapy: Proof-of-concept study", *Med. Phys.*, vol. 45, no. 11, pp. 5234–5243, Oct. 2018. doi:10.1002/mp.13219

[5] J.J. Hardt *et al.*, "The potential of mixed carbon-helium beams for online treatment verification: a simulation and treatment planning study", *Phys. Med. Biol.*, vol. 69, p. 125028, 2024. doi:10.1088/1361-6560/ad46db

[6] M. Dick, L. Volz, M. Durante, and C. Graeff, "Range prediction for a mixed helium-carbon beam", *Int. J. Part. Ther.*, vol. 12, p. 100362 (abstract), 2024. doi:10.1016/j.ijpt.2024.100362

[7] E. Renner *et al.*, "Towards the slow extraction of mixed C^{6+} and He^{2+} beams for online range verification", in *Proc. IPAC'24*, Nashville, TN, May 2024, pp. 3603-3606. doi:10.18429/JACoW-IPAC2024-THPR43

[8] M. Kausel *et al.*, "A double multi-turn injection scheme for mixed C^{6+} and He^{2+} beams", in *Proc. IPAC'24*, Nashville, TN, May 2024, pp. 3599-3602. doi:10.18429/JACoW-IPAC2024-THPR42

[9] D. Ondreka *et al.*, "Slow extraction of a dual-isotpe beam from SIS18", in *Proc. IPAC'24*, Nashville, TN, May 2024, pp. 1698-1701. doi:10.18429/JACoW-IPAC2024-TUPS29

[10] M. Galonska *et al.*, "First dual isotope beam production for simultaneous heavy ion radiotherapy and radiography", in *Proc. IPAC'24*, Nashville, TN, May 2024, pp. 1893-1896. doi:10.18429/JACoW-IPAC2024-WEAN1

[11] Ocean Optics, https://www.oceaninsight.com

[12] F. Maimone *et al.*, "Research and development activities to increase the performance of the CAPRICE ECRIS at GSI", *J. Phys.: Conf. Ser.*, vol. 2743, p. 012048, 2024. doi:10.1088/1742-6596/2743/1/012048

[13] C. Graeff *et al.*, "First experimental demonstration of a mixed helium/carbon beam for image guidance and range verification", *Physica Med.*, vol. 125, p. 103892 (abstract), Sep. 2024. doi:10.1016/j.ejmp.2024.103892

[14] C. Graeff *et al.*, "First experimental production of a mixed helium/carbon beam for online range monitoring and image guidance", *Int. J. Part. Ther.*, vol. 12, p. 100185 (abstract), Jun. 2024. doi:10.1016/j.ijpt.2024.100185

ISBN: 978-3-95450-257-8 ISSN: 2222-5692 doi:10.18429/JACoW-ECRIS2024-WEB2

APPLYING MACHINE LEARNING TECHNIQUES TO THE OPERATION OF THE SUPERCONDUCTING ECR ION SOURCE VENUS*

D. S. Todd†, J. Y. Benitez, H. L. Crawford, A. Kireef, Y. S. Lai, M. Satathe, V. Watson
Lawrence Berkeley National Laboratory, Berkeley, U.S.A.

Abstract

An operator of the superconducting ECR ion source VENUS tasked with optimizing the current of a specific ion species or finding a stable operating mode is faced with an operation space composed of ten-to-twenty knobs in which to determine the next move. Machine learning techniques are well-suited to multidimensional optimization spaces. Over the last three years we have been working to employ such techniques with the VENUS ion source. We will present how the introduction of computer control has allowed us to automate tasks such as source baking or to utilize optimization tools to maximize beam currents with no human intervention. Finally, we will discuss control and diagnostic changes that we have employed to exploit the faster data collection and decision making abilities when VENUS is under computer control.

INTRODUCTION

Electron cyclotron resonance (ECR) ion sources are employed as injector sources for many accelerator facilities around the world. The reason for this is simple: these sources are capable of producing high current, highly-charged ion beams from any material that can be introduced to the ECR ion source plasma without destroying the plasma.

The typical ion source has an operation space defined by ten-to-twenty control parameters, depending on the ion beam being produced. Though this results in an enormous operation space, the operator is typically tasked with maximizing or minimizing some beam quantity. For example, it may be required that the species current be maximized, its emittance be minimized, its stability kept below some threshold, or some combination of these. Therefore, though the operation space is broad, the problem is made somewhat more tractable by the fact that much of that space may be eliminated from contention.

Bayesian optimization [1] operates in this spirit: an operation space is populated (typically) randomly with some number of exploratory measurements . The code models a distribution over the operation space using these measurements and, using a user-determined balance between exploring far from measured points and searching near currently known extrema, searches a new point where it has determined the probability of being an extrema is largest. The newly-measured point is used to update the modeled distribution and the process repeats. In this work, we use Bayesian optimization to maximize the beam current of a species of interest from LBNL's superconducting ECR ion source, VENUS, discuss the results, and use these results to motivate and implement improvements to data collection times that will aid our continued machine learning efforts with this ion source.

VENUS ION SOURCE AND COMPUTER INTERFACE

LBNL's VENUS ion source is a fully-superconducting ECR ion source optimized for 28 GHz operation [2]. The plasma-confining magnetic field is produced through a superposition of solenoidal and sextupolar NbTi coils. A sextupole at each end provides radial confinement while one in the center opposes these fields and helps set the center minimum field. The source is able to produce over 2 tesla fields on the radial walls and on axis at extraction, and up to 4 tesla axially opposite the plasma from extraction. Two frequency heating, 28 and 18 GHz, is used with up to 10 kW and 4.4 kW available, respectively.

In recent years we have established the ability to both completely control and read all of VENUS' diagnostics by computer. This was achieved by employing the Python library pylogix [3] to interface with VENUS' programmable logic controller (PLC). We created a Python class so the computer could set and read all parameters that a human operator can when running VENUS.

Controlling VENUS through the PLC has the distinct advantage that the computer is operating the source just as human operators do, and the more-than-two-decades of safety logic written into the PLC to preserve safe operation immediately applies to computer operation. However, this comes at the cost of speed as the PLC has been designed for human interaction rates, so data can only be written or read at about 3 Hz.

Using this interface, we have been able to automate a number of tasks that previously were time-consuming. Experimental data taking (e.g. sweeping a parameter between two values and recording all source data) is now trivial. Baking, the process where materials on plasma chamber surfaces from previous runs, contaminants, or exposure to atmosphere are removed by plasma-chamber interaction, has been performed many times now with absolutely no human interaction with the source. The heating microwave power is brought up by the computer in a controlled manner until full power is reached. At that point the confining magnetic fields are adjusted by computer to alter the wall-plasma interaction and accerate the removal of material from the wall. The methods of doing this are no different than those that might be undertaken by a human, but the computer is continually

* This work is supported by the U.S. Department of Energy, Office of Science, Nuclear Physics program under Award Number DE-FOA-0002490.
† dstodd@lbl.gov

ISBN: 978-3-95450-257-8 ISSN: 2222-5692 doi:10.18429/JACoW-ECRIS2024-WEB2

monitoring and making changes in a way that all but the most attentive operators do not. The data retrieved from these computer-driven baking efforts will be used to inform future machine learning efforts to reduce this process that typically takes tens of hours.

BAYESIAN OPTIMIZATION

Though somewhat limited by the slow interface speeds, we were able to perform full optimizations of a $^{124}Xe^{37+}$ beam from VENUS where all source control parameters were under computer control. It is worth noting that the computer has no information about VENUS: the computer sets the nine control parameters within the operation range, sends these settings to the PLC, and reads out a beam current. The first 50 points are explored randomly from within the operation space listed in Table 1. The computer uses currents measured at these random points to estimate the operation space topography and predict what point in the operation space (balancing exploratory searches away from measured points and exploiting attained knowledge and searching nearer measured extrema) is most likely to provide the peak $^{124}Xe^{37+}$ current and measure there. The new point is used to better estimate the operation space, and the process is repeated for a set number of new measurements. All measured data can be used to initialize additional searches in the same operation space.

Table 1: Exploration Range for Bayesian Optimization of $^{124}Xe^{37+}$ Beam Current from VENUS

Parameter [unit]	Minimum	Maximum
Bias voltage [V]	40	105
Oxygen valve [arb]	11.6	12.5
Xenon valve [arb]	8.0	13.0
Injection coil [A]	185.6	186.0
Extraction coil [A]	136.6	136.8
Middle coil [A]	152.0	152.3
Sextupole coils [A]	430.3	430.5
28 GHz RF [W]	5200	6000
18 GHz RF [W]	1400	1800

As can be seen in Fig. 1, a Bayesian optimization of the operation space defined in Table 1 was able to achieve approximately 7.5 µA of $^{124}Xe^{37+}$. Though this result is much less than the ~50 µA record beams seen at IMP in Lanzhou, China with their SECRAL II source, this result compares favorably with the performance of relatively experienced VENUS tuners. Additionally, it should be noted that the operation space in Table 1 was severely limited to prevent any damage to the VENUS plasma chamber while a spare is being produced, and it is known that VENUS settings that produced over 40 µA beams are outside the prescribed range.

Each of the search points took approximately 5 minutes to complete. Part of the reason for this is that changes to the superconducting coil setting, even for small current changes, usually require a couple of minutes to complete. Additionally, after any changes are complete, the source is allowed to settle and then 50 beam current measurements at 3 Hz were taken to provide beam current statistics.

Later Bayesian optimizations were performed where the optimal coil setting was maintained from a full optimization in order to speed up the exploration. For these runs, charge state distributions (CSDs) taken at each search point indicated that many of the higher current results had nearly the same species current but wildly different current distributions, as shown in Fig. 2.

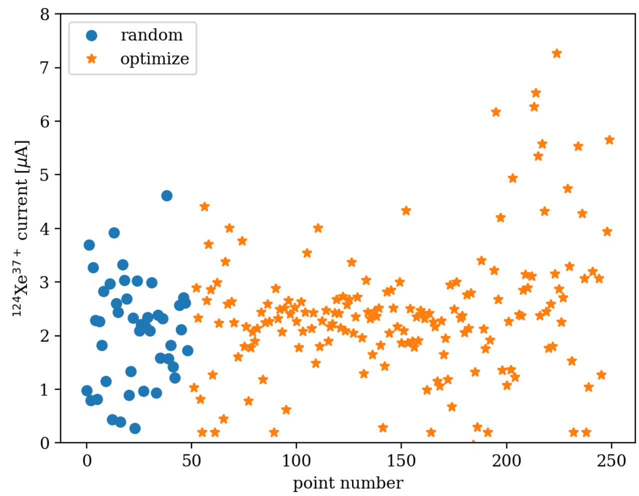

Figure 1: $^{124}Xe^{37+}$ current plotted as a function of Bayesian optimization search number. The first 50 searches are random while later searches are based on the model's understanding of the space based an all explorations to this point.

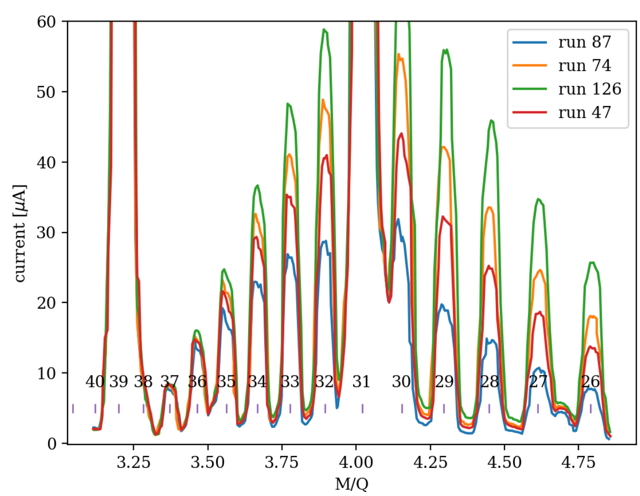

Figure 2: Charge state distributions for four control parameter settings ("runs") yielding nearly-identical $^{124}Xe^{37+}$ currents during a Bayesian optimization of that species. This distribution information was not provided to the optimization code.

ISBN: 978-3-95450-257-8 ISSN: 2222-5692 doi:10.18429/JACoW-ECRIS2024-WEB2

From Fig. 2, one can clearly see that optimizing a specific beam species current (here, $^{124}Xe^{37+}$) while only looking at the species of interest leaves the source operator missing critical information. Human operators are able to glean general trends with this CSD information, but computers have the potential to use this information with tools like neural network techniques to better understand and optimize source performance within the operation space. However, the only way for this to be useful in reasonable timescales is to reduce the time to gather charge state distribution information from the 3–4 minutes required using the PLC's 3 Hz bottleneck.

FASTER DIAGNOSTICS

Though the 3 Hz beam current update rate through the PLC has proven sufficient to determine beam stability for delivery to LBNL's 88-Inch Cyclotron, this is an unacceptably low rate when trying to calculate statistics to inform the machine learning effort. In order to improve the data collection rate for beam current, a faster ammeter was employed, its current read by computer, and then the rapid signal was averaged at a 3 Hz rate and fed back to the PLC to maintain current display capabilities. The ammeter, a Keysight B2983A, has the capability of reading beam current at 20 kHz, but as discussed in [4] in detail, the Faraday cup does not serve as a great diagnostic for fast instabilities. Therefore we typically do not measure currents at a rate faster than 1 kHz and use standard deviation calculations with these measurements as a gross, and faster, stability measure.

Combining the faster ammeter measurements with computer control of the VENUS analyzing dipole allows for a significant decrease in the time needed to collect charge state distribution data. By requesting dipole current changes and reading the Faraday cup at 100 Hz each, charge state distributions for M/Q from 2 to 8 to be completed in 5–6 seconds with the same amount of information as the 3–4 minute sweeps through the PLC. Sudden dipole current changes from the top of the the CSD to the bottom to start the next sweep were deemed hard on the dipole's power supply, so we now sweep the current up, sit for a second at the top of the range, sweep down, wait a second at the bottom of the range, and repeat. The full cycles take ~12 seconds, as can be seen in Fig. 3, where a xenon-124 beam is analyzed.

In one full cycle of the dipole, as shown in Fig. 3, we get two CSDs, as visible by the near-mirroring about the center of that plot. By plotting the measured current as a function of mass-to-charge ratio, as in Fig. 4, it can be seen that the two CSDs agree relatively well. However, it can also be seen that on the downward sweep the measured currents for higher charge states are reduced relative to the upward sweep. This is a result of all of the overbent species being intercepted on a relatively small area of the wall of the beam pipe. The temperature of this area increases as does the pressure after the dipole, leading to beam losses. However, this transient has settled for the most part by the start of the next upward sweep, and therefore only upward sweeps are used for diagnostic purposes.

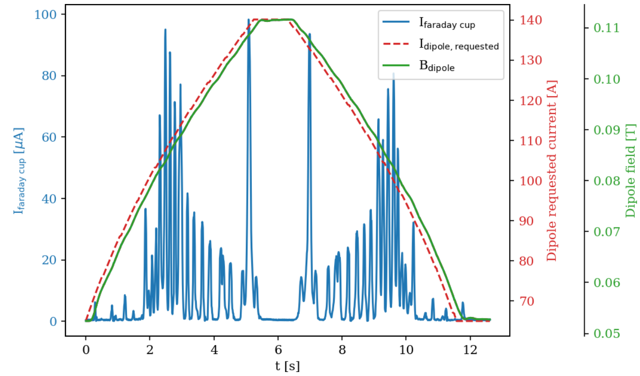

Figure 3: Faraday cup current, requested dipole current and dipole field are plotted as a function of time for one full up-down cycle when measuring fast charge state distributions. The field lags behind the requested current, so a second is spent with constant requested current before sweeping in the opposite direction.

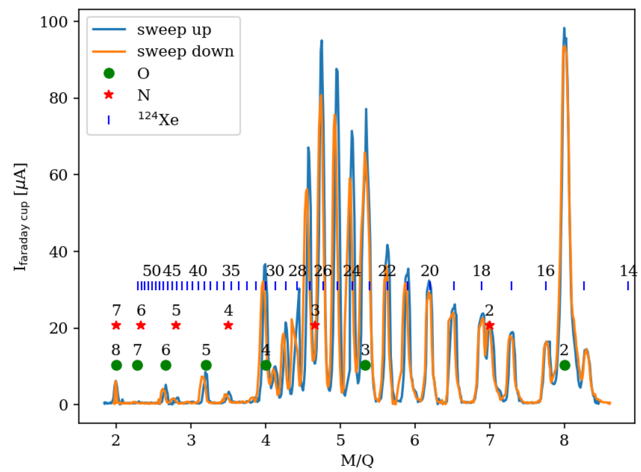

Figure 4: Charge state distributions with increasing dipole current (blue) and decreasing (orange). Expected mass-to-charge ratios for different species are indicated with symbols.

The ability to take charge state distributions faster allows for the measurement of dynamic systems and get more rapid feedback on how those changes are affecting the all ion species. As an example of this, when running a 124-xenon beam using oxygen as a mixing gas, we closed the valve in regular steps over an hour. After each closing the system was able to settle and charge state distributions were continually measured at 12 second intervals. From each charge state distribution we identified the species peaks and provided some smoothing of each species' current as a function of time to get rid of measurement noise. As is well-known in the field, the lowering of pressure caused a shift in the charge state distribution from lower to higher charge states. To visualize this, we normalized each species' current over the hour to its maximum and made the plot shown in Fig. 5.

Plots like Fig. 5 are very useful for ion source operators to understand general behaviors and trends for ECR ion sources. The data underlying this plot and similar data in

ISBN: 978-3-95450-257-8 ISSN: 2222-5692 doi:10.18429/JACoW-ECRIS2024-WEB2

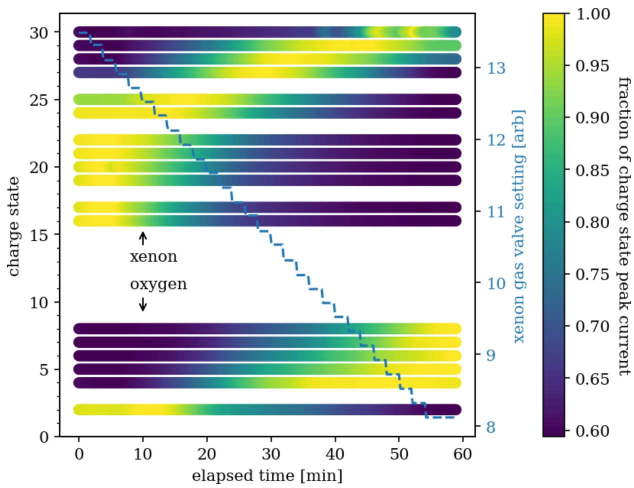

Figure 5: Beam current for twelve 124-xenon ion species and six oxygen species are plotted as a function of time as the xenon valve is closed over an hour. Each species is normalize to its maximum value during this hour. Both oxygen and xenon distributions shift to higher charge state as the valve is closed.

explorations of the ECR operation space will be essential in the application of machine learning techniques not just focused on optimizing the beam current, but also with the goal of better understanding general source operation. For example, after metals have been used in the source, metal beams still appear in extracted beams for days after. The amount of these unwanted elements in the beam decays with time, and as it goes away it affects the charge state distributions. Without the machine learning computer (or a human, even) knowing about the changing presence of these extra elements in the plasma and extracted beam, it is very difficult to generalize results. The ability to gather this information rapidly gives machine learning a much better chance at succeeding at characterizing the operation space by providing previously unobservable information and predicting how we might improve our source operation.

CONCLUSIONS

We now have the ability to completely control the VENUS ion source by computer. Using Bayesian optimization, we are able to have the computer optimize the ion source for a given ion species and achieve currents that are comparable with those a moderately trained ion source tuner could produce. The operation space for this effort was limited and distinct from regions where significantly higher currents have been achieved with VENUS. It is expected that opening the search space will lead to significantly increase achieved currents.

The recent addition of the capability to read the source Faraday cup at frequencies of at least 100 Hz significantly reduces the time to determine the level of general beam stability, and coupling this with faster analyzing magnet operation has reduced charge state distribution times to approximately 10 seconds. We expect that these faster charge state distributions will be extremely impactful as this machine effort continues, both in terms of faster data and a more complete understanding of what is in the source and what is coming out.

REFERENCES

[1] Roman Garnett, *Bayesian Optimization*, Cambridge, UK: Cambridge University Press, 2023. doi:10.1017/9781108348973

[2] D. Xie, J. Y. Benitez, C. M. Lyneis, D. S. Todd, and W. Lu, "Recent production of intense high charge ion beams with VENUS", in *Proc. ECRIS'16*, Busan, Korea, Aug.-Sep. 2016, pp. 141-145. doi:10.18429/JACoW-ECRIS2016-THAO01

[3] B. Peterson and D. Roeder, pylogix, GitHub repository, 2017. https://github.com/dmroeder/pylogix

[4] V. Toivanen, B.S. Bhaskar, I.V. Izotov, H. Koivisto, and O. Tarvainen, "Diagnostic techniques of minimum-B ECR ion source plasma instabilities", *Rev. Sci. Instrum.*, vol. 93, p. 013302, 2022. doi:10.1063/5.0075443

ISBN: 978-3-95450-257-8 ISSN: 2222-5692 doi:10.18429/JACoW-ECRIS2024-WEB3

BEAM INTENSITY PREDICTION USING ECR PLASMA IMAGES AND MACHINE LEARNING

Y. Morita*, RIKEN Nishina Center for for Accelerator-Based Science, Saitama, Japan
K. Kamakura, Center for Nuclear Study, the University of Tokyo, Tokyo, Japan
A. Kasagi, Rikkyo University, Tokyo , Japan
T. Nishi, RIKEN Nishina Center for for Accelerator-Based Science, Saitama, Japan
N. Oka, National Institute of Information and Communications Technology, Tokyo, Japan

Abstract

Long-term beam stability is crucial for supplying multivalent heavy-ion beams using an electron cyclotron resonance (ECR) ion source . When the beam intensity drops during long-term operation, the ECR ion source parameters must be adjusted to restore the original beam intensity. Continuous measurement of beam intensity using a Faraday cup (FC) while using the beam is impractical. Currently, we estimate the beam intensity during beamtime by monitoring the total drain current, which is an unreliable method. Therefore, we propose a new method for predicting the beam intensity at FC using machine learning. In the proposed method, plasma images captured through a hole in the beam extraction electrode and the operating parameters are considered as input data for training a machine learning model. The proposed method successfully produced rough predictions of beam intensity in short-term validation datasets. This paper presents the prediction model and its prediction results using validation data. The developed model can immediately respond to fluctuations in beam intensity and enable efficient operation of the ECR ion source over extended periods.

INTRODUCTION

In the long-term operation of electron cyclotron resonance (ECR) ion sources, the beam intensity frequently fluctuates during delivery. However, methods such as Faraday cups (FC) cannot be used to diagnose beam intensity during delivery because FC interferes with the beam. Consequently, we have been operating ECR ion sources by inferring changes in beam intensity using the drain current as the leading indicator. Nevertheless, a non-destructive beam intensity measurement method must be developed to automate its long-term operation. Based on the empirical knowledge that operators consider plasma light in the visible light region crucial when tuning ECR ion sources, we devised a method to predict beam intensity from plasma light. In this study, we created and evaluated a model to predict the beam intensity by processing images of visible plasma light obtained through a CCD camera using machine learning. Previous studies have suggested a relationship between plasma light intensity and beam intensity [1]; consequently, this study further aims to predict the absolute value of beam intensity based on this relationship.

* yasuyuki.morita@riken.jp

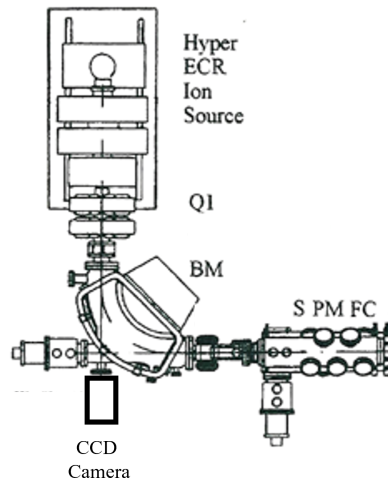

Figure 1: Schematic representation of the LEBT, where beams extracted from the HyperECRIS are focused by quadrupole magnets and then selected for the required charge by bending magnets and slits. The plasma light was captured using a CCD camera through a window in the bending magnet and through an extraction electrode.

EXPERIMENTAL CONDITIONS

HyperECR Ion Source

The 14-GHz ECR ion source “HyperECR Ion Source” (HyperECRIS) [2] at the Center for Nuclear Study, The University of Tokyo, was used to acquire training and validation data for developing the machine learning model. The HyperECRIS can supply gas ion species such as proton, helium, and argon and metal ions such as lithium and iron. In the HyperECRIS, a crucible containing metallic material was attached to a rod tip, and the heat of the plasma was used to vaporize the metallic material to provide metal ions. Therefore, compared to gas ion species, the intensity of the beam tends to fluctuate when metal ion species are supplied. In this experiment, we used a $^{56}Fe^{15+}$ beam, considering that a more stable gas ion species would not be suitable for evaluating the prediction accuracy, mainly because the fluctuation of the beam intensity is slight.

Parameters

The low energy beam transport (LEBT) from HyperECRIS to FC is shown in Fig. 1. The beam extracted from HyperECRIS was selected through the bending magnets and slits, and the beam intensity was measured at FC. The param-

ISBN: 978-3-95450-257-8 ISSN: 2222-5692 doi:10.18429/JACoW-ECRIS2024-WEB3

eters of HyperECRIS and LEBT are summarized in Table 1. For these parameters, EPICS was used, and an acquisition system was established to acquire data simultaneously. The acquisition time was synchronized with the timing of the plasma light imaging described below.

Table 1: Operation Parameters

Controllable parameters	**Observable parameters**
RF power	Reflection power
Main gas valve	Drain current
Sub gas valve	Plasma light
Main coil current 1	Beam intensity
Main coil current 2	Degree of vacuum
Rod position	
Extraction voltage	
· Slits position	
(Up, Down, Left, Right)	
Q magnet current	
Einzel electrode voltage	
Bending magnet current	

Plasma Light Image

The novel aspect of this study is the use of plasma light images. As shown in Fig. 1, plasma light images were obtained through the window of the bending magnet at the extraction and plasma electrodes. A CCD camera with sensitivity in this region was used to capture RGB information of the emission in the visible light region. An example of an actual plasma light image during the $^{56}Fe^{15+}$ beam supply is shown in Fig. 2. Due to the 10 mm diameter of the plasma electrode, the entire ECR zone was not captured. Nevertheless, the star shape of the plasma can be observed. Moreover, the image confirms that the star shape is twisted at the upstream and downstream sides due to the mirror magnetic field.

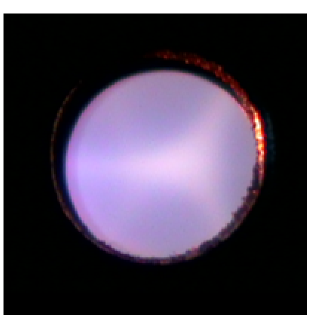

Figure 2: Plasma light obtained through the extraction electrode. The CCD camera captures only the visible light. Although the entire ECR zone is not visible because the diameter of the extraction electrode limits the visible area, the star shape is clearly observed.

MACHINE LEARNING MODEL

Input Data

This study aims to develop a machine learning model to predict beam intensity. As beam intensities are the prediction target, they cannot be used as input data. Thus, plasma light image and operation parameters other than the beam intensity should be considered as the input data for the machine learning model. In addition to tuneable parameters, other parameters cannot be directly controlled but can be observed, such as the degree of vacuum and RF reflected waves. Other parameters can be tuned but are must be fixed due to the accelerator requirements, such as the extraction voltage and current value of the bending magnet. In this study, all of these parameters were introduced into machine learning without differentiating them using, for example, weighting factors.

Neural Network Model

A machine learning model was developed using a neural network. An overview of the neural network model is shown in Fig. 3 . For the plasma light image, ResNet50 [3], a convolutional neural network, was used. The image was cropped to a size of 224 × 224 pixels to fit the input of ResNet50, and one fully-connected layer after the output layer of ResNet50 was included. The output and operation parameters of the fully-connected layer after ResNet50 were combined with the output of the fully-connected layer after ResNet50. Two more layers of fully-connected layers were used to model the output of the beam intensity values. The output layer is a single continuous number. During training, the mean squared error was used as the loss function.

RESULTS

The performance of machine learning was evaluated using data acquired during the $^{56}Fe^{15+}$ beam tuning and beam experiments conducted on March 18–19, 2024. After the beam supply ended on March 19, an experiment was conducted to evaluate the effect of changing the current values of main coils 1 and 2 on the $^{56}Fe^{15+}$ beam. The set of operation parameters and plasma light images obtained simultaneously were used as training data. The training data contained 72619 data points. The validation data were used from the start of the accelerator tuning on March 18 to the end of the beam supply on March 19. A validation dataset was used to verify whether machine learning after training can predict new data. The validation data contained 31646 data points. The beam intensity predictions for the validation data and the beam intensity measured at the FC are shown in Fig. 4. In the validation data, the FC was evacuated most of the time for the accelerator tuning and the beam supply; thus, the beam intensity during that period was not measured, and its value is shown as 0 μA. The developed machine learning model can predict the beam intensity even when the FC is evacuated and the direct measurement is impossible. Although some errors in absolute values remain, the model reproduces the decreasing timing trend of the beam intensity well. These results suggest that this machine learning model is practical as an indicator of the change of the beam intensity during the beam supply.

ISBN: 978-3-95450-257-8 ISSN: 2222-5692 doi:10.18429/JACoW-ECRIS2024-WEB3

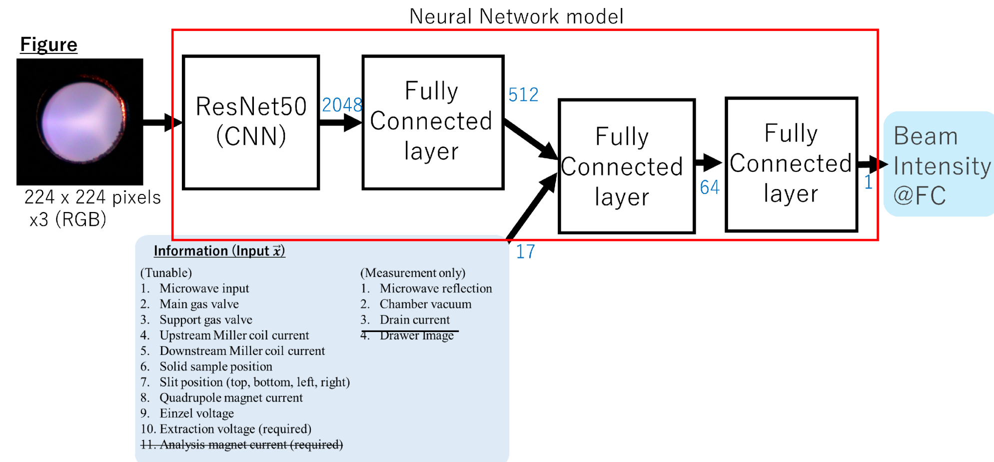

Figure 3: Schematic representation of the machine learning model. Images are input to ResNet50 and then pass through one fully-connected layer. Two additional fully-connected layers are used to predict beam intensity with operating parameters.

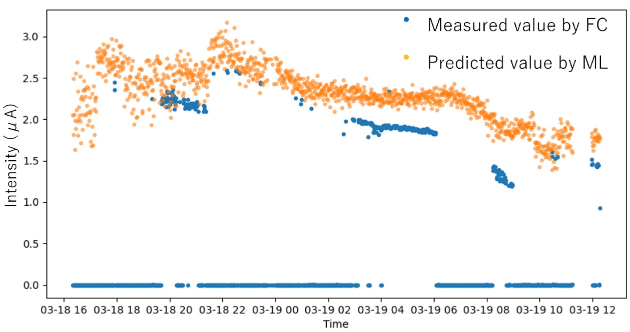

Figure 4: Results of machine learning beam intensity prediction. The model could predict even though the measured values were 0 because the FC were evacuated during accelerator tuning and the beam supply. Although an error in the absolute value remains, the model could predict the beam current without an FC.

CONCLUSION

This study developed a beam intensity prediction method using plasma light images and machine learning for long-term stable control of ECR ion sources. In the proposed method, visible plasma light was captured through the extraction electrodes and used as an input for machine learning along with operating parameters. Although the method still has some limitations, such as absolute value errors, the results indicate that it performs well enough to identify trends in beam intensity, such as a decrease in beam intensity. The results suggest that predicting changes in beam intensity is possible at any time during the beam supply. This method enables us to respond immediately to changes in beam intensity and operate the ECR ion source more efficiently for long periods.

REFERENCES

[1] R. Rácz, S. Biri, and J. Pálinkás, "Electron cyclotron resonance plasma photos", *Rev. Sci. Instrum.*, vol. 81, no. 2, p. 02B708, 2010. doi:10.1063/1.3267289

[2] Y. Ohshiro, S. Yamaka, S. Kubono, and S. Watanabe, "Development of an ECR ion source at CNS", in *Proc. of 17th Int. Conf. Cyclotrons Appl. (Cyclotrons'04)*, Tokyo, Japan, paper 19P20, 2004. https://jacow.org/c04/data/CYC2004_papers/19P20.pdf

[3] K. He, X. Zhang, S. Ren, and J. Sun, "Deep Residual Learning for Image Recognition", in *Proc. IEEE Conf. Comput. Vision Pattern Recognit. (CVPR'16)*, Las Vegas, NV, USA, pp. 770–778, 2016. doi:10.1109/CVPR.2016.90

ISBN: 978-3-95450-257-8 ISSN: 2222-5692 doi:10.18429/JACoW-ECRIS2024-THA2

NUMERICAL DESIGN OF AN INNOVATIVE SUPERCONDUCTING MAGNETIC TRAP FOR PROBING β-DECAY IN ECR PLASMAS

G. S. Mauro*, L. Celona, G. Torrisi, A. Pidatella, E. Naselli, F. Russo, B. Mishra, G. Finocchiaro, D. Santonocito, D. Mascali, INFN-LNS, Catania, Italy
A. Galatà, INFN-LNL, Legnaro, Italy

Abstract

The main aim of Plasmas for Astrophysics Nuclear Decays Observation and Radiation for Archaeometry (PANDORA) project is to build a flexible magnetic plasma trap where plasma reaches a density $n_e \sim 10^{11} - 10^{13}\,\mathrm{cm}^{-3}$, and a temperature, in units of kT, $kT_e \sim 0.1 - 30\,\mathrm{kV}$ in order to measure, for the first time, nuclear β-decay rates in stellar-like conditions. Here we present the numerical design of the PANDORA magnetic system, carried out by using the commercial simulators OPERA® and CST Studio Suite®. In particular, we discuss the design choices taken to: 1) obtain the required magnetic field levels at relevant axial and radial positions; 2) avoid the magnetic branches along the plasma chamber wall; 3) find the optimal position for the set of plasma diagnostics that will be employed. The magnetic trap has been conceived to be as large as possible, both in radial and axial directions, in order to exploit the plasma confinement mechanism on a bigger plasmoid volume. The plasma chamber will have a length of 700 mm and a diameter of 280 mm. The magnetic trap tender procedure has been completed in June 2024 and the structure realization is expected to start in late 2024.

INTRODUCTION AND MOTIVATION

In the last decades, much experimental and theoretical efforts have been dedicated to investigate various possible scenarios which can influence nuclear decays rates. It has been predicted that sizeable variations in the decay properties can be observed in highly ionized nuclides. This would have a strong impact in the stellar nucleosynthesis where a hot plasma is formed and atoms can be found in different ionization states. In particular, β decay properties of radioactive nuclei can be strongly affected by the high-temperature plasma of stellar environment. Few experimental evidences showing variations in the beta decay rates as a function of the atomic ionization state have been collected, up to now, using storage rings. However, the storage ring approach is based on the investigations of a single charge state at a time: while clearly showing the role played by the high ionization state of an atom in the β-decay process, is not able to reproduce stellar-like conditions where, due to the high temperature of the plasma, a Charge State Distribution (CSD) of the ions is established. A totally new and challenging approach, based on the study of decays rates in a plasma whose conditions can mimic the hot stellar environment, has been conceived in the PANDORA project [1]. The main idea is to build a flexible magnetic plasma trap and use it to measure, for the first time, nuclear β-decay rates in stellar-like conditions. The decay rates of the radioactive ions will be measured through the detection of the γ-rays emitted by the β-decaying daughter nuclei, as a function of the charge state distribution of the in-plasma ions by varying plasma conditions. This task will be accomplished by an array of several Hyper-Pure Germanium (HPGe) detectors placed around the trap, in specific positions where holes were made in the cryostat structure to directly look into the plasma through thin aluminium windows. This new approach is expected to have a major impact in the study of nuclear-astrophysics processes and cosmology. The magnetic field, necessary for plasma confinement, will be produced by employing a superconducting magnetic system (as typical for ECR ion sources), consisting of six hexapole coils (for radial confinement) nested inside three solenoid coils (for axial confinement), i. e. a SEXT-IN-SOL configuration. This magnetic system configuration is called *minimum-B* and allows the confinement of a plasma located around the plasma chamber axis (here z axis), providing magnetohydrodynamical (MHD) equilibrium and stability.

MAGNETIC TRAP NUMERICAL DESIGN

Some considerations can be made for the design of a magnetic system for ECRIS plasma confinement [2]. The optimum charge state is proportional to the average magnetic field as $q_{\mathrm{opt}} \propto B^{3/2}$, so it is of our interest to increase the average confining field. The highest value of the magnetic field will be in correspondence of the injection and/or extraction axial coils inner surface, so during the numerical design of the magnetic system one has to be careful at not exceeding the threshold field values relative to the magnet material. In superconducting traps, special attention must be paid to the minimum field, B_{min}, that should be tuneable within a wide range of values: it has been experimental observed that, in order to obtain the highest electron density and to reach the optimal charge state, one has to have $0.65 < B_{\mathrm{min}}/B_{\mathrm{ECR}} < 0.75$ [3–5]. If this ratio exceeds the upper value, sudden non linear effects arise, increasing the plasma x-ray emission and thus the heat load on the cryostat. The requirements and considerations previously discussed, together with the necessity to have enough space for non-invasive diagnostic tools and for the array of γ-ray detectors [6], allowed us to fix the plasma chamber dimensions (internal radius $R_{\mathrm{CH\_IN}} = 140\,\mathrm{mm}$ and axial length $L = 700\,\mathrm{mm}$) and RF pumping frequencies ($f_{\mathrm{RF1}} = 18\,\mathrm{GHz}$, $f_{\mathrm{RF2}} = 21\,\mathrm{GHz}$). Taking into account these values, the PANDORA magnetic system field specifications have been ob-

* mauro@lns.infn.it

ISBN: 978-3-95450-257-8 ISSN: 2222-5692 doi:10.18429/JACoW-ECRIS2024-THA2

tained. The structure 3D conceptual model is shown in Fig. 1: it is composed by three axial coils and six radial coils: the field values as well as the operative ranges are reported in Table 1. The structure has been simulated with the commercial software packages OPERA® and CST Studio Suite®. The simulated coil dimensions are reported in Fig. 2 and Table 2. This model takes also into account a 25 mm thick iron yoke (ARMCO iron), distant 20 mm from the injection and extraction coils outer radius, employed to minimize the stray field that could otherwise interfere with the external detectors. The realized superconducting coils assembly will be encased inside a cryostat that will include a central warm bore for plasma chamber insertion.

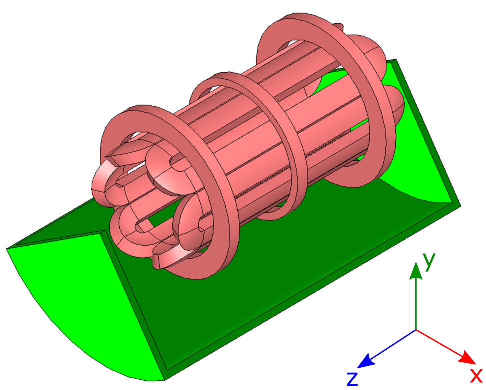

Figure 1: 3D conceptual model of the structure comprehensive of the magnetic system (pale red objects) and the iron yoke (green object, only 1/4 visible).

Table 1: PANDORA Magnetic Field Operative Ranges

Parameter	Value [T]
B_{inj} max @ $z = 350$ [mm]	3
B_{inj} operative range	1.7 - 3
B_{ext} max @ $z = -350$ [mm]	3
B_{ext} operative range	1.7 - 3
B_{min} @ $z = 0$ [mm]	0.4
B_{hex} @ $R_{\mathrm{CH\_IN}}$	1.6

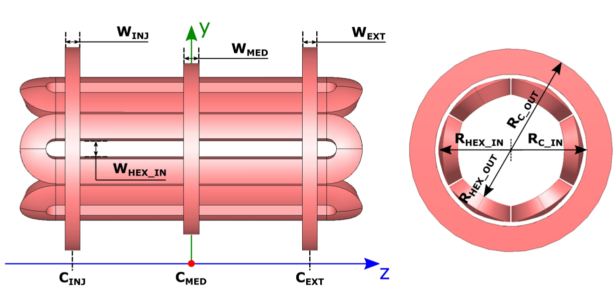

Figure 2: Side and front view of the simulated magnetic system with dimensional parameters. Note: iron yoke does not appear in the picture.

The axial and radial magnetic field profiles are reported in Fig. 3 and Fig. 4, scaled for the case $f_{\mathrm{RF}} = 18$ GHz.

Table 2: Simulated Coil Dimensions

Axial coils	
Parameter	**Value [mm]**
$R_{\mathrm{C\_IN}}$	225 / 225 / 225
$R_{\mathrm{C\_OUT}}$	300 / 253 / 300
$C_{\mathrm{INJ,MED,EXT}}$	-350 / 0 / 350
$W_{\mathrm{INJ,MED,EXT}}$	44 / 46 / 44
Hexapole	
Parameter	**Value [mm]**
$R_{\mathrm{HEX\_IN}}$	165
$R_{\mathrm{HEX\_OUT}}$	212
$W_{\mathrm{HEX\_IN}}$	78

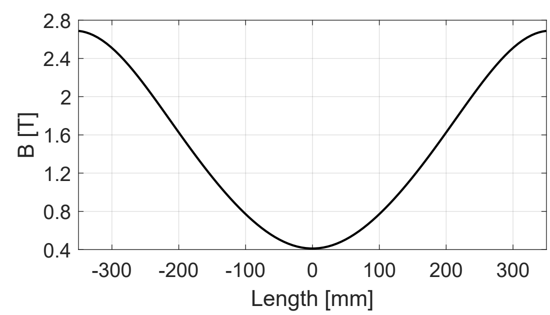

Figure 3: Magnetic field module, $|B|$, along plasma chamber z-axis for pumping frequency $f_{\mathrm{RF}} = 18$ GHz.

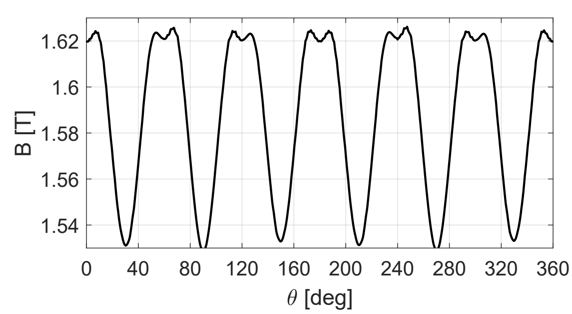

Figure 4: Magnetic field module, $|B|$, along a circumference of radius $R_{\mathrm{CH\_IN}} = 140$ mm (plasma chamber inner radius) and axial position z = 0 mm.

Numerical simulations have also been performed to identify the positions of the magnetic branches that need to be avoided when placing the array of gamma ray detectors. In fact, in these positions a rather strong Bremsstrahlung radiation generated on the plasma chamber wall is present due to the intense flux of electrons escaping the magnetic trap, leading to a high background rate on the detectors and thus limiting their performances. The magnetic branches are clearly visible in Fig. 5, which shows the $|B|$ vector plots (normalized to the value of 2.7 T) in the xy plane at the axial positions $z = -100,\ 0, 100$ mm.

By employing the magnetic field profile obtained in the simulations, the distribution of lost electrons on chamber walls due to the magnetic branches has been calculated

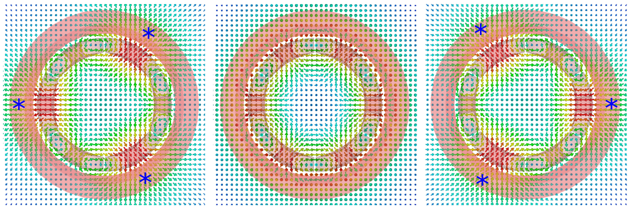

Figure 5: From left to right, $|B|$ vector plot along the xy plane at the positions $z = -100,\ 0, 100$ mm. The magnetic branches position are indicated by a blue marker.

through the use of a MATLAB particle mover code. Figure 6 shows the obtained lost electrons mask on chamber walls. The numerical study matches the expected branches position given from CST® and at the same time provides a lower boundary thickness of particle loss regions along the branches. These information are relevant for both designing the size of the bias-disk foreseen at the injection, and to find the optimal position for plasma diagnostics, microwave injection waveguides along the injection flange, as well as for the isotope injection systems (e. g., resistive oven).

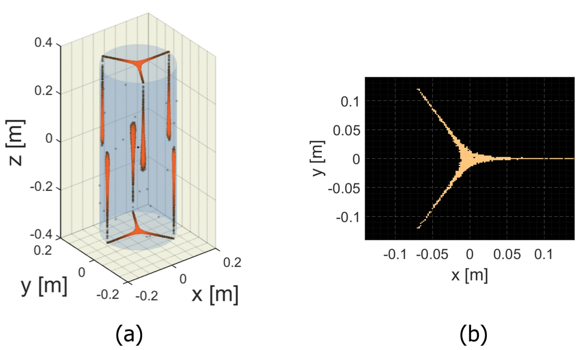

Figure 6: (a) 3D lost electron mask on chamber wall due to PANDORA magnetic branches disposition; (b) detail of lost electron mask on the injection end-plate ($z = 350$ mm, see reference system of Fig. 2).

CONCLUSION AND PERSPECTIVES

In this work the numerical design of the PANDORA magnetic system, for plasma confinement, has been presented. The design, whose scaling is based on the employment of 18 and 21 GHz pumping frequencies, has been carried out by using the commercial simulators OPERA® and CST®, whose results are in agreement between each other. By employing the obtained magnetic field profiles, the positions of the magnetic branches have been identified. These positions, along the plasma chamber side walls, are critical due to generated strong Bremsstralhung radiation and needs to be avoided when placing the gamma array detectors. Furthermore, the lost electron maps on the plasma chamber end plates have been calculated through the magnetic field profile: this information will be relevant both for the design of the bias-disk (at the injection end-plate) and for the correct placement of the plasma chamber diagnostics.

ACKNOWLEDGMENTS

The authors wish to thank INFN for the support through the project PANDORA Gr3 funded by 3rd Nat. Sci. Comm., and to thank the whole PANDORA collaboration.

REFERENCES

[1] D. Mascali *et al.*, "A novel approach to beta-decay: Pandora, a new experimental setup for future in-plasma measurements", *Universe*, vol. 8, no. 2, p. 80, 2022. doi:10.3390/universe8020080

[2] D. Leitner, "High Performance ECR Sources for Next-Generation Nuclear Science Facilities", in *Proc. 10th Int. Part. Accel. Conf. (IPAC'19)*, Melbourne, Australia, 19-24 May 2019, pp. 2224–2229. doi:10.18429/JACoW-IPAC2019-WEXPLS1

[3] J. Benitez, C. Lyneis, L. Phair, D. Todd, and D. Xie, "Dependence of the bremsstrahlung spectral temperature in minimum-B electron cyclotron resonance ion sources", *IEEE Trans. Plasma Sci.*, vol. 45, no. 7, pp. 1746–1754, 2017. doi:10.1109/TPS.2017.2706718

[4] M. Mazzaglia *et al.*, "Study of the Influence of Magnetic Field Profile on Plasma Parameters in a Simple Mirror Trap", in *Proc. ECRIS'18*, Catania, Italy, Sep. 2018, pp. 144–147. doi:10.18429/JACoW-ECRIS2018-TUP25

[5] D. Neben *et al.*, "X-ray investigation on the superconducting source for ions (SuSI)", *J. Instrum.*, vol. 14, no. 02, pp. C02008–C02008, 2019. doi:10.1088/1748-0221/14/02/c02008

[6] E. Naselli *et al.*, "Design study of a HPGe detectors array for β-decays investigation in laboratory ECR plasmas", *Front. Phys.*, vol. 10, 2022. doi:10.3389/fphy.2022.935728

ISBN: 978-3-95450-257-8 ISSN: 2222-5692 doi:10.18429/JACoW-ECRIS2024-THA3

WAVEGUIDE DC BREAKS WITH OPTIMIZED IMPEDANCE MATCHING NETWORKS*

M. Kireeff Covo†, J. Benitez, D. Todd, J. Cruz Duran, P. Bloemhard, M. Johnson, J. Garcia, B. Ninemire, D. Xie, and L. Phair, Lawrence Berkeley National Laboratory, CA, USA

Abstract

A custom 18 GHz waveguide DC break with a built-in impedance matching network, consisting of two inductive irises adjacent to a capacitive gap assembled around a quartz disk, was built for Versatile ECR for Nuclear Science (VENUS) ion source and simulated using the ANSYS High Frequency Structure Simulator, a finite element analysis tool. The DC break effectively doubled the RF power available for plasma production at the secondary frequency of 18 GHz while maintaining a DC isolation of 32 kV. Measurements of the forward and reflected power coefficients, performed with a network analyzer, showed excellent agreement with the simulations [1]. Additionally, an extended study was conducted to tailor the frequencies of 28, 35, and 45 GHz using WR-34, WR-28, and WR-22 waveguides with built-in impedance matching networks, aiming to predict performance for our upcoming 4th generation low-power, multi-frequency operation of the MARS-D ion source.

INTRODUCTION

The Versatile Electron Cyclotron Resonance (VENUS) ion source, developed at Lawrence Berkeley National Laboratory's 88-Inch Cyclotron [2], operates at frequencies of 28 GHz and 18 GHz. It utilizes a superconducting magnet system to generate a strong, well-defined magnetic field for confinement, creating two enclosed regions for plasma heating and enabling the production of ion beams with high charge states and intensities.

Since the VENUS ion source operates on a high-voltage platform meanwhile the RF system is at ground potential, a waveguide HV DC break is required to maintain isolation while allowing RF signals to pass with minimal microwave leakage and insertion losses [3].

DC breaks can be mainly categorized into two types. One common type is the choke flange [4–6], which creates a gap in the waveguide using dielectric materials to achieve isolation. Another type is the multi-layer DC break [7, 8], which uses multiple layers of insulating materials between sections of metal, enhancing the overall dielectric strength and reducing RF leakage. Some advanced designs use innovative techniques, such as a lattice structure made of dielectric materials [9] or tapered waveguide transitions combined with low-loss dielectrics [10]. To further enhance RF power delivery and compensate for waveguide mismatches, tuners equipped with screws, posts, or stubs are often used just before the DC break, improving impedance matching and maximizing power transfer to the plasma [11–13].

WAVEGUIDE DC BREAK

The DC break is constructed using two open-ended copper sections that conform to the WR-62 waveguide's dimensions, with a width of 15.8 mm and a height of 7.9 mm. This break includes a gap within the waveguide filled by a fused quartz disk, measuring 100 mm in diameter and 1 mm in thickness [14]. The quartz, known for its excellent thermal properties and high dielectric strength, allows the system to withstand up to 32 kV DC, furthermore, its low dielectric constant of 3.9 and very low dielectric loss tangent of less than 1×10^{-3} ensure minimal RF energy loss, calculated to be about 0.003 dB. This results in the primary losses being due to RF leakage, calculated by subtracting the total transmitted and reflected power from 100 %.

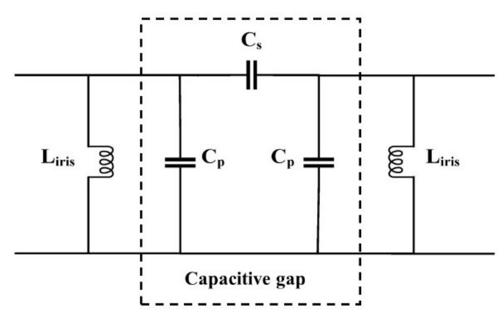

Figure 1: Waveguide DC break equivalent circuit.

To address impedance mismatches caused by the gap, the design incorporates two symmetrical inductive matching irises [15], each 1.85 mm thick, positioned adjacent to the gap. As illustrated in Fig. 1, the gap introduces lumped capacitance C_p due to fringing fields at the open-ended waveguides and series capacitive coupling C_s across the gap, leading to impedance mismatch. The irises generate lumped shunt inductances L_{iris}, which compensates for the lumped shunt capacitances C_p, effectively creating a band-pass filter centered around the desired frequency. Additionally, the waveguide apertures near the gap are expanded to form a

* Work supported by the Director, Office of Science, Office of Nuclear Physics, Division of Nuclear Physics, U.S. Department of Energy under Contract No. DE-AC02-05CH11231 and by the U.S. Army Program Executive Office, Simulation, Training and Instrumentation (PEO STRI), Test Resource Management Center (TRMC) Test and Evalua-tion/Science & Technology (T&E/S&T) Program. These projects are funded by the T&E/S&T Program through the U.S. Army Program Executive Office for Simulation, Training, and Instrumentation (PEO STRI) Instrumentation Management Office (IMO). Disclaimer: Any opinions, findings, and conclusions, or recommendations expressed in this material are those of the author(s) and do not necessarily reflect the views of the Test Resource Management Center (TRMC) Test and Evaluation/Science & Technology (T&E/S&T) Program and/or the Program Executive Office for Simulation, Training & Instrumentation (PEO STRI).
† mkireeffcovo@lbl.gov

ISBN: 978-3-95450-257-8 ISSN: 2222-5692 doi:10.18429/JACoW-ECRIS2024-THA3

circular surface with a diameter of 67.06 mm, resulting in a series capacitance of approximately 1207 pF at 18 GHz. This setup helps reduce reflections and minimize power loss.

Using Marcuvitz's formula, as shown in Eq. (1), for estimating inductive reactance [16], the design achieves an inductive reactance of 485.33 Ω, equivalent to an inductance of 4.29 nH, by choosing a window width of 7.87 mm and an iris width of 3.96 mm.

$$\frac{X_L}{Z_0} \approx \frac{a}{\lambda_g}\cot^2\frac{\pi d'}{a}\left[1+\frac{2}{3}\left(\frac{\pi d'}{\lambda}\right)^2\right], \quad \frac{d'}{a} \ll 1\,, \tag{1}$$

where X_L represents the inductive reactance, Z_0 is the characteristic impedance of the waveguide, a is the width of the waveguide, λ_g is the guide wavelength, d' is the effective width of the iris or discontinuity within the waveguide, and λ is the free-space wavelength.

The resonance frequency $\mathrm{f_r}$ can be calculated with the $\mathrm{L_{iris}}$ lumped inductance resultant from the iris in parallel with the $\mathrm{C_p}$ lumped parallel capacitance resultant from the open-ended waveguide, obtained from Eq. (2):

$$\mathrm{f_r} = \frac{1}{2\pi\sqrt{\mathrm{L_{iris}C_p}}}\,. \tag{2}$$

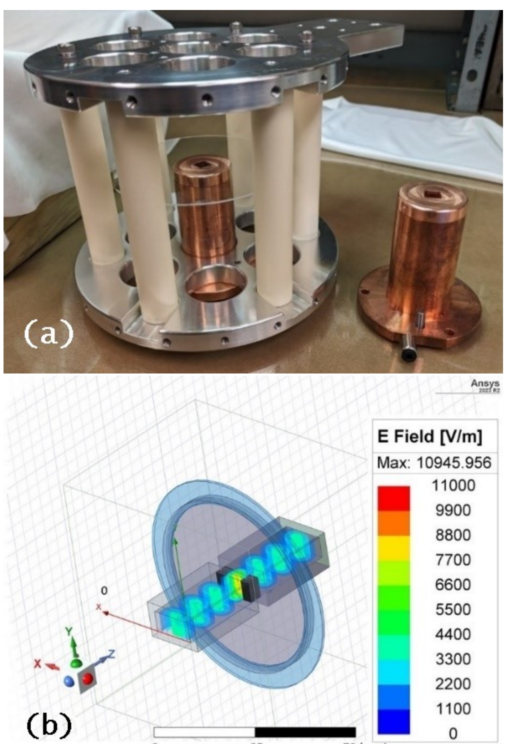

Figure 2: Waveguide DC break: (a) hardware with an inductive iris impedance matching network. One open ended waveguide section is placed aside. (b) HFSS simulated magnitude of the electric field for the TE10 mode.

Adjusting the iris width allows fine-tuning of the resonance frequency by changing $\mathrm{L_{iris}}$. This design ensures efficient RF transmission and minimizes losses, validated through simulations and experimental measurements to optimize the device for use at the klystron frequency of 18 GHz.

HARDWARE

The hardware shown in Fig. 2(a) consists of a WR-62 waveguide within a copper cylindrical structure, featuring a gap for series capacitance, nitrogen gas injection for a non-reactive environment, and ceramic standoffs securing the components, all encased in a metallic shield to prevent RF leakage (not shown in the image).

The HFSS [17] 3D model shown in Fig. 2(b) displays the electric field distribution for the TE10 mode at 18 GHz and it is used for simulating RF transport. The mesh was refined to a maximum element length of 5 mm, utilizing broadband adaptive solutions from 11.6 to 18.6 GHz, with the waveguide constructed from a perfect electric conductor.

Figure 3 shows that the resonance frequency is determined by the minimum S_{11} value in the simulation, indicating optimal impedance matching, while the S_{21} parameter measures the efficiency of RF power transmission through the waveguide. Measurements performed with a network analyzer show excellent agreement with the simulation.

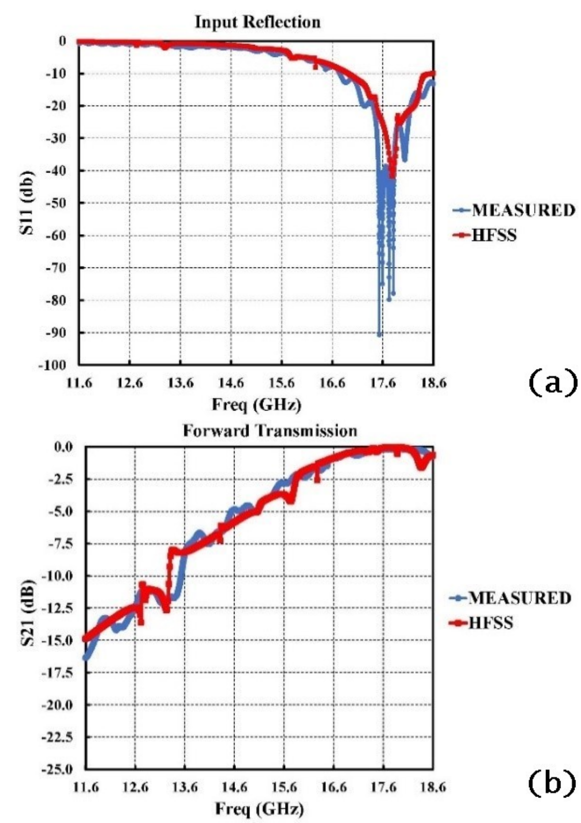

Figure 3: Comparison of S parameters obtained with HFSS simulations and measurements: (a) S_{11} input reflection, (b) S_{22} forward transmission.

The new DC break effectively doubled the RF power available for plasma production at the secondary frequency of 18 GHz while maintaining a DC isolation of 32 kV.

26th Int. Workshop Electron Cyclotron Resonance Ion Sources ECRIS2024, Darmstadt, Germany JACoW Publishing
ISBN: 978-3-95450-257-8 ISSN: 2222-5692 doi:10.18429/JACoW-ECRIS2024-THA3

OPTIMIZATION

To predict performance for our upcoming 4th generation low-power, multi-frequency operation of the MARS-D ion source, an extended study was conducted to tailor the frequencies of 28, 35, and 45 GHz using WR-34, WR-28, and WR-22 waveguides with built-in impedance matching networks, aiming to optimize the HV DC break.

Since MARS-D requires an isolation of 45 kV, a feasibility study was performed with the WR-22 waveguide dimensions. In the simulation, the quartz thickness was gradually increased until it nearly doubled, with the corresponding resonant frequency shown in Fig. 4. As the thickness increased, the resonant frequency f_r decreased due to the increase in shunt capacitance C_p and decrease of the series capacitance C_s. Simultaneously, the insertion loss and the RF leakage also increases.

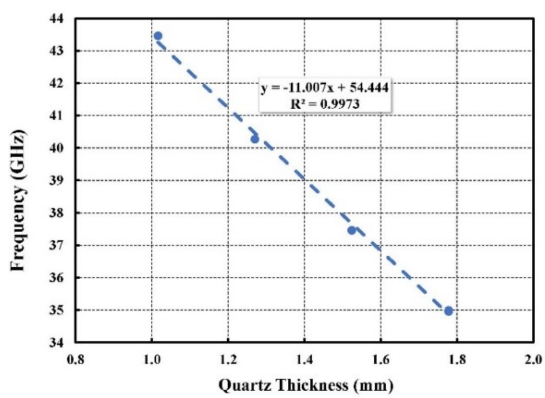

Figure 4: Resonant frequency versus Quartz thickness.

An improved approach to achieve 45 kV isolation is to maintain the quartz thickness of 1 mm and introduce a second gap with additional set of irises, placed at least a couple of wavelengths apart in the waveguide, as shown in the model of Fig. 5. The impedance matching is expected to occur at the same frequency as the first set of irises, with reduced RF leakage and enhanced impedance matching.

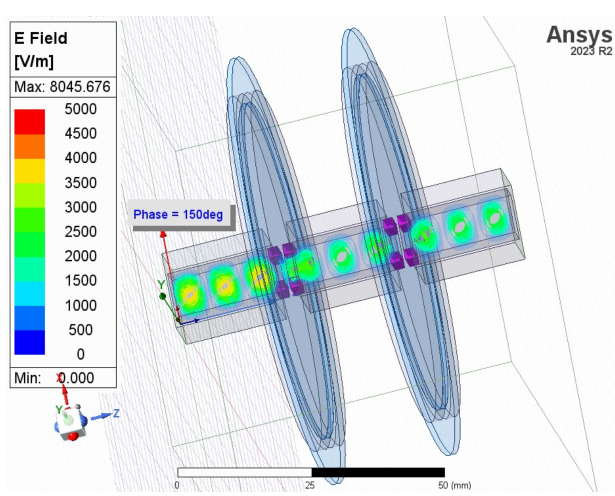

Figure 5: Waveguide DC break with DC isolation of 64 kV.

RESULTS

Table 1 summarizes the required inductive iris aperture *W* for each waveguide type in the new configuration, ensuring proper impedance matching at the target frequencies.

Table 1: Inductive Iris Aperture

Waveguide	*W* [mm]	*f* [GHz]	S_{11} [dB]	S_{21} [dB]
WR34	4.32	28	–39.21	–0.06
WR28	3.20	35	–37.97	–0.04
WR22	2.23	45	–24.30	–0.03

CONCLUSION

The inclusion of inductive irises and quartz-filled capacitive gaps within the waveguide structure has effectively reduced power loss and minimized mismatches at the target frequencies. The successful simulations and measurements underscore the reliability of this design, not only for the VENUS ion source but also as a scalable solution for future MARS-D multi-frequency ion sources.

ACKNOWLEDGEMENTS

The authors thank Brendan P. Ford, Nathaniel Bohm, Erik Line, and Collin Anderson, Shane Blim for their electronics support; Alexander Donoghue, Scott M. Small, Nicholas M. Brickner, Nishi Intwala, Patrick Coleman, and Devin T. Thatcher for their operations support; and Nathan Seidman, Roman Nieto, Donald Bell, and Sixuan Zhong for their mechanical support of the LBNL 88-Inch Cyclotron.

REFERENCES

[1] M. Kireeff Covo *et al.*, "Inductive Iris Impedance Matching Network for a Compact Waveguide DC Break", *IEEE Trans. Microwave Theory Tech.*, early access 2024. doi:10.1109/TMTT.2024.3409470

[2] M. Kireeff Covo *et al.*, "The 88-Inch Cyclotron: A one-stop facility for electronics radiation and detector testing", *Meas.*, vol. 127, pp. 580-587, 2018. doi:10.1016/j.measurement.2017.10.018.M

[3] M.S. Dmitriyev, M.V. Dyakonov, S.A. Tumanov, and M.I. Zhigailova, "DC break design for a 2.45 GHz ECR ion source", in *Proc. 12th Int. Particle Acc. Conf. (IPAC'21)*, São Paulo, Brazil, 2021, pp. 3064-3065. doi:10.18429/JACoW-IPAC2021-WEPAB190

[4] V. Buiculescu and A. Ştefănescu, "Choke flange-like structure for direct connection of cascaded substrate integrated waveguide components", *Electron. Lett.*, vol. 48, no. 21, pp. 1349-1350, Oct. 2012. doi:10.1049/el.2012.2901

[5] A. Misra, I. Chatterjee, and P.Y. Nabhiraj, "Studies on equivalent circuit approach to design waveguide break for 14.45 GHz ECR ion source", in *Proc. IEEE MTT-S Int. Microwave RF Conf. (IMaRC)*, Kolkata, India, 2018, pp. 1-3. doi:10.1109/IMaRC.2018.8877158

ISBN: 978-3-95450-257-8 ISSN: 2222-5692 doi:10.18429/JACoW-ECRIS2024-THA3

[6] M.S. Dmitriev, M.V. Dyakonov, and S.A. Tumanov, "Waveguide Development for a 2.46 GHz Electron Cyclotron Resonance Ion Source", *Phys. Atom. Nuclei*, vol. 85, pp. 1899-1901, 2022. doi:10.1134/S1063778822100143

[7] Y.S. Cho, D.I. Kim, H.S. Kim, K.T. Seol, and H.J. Kwon, "Multi-layered waveguide DC electrical break for the PEFP microwave proton source", *J. Korean Phys. Soc.*, vol. 63, pp. 2085-2088, 2013. doi:10.3938/jkps.63.2085

[8] J. Jo, S.H. Kim, J.-T. Jin, and S.-R. Huh, "Development of waveguide DC break for power transmission at 2.45 GHz and 100-kV insulation", *IEEE Microw. Wireless Compon. Lett.*, vol. 30, no. 4, pp. 339-342, Apr. 2020. doi:10.1109/LMWC.2020.2978639

[9] G.S. Mauro, A. Locatelli, G. Torrisi, L. Celona, C. De Angelis, and G. Sorbello, "Woodpile EBG waveguide as a DC electrical break for microwave ion sources", *Microw. Opt. Technol. Lett.*, vol. 61, pp. 610-614, 2019. doi:10.1002/mop.31628

[10] O. Leonardi, G. Torrisi, G. Sorbello, L. Celona, and S. Gammino, "A compact DC-break for ECR ion source @ 18 GHz", *Microw. Opt. Technol. Lett.*, vol. 60, pp. 3026-3029, 2018. doi:10.1002/mop.31421

[11] L. Celona, G. Ciavola, and S. Gammino, "Study of microwave coupling in electron cyclotron resonance ion sources and microwave ion sources", *Rev. Sci. Instrum.*, vol. 69, no. 2, pp. 1113-1115, Feb. 1998. doi:10.1063/1.1148640

[12] T. Taylor and J.F. Mouris, "An advanced high-current low-emittance dc microwave proton source", *Nucl. Instrum. Methods Phys. Res., Sect. A*, vol. 336, no. 1-2, pp. 1-5, Jan. 1993. doi:10.1016/0168-9002(93)91074-W

[13] F. Maimone, L. Celona, and F. Chines, "Status of the versatile ion source VIS", in *Proc. EPAC'08*, Genoa, Italy, 2008, paper MOPC151. https://jacow.org/e08/papers/mopc151.pdf

[14] Valley Design Corp., https://valleydesign.com/

[15] D.M. Pozar, *Microwave Engineering*, 4th ed., New York, NY, USA: Wiley, 2011.

[16] N. Marcuvitz, *Waveguide Handbook*, MIT Radiation Laboratory Series, New York, NY, USA: McGraw-Hill, 1986, pp. 223-224.

[17] Ansys HFSS, https://www.ansys.com/products/electronics/ansys-hfss

ISBN: 978-3-95450-257-8 ISSN: 2222-5692 doi:10.18429/JACoW-ECRIS2024

ISBN: 978-3-95450-257-8 ISSN: 2222-5692 doi:10.18429/JACoW-ECRIS2024

List of Authors

Bold papercodes indicate primary authors; ~~strike through/black~~ papercodes indicate **no submission received**

ISBN: 978-3-95450-257-8 ISSN: 2222-5692 doi:10.18429/JACoW-ECRIS2024

ISBN: 978-3-95450-257-8 ISSN: 2222-5692 doi:10.18429/JACoW-ECRIS2024

ISBN: 978-3-95450-257-8 ISSN: 2222-5692 doi:10.18429/JACoW-ECRIS2024

Institutes List

Aarhus University
Aarhus, Denmark
- Ioppolo, S.

Abstract Landscapes
Montpellier, France
- Penescu, L.C.

ANL
Lemont, Illinois, USA
- McLain, J.T.
- Scott, R.H.
- Vondrasek, R.C.

Atomki
Debrecen, Hungary
- Biri, S.
- Herczku, P.
- Juhász, Z.
- Kovács, S.T.S.
- Kushwaha, R.K.
- Lakatos, G.
- Mifsud, D.V.
- Perduk, Z.
- Rácz, R.
- Sulik, B.

CEA-IRFU
Gif-sur-Yvette, France
- Barant, M.
- Bolzon, B.
- Cadoux, T.
- Delferrière, O.
- Dubois, A.
- Felice, H.
- Ferrand, G.
- Gauthier, Y.
- Plouin, J.
- Sauce, Y.
- Schwindling, J.
- Simon, D.
- Thézé, A.
- Tuske, O.
- Uriot, D.

CERN
Geneva, Switzerland
- Bellodi, G.
- Bhaskar, B.S.
- Bruchon, N.
- Kain, V.
- Küchler, D.
- Rodriguez Mateos, B.
- Scrivens, R.
- Slupecki, M.

D-Pace
Nelson, British Columbia, Canada
- Dehnel, M.P.
- George, A.M.
- Melanson, S.V.
- Sumar, S.

DREEBIT
Großröhrsdorf, Germany
- Molodtsova, M.
- Philipp, A.
- Ritter, E.

EBG MedAustron
Wr. Neustadt, Austria
- Gambino, N.
- Guidoboni, G.
- Kausel, M.
- Maderböck, C.
- Myalski, S.
- Rizzoglio, V.
- Schmitzer, C.

FRIB
East Lansing, MI, USA
- Cheng, H.Y.
- Guo, J.W.
- Machicoane, G.
- Tobos, L.

Fundación TEKNIKER
Ebar (Gipuzkoa), Spain
- Ariz, I.
- Seara Eizaguirre, J.M.

GANIL
Caen, France
- Chauveau, P.
- Dessay, E.
- Dubois, A.
- Dubois, M.
- Frigot, R.
- Gouleuf, L.
- Jacquot, B.
- Lalande, M.
- Lemagnen, F.
- Lucarz, B.
- Metayer, V.
- Michel, C.B.
- Osmond, B.

Grenoble High Magnetic Field Laboratory
Grenoble, France
- Debray, F.

GSI
Darmstadt, Germany
- Andreev, A.
- Boos, E.
- Franchetti, G.
- Galonska, M.
- Graeff, C.
- Hollinger, R.
- Lang, R.
- Maimone, F.
- Mäder, J.
- Volz, L.
- Zhang, C.

ISBN: 978-3-95450-257-8 ISSN: 2222-5692 doi:10.18429/JACoW-ECRIS2024

HFHF
Frankfurt am Main, Germany
- Zhang, C.

HIT
Heidelberg, Germany
- Cee, R.
- Haberer, Th.
- Naas, B.
- Peters, A.
- Winkelmann, T.

IAP
Frankfurt am Main, Germany
- Boos, E.
- Händler, M.A.
- Zhang, C.

IBS
Daejeon, Republic of Korea
- Heo, Q.
- Hong, I.S.
- Kim, H.J.

Ikerbasque
Bilbao, Spain
- Feuchtwanger, J.

IMP/CAS
Lanzhou, People's Republic of China
- Cao, Y.
- Fang, X.
- Feng, Y.C.
- Hitz, D.
- Li, J.B.
- Li, J.Q.
- Li, L.B.
- Li, L.X.
- Liu, Y.G.
- Lu, W.
- Ma, H.Y.
- Ma, J.D.
- Mei, E.M.
- Ou, X.J.
- Peng, P.
- Qian, C.
- Sun, L.T.
- Wang, X.D.
- Wu, B.M.
- Wu, Q.
- Wu, W.
- Yang, T.
- Zhang, W.H.
- Zhang, X.Z.
- Zhao, H.W.
- Zheng, S.J.
- Zhu, L.

INFN-LNL
Legnaro (PD), Italy
- Bellan, L.
- Carletto, O.
- Comunian, M.
- Francescon, P.
- Galatà, A.
- Gallo, C.S.
- Grespan, F.
- Martini, D.
- Santonocito, D.

INFN-LNS
Catania, Italy
- Castro, G.
- Celona, L.
- Finocchiaro, G.
- Gammino, S.
- Leonardi, O.
- Marletta, S.
- Mascali, D.
- Mauro, G.S.
- Miraglia, A.
- Mishra, B.
- Naselli, E.
- Neri, L.
- Passarello, S.
- Peri, B.
- Pidatella, A.
- Russo, A.D.
- Russo, F.
- Santonocito, D.
- Torrisi, G.

INFN/LNL
Legnaro (PD), Italy
- Mascali, G.R.

Institute for Plasma Research
Bhat, Gandhinagar, India
- Abhangi, M.
- Kumar, R.
- Swami, H.L.
- Vala, S.J.

IUAC
New Delhi, India
- Rodrigues, G.O.

LANITH
Lanzhou, People's Republic of China
- Jin, G.

LBNL
Berkeley, CA, USA
- Benitez, J.Y.
- Bloemhard, P.
- Covo, M.K.
- Crawford, H.
- Cruz Duran, J.
- Garcia, J.P.
- Holter, S.
- Johnson, M.B.
- Kireeff, A.
- Lai, Y.S.
- Ninemire, B.
- Phair, L.
- Salathe, M.

ISBN: 978-3-95450-257-8 ISSN: 2222-5692 doi:10.18429/JACoW-ECRIS2024

- Todd, D.S.
- Watson, V.
- Xie, D.Z.

LPSC
Grenoble Cedex, France
- Angot, J.
- Cernuschi, A.
- Cheymol, B.
- Kasulja, M.
- Lagorio, E.
- Peaucelle, C.
- Thuillier, T.
- Vezzu, F.

LPSC-IN2P3
Grenoble Cedex, France
- Andre, T.
- Angot, J.
- Baylac, M.A.
- Cernuschi, A.
- Dumont, P.-O.
- Labussière, E.
- Migliore, M.
- Peaucelle, C.
- Sole, P.
- Thuillier, T.
- Zimmermann, O.

Mirrotron Ltd.
Budapest, Hungary
- Mezei, F.

National Institute of Information and Communications Technology
Tokyo, Japan
- Oka, N.

NSCL
East Lansing, Michigan, USA
- Rencsok, R.J.

Osservatorio Etneo Sezione di Catania
Catania, Italy
- Bilotta, G.

PKU
Beijing, People's Republic of China
- Chen, J.E.
- Cui, B.J.
- Dong, Y.C.
- Guo, Z.Y.
- Li, K.
- Ma, T.H.
- Peng, S.X.
- Wu, W.B.

Private Address
,
- Kövener, T.

PSI
Villigen PSI, Switzerland
- Wang, X.

Queen's University Belfast
Belfast, United Kingdom
- Field, T.A.
- McCullough, R.W.

R&M Technical Enterprises
Pleasanton, CA, USA
- Hamm, R.W.

RIKEN
Saitama, Japan
- Morita, Y.
- Nishi, T.

RIKEN Nishina Center
Wako, Japan
- Higurashi, Y.
- Kamigaito, O.
- Nagatomo, T.
- Ohnishi, J.
- Saquilayan, G.Q.

Rikkyo University
Tokyo, Japan
- Kasagi, A.

Sapienza University of Rome
Rome, Italy
- Mascali, G.R.

SHI
Kanagawa, Japan
- Mikami, Y.
- Murase, R.
- Murata, H.
- Takahashi, N.
- Yokoyama, K.

STFC/RAL/ISIS
Chilton, Didcot, Oxon, United Kingdom
- Tarvainen, O.A.

The Hebrew University of Jerusalem
Jerusalem, Israel
- Bhattacharya, S.
- Paul, M.

TRIUMF
Vancouver, Canada
- Adegun, J.A.
- Ames, F.
- Charles, C.R.J.
- Jayamanna, K.
- Kester, O.K.
- Schultz, B.E.

TU Darmstadt
Darmstadt, Germany
- Graeff, C.

UCAS
Beijing, People's Republic of China
- Zhao, H.W.

ISBN: 978-3-95450-257-8 ISSN: 2222-5692 doi:10.18429/JACoW-ECRIS2024

UCL
Louvain-la-Neuve, Belgium
- Hocquet, F.-P.
- Postiau, N.
- Standaert, L.

UGR
Granada, Spain
- Praena, J.
- Roldán, A.

University of Eastern Finland
Joensuu, Finland
- Huovila, J.O.

University of Jyväskylä
Jyväskylä, Finland
- Koivisto, H.A.
- Toivanen, V.

University of Kent
Canterbury, United Kingdom
- Mason, N.J.

University of Salzburg
Salzburg, Austria
- Hirlaender, S.

University of the Basque Country (UPV/EHU)
Leioa, Spain
- Arredondo, I.
- Fernández-Rua, A.
- Feuchtwanger, J.
- Justo, R.
- Usabiaga, P.

University of the Basque Country, Faculty of Science and Technology
Bilbao, Spain
- Arredondo, I.
- Etxebarria, V.
- Portilla, J.
- Pérez, A.
- Vivas, J.

University of Tokyo
Tokyo, Japan
- Kamakura, K.

Università degli Studi di Catania
Catania, Italy
- Boscarino, S.
- Coco, A.
- Russo, G.

ISBN: 978-3-95450-257-8 ISSN: 2222-5692 doi:10.18429/JACoW-ECRIS2024

Participants List

— A —

Adegun, Adedapo J.
TRIUMF
Canada

Adonin, Aleksey
GSI Helmholtzzentrum für Schwerionenforschung GmbH (GSI)
Germany

Ames, Friedhelm
TRIUMF
Canada

André, Thomas
Université Grenoble-Alpes (CNRS-IN2P3)
France

Andreev, Aleksandr
GSI Helmholtzzentrum für Schwerionenforschung GmbH (GSI)
Germany

Angot, Julien
Université Grenoble-Alpes (CNRS-IN2P3)
France

Arredondo, Iñigo
University of the Basque Country
Spain

— B —

Benitez, Janilee
Lawrence Berkeley National Laboratory (LBNL)
USA

Berezov, Rustam
GSI Helmholtzzentrum für Schwerionenforschung GmbH (GSI)
Germany

Bertrand, Vincent
Pantechnik
France

Bhaskar, Bichu
European Organization for Nuclear Research (CERN)
Switzerland

— C —

Calabretta, Luciano
Transmutex SA
Italy

Castro, Giuseppe
Istituto Nazionale di Fisica Nucleare (INFN/LNS) Laboratori Nazionali del Sud
Italy

Cavellier, Matthieu
Pantechnik
France

Celona, Luigi
Istituto Nazionale di Fisica Nucleare (INFN/LNS) Laboratori Nazionali del Sud
Italy

Cernuschi, Andrea
Université Grenoble-Alpes (CNRS-IN2P3)
France

Covo, Michel Kireeff
Lawrence Berkeley National Laboratory (LBNL)
USA

Cui, Bujian
State Key Laboratory of Nuclear Physics and Technology, Peking University
China

— D —

Debes, Markus
PINK GmbH Vakuumtechnik
Germany

Delferrière, Olivier
Commissariat à l'Energie Atomique (CEA-IRFU)
France

Dubois, Augustin
Commissariat à l'Energie Atomique (CEA-IRFU)
France

Dubois, Mickael
Grand Accélérateur Nat. d'Ions Lourds (GANIL)
France

Dyck, Käthy
Kashiyama Europe GmbH
Japan

— E —

Euler, Andreas
Sumitomo SHI Cryogenics Group
Japan

— F —

Feuchtwanger Morales, Jorge
University of the Basque Country
Spain

Filliger, Michel
Institut Pluridisciplinaire Hubert Curien (CNRS/IPHC)
France

Frigot, Romain
Grand Accélérateur Nat. d'Ions Lourds (GANIL)
France

Funcke, Robert
InfraSolution AG
Germany

— G —

Galatà, Alessio
Istituto Nazionale di Fisica Nucleare (INFN/LNL) Laboratori Nazionali di Legnaro
Italy

Gall, Benoit
Institut pluridisciplinaire Hubert Curien
France

Gallo, Carmelo S.
Istituto Nazionale di Fisica Nucleare (INFN/LNL) Laboratori Nazionali di Legnaro
Italy

ISBN: 978-3-95450-257-8 ISSN: 2222-5692 doi:10.18429/JACoW-ECRIS2024

Galonska, Michael
GSI Helmholtzzentrum für
Schwerionenforschung GmbH (GSI)
Germany

Gambino, Nadia
MedAustron EBG
Austria

Geithner, Wolfgang
GSI Helmholtzzentrum für
Schwerionenforschung GmbH (GSI)
Germany

González Caminal, Pau
Fusion for Energy (External)
Spain

Guo, Junwei
Facility for Rare Isotope Beams
Michigan State University (FRIB/MSU)
USA

— H —

Händler, Michael
Institut für Angewandte Physik (IAP),
GSI Helmholtzzentrum für
Schwerionenforschung GmbH (GSI)
Germany

Heo, Jeong Il
Institute for Basic Science (IBS)
South Korea

Herfurth, Frank
GSI Helmholtzzentrum für
Schwerionenforschung GmbH (GSI)
Germany

Hocquet, François-Philippe
Université Catholique de Louvain - Centre de
Recherches du Cyclotron (UCLouvain/CRC)
Blgium

Hollinger, Ralph
GSI Helmholtzzentrum für
Schwerionenforschung GmbH (GSI)
Germany

Höltermann, Holger
BEVATECH GmbH
Germany

Hufnagel, Alexander
Sumitomo SHI Cryogenics Group
Japan

Hustings, Jeroen
Belgian Nuclear Research Centre in Mol
(SCK CEN)
Belgium

— J —

Jakhar, Niketan
Jawaharlal Nehru University, New Delhi
India

— K —

Koivisto, Hannu
University of Jyväskylä
Department of Physics
Finland

Kremers, Herman
University of Groningen
Netherlands

Küchler, Detlef
European Organization for Nuclear Research
(CERN)
Switzerland

— L —

Lang, Ralf
GSI Helmholtzzentrum für
Schwerionenforschung GmbH (GSI)
Germany

Li, Jiaqing
Institute of Modern Physics (IMP/CAS)
China

Li, Lixuan
Institute of Modern Physics (IMP/CAS)
China

Lindenberg, Paola
GSI Helmholtzzentrum für
Schwerionenforschung GmbH (GSI)
Germany

Liu, Yirou
WISMAN – HV Power Supply
China

Lu, Wang
Institute of Modern Physics (IMP/CAS)
China

— M —

Machicoane, Guillaume
Facility for Rare Isotope Beams
Michigan State University (FRIB/MSU)
USA

Mäder, Jan
GSI Helmholtzzentrum für
Schwerionenforschung GmbH (GSI)
Germany

Maimone, Fabio
GSI Helmholtzzentrum für
Schwerionenforschung GmbH (GSI)
Germany

Mascali, David
Istituto Nazionale di Fisica Nucleare
(INFN/LNS) Laboratori Nazionali del Sud
Italy

Mascali, Giada Rachele
Sapienza University of Rome,
Istituto Nazionale di Fisica Nucleare
(INFN/LNL) Laboratori Nazionali di Legnaro
Italy

Mathias, Barant
Commissariat à l'Energie Atomique
(CEA-IRFU)
France

Maunoury, Laurent
Normandy Hadrontherapy
France

Mauro, Giorgio Sebastiano
Istituto Nazionale di Fisica Nucleare
(INFN/LNS) Laboratori Nazionali del Sud
Italy

McLain, Jake
Argonne National Laboratory (ANL)
USA

ISBN: 978-3-95450-257-8 ISSN: 2222-5692 doi:10.18429/JACoW-ECRIS2024

Mei, Enming
Institute of Modern Physics (IMP/CAS)
China

Melanson, Stephane
D-pace
USA

Meng, Xiancai
Institute of Energy, Hefei Comprehensive National Science Center
China

Molodtsova, Maria
DREEBIT GmbH
Germany

Morita, Yasuyuki
Nishina Center for Accelerator-Based Science (RIKEN)
Japan

Mueller, Raphael
GSI Helmholtzzentrum für Schwerionenforschung GmbH (GSI)
Germany

Murase, Ryu
Sumitomo Heavy Industries, Ltd.
Japan

— N —

Naselli, Eugenia
Istituto Nazionale di Fisica Nucleare (INFN/LNS) Laboratori Nazionali del Sud
Italy

Neilson, Joshua
Nusano
USA

Neri, Lorenzo
Istituto Nazionale di Fisica Nucleare (INFN/LNS) Laboratori Nazionali del Sud
Italy

— P —

Peng, Shixiang
Peking University
China

Pérez, Andoni
University of the Basque Country
Spain

Philipp, Alexandra
Dreebit GmbH
Germany

Pidatella, Angelo
Istituto Nazionale di Fisica Nucleare (INFN/LNS) Laboratori Nazionali del Sud
Italy

— Q —

Qian, Cheng
Institute of Modern Physics (IMP/CAS)
China

— R —

Rácz, Richard
HUN-REN Institute for Nuclear Research (ATOMKI)
Hungary

Rodrigues, Gerard
Inter University Accelerator Centre
India

Rosenthal, Glenn
Nusano
USA

— S —

Saquilayan, Glynnis Mae
Nishina Center for Accelerator-Based Science (RIKEN)
Japan

Schaa, Volker RW
GSI Helmholtzzentrum für Schwerionenforschung GmbH (GSI)
Germany

Scott, Robert
Argonne National Laboratory (ANL)
USA

Solodko, Evgeny
Transmutex
Switzerland

Standaert, Laurent
Université Catholique de Louvain - Centre de Recherches du Cyclotron (UCLouvain/CRC)
Belgium

Strehl, Dirk
BEVATECH GmbH
Germany

Sun, Liangting
Institute of Modern Physics (IMP/CAS)
China

— T —

Thuillier, Thomas
Université Grenoble-Alpes (CNRS-IN2P3)
France

Todd, Damon
Lawrence Berkeley National Laboratory (LBNL)
USA

Toivanen, Ville
University of Jyväskylä Department of Physics (JYFL)
Finland

Tuske, Olivier
Commissariat à l'Energie Atomique (CEA-IRFU)
France

— V —

Vala, Sudhirsinh
Institute for Plasma Research
India

— W —

Weissmann, Leonid
Soreq, NRC
Israel

Winkelmann, Tim
HIT Heidelberg
Germany

Wu, Qi
Institute of Modern Physics (IMP/CAS)
China

ISBN: 978-3-95450-257-8 ISSN: 2222-5692 doi:10.18429/JACoW-ECRIS2024

Wunderlich, Lea
GSI Helmholtzzentrum für Schwerionenforschung GmbH (GSI)
Germany

— Y —

Yan, Mei
WISMAN – HV Power Supply
China

— Z —

Zhang, Chuan
GSI Helmholtzzentrum für Schwerionenforschung GmbH (GSI)
Germany

Zhao, Hongwei
Institute of Modern Physics (IMP/CAS)
China